The University of Sheffield

Investigation of Partitioned Stator Permanent Magnet Linear Machines

Ahlam Luaibi Shuraiji Al-Lami

A thesis submitted for the degree of Doctor of Philosophy

Department of Electronic and Electrical Engineering

The University of Sheffield

Mapping Street, Sheffield, S1 3JD, UK

December 2016

Abstract

Three novel types of permanent magnet linear machines have been investigated in this thesis, viz. partitioned stator flux reversal permanent magnet (PS-FRPM) planar machine, partitioned stator permanent magnet (PS-PM) tubular machines and partitioned stator single phase short stroke permanent magnet (PS-SPSSPM) tubular machines.

PS-PM machines are distinguished by having two active stators and one passive mover. Such configurations offer better inner space utilization as well as enhanced electrical and magnetic loadings. A novel PS-FRPM linear machine is introduced by adopting the idea of PS-PM machine. The machine structure and operation principle are described. In addition, the force production mechanism of the proposed machine is analysed. Furthermore, the machine performance in terms of open circuit and load characteristics, losses and demagnetization withstand capability are investigated. To validate finite element predicted results, a prototype is manufactured and tested.

Linear machine with tubular configuration is of great interest in terms of no end winding effect and no net attractive force between the stator and the mover. PS-PM tubular machines, i.e. PS-SPM and PS-IPM are designed and optimized for maximum thrust force capability. Moreover, the influence of the major design parameters on the machine thrust force is investigated. A comparison between both PS-PM tubular machines is carried out. Furthermore, PS-PM tubular machines having single-layer winding configuration are designed and compared to that with double-layer winding configuration counterparts. It is found that better performance can be delivered by single-layer winding PS-PM tubular machines.

The interest of single phase short stroke permanent magnet tubular machines (SPSS-PMTMs) is considerably increased over last few years, and they have been employed in healthcare, wave energy extraction, and household appliance. Novel PS-SPSS-PMTMs, named as PS-SPSS-SPMTM and PS-SPSS-IPMTM, are investigated. The optimized machine performances are analysed and compared. It is shown that the machines have the advantages of light mover mass and low eddy current loss.

Finally, comparisons between the proposed machines and their conventional counterparts are carried out. It is found that the proposed PS-FRPM linear and PS-PM tubular machines exhibit higher thrust force density, better PM utilization, lower magnet eddy current loss and better demagnetization withstand capability compared to their conventional counterparts, i.e. FRPM, SFPM linear machines and SFPM tubular machine, respectively.

Acknowledgements

I would like to express my sincere gratitude to my supervisor, Prof. Z. Q. Zhu, for his professional technical guidance, encouragement, advice, and unlimited patience throughout this PhD study. Without our weekly meetings and his valuable feedbacks, I would not be able to complete this thesis.

I am grateful to Prof. Qinfen Lu at Zhejiang University, China, for her beneficial help to manufacture and test the prototype.

My deep thanks also go to the members of the Electrical Machines and Drive Group at the University of Sheffield who support and advise me through my study.

I would like to thank the Iraqi Government/Ministry of Higher Education and Scientific Research, for financial support for my PhD study.

My deep thanks and appreciations also go to my family members and friends, for their continuous support, encouragement and endless care.

I dedicate this thesis to my dad (1948-2016), and to Imam Al-Mahdi Al-Muntadhar (Allah hasten his reappearance).

Nomenclature

B_{max}	Flux density	T
F_b	Backward MMF	A
F_{cog}	Cogging force of the actual model	N
$F_{end\ effect}$	Cogging force due to the longitudinal end effect	N
F_f	Forward MMF	A
$F_{o/p}$	Output thrust force	N
F_s	Total MMF distribution of three phase windings	A
F_{slot}	Cogging force of the periodic model	N
I	Current amplitude	A
I_a	Phase A current	A
I_b	Phase B current	A
I_c	Phase C current	A
I_d	d-axis current	A
I_q	q-axis current	A
I_{rms}	RMS value of phase current	A
K_h, K_e, a_h, b_h	Material coefficients	
K_f	Friction factor	
L_{AA}	Phase A self- inductance	H
L_{AB}	Mutual-inductance between phases A and B	H
L_d	d-axis inductance	H
L_q	q-axis inductance	H
N_C	Common multiple between N_S and N_m	
N_a	Number of turns per phase	
$N_a(\phi)$	Winding function of phase A	
$N_b(\phi)$	Winding function of phase B	
$N_c(\phi)$	Winding function of phase C	
N_m	Number of mover pole	
N_n	Magnitude of the nth- order MMF harmonic	
N_s	Stator slo number	
P_{hyst}	Hysteresis loss	W

P_{class}	Classical eddy-current loss	W
P_{cu}	Copper loss	W
P_{excess}	Excess eddy-current loss	W
P_{iron}	Iron loss	W
T_{cycle}	Time cycle	s
V_a	Phase A voltage	V
V_b	Phase B voltage	V
V_c	Phase C voltage	V
V_d	d-axis voltage	V
V_q	q-axis voltage	V
V	Velocity	m/s
R	Phase resistance	Ω
S_a	Slot area	m^2
d_{iron}	Iron lamination thickness	m
k_{pf}	Packing factor	
l_a	Active length	m
m	Mover mass	g
m_v	Iron lamination mass density	g/m^3
θ_e	Mover position in electrical degree	elec.˚
θ_m	Mover position in mechanical degree	mech.˚
ρ_{iron}	Iron lamination resistance	Ωm
ψ_d	d-axis flux linkage	Wb
ψ_{PM}	Flux linkage due to permanent magnet	Wb
ψ_a	Phase A flux linkage	Wb
ψ_b	Phase B flux linkage	Wb
ψ_c	Phase C flux linkage	Wb
ψ_q	q-axis flux linkage	Wb
ρ	Copper resistivity	Ωm
ϕ	Spatial angle	rad
ω	Angular frequency	rad/s
τ	Pole pitch	m

Abbreviations

CAD	Computer aided design
DC	Direct current
EMF	Electromotive force
FE	Finite element
FRPM	Flux reversal permanent magnet
GA	Genetic Algorithm
IPM	Interior permanent magnet
MMF	Magneto motive force
NEMC	Nonlinear equivalent magnet circuit
PM	Permanent magnet
PS-FRPM	Partitioned stator flux reversal permanent magnet
PS-PM	Partitioned stator permanent magnet
PS-SPSS-PM	Partitioned stator single-phase short stroke permanent magnet
SFPM	Switched flux permanent magnet
SPM	Surface mounted permanent magnet
SR	Switched reluctance
VPM	Verner permanent magnet

Contents

Chapter1. General Introduction

1.1 Introduction

Permanent magnet (PM) machines have dominated the research field in literature since the development of high energy-product PM materials, such as NdFeB in the early 1980s and SmCo in the late 1960s. Due to these strong magnets, PM machines possess unique features including high efficiency and high torque density [MER55], [MIL89], [ZHU07], [CHE11]. PM machines have many configurations. Based on the PM location either on the rotor part or the stator part they can be divided into rotor PM machines and stator PM machines, respectively. In addition, rotor PM machines can be categorized as surface mounted permanent magnet (SPM) machines with radial magnetization and interior permanent magnet (IPM) machines with radial or parallel magnetization. Moreover, PM machines may be categorized into outer or inner rotors. On the other hand, stator PM machines are classified according to the magnet configurations into flux reversal permanent magnet (FRPM) machines where the magnets are mounted on the stator tooth surface, doubly salient permanent magnet and switched flux permanent magnet (SFPM) machines in which the magnets are sandwiched between the stator teeth.

The interest of stator PM machines has been dramatically increased, because such machines combine the merits of switched reluctance (SR) and PM machines. They have a passive rotor like SR machines with high power density and efficiency similar to the PM machines [LI07].

Like their corresponding electrical machines, PM machines can be designed as rotating or linear machines. In general, the performance of linear machines in terms of power factor and efficiency is less than that would be expected from their rotating counterparts. However, this reduction may be compromised by many characteristics that can be offered by linear machines only. Linear machines have the advantages of high dynamic performance and enhanced reliability, due to the elimination of the conversion mechanism from rotary to linear motion, which should be used if the rotating machines are utilized for linear applications [SAD71] [MCL88].

The history of linear machines can be dated back to more than a century ago, and is as old as the rotating counterparts. The first linear machine was introduced in 1845 by Charles Wheatstone [HEL09].

The operation principle of linear machines is similar to that of the rotating machines. However, their major differences include that the air gap of the linear machines is larger than that of the rotating machines, the linear machines having a start and an end, while the rotating machines do not.

It has been confirmed that the PM linear machines possess the best performances among other linear machine technologies, i.e. induction and SR linear machines [MOG96] [AKM92]. Therefore, they have been increasingly employed in various applications [BOL99] [POL03]. However, the high manufacturing cost can be considered as one of the most crucial problems of the PM linear machines, particularly in long stroke applications in which a large amount of either permanent magnet or copper would be required [WAN08a]. Because of that the PM linear machines, which have both excitation sources in one part whilst the other part is passive, have become more favored in industrial applications and traction systems [CAO13].

On the other hand, having both armature winding and PM in one machine part may present the limitations of thrust force capability and PM demagnetization withstand capability. Thus, in order to compromise such demerits, novel PM linear machines are developed in this thesis. The proposed PM linear machines are designed by adopting the concept of partitioned stator in which each stator part has one excited source while the mover is passive.

1.2 Linear Machine Configurations

A linear machine could be simply evolved from a rotational machine by cutting radially and unrolled out flat. Thereby, the obtainable number of linear machine types coincides precisely with the number of the rotating equivalents. Hence, the aforementioned classifications of the rotating PM machines can be applied to the PM linear machines. However, depending on the machine geometric configurations, linear machines can be generally classified as:

- Planar (single- or double-sided, i.e. the mover faces the stator from one side, Fig. 1.1, or two sides, Fig. 1.2) or tubular, Fig. 1.3 (in term of magnetization direction they can be radial or axial) [ASH10].
- They can be either short or long stroke according to the excursion length of the moving part of the machines. In the long stroke machine the excursion can be extended for kilometres, while in the short stroke, which is also known as linear actuator, it is no more than one pole pitch.
- Regarding the mover part, they can be iron-mover or magnet-mover. Also they can be organized as slotless ironless, slotless iron and slotted iron [YU07].

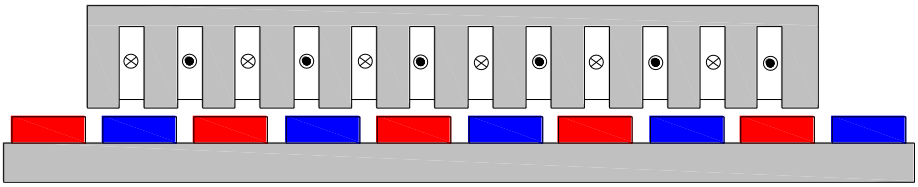

Fig. 1.1 Single-sided PM linear machine.

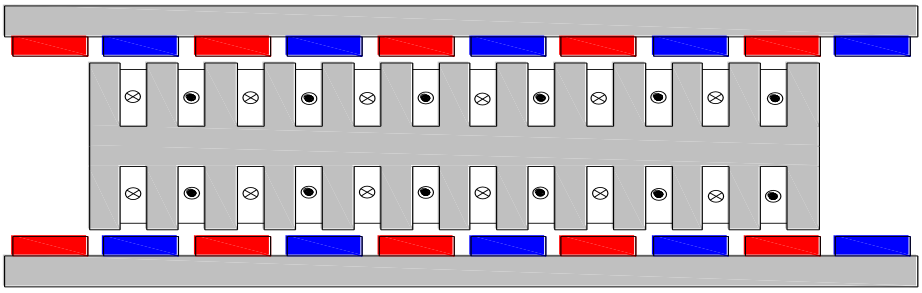

Fig. 1.2 Double-sided PM linear machine.

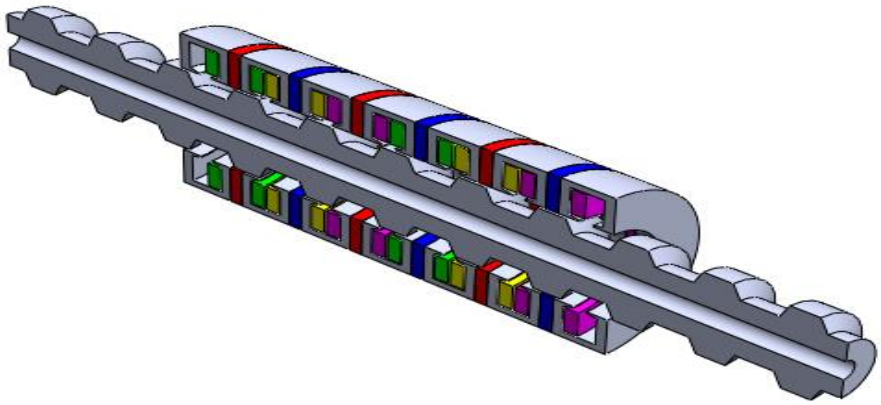

Fig. 1.3 Tubular SFPM linear machine.

Based on the rotating machine types, numerous types of linear machines are available, i.e. for any rotating machine there is a linear counterpart. Thus, linear machines can be induction, synchronous, SR, FRPM and SFPM machines.

The aim of this chapter is to introduce a working knowledge of the PM linear machines in which both the excitation sources, i.e. the PMs and armature windings, are placed in one machine part.

1.2.1 Doubly Salient Permanent Magnet Linear Machines

The concept of the doubly salient permanent magnet (DSPM) machine, where the windings and the PMs are housed on the stator, and the rotor is made of iron only, was introduced in [RAU55]. However, such a machine has been forgotten for more than three decades due to the limitation of the PM property. In 1992 a new stator PM machine configuration, in which the permanent magnets are embedded on the stator core was unveiled [LIA92]. It was stated that the machine has the advantages of robust rotor structure, high torque capability as well as efficiency. Since this period, the DSPM machines have been widely researched, due to their prominent features. Many types of DSPM machines have been developed, such as SFPM, FRPM and Vernier permanent magnet (VPM) machines, which all can be considered as the topologies developed from the DSPM machine with different stator PM configurations and the same passive rotor. As mentioned before, the linear machines can be directly evolved from their rotating counterparts. Hence, DSPM linear machines have the same topologies as the rotating machines, i.e., SFPM, FRPM and VPM linear machines.

1.2.2 Switched Flux Permanent Magnet Linear Machines

As an alternative candidate of the conventional rotor PM machines, SFPM machines have been widely applied to many market sectors, such as aerospace, electric and hybrid electric vehicles, industrial application and so on. This is because the SFPM machines have compact rotor structure, easy thermal management, high power density and efficiency [FEI12] [FAS14]. Although the first generation of the SFPM machines was revealed in 1955, the interest in these machines has been significantly emerged after the introduction of the strong PM materials. Three-phase SFPM machine was designed in 1997 [HOA97]. As mentioned before, such machines are designed based on doubly salient structure. The rotor has iron salient poles, while one stator pole consists of two U shaped laminations in between where one tangentially PM is placed and a concentrated winding is wounded on the stator pole [CHE10]. Since this time, the SFPM machines have dominated the research area, apparently, because of their above mentioned advantages.

1.2.2.1 Planar Single-sided Switched Flux Permanent Magnet Linear Machines

Planner single-sided linear machines consist of one stator and one mover. They have the advantages of simple structure, low cost and easy maintenance [ZYI07]. A single-sided SFPM linear machine, which was directly developed from the conventional SFPM rotating machine, was firstly introduced in [WAN08]. The machine has 6/5 slot/pole, both the PMs and armature windings are housed on the mover, while the stator is salient pole made of iron, Fig. 1.4. It was demonstrated that such a configuration has the features of PM linear and SFPM rotating machines. In addition, the higher manufacturing cost of the mover PM linear machines could be overcome by such a machine. However, it suffers from high cogging force, which has a negative influence on the machine performance. It causes a periodic force oscillation with the mover position leading to mechanical vibration, noise and velocity oscillation, particularly at low velocity [ZHU09]. Therefore, minimising the cogging force is necessary to improve the performance of the SFPM linear machine. As an attempt to minimize the cogging force of such a machine, [WAN09] has demonstrated a novel technique to reduce this undesirable feature by setting additional iron teeth at both ends of the mover. It was delivered that the additional teeth could be an effective method to reduce the cogging force, when an appropriate distance between the inner sides of the assistant teeth and the

initial mover ends would be selected. Hence, such a distance should be optimized in order to obtain a proper reduction on the cogging force of the SFPM linear machine.

Furthermore, to maximize the thrust capability of the SFPM linear machine, the major design parameters of the machine were optimized individually and globally for maximum thrust force in [MIN10]. The individual optimization results were compared to those of the global optimisation. In addition, the widths of the additional teeth as well as their slot opening ratio were optimized to minimize the cogging force of the machine. It was shown that both methods are effective to obtain the optimum performance. However, the globally optimized machine has slightly higher thrust force compared to the individually optimized machine.

A new mover/stator pole number combination with an odd mover pole number was investigated in [LI13]. By keeping the same mover pole number, four machines with different stator poles, i.e. 9/7, 9/8, 9/10 and 9/11 were designed and optimized for maximum thrust force. The performances of the designed machines were compared. It has been stated that the mover of the SFPM linear machines can be designed with an odd number, and the machine with 9/10 mover/stator pole number combination exhibits the best performance among the other machines. Additionally, a periodic model, i.e. infinite model of the 9/10 SFPM linear machine has been simulated, to high light the influence of the longitudinal end effect on the performance of the SFPM linear machine. A comparison between the practical model with longitudinal end effect and the periodic model without longitudinal end effect was carried out.

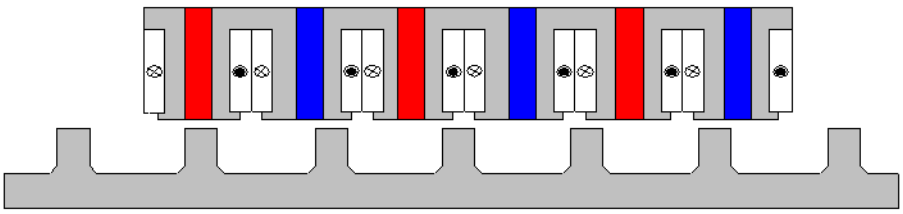

Fig. 1.4 6/5 SFPM linear machine [WAN08].

In order to reduce the cost and improve the performance of the SFPM machine at low electrical loading as well as low speed operating conditions, a multi-tooth SFPM rotating machine was designed and investigated in [ZHU08a]. This topology has been employed to the SFPM linear machines in [CAI11]. It was reported that high thrust force with low thrust force ripple can be achieved by the multi-tooth SFPM linear machine. Therefore, such a configuration is suitable for high force and low velocity direct drive applications. Additionally, the quantity of the permanent magnet usage was

reduced to half, resulting in reduction of the machine cost. Fig. 1.5 depicts the multi-tooth SFPM linear machine. However, the electrical loading of the aforementioned machine is restricted due to the small slot area. Hence, a new configuration of multi-tooth SFPM linear machine with single-layer winding arrangement was investigated in [ZHO12a]. A nonlinear equivalent magnet circuit (NEMC) model was introduced to predict the electromagnetic performance of the machine. The results were verified by finite element (FE) method and experimentally. It was shown that the NEMC and FE results have a good agreement, and also the machine takes the advantage of high electrical loading, due to the larger slot area. Furthermore, to reduce the total PM volume, a new structure of the conventional multi-tooth SFPM linear machine in which the PM height is not the same as the stator core was introduced in [CAI15]. It was concluded that the machine with short PM height has better performance in terms of back-EMF, thrust force capability and force ripple. Moreover, [ZHO11] modified the conventional multi-tooth SFPM linear machine to reduce the cogging force. The magnet of each phase was cut into two equal parts and put on the top of their corresponding stacks, as shown in Fig. 1.6. Although the modified machine exhibits about 40% less cogging force than that of the original machine, it has less back-EMF, due to the increase of the flux leakage. The author also introduced an analytical model to calculate the cogging force of the machine based on Fourier algorithm. The results were verified by both FE method and experiment. It was reported that the mathematical approach is valid and can be used to predict the SFPM linear machine cogging force.

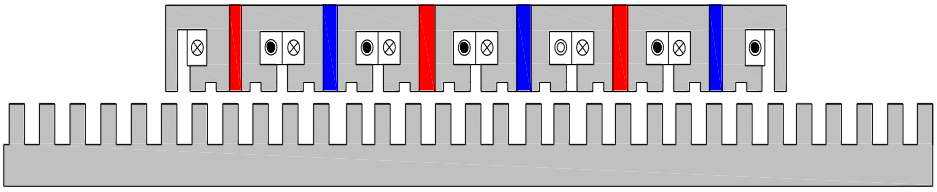

Fig. 1.5 Multi-tooth SFPM linear machine [CAI11].

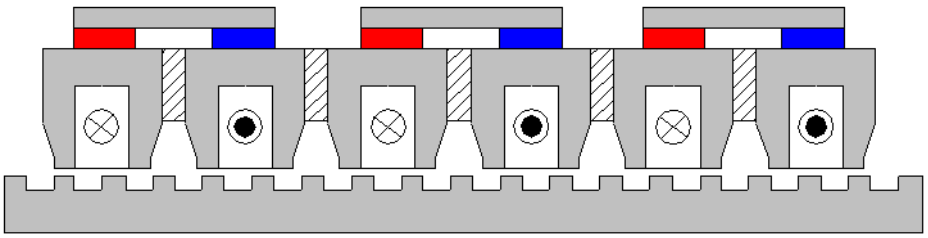

Fig. 1.6 Cross-section of the SFPM machine with PMs at back [ZHO11].

As a promising candidate for fault tolerant applications, a modular SFPM linear machine was developed in [JIN09] by adopting the idea of modular SFPM rotating machines, which were proposed and analysed in [OWE08]. The one phase of the modular SFPM linear machine comprises of two E-shaped modules, each module has two U-shaped lamination cores. A magnet is sandwiched between them and a concentrated coil is wound around the adjacent teeth of the two U-modules. Each two adjacent E-modules are separated by a flux barrier made of nonmagnetic material. Fig. 1.7 illustrates a cross-section of the machine. A comparison between the modular SFPM and the conventional SFPM linear machines was carried out. It has been shown that the modular SFPM linear machine has higher fault tolerance, and higher power capability compared to the conventional SFPM linear machine, when they were compared under the same permanent magnet volume.

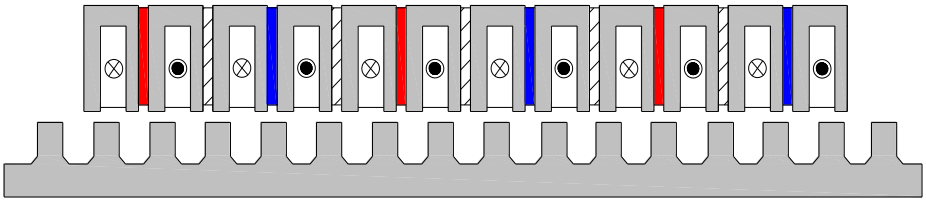

Fig. 1.7 Modular SFPM linear machine [JIN09].

Moreover, a new configuration of the modular SFPM linear machine, named as complementary and modular SFPM linear machine was proposed in [CAO12]. The difference between the conventional and the proposed modular SFPM linear machines is the flux barrier, which isolates the coils of each phase from the other phases. It has been concluded that the modified machine shows balanced back-EMF waveforms and low cogging force due to the complementary structure. On the other hand, based on d-q frame a mathematical model of the complementary and modular SFPM linear machine was developed in [CAO12]. The analytical results have been validated by FE and experimental results. It was stated that the experimental and simulation results have some discrepancies, due to the end effect. In addition, a modular and complementary SFPM linear motor with hybrid excitation has been developed and investigated for urban rail transit application [CAO11b], Fig. 1.8. Thanks to the DC current flux, the total flux of the machine can be regulated, i.e. weakening or boosting by changing both the polarity and the magnitude of the applied DC current. Hence, the range of the motor velocity could be extended, which results in wider flux weakening regain. Therefore, the system efficiency can be enhanced for different velocities and loads. Recently, a

general design principle of the complementary and modular SFPM linear machines with two different mover/stator pole pitch ratios was introduced in [CAO13a]. It was found that the machine with a mover/stator pole pitch ratio of about one has a higher thrust force and a lower electric frequency than that of the mover/stator pole pitch ratio, which equals three. Furthermore, complementary and modular SFPM linear machines having different mover/stator combinations were designed, analysed and compared in [CAO13b]. It has been reported that the best mover/stator combination for the complementary and modular SFPM linear machine, in terms of the highest thrust force and the lowest thrust force ripple is 12/13 mover/stator.

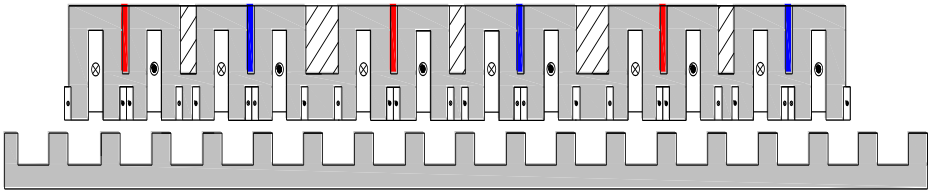

Fig. 1.8 Complementary and modular hybrid SFPM linear machine [CAO11b].

Efforts have been spent to design a SFPM machine with low PM volume in order to reduce the manufacturing cost of the machine, as the rare-earth PM price is very high. Thereby, new configurations for SFPM rotating machine, known as C-core and E-core SFPM machines, were developed in [ZHU10]. Similarly, these concepts were adopted to the SFPM linear machine. Thus, new SFPM linear machine topologies with C-core and E-core, were designed and investigated in [MIN11], Fig. 1.9. The mover of the E-core SFPM linear machine consists of E-shaped segments, while C-shaped segments are employed in the mover of the C-core SFPM linear machine. It was reported that although the total PM volumes for both E- and C-core SFPM linear machines are about 40% less than that of the conventional SFPM linear machine, the C-core SFPM linear machine exhibits about 16% higher thrust force capability compared to the conventional SFPM linear machine. On the other hand, the E-core SFPM linear machine shows a compatible thrust force capability to that of the conventional SFPM linear machine. Despite the fact that the C-core SFPM linear machine has higher thrust force capability than that of the E-Core SFPM linear machine, the latter possesses higher fault tolerance capability, since its phase windings are physically isolated by the middle teeth. Furthermore, the thrust force equations of E-core SFPM linear machine under normal and open circuit operation modes have been derived by [HUA11b]. Also to keep the thrust force invariable under normal and fault condition operations a new current fault

tolerant control strategy based on the current harmonic injection method has been carried out in this study. It was stated that by such a strategy the thrust force ripple would be suppressed, when the fault occurred. However, the analytical results are different from both the FE and experimental results, particularly in high current condition, due to the inconsiderable iron core saturation.

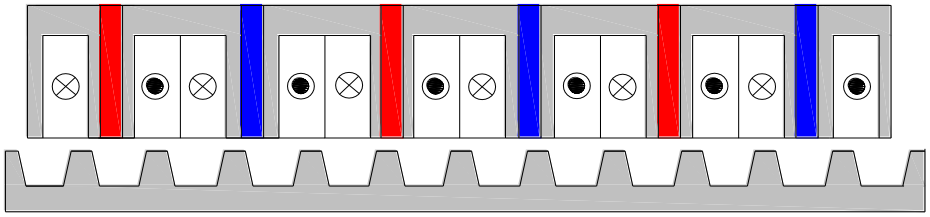

(a) C-core SFPM linear machine.

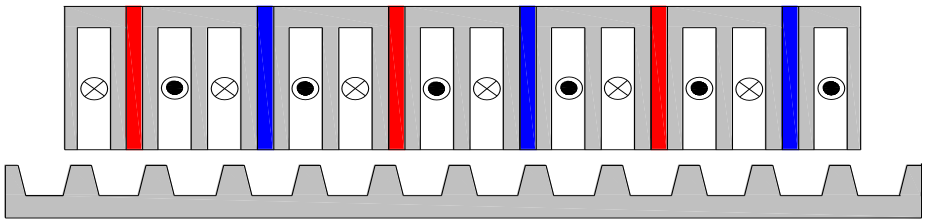

(b) E-core SFPM linear machine.

Fig. 1.9 C-core and E-core machine Configurations [MIN11].

Moreover, a modified configuration of the C-core SFPM linear machine has been proposed in [XIA14] for rope elevator application, as shown in Fig. 1.10. In order to improve the machine performance, particularly reducing the longitudinal end effect, an additional tooth, which consists of two iron teeth and one magnet, was placed on each end of the proposed machine. The machine performance was predicted and compared with the conventional machine, i.e. without additional teeth. Although using such additional teeth leads to reduce the DC component in the flux linkage waveforms of the proposed machine, the machine thrust force ripple is increased, due to the increase of the cogging force.

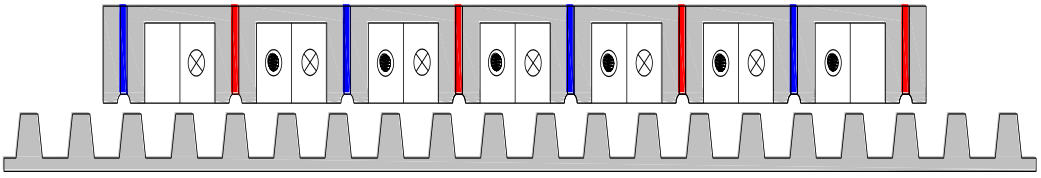

Fig. 1.10 Modified C-core SFPM linear machine [XIA14].

Furthermore, based on the topology of the hybrid excitation rotating SFPM machine that was presented in [HON07], a hybrid excitation SFPM linear machine was designed in [HWA12], in which a ferrite magnet is used instead of a rare earth magnet, in order to reduce the manufactory cost of the machines.

1.2.2.2 Planar Double-sided Switched Flux Permanent Magnet Linear Machines

Double-sided linear machines usually consist of two stators and one mover. Such a configuration was proposed in order to overcome the main demerits of the single-sided linear machine, i.e. high normal force, which can negatively affect the drive system [CAO14]. A double-sided SFPM yokeless linear machine was designed in [GAN12], Fig. 1.11. The machine was optimized for maximum thrust force, and a comparison between the single- and double-sided SFPM linear machines was carried out in [GAN13]. It was stated that the double-sided SFPM linear machine offers higher thrust force and almost zero normal force.

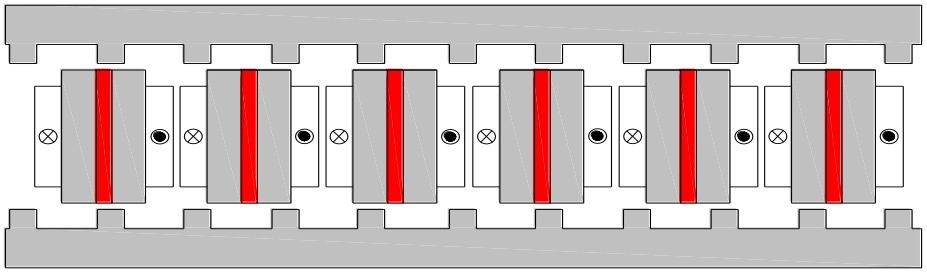

Fig. 1.11 Double-sided SFPM linear machine [GAN12].

In order to enhance the thrust force capability of the aforementioned machine, it was redesigned with two PM poles per mover modular [ZHA15a], Fig. 1.12. It was concluded that the new PM configuration machine exhibits about 1.96% higher thrust force and lower thrust force ripple compared to the conventional machine under the same permanent magnet volume.

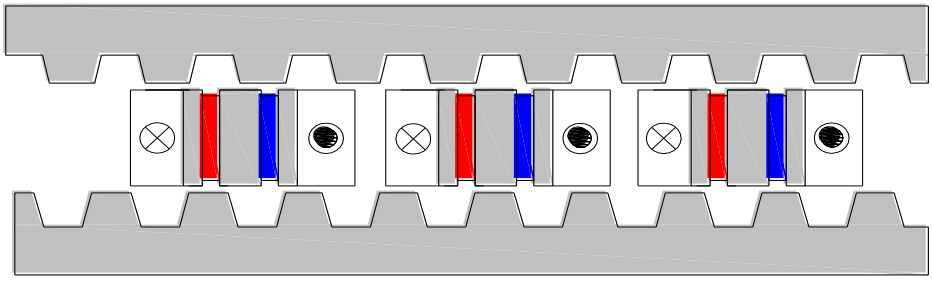

Fig. 1.12 Multi-PM machine configuration [ZHA15a].

A double-sided multi-tooth SFPM linear machine was developed in [KRO10], Fig. 1.13 depicts a cross-section of the machine. Despite the fact that such a configuration shows low cogging force, additional teeth on both ends of the mover were used to achieve balanced three phase back-EMF waveforms. Moreover, in order to guide the flux linkage of such a machine, it was modified in [LU15] by shifting the poles of the first and second stator by one pole pitch. In addition, the influence of the mover yoke and the additional teeth on the performance of the modified machine was also investigated. It was shown that higher thrust force capability with about 1.8% can be obtained by the modified machine with a yokeless mover and without additional teeth. That also was confirmed in [ZHA15b] in which modular yokeless multi-tooth SFPM linear machines with three different magnet polarities and phase modular distance were analysed and compared.

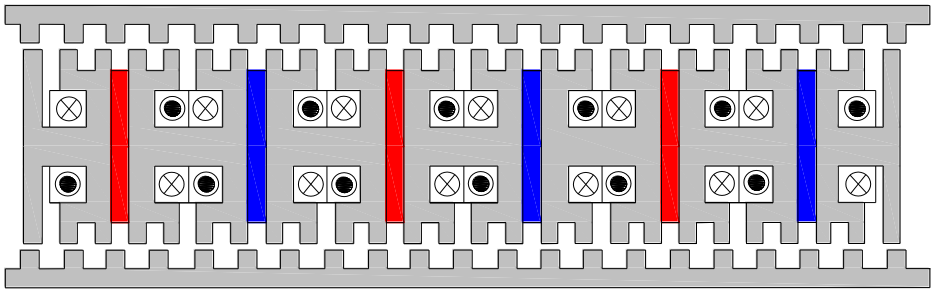

Fig. 1.13 Double-sided multi-tooth SFPM linear machine [KRO10].

As a candidate for fault tolerance application a multi-phase double-sided SFPM linear machine was developed in [LUI14], while [GAN11] introduced five-phase double-sided yokeless SFPM linear machine. A parametric optimization was carried out in order to achieve the highest average thrust force. Furthermore, the machine was analysed under different open-circuit fault conditions. In order to enhance the machine fault capability under short circuit fault condition, the aforementioned machine was redesigned with both PM and DC excitations, Fig. 1.14 [GAN15]. The DC field coil has been used for two different purposes, i.e. it aids the PM field in healthy condition, while it will be utilized to demagnetize the PM when the short circuit fault occurs. It should be mentioned that Alnico magnet was used in such machine. This is because this type of PM has high energy product and low coercively. Hence, it can be easily demagnetized under the short circuit fault. On the other hand, a double-sided modular and complementary SFPM linear machine was designed in [CAO14]. The machine was proposed with two stator structures, i.e. yoke and yokeless stator as illustrated in

Fig. 1.15. The main design parameters of both machines were optimized for maximum thrust force and minimum force ripple, respectively. The machine performances were compared. It was confirmed that the yokeless machine has higher thrust force with less force ripple and stator mass.

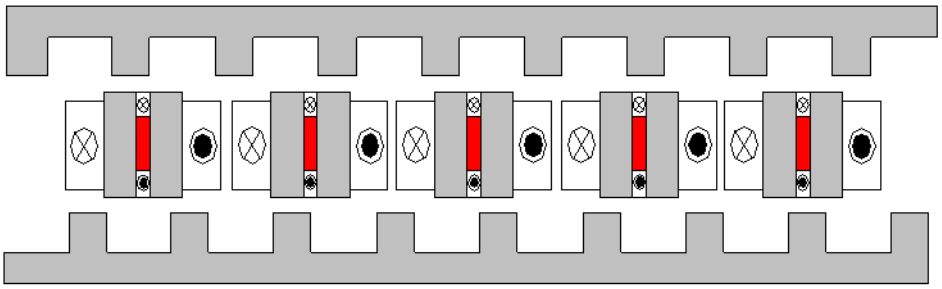

Fig. 1.14 Hybrid excitation double-sided SFPM linear machine [GAN15].

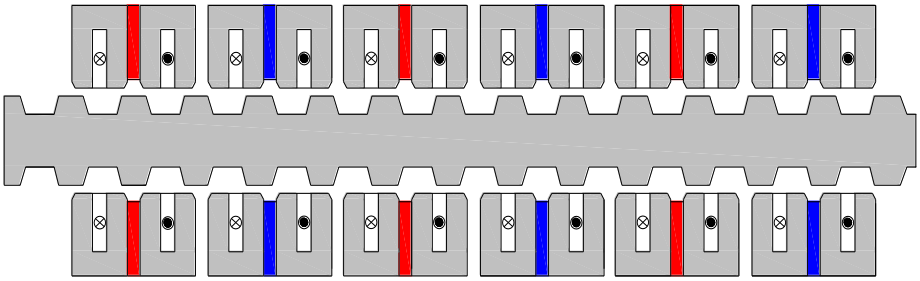

(a) With yoke

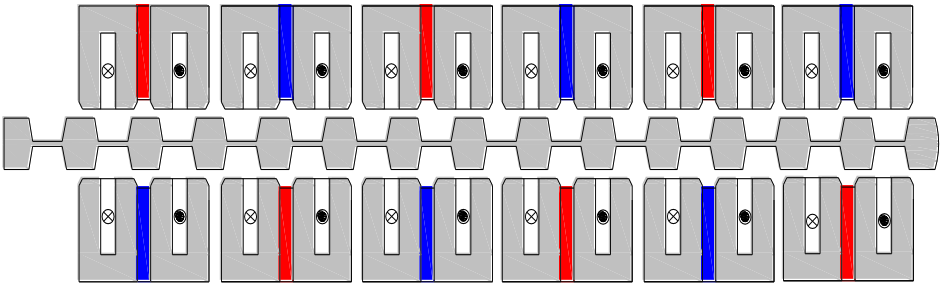

(b) Yokeless

Fig. 1.15 Double-sided modular and complementary SFPM linear machine [CAO14].

For the electromagnetic launch system, a double-sided SFPM linear machine, in which the PMs and the armature windings are embedded on the long stator, while the mover is salient pole structure, was introduced in [HUA13]. A wedge-type end design method has been used to reduce the thrust force ripple. It was shown that the cogging force component caused by longitudinal end effect has been significantly reduced by using such a method.

1.2.2.3 Tubular Switched Flux Permanent Magnet Linear Machines

Tubular linear machines can be created by rolling up the single-sided flat linear machines around the longitudinal axis. Hence, the mover is entirely surrounded by the stator [ZYI07]. As stated in [RIN07] these topologies exhibit the highest force density and efficiency compared with the other linear machines topologies. Also they have no end-winding and no net attractive force between the mover and the stator. The interest of applying the idea of SFPM machines to tubular machines has been emerged during the last decade. Due to the fact that the SFPM machines have both excitation sources on the stator with a rotor being made of iron only, and hence, with this structure, heat dissipation problem, which exists in the mover-magnet PM tubular machines [WAN08a], can be eliminated. A three-phase SFPM tubular machine has been developed in [WAN08a] and the effects of the split ratio, the mover pole width to mover pole pitch ratio, and the stator teeth width on the thrust force capability were investigated in this study. It was shown that the machine performance can be enhanced with adequate determination of the machine main design parameters, and also such configuration is convenient for the applications in which a robust mover is needed, since both the PM and the coils are located on the stator. Furthermore, the influence of the slot/pole number combinations on the SFPM tubular machines was investigated in [WAN08c]. Also, a comparison between all and alternative stator teeth wound configurations has been demonstrated. It was reported that the combinations of slot/pole numbers have a considerable impact on the machine electromagnetic performance, and higher thrust force can be achieved by using alternative teeth wound configurations. Moreover, 6/5 and 6/7 tubular SFPM machines with variant winding arrangements were designed and examined in [ZHU08b] as shown in Fig. 1.16. Three winding configurations were investigated in this study. After optimising the main design parameters of these machines, their electromagnetic performance have been analysed and compared. It was concluded that using single layer or single annular winding configurations results in reducing the cost of the SFPM tubular machine without compromising the machine performance.

As a candidate to the vehicle suspension application, a SFPM tubular machine with fault tolerant capability has been designed in [KAN12]. E-shaped laminated segments were employed in construct the machine stator. The phase windings of adjacent stator poles were ultimately isolated, due to the presence of an E-core structure. Hence, the phase decoupling was obtained, which is preferable for fault-tolerant operating. It was

found that the proposed machine shows higher back EMF, higher thrust force and less force ripple than those of the conventional machine, as well as the cost being reduced since half the amount of permanent magnet is used in this machine.

Furthermore, a complementary phase structure and a modular design were employed in design the tubular SFPM machine in order to reduce cogging force and enhance system interchangeability [YAN14]. Both flux linkage and thrust force were computed mathematically using an equivalent magnetic circuit. On other hand, FE method was utilised to validate the results. In addition, the influence of the PM width on the thrust force capability as well as the cogging force was investigated. It was found that the machine possesses the advantages of a good thrust force density and low thrust ripple. In [WAN15] the aforementioned machine was compared to the conventional SFPM tubular machine in terms of open circuit and on load performances. It was reported that symmetrical back-EMF and higher output power can be obtained by the complementary SFPM tubular machine.

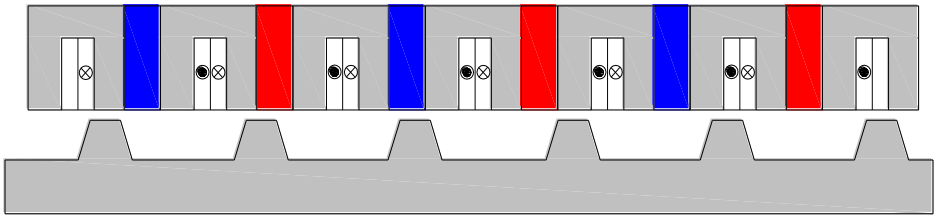

(a) Double-layer winding.

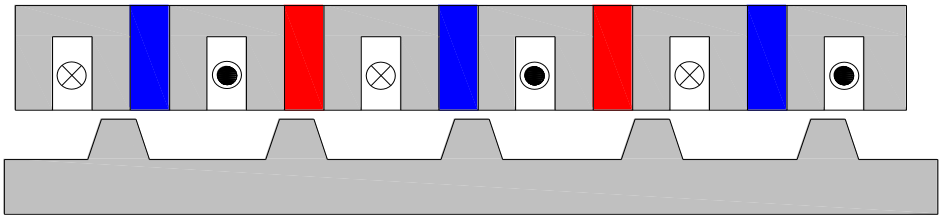

(b) Single annular winding.

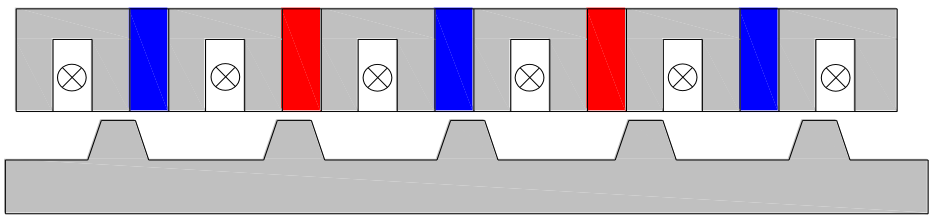

(c) Single-layer winding.

Fig. 1.16 2D-axisymmetry cross-sections of SFPM tubular machines [ZHU08b].

1.2.3 Flux Reversal Permanent Magnet Linear Machines

The idea of FRPM machines has been developed to merge the merits of the SR as well as the PM machines. They have a simple salient pole rotor structure made of iron only, while the stator is active having the armature windings as well as the PMs. The PM is mounted on the stator teeth in such a way that each tooth has two pieces of magnets with opposite polarity and every adjacent tooth will be of alternating polarity.

A single phase FRPM machine was firstly introduced in 1997 as an alternative to the standard claw pole alternator [DEO97]. A comparison between the FRPM machine and other machines including brushless DC (BLDC) machine, SR machine was carried out. It was concluded the FRPM machine processes a similar features to that of the BLDC machine, and in addition, it has the advantages of low rotor inertia. Hence, it is preferable for high speed applications. While the single phase FRPM machine can be used as a generator only, the three phase topology can be worked as a motor and generator. Three-phase FRPM machine was described, and optimized for high flux linkage variation, minimum cogging torque and better permanent magnet utilization in [WAN99]. It was stated that the proper values of the air-gap length, the permanent magnet height, and the stator and rotor pole pitches contribute to optimal machine performances.

1.2.3.1 Planar Single-sided Flux Reversal Permanent Magnet Linear Machines

A FRPM linear machine, which was directly evolved from the three-phase FRPM rotating machine, was introduced in [CHU08]. The machine has been designed with two different PM configurations, Fig. 1.17. A comparison between both machines was carried out. It was revealed that higher back-EMF and average thrust force with the half amount of the PM usage can be achieved by the FRPM linear machine with consequent PM pole arrangement.

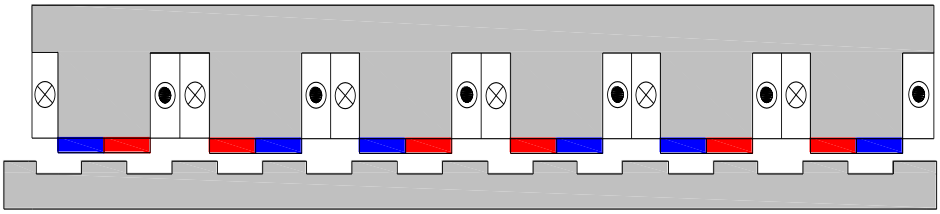

(a) Conventional FRPM linear machine.

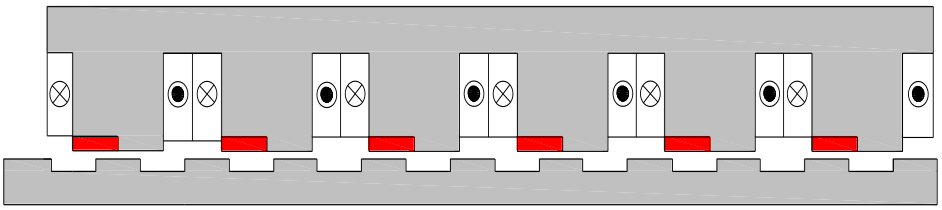

(b) Consequent PM pole FRPM linear machine.

Fig. 1.17 FRPM machines configurations [CHU08].

In order to increase the thrust force capability of the conventional FRPM linear machine, it was modified by using a salient tooth between the adjacent permanent magnets resulting in having all the permanent magnets in the same direction instead of opposite polarity. Consequently, the machine manufacturing would be simplified. It was stated that the modified machine shows higher thrust force than the conventional FRPM linear machine due to the less flux leakage [CHU07].

Although the aforementioned machine exhibits higher thrust force capability compared to the conventional machine, it has a magnetic unbalanced problem, due to the same polarity for all the PMs. Hence, a modular mover configuration was adapted as shown in Fig. 1.18 [CHU11], to overcome as above problem.

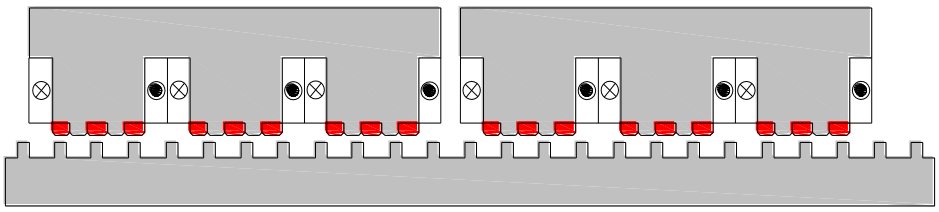

Fig. 1.18 Modular FRPM linear machine [CHU11].

A new configuration of the FRPM linear machine with fault tolerant capability has been developed in [ZHA14]. It was stated that the introduced machine offers better thrust force per permanent magnet volume capability and about 90% less mutual- to self-inductance ratio compared to the conventional FRPM linear machine, leading to higher fault tolerant capability. Moreover, in order to enhance the flux-regulation capability of the FRPM linear machine as well as to reduce the risk of PM irreversible demagnetisation, a hybrid FRPM linear machine was introduced in [XU14a]. The modular structure has been adapted in this machine to reduce the longitudinal end effect. It has been concluded that the machine has symmetrical and sinusoidal back-EMF. Fig. 1.19 depicts a cross-section of the machine.

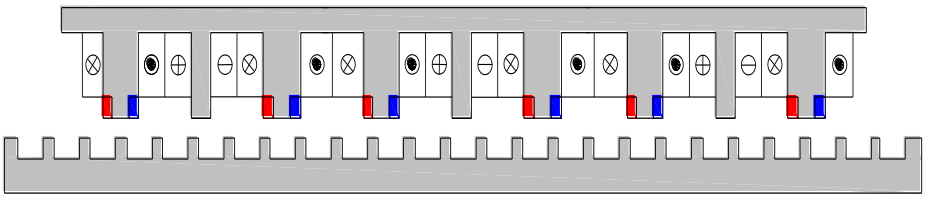

Fig. 1.19 Hybrid excitation FRPM linear machine [XU14a].

1.2.3.2 Planar Double-sided Flux Reversal Permanent Magnet Linear Machines

A double-sided FRPM linear machine was designed and compared with that of the single-sided FRPM linear machine in [GAN11]. Fig. 1.20 presents the configuration of the proposed machine. It was found that by adopting the double-sided structure the machine performance is improved without any changing of excitation sources. Moreover, in order to enhance the thrust force density and reduce the cogging force a five-phase double sided FRPM linear machine has been developed in this study. It was stated that the five-phase machine exhibits higher thrust force as well as acceleration and low cogging force compared to that of the three phase machine.

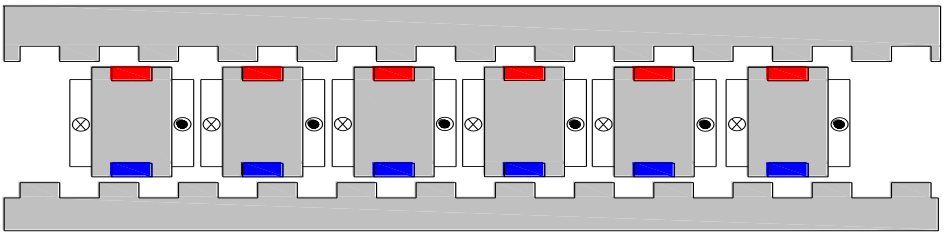

Fig. 1.20 Double-sided FRPM linear machine [GAN11].

1.2.4 Vernier Permanent Magnet Linear Machines

Vernier permanent magnet (VPM) machine has been introduced for high torque capability and low speed operation, by employing the concept of magnetic gear effect in the PM machine. Although both VPM and magnetically geared machines operate under the same principle operation, the VPM machine has a simpler structure compared to the magnetically geared machine. This is because the magnetically geared machines have multiple airgaps leading to more manufacturing difficulties, while the VPM machines have one airgap. Like other PM machines, such a configuration may be designed with active rotor or salient pole passive rotor [ISH95]. However, VPM machine with passive mover has the advantage of the easier temperature rise management, since both the excitations source are located on the stator [SPO03]. VPM rotary machine which has active stator and passive rotor was first introduced in [SPO03].

1.2.4.1 Planar Single-sided Vernier Permanent Magnet Linear Machines

VPM linear machine was designed and analysed in [DU11b]. The operating principle as well as the standard design of the VPM linear machine was discussed. The stator of the machine consists of salient poles, while the mover is the active part, as shown in Fig. 1.21. It was confirmed that the machine offers the advantages of the high no-load back-EMF, low cogging force and high thrust force capability.

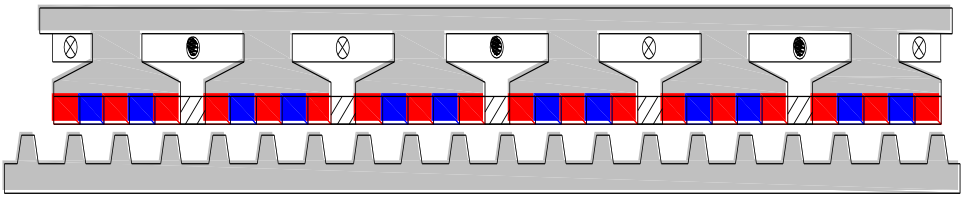

Fig. 1.21 VPM linear machine [DU11b].

In order to enhance the conventional VPM linear machine as well as to reduce the amount of the magnet usage, a new magnet configuration was introduced in [LIU14]. The machine was compared to the conventional VPM linear machine. It was shown that due to the less fringing flux the modified machine possesses the advantage of higher flux linkage leading to higher back-EMF, and consequently, better thrust force capability. Furthermore, the modified machine exhibits lower thrust force ripple, and the total magnet usage has been reduced.

Since the reliability is a crucial issue, particularly in applications that can directly affect the life safety, a machine with high fault tolerant ability would be more preferable

for such applications. Therefore, with the aim of enhancing the conventional VPM linear machine's fault-tolerant capability, the machine was modified by adding fault tolerant teeth between the armature teeth, as illustrated in Fig. 1.22. The machine was compared with the conventional counterpart. It was confirmed that the fault tolerant VPM linear machine shows better performance than that of the conventional VPM linear machine in terms of back-EMF, average thrust force and thrust force ripple, under the same copper and magnet usage comparison. However, the thrust force density of the conventional machine is higher compared to the modified machine. Furthermore, the modified machine has a higher fault tolerant capability due to the fact that the machine phases are magnetically and physically isolated by the fault tolerant teeth. Thereby, such configuration is a good candidate for rail transit system application [FAN13].

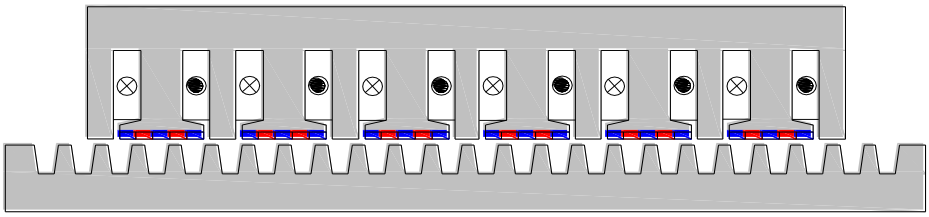

Fig. 1.22 Fault tolerant VPM linear machine [FAN13].

By adopting a modular and complementary structure for the mover, a new configuration of the VPM linear machine was introduced in [XU14b], Fig. 1.23 shows a cross-section of the machine. It was stated that the proposed machine has symmetrical back-EMFs due to the complementary structure. Besides, it possesses the advantage of higher thrust force capability with lower total PM volume compared to the conventional VPM linear machine. It is worth mentioning that the total magnet volume of the proposed machine is about 50% less than that of the conventional machine. Furthermore, the proposed structure leads to phases decoupling, resulting in good fault tolerant ability without reduction in the slot area, as the need of the fault tolerant teeth or flux barrier is eliminated.

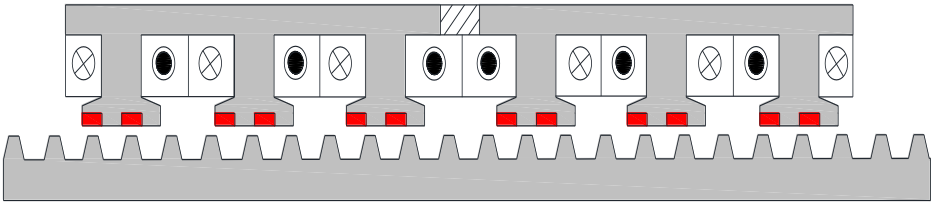

Fig. 1.23 Modular and complementary VPM linear machine [XU14b].

A new VPM linear machine with spoke-type PM configurations was proposed in [IMA14] to enhance the force capability of the conventional machine. The PMs have been placed in parallel to the armature windings, Fig. 1.24 displays the proposed machine. It has been confirmed that the spoke-type VPM machine can achieve about 69% higher thrust force compared to the conventional VPM linear machine.

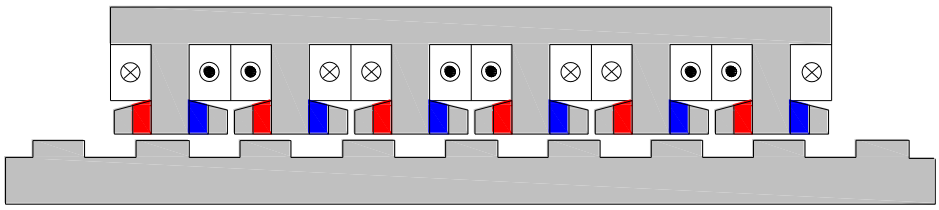

Fig. 1.24 Cross-section of spoke-type VPM linear machine [IMA14].

1.2.4.2 Planar Double-sided Vernier Permanent Magnet Linear Machines

As a promising candidate for ropeless elevator drive application, a double-sided VPM yokeless mover linear machine was designed in [DU15], Fig. 1.25. The machine was optimized for maximum no-load back-EMF and minimum thrust force ripple. It was concluded that the proposed machine shows higher thrust force density than that of the single-sided VPM counterpart. However, the latter has better magnet utilization compared to the former.

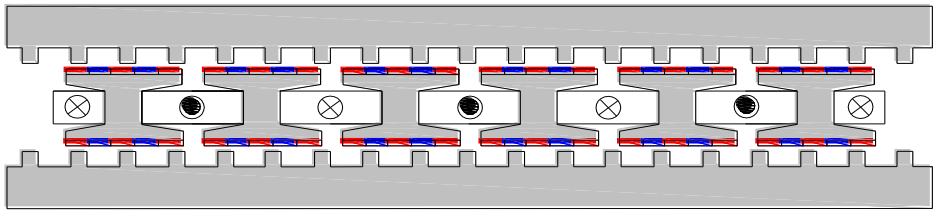

Fig. 1.25 Double-sided VPM linear machine [DU15].

A double-sided spoke-type VPM linear machine was introduced in [IMA15], to overcome the thrust force capability limitation in the single-sided spoke-type VPM linear machine. Fig. 1.26 presents a cross-section of the proposed machine. A comparison between the double- and the single-sided machines was carried out. It was shown that unlike the single-side machine, which suffers saturation at the rated current, the double-sided machine has linear thrust force-current performance over the rated current.

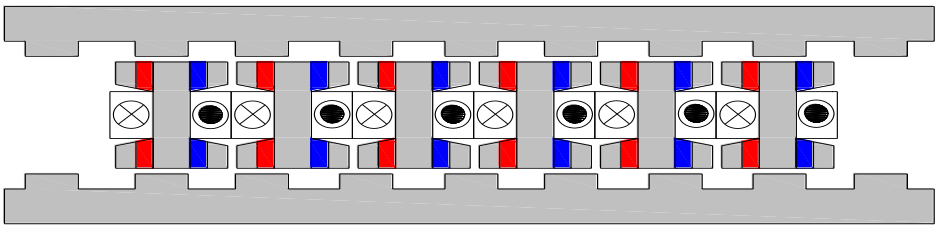

Fig. 1.26 Double-sided spoke-type VPM linear machine [IMA15].

Furthermore, [KHA15] proposed a dual stator spoke type VPM linear machine for wave energy extraction application. The machine consists of two stators where the armature winding are placed, while the mover is composed of spoke type permanent magnets sandwiched between iron cores, as shown in Fig. 1.27. It was reported that the introduced machine has higher thrust force density than the conventional single stator machine.

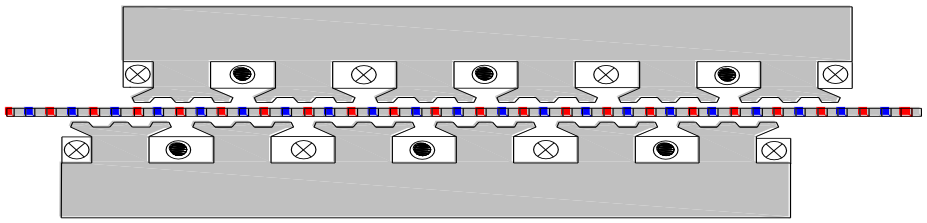

Fig. 1.27 Dual stator spoke type VPM linear machine [KHA15].

1.2.4.3 Tubular Vernier Permanent Magnet Linear Machines

A tubular VPM linear machine was firstly presented in [DU11a] for high thrust force density and low velocity application, such as wave energy conversion. Fig. 1.28 displays a cross-section of the mentioned machine. The PM thickness as well as the mover tooth thickness were optimized for maximum thrust force. It was confirmed that the machine delivers a good thrust force capability at low velocity operation. However, the flux leakage in the mover teeth limits the machine performance at the rated current, due to the iron saturation. Hence, in order to increase the machine thrust force capability, [DU12] modified the mentioned machine by placing high temperature superconductor (HTC) bulks between every two adjacent mover teeth. The flux leakage in the mover core would be reduced because of the zero relative permeability of the HTC, due to the Meissner effect. Thereby, the machine performance would be enhanced.

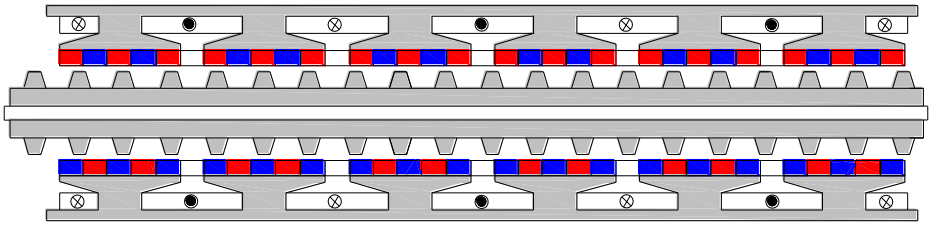

Fig. 1.28 Cross-section of tubular VPM linear machine [DU11a].

1.3 Scope of the research and thesis contributions

1.3.1 Scope of the research

The objective of this thesis is to investigate a new configuration of the DSPM linear machine, in order to overcome the main drawbacks of the existing DSPM linear machine, i.e. limitations of electrical and magnetic loadings and the PM demagnetization risk possibility. Hence, novel DSPM linear machines named as PS-PM linear machines are designed based on the idea of having two active stators with one passive mover. It should be mentioned that three types of PS-PM linear machines have been investigated, which are

- Partitioned stator (PS) FRPM linear machine, Fig. 1.29.
- Partitioned stator (PS) PM tubular machines, Fig. 1.30.
- Partitioned stator (PS) single phase short stroke PM tubular machines, Fig. 1.31.

The operation principle of each type is explained. The force production mechanism for the PS-FRPM linear machine is analysed. Moreover, the optimum slot/pole combination of the PS-FRPM linear and the PS-PM tubular machines has been determined. Furthermore, the main design parameters of the mentioned machines are globally optimized for maximum thrust force, the electromagnetic performances, iron loss, PM eddy current loss and PM demagnetization are investigated. A prototype of the PS-FRPM linear machine has been built and tested to validate the FE results. Fig. 1.32 shows the research structure and methodology.

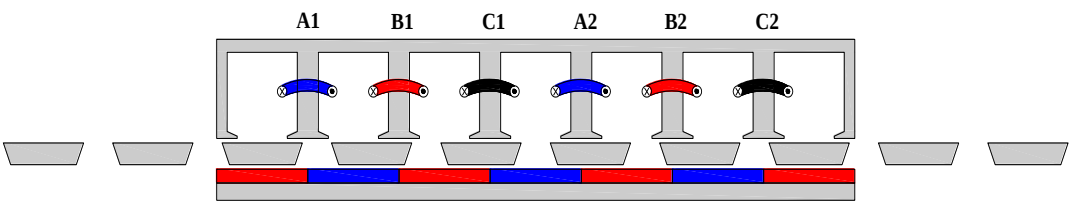

Fig. 1.29 Cross-section of PS-FRPM linear machine.

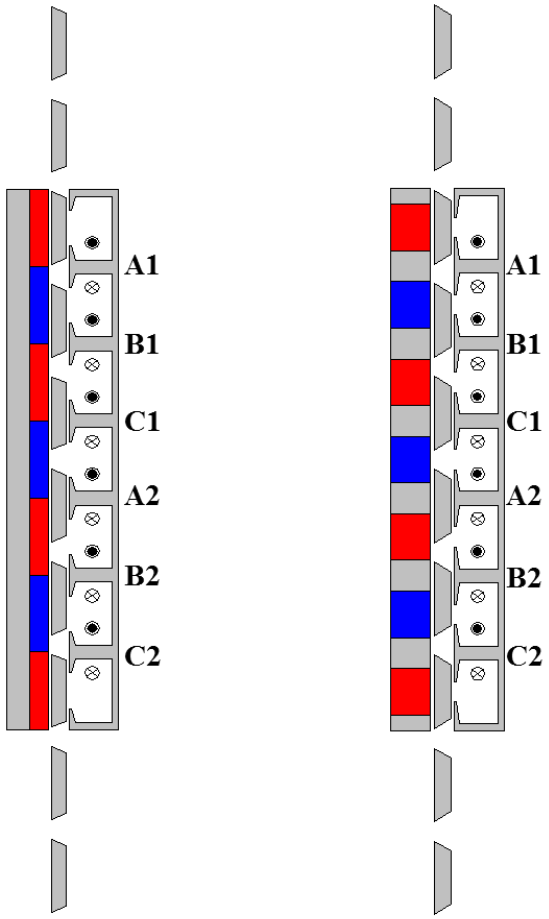

Fig. 1.30 2D- axisymmetric cross-sections of PS-PM tubular machines.

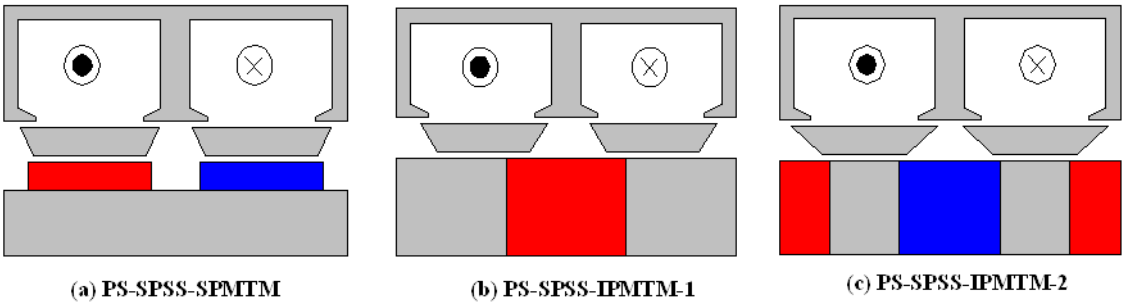

Fig. 1.31 2D- axisymmetric cross-sections of PS-SPSS-PM tubular machines.

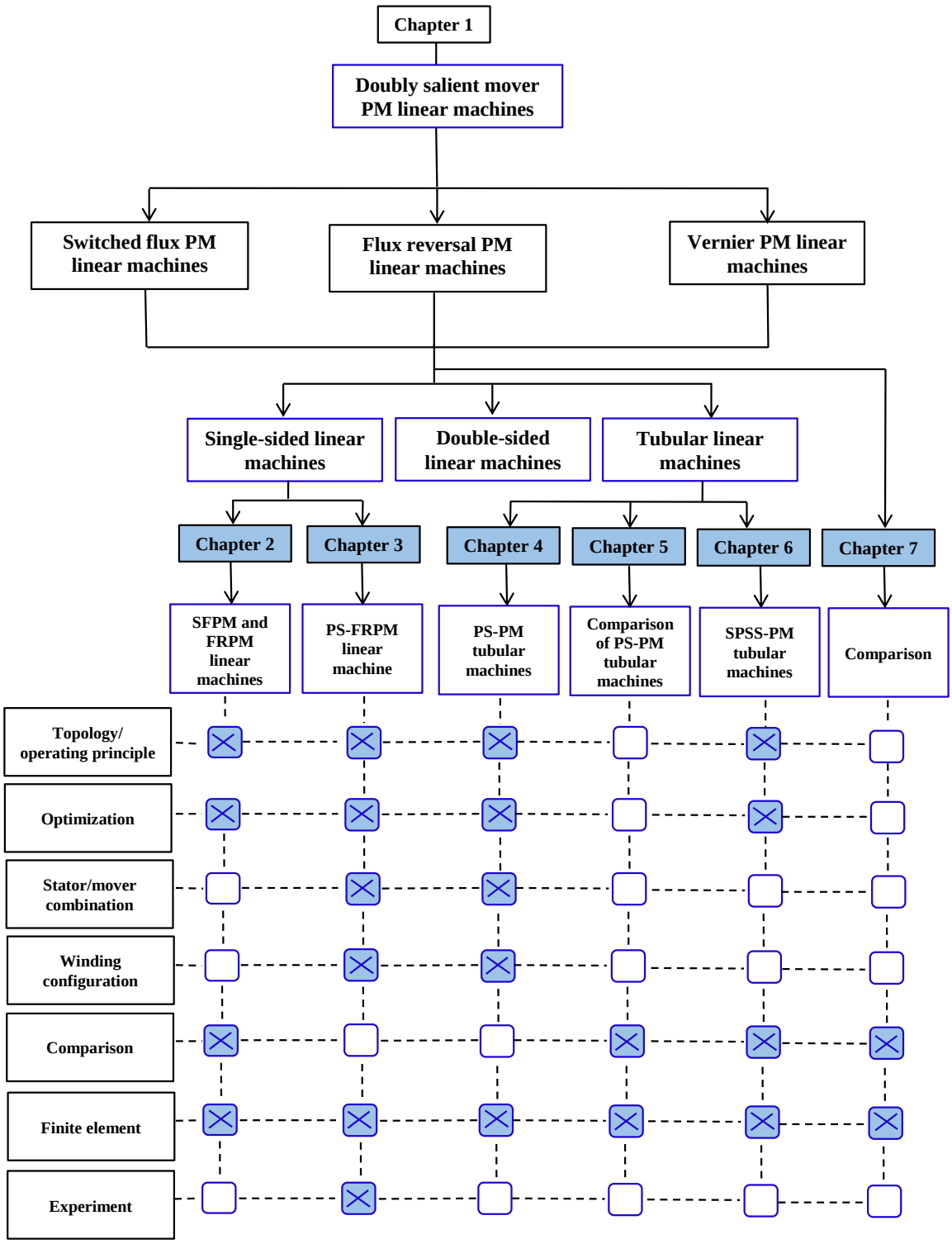

Fig. 1.32 Schematic of chapter arrangement and research methods.

The arrangement for the rest of this thesis can be summarized as follows:

Chapter Two

Two conventional DSPM linear machines, i.e. FSPM and FRPM linear machines, are designed, optimized under the same specifications and conditions. The operating principle for each machine is illustrated. Furthermore, the no-load and load performances of these machines are analysed. A comparison between both machines is carried out in order to highlight the merits and demerits of the mentioned machines.

Chapter Three

In this chapter, a novel PM linear machine known as PS-FRPM linear machine is designed, and the machine configuration and the operating principle are explained. The force production mechanism in such a topology is analysed. Moreover, the main design parameters are optimized for maximum thrust force capability. The influence of the longitudinal end effect on the machine performance is investigated by adopting an infinite model of the proposed machine. Furthermore, PS-FRPM linear machines with constant stator slot and different mover pole numbers are designed and compared to determine the optimal stator/ mover combination of the PS-FRPM linear machine. In addition, the machine performance is analysed.

Chapter Four

Two PS-PM tubular machines, i.e. PS-SPM and PS-IPM tubular machines, are proposed. The machines are globally optimized to achieve the maximum thrust force. The operation principle of the proposed machines is described. The influence of the major design parameters on the thrust force capability of both machines is highlighted. In addition, the optimal stator/mover combinations in terms of higher no-load back-EMF and consequently higher thrust force for both machines have been found.

Chapter Five

The electromagnetic performances, including open circuit flux linkage and back-EMF, thrust force capability, thrust force ripple, winding inductances, and the demagnetization withstand capability for both PM-SPM tubular machines, are compared. Moreover, the influence of the winding configuration on both machine performances is investigated. PS-PM tubular machines having single-layer windings are designed. The performances of the PS-PM tubular machine with single-layer winding are compared to their double-layer winding counterparts.

Chapter Six

Based on the concept of the partitioned stator PM machine, a new configuration of the single phase short stroke (SPSS) PM tubular machine is introduced in this chapter. With surface mounted and interior PM, two PS-SPSSPM tubular machines are designed. The machine configurations are described. The influence of the PM alignment either with stator tooth or stator slot on the machine performances is investigated. Furthermore, the leading design parameters of the mentioned machines are globally optimized for maximum thrust force capability. A comparison between the proposed machines has been carried out in terms of open circuit and load performances as well as losses.

Chapter Seven

This chapter aims to highlight the advantages and disadvantages of the proposed PS-PM linear machines compared to their conventional counterparts. Hence, a comparison between the PS-FRPM and the existing SFPM and FRPM linear machines is carried out. In addition, the PS-PM tubular machines are compared to the conventional SFPM tubular machine. Moreover, the performance of the PS-SPSS-SPM tubular machine is compared to that of the conventional SPSS-SPM tubular machine.

Chapter Eight

General conclusions are given and future work is suggested.

Appendices

The dynamic performance of the PS-FRPM linear machine is analysed, and a mathematical model of the mentioned machine is established in d-q frame in Appendix A. The drawing and parameters of the prototype of the PS-FRPM linear machines are detailed in Appendix B.

1.3.2 Thesis contributions

The contributions of this thesis are outlined as below:

- A new configuration of the FRPM linear machine, named as PS-FRPM linear machine, is proposed, in which the main drawbacks of the conventional FRPM linear machine, i.e. limitation of electrical and magnetic loadings, are overcome.
- Two novel PS-PM tubular machines are developed and analysed. They have both excitation sources, i.e. the PMs and the armature windings in two separated

stators, while the mover is iron pieces located between the two stators. The performances of PS-PM tubular machines with double- and single-layer winding are investigated.

- Two novel short-stroke PS-SPSSPM tubular machines are developed and compared. They have dual active stators and one passive mover, which is sandwiched between the two stators.

Chapter2. Comparison of Two Types of Doubly Salient Permanent Magnet Linear Machines

2.1 Introduction

Due to the development of the advanced permanent magnet materials, such as NdFeB magnets, PM machines have gained compatible or even better features compared to other machine topologies [ZHA14], [CHE11], [LIU13], [ZHU08], [KAN01]. PM linear machines have become promising candidates where ever a direct drive is required, since they combine the advantages of PM machines and linear machines [ZHA14], [GAN13], [ABD14].

Up to date, PM linear machines have been documented with many topologies. However, those in which both the PMs and the armature windings are being in one machine part are more preferable [CAO12], [ZHU11], [LU14], [CHU08]. This is because of the demerits of conventional PM machines can be overcome by such configuration. In addition, such topologies have one passive part made of iron only making the structure of such part easy to be manufactured [ZHU08], [CAO11a], [ABD14].

In this chapter, two types of aforementioned machines, i.e. SFPM and FRPM linear machines are designed, and the operation principle of each topology is described. Moreover, the machines are optimized for maximum thrust force. Additionally, open circuit and load performances of these machines are analysed. Finally, a comparison between both machines is carried out.

2.2 Switched Flux Permanent Magnet Linear Machine

Through the last decade, the interest of SFPM linear machines has been significantly increased, due to the fact that they incorporate the advantages of both SFPM rotational machines and PM linear machines [HUA11a], [ZHO12a], [JIN09], [CAO11b]. SFPM linear machines are characterized by desirable features, such as bipolar flux linkage, high thrust force and power density, rigid stator. Both magnets and coils are placed on the short mover, and therefore, SFPM linear machines become promising candidates for long stroke applications [LU13], [WAN09], [ZHU14].

2.2.1 Topology and Operation Principle

A cross-section of the SFPM linear machine is shown in Fig. 2.1, whilst its design parameters are listed in Table 2.1. The stator is salient pole made of iron only, and hence, the machine has a robust stator similar to that of SR linear machine. On the other hand, the mover consists of U shaped laminated segments and the PMs are sandwiched between them. The PMs are longitudinally magnetized in alternatively opposite polarity. The armature windings are concentrated windings, which are desirable due to low copper loss, and consequently improved machine efficiency.

Fig. 2.2 can be used to explain the operation principle of the SFPM linear machine. Like their rotational machine counterparts, SFPM linear machines operate under the concept of flux switched where both value and direction of the flux linkage are varied due to the change of the permeance seen by the armature. As shown in Fig.2.2, the flux is constantly presented in the machine by the permeant magnets. When the mover moves the amount and direction of the flux linkage in the mover coils will be varied, and consequently a back electromotive force (EMF) will be induced, which results from the changing of the flux path with the mover position. When the coils are fed by appropriate currents, a thrust force will be generated due to the interaction of permanent magnet flux linkage and the armature current.

Table 2.1 Main design parameters of SFPM linear machine

Items	Value
Number of phases	3
Number of mover poles	5
Number of stator slots	6
Stator slot pitch	28.32mm
Mover pole pitch	23.6mm
Air gap length	1mm
Total machine height	35mm
Machine length Z-direction	25mm
Current density (rms)	7A/mm^2
Velocity	1m/s

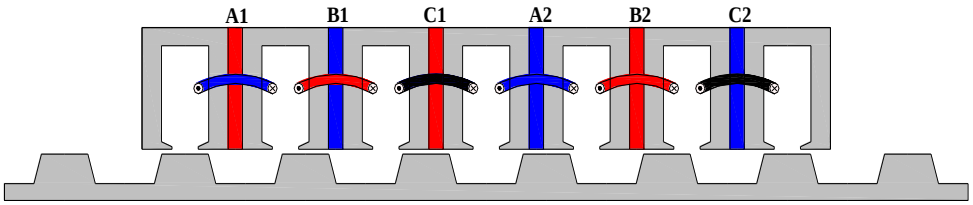

Fig. 2.1 Cross-section of SFPM linear machine.

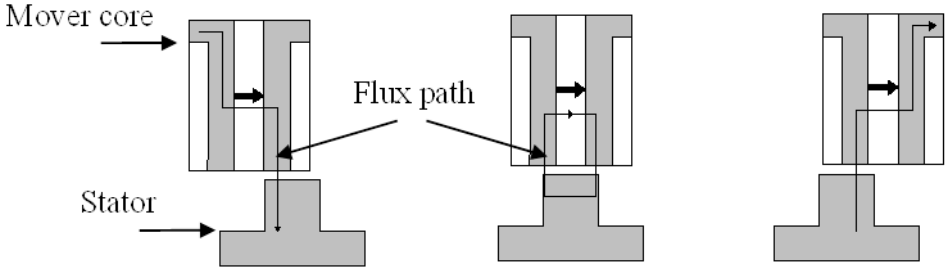

Fig. 2.2 Operation principle of SFPM linear machine.

2.2.2 Design Optimization

Linear machines with high force density are required for many applications. Therefore, machine optimization for maximum thrust force is an important issue at machine design stage. Genetic algorithm (GA) approach has been widely utilized to search the optimal solution in machine design application, since it is an efficient numerical optimization method [ZHU11]. Thanks to the advance on the computer aid design (CAD), global optimization of electrical machines can be carried out by utilizing FE based on GA. It should be mentioned that the FE package that is used in this thesis is (ANSYS Maxwell). In this section, the SFPM linear machine will be globally optimized for maximum thrust force using FE based on GA. The unvaried parameters through the optimization process are listed in Table 2.1. On the contrary, the parameters that are varied in the optimization process and their definitions are shown in Table 2.2, while Fig. 2.3 is a schematic of main parameters of the machine.

It is should be mentioned that the influence of PM thickness on the machine performance is individually investigated, in order to determine appropriate PM volume usage without sacrificing the machine performance. Fig. 2.4 depicts the variation of average thrust force with PM thickness. It can be observed that 4mm is the optimal PM thickness by which the average thrust force reaches the highest value. After this value the average thrust force decreases with the increasing of the PM thickness, due to the reduction of the slot area, which consequently reduces the electrical loading of the

machine. However, considering the cost of the PM, the PM thickness is decided to be 3.5mm.

Table 2.2 Definitions of variable parameters of SFPM linear machine for optimization

Items	Symbols	Definitions
Split ratio	*SR*	$\frac{TSH}{TMH}$
Mover back iron thickness ratio	*MBITHR*	$\frac{MBITH}{MH}$
Stator pole highest ratio	*SPHR*	$\frac{SPH}{TSH}$
Stator pole width ratio	*SPWR*	$\frac{SPW}{SPP}$
Mover teeth width ratio	*MTWR*	$\frac{MTW}{MSP}$

In Table 2.2, *SPH* and *TSH* indicate the stator pole height and the total stator height, respectively. *MBITH*, *MH*, *MTW*, and *MSP* represent the mover back iron thickness, the total mover height, the mover tooth width and the mover slot pitch, respectively. Additionally, *SPW* is referred as the stator pole width, while the stator pole pitch is donated as *SPP*. In Fig. 2.3 the value of stator pole angle (Ø) is 106°.

Initial, constrain and optimal values of the parameters, which are varied during the optimization process, are summarized in Table 2.3.

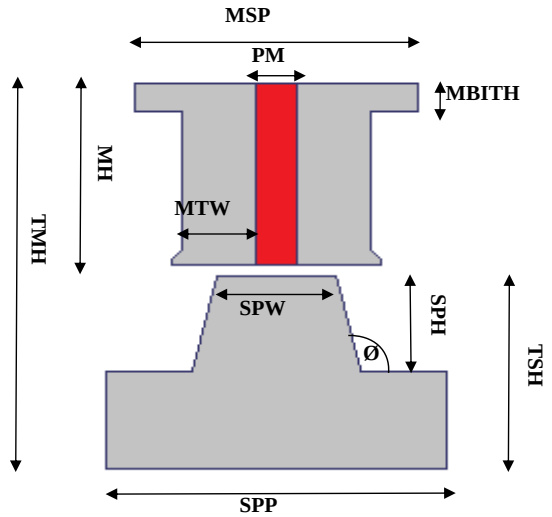

Fig. 2.3 SFPM linear machine main design parameters.

Table 2.3 Initial, constrain and optimal values of variable parameters for optimization

Items	Initial	Constrain	Optimal
SR	0.5	[0.2, 0.7]	0.33
MBITHR	0.2	[0.1,0.5]	0.15
SPHR	0.5	[0.3, 0.8]	0.75
SPWR	0.5	[0.12,0.544]	0.3
MTWR	0.207	[0.1, 0.4]	0.162

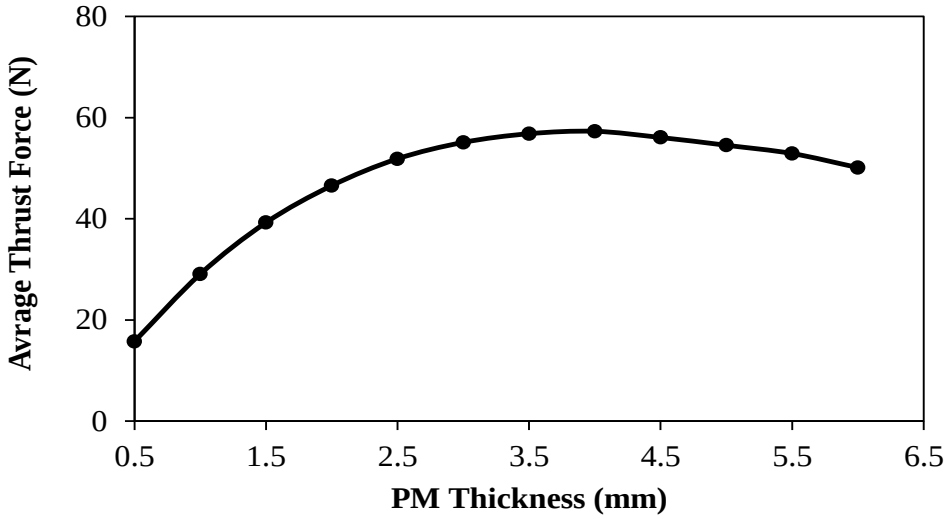

Fig. 2.4 Variation of average thrust force with PM thickness.

2.2.3 Electromagnetic Performance

In the following section the electromagnetic performance of the understudying machine will be analysed by EF, in terms of open and on load performances. Fig. 2.5 shows the air gap flux density due to the PM only. The peak value of the air gap flux density is about 1.24 T. However, it is not sinusoidal and has considerable harmonics due to the doubly salient structure of the machine. Flux linkage waveforms and corresponding harmonics are illustrated in Fig. 2.6. Obviously, the machine exhibits asymmetric flux linkages. The asymmetric flux linkage is caused by longitudinal end effect [CAI11], as it will be explained in Chapter 3. Fig. 2.7 presents back-EMF waveforms and associated harmonics of the analysed machine. It can be clearly seen that both phases A and C, which have coil located on the left and right ends of the machine, exhibit less back-EMF than that of phase B due to the longitudinal end effect. Thereby, the machine has unbalanced back-EMF.

In general, the main drawback of the PM machines is the attraction between the salient teeth/poles and the PMs, which causes the undesirable torque/force named as cogging torque/force. In PM linear machines cogging force is also contributed by the longitudinal end effect. Cogging force of the SFPM linear machine is shown in Fig. 2.8. It can be noted that the machine has slightly high cogging force with peak about 10 N. Furthermore, Fig. 2.9 depicts thrust force variation with mover position at rated current density (7 A/mm^2), the average thrust force is 62 N and the force ripple is about 55%. The thrust force ripple is calculated by:-

$$\text{Thrust force ripple} = \frac{Thf_{max} - Thf_{min}}{Thf_{avg}} \times 100\% \qquad (2.1)$$

On the other hand, the average thrust force against the current density is demonstrated in Fig. 2.10. Apparently, the machine has a linear force-current density characteristic at low current density value.

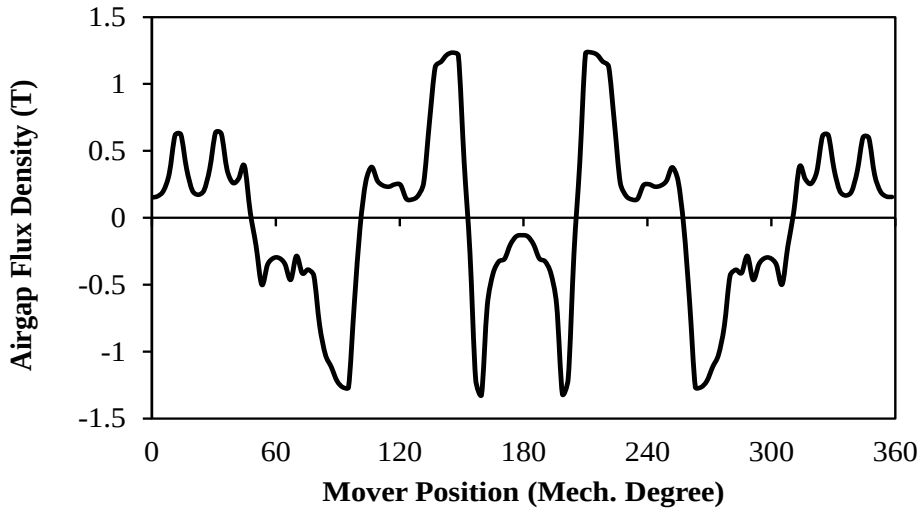

Fig. 2.5 Air-gap flux density.

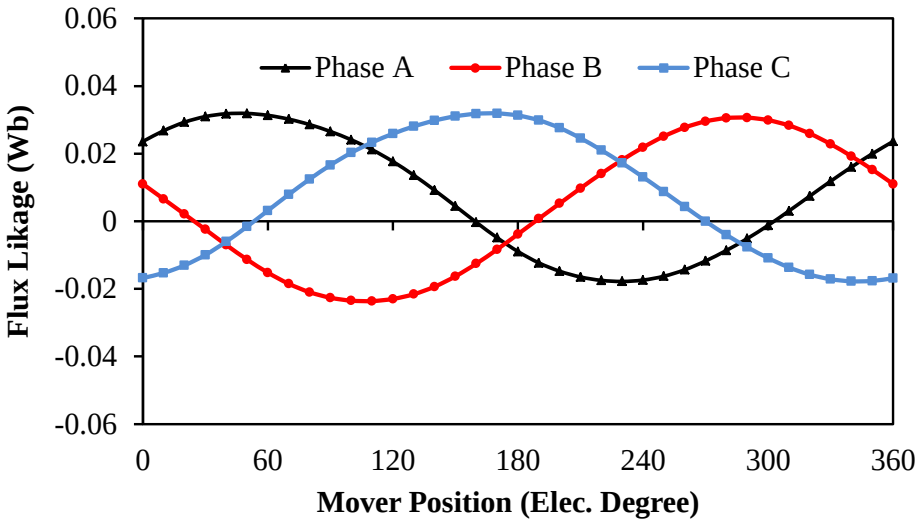

(a) Waveform

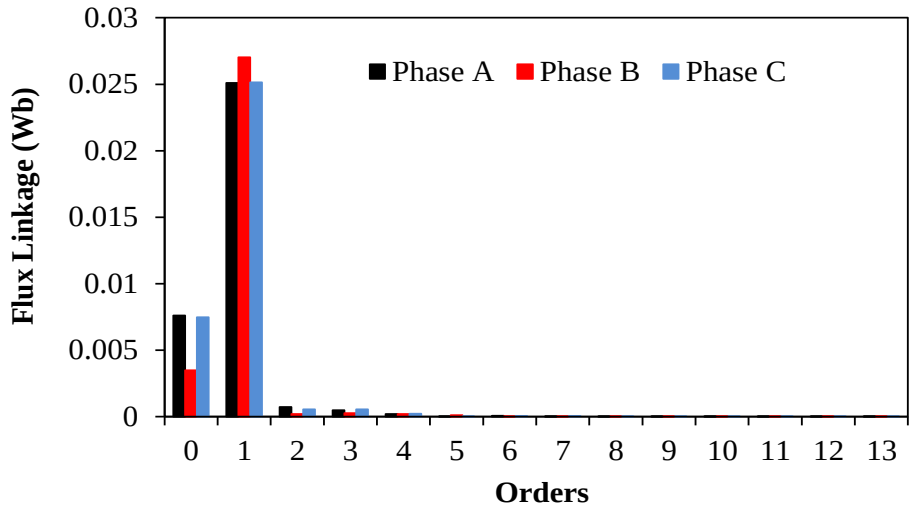

(b) Spectrum

Fig. 2.6 Flux linkage.

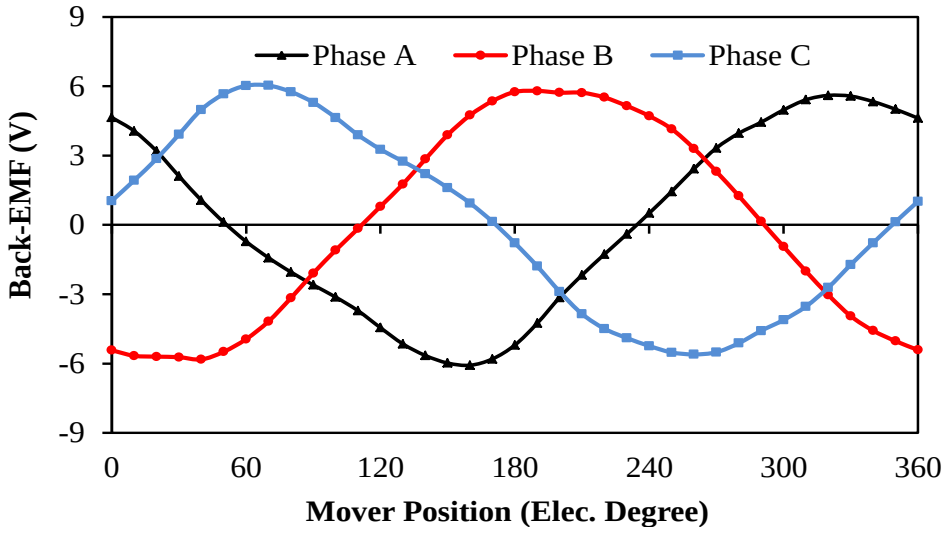

(a) Waveform

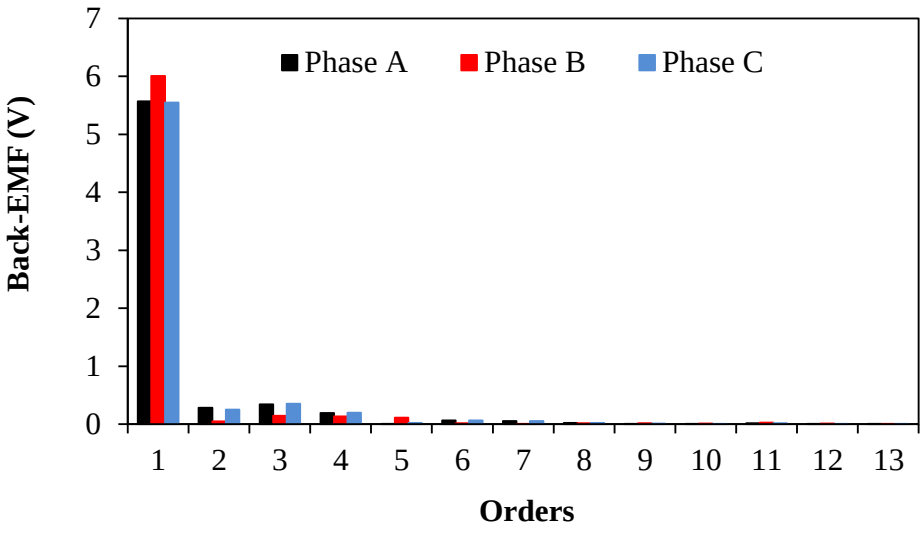

(b) Spectrum

Fig. 2.7 Back-EMF.

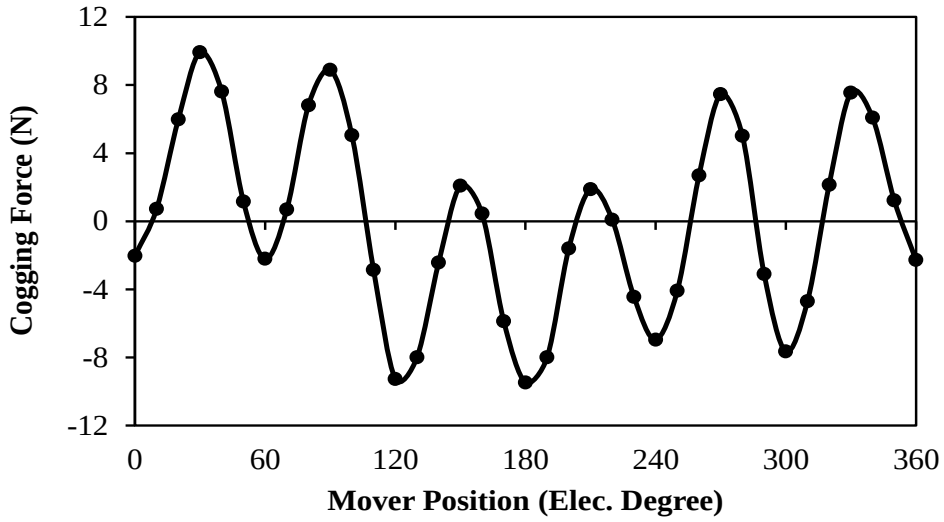

Fig. 2.8 Cogging force.

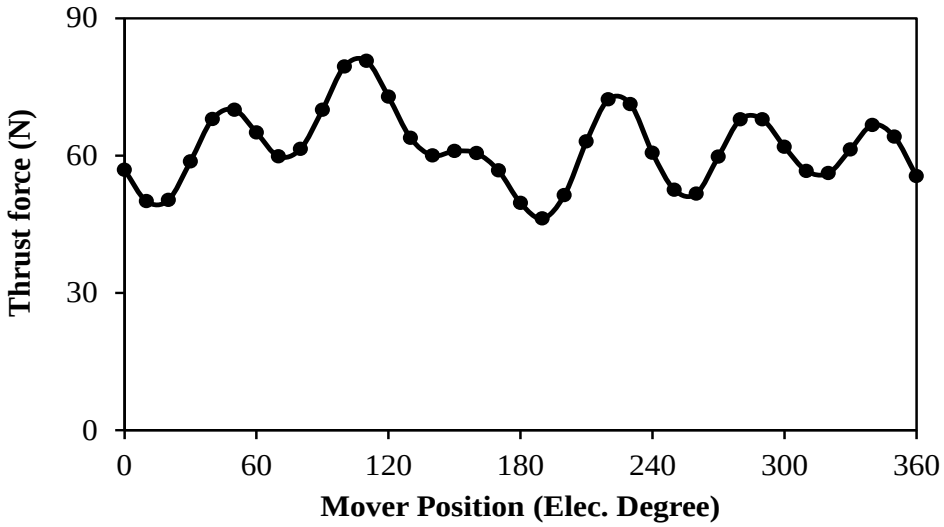

Fig. 2.9 Thrust force (current density = 7A/mm^^{2} rms).

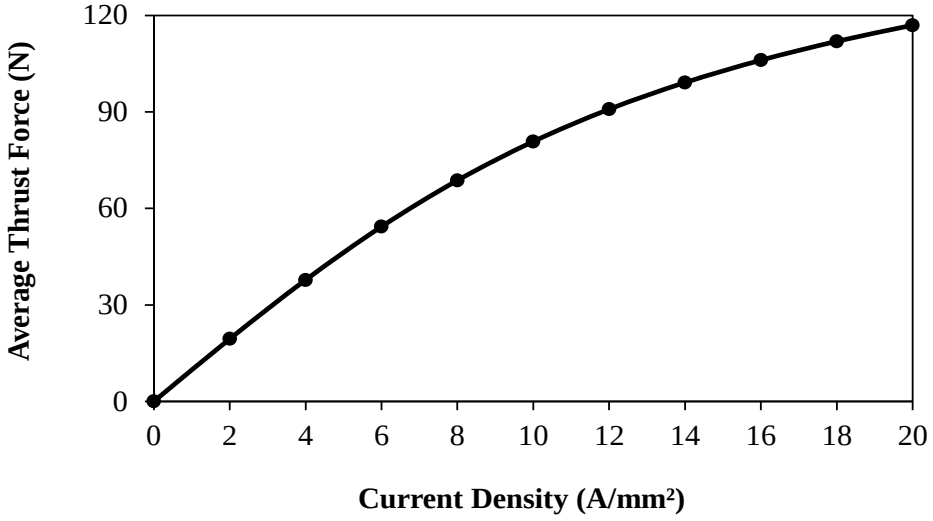

Fig. 2.10 Thrust force variation with current density.

2.3 Flux Reversal Permanent Magnet Linear Machine

FRPM machines have been introduced to many applications, such as defence, aerospace, automotive and industrial applications. Such machines fall into PM machine category, which consist of one active part and another passive part. Therefore, FRPM machines inherently exhibit the merits of simple and robust structure, high power density and high reliability [LIA95], [DEO97], [CHU11].

In the following sections, FRPM linear machines will be designed and analysed in terms of airgap flux density, flux linkage, back-EMF, force ripple and thrust force.

2.3.1 Topology and Operation Principle

The FRPM linear machine to be investigated is shown in Fig. 2.11. The machine has simple stator, while the mover hosts both the excitation sources. The mover tooth surfaces are equipped by two PM pieces of alternative polarities. The machine is designed with same specifications as that of the SFPM linear machine for fair comparison. The operation principle of the FRPM linear machine can be demonstrated by utilising Fig. 2.12 and Fig. 2.13, which show phase A open circuit flux linkage and its corresponding potential distribution at four different mover positions, respectively. It can be noted that both value and polarity of the flux are changing with the mover position. It is worth mentioning that maximum flux linkage would be obtained when half of mover tooth aligns with stator pole, Fig. 2.13 (b and d). In contrast, zero flux linkage will be achieved at two mover positions, i.e. when the centre of the mover tooth aligns with the centre of stator pole, and when the mover tooth faces stator inter-pole area, Fig. 2.13 (a and c). The variation of flux amplitude and direction with mover position induces back-EMF. When the machine windings are excited by three phase currents, a thrust force will be resulted from the interaction between PM flux linkages and the coil currents.

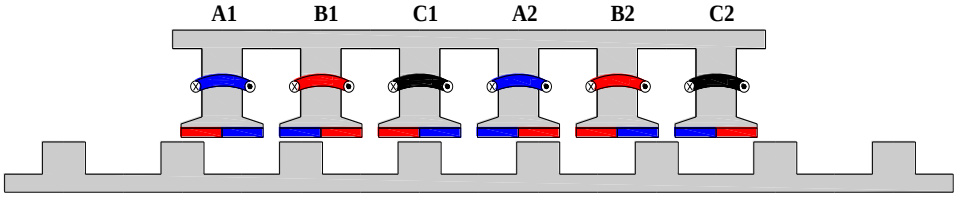

Fig. 2.11 FRPM linear machine cross-section.

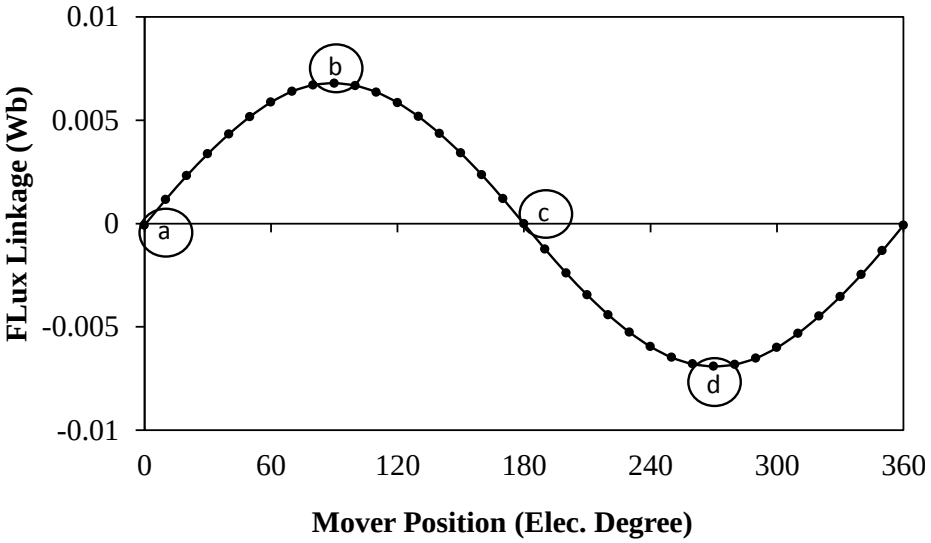

Fig. 2.12 Typical phase A flux linkage.

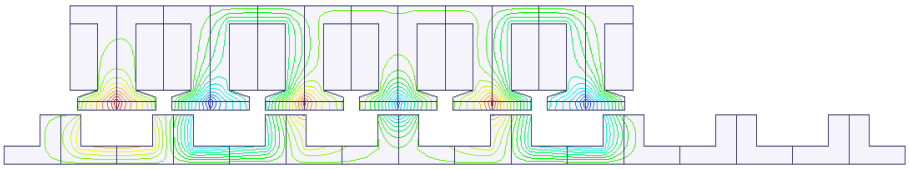

(a) Mover position (Zero flux)

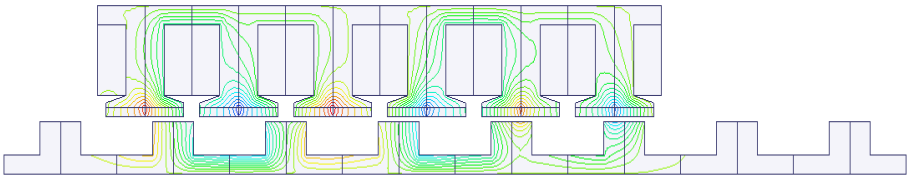

(b) Mover position (Maximum positive flux)

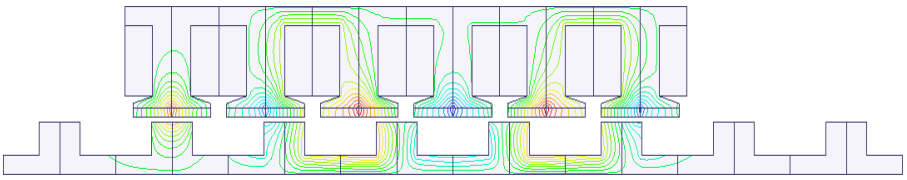

(c) Mover position (Zero flux)

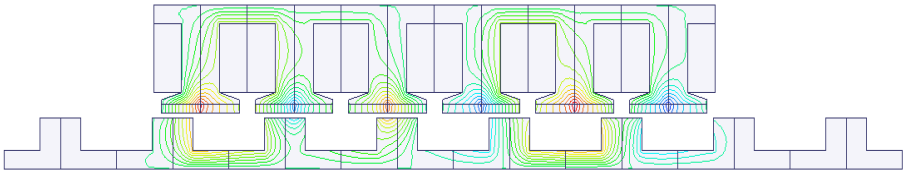

(d) Mover position (Maximum negative flux)

Fig. 2.13 Open circuit flux line distributions.

2.3.2 Design Optimization

The machine is globally optimized under the same optimization conditions as those of the SFPM linear machine. The main design parameters of the FRPM linear machine are shown in Fig. 2.14. The definitions of the varied parameters during the optimization process are illustrated in Table 2.2. On the other hand, Table 2.4 lists initial, constraint and optimal values of these parameters. It should be emphasised that the impact of the PM thickness on the thrust force capability of the FRPM linear machine is investigated before the optimization process, in order to determine adequate PM thickness of the machine. Fig. 2.15 shows the variation of the average thrust force with the PM thickness. It can be noted that the machine has an optimal PM thickness, i.e. 2 mm in which the average thrust force is maximum, and the performance would be deteriorated beyond this value. It is worth mentioning that the PM thickness of the FRPM linear machine is chosen to be equal to the optimal value.

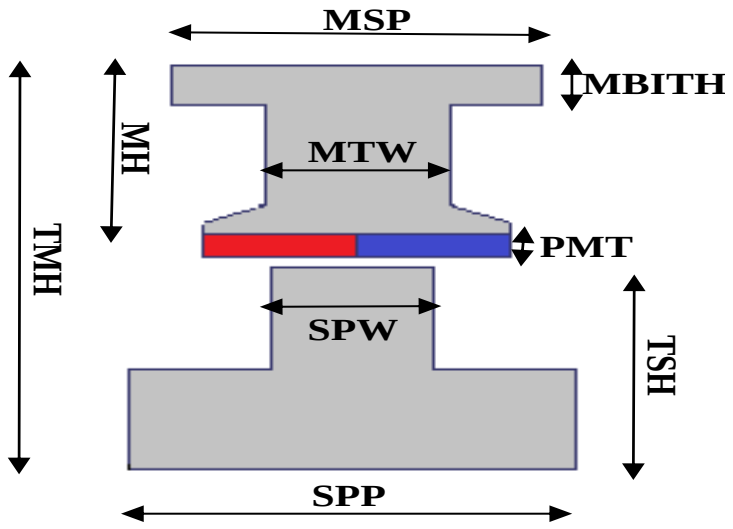

Fig. 2.14 FRPM linear machine main design parameters.

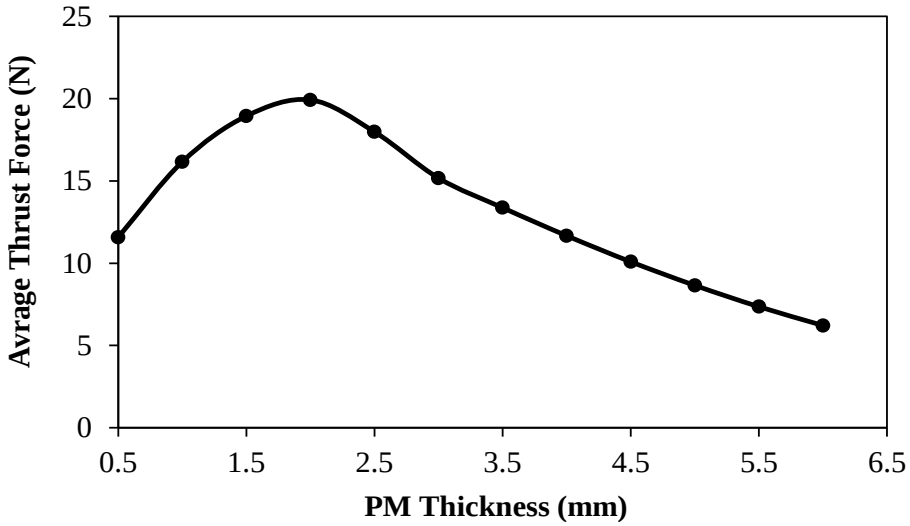

Fig. 2.15 Thrust force variation with PM thickness.

Table 2.4 Initial, constrain and optimal values of variable parameters for optimization.

Items	Initial	Constrain	Optimal
SR	0.5	[0.2, 0.7]	0.33
MBITHR	0.2	[0.1,0.5]	0.15
SPHR	0.5	[0.3, 0.8]	0.75
SPWR	0.5	[0.12,0.544]	0.3
MTWR	0.207	[0.1, 0.4]	0.162

2.3.3 Electromagnetic Performance

No load airgap flux density of the FRPM linear machine is shown in Fig. 2.16. Similar to the doubly salient machines, the FRPM linear machine has non sinusoidal airgap because of the salient structure of both machine parts, i.e. stator and mover. It is noted that the peak airgap flux density is about 0.8 T. Flux linkage waveforms with corresponding harmonics and back-EMF waveforms with equivalent harmonics are presented in Fig. 2.17 and Fig. 2.18, respectively. It can be observed that the machine exhibits symmetrical flux linkage waveforms and consequently balanced back-EMF waveforms. Hence, the longitudinal end effect does not significantly impact the machine performance. Moreover, Fig. 2.19 shows the cogging force of the understudying machine. Obviously, the FRPM linear machine has low cogging force due to low longitudinal end effect influence. Thereby, thrust force ripple, which is mainly caused by the cogging force, is low compared to other PM linear machines.

Fig. 2.20 illustrates the thrust force waveform when sinusoidal current in phase with the back-EMF at rated current density (7 A/mm^2) is applied to the machine windings. Despite of the low thrust force capability of such topology, it shows low thrust force ripple about 29%. Furthermore, average thrust force variation with current density is shown in Fig. 2.21. Obviously, the machine has a good linear characteristic.

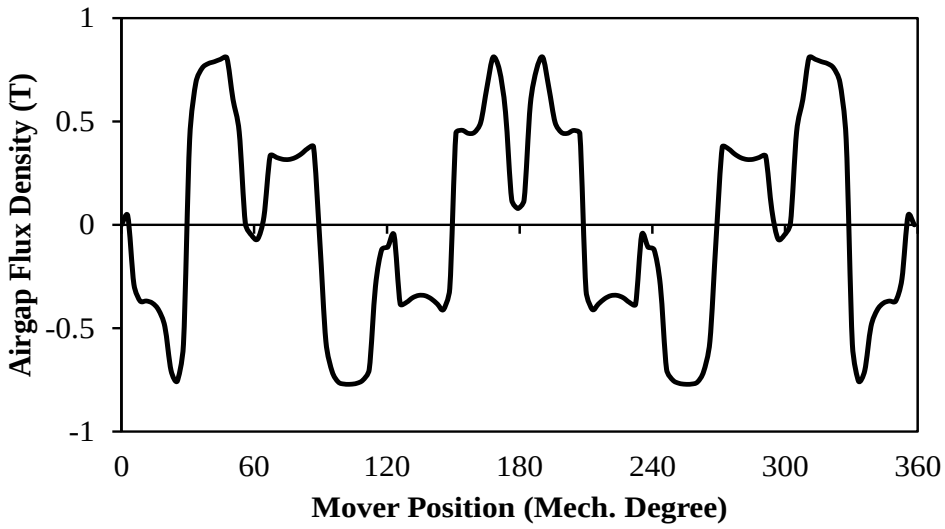

Fig. 2.16 Air-gap flux density.

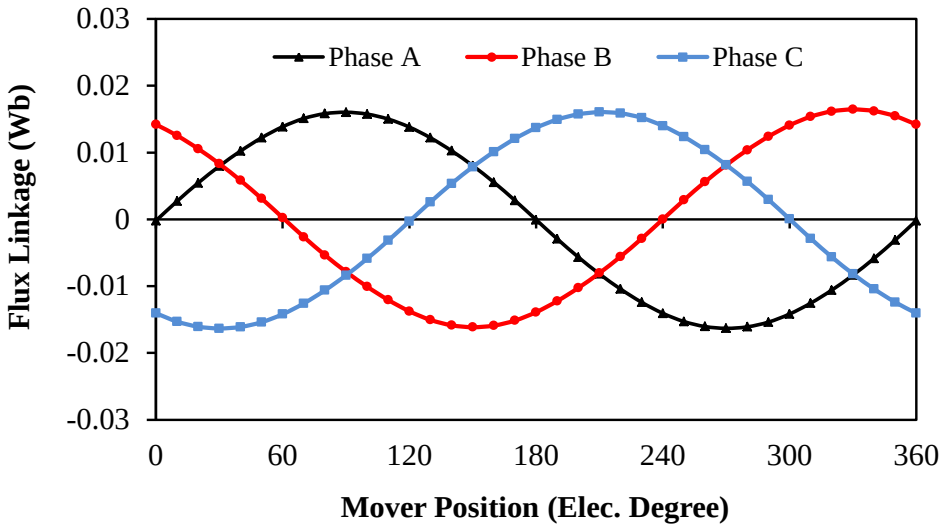

(a) Waveform

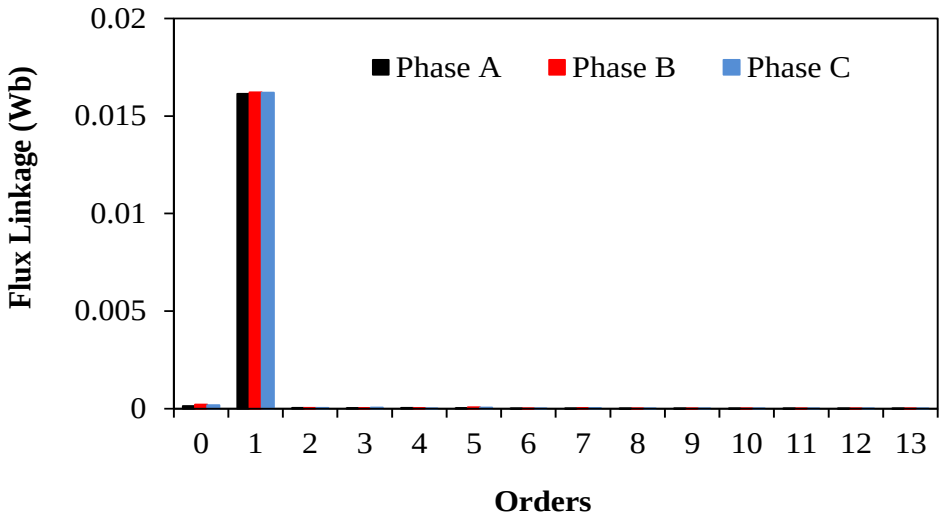

(b) Spectrum

Fig. 2.17 Flux linkage.

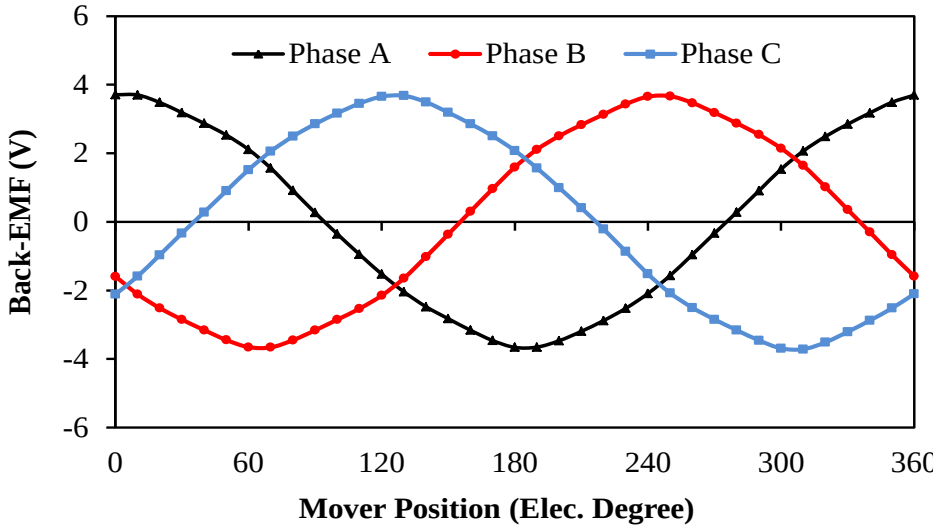

(a) Waveform

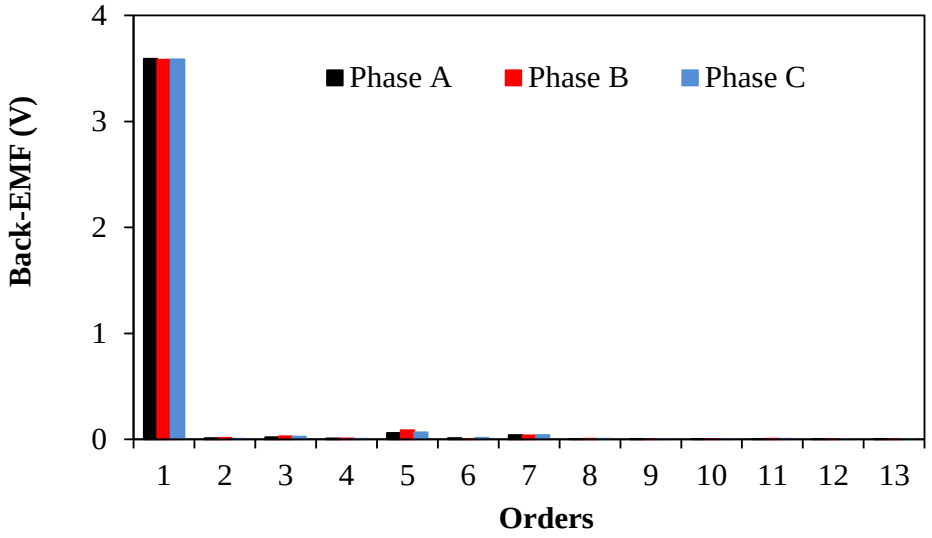

(b) Spectrum

Fig. 2.18 Back-EMF.

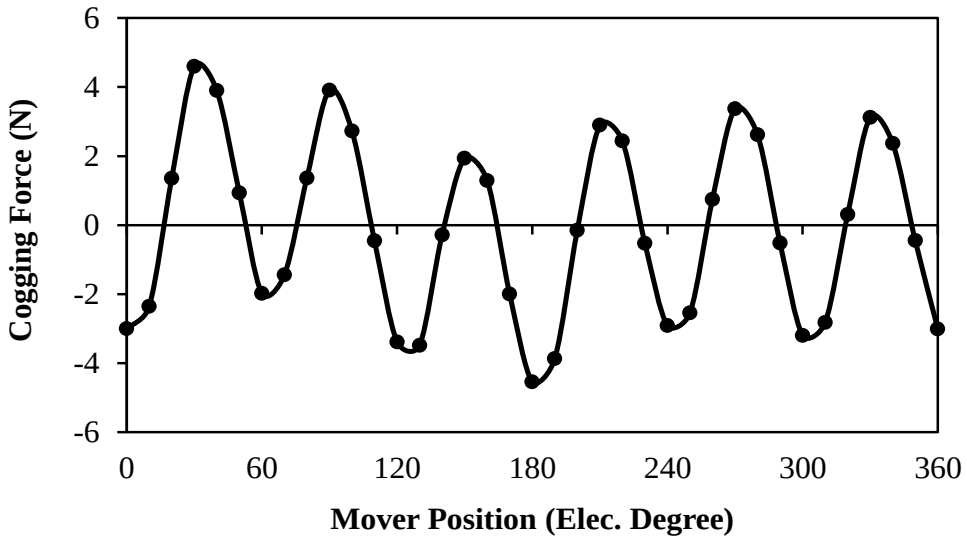

Fig. 2.19 Cogging Force.

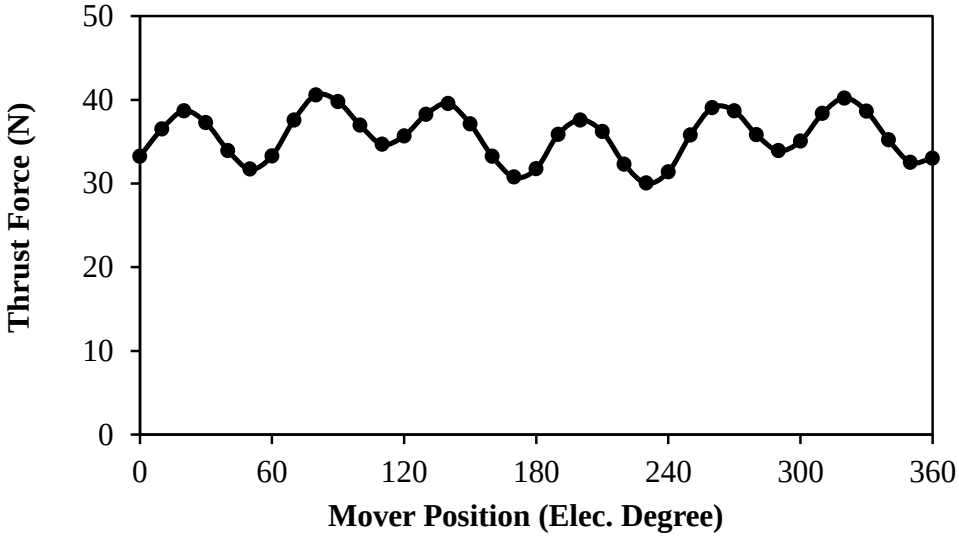

Fig. 2.20 Thrust force (current density = 7A/mm^2 rms).

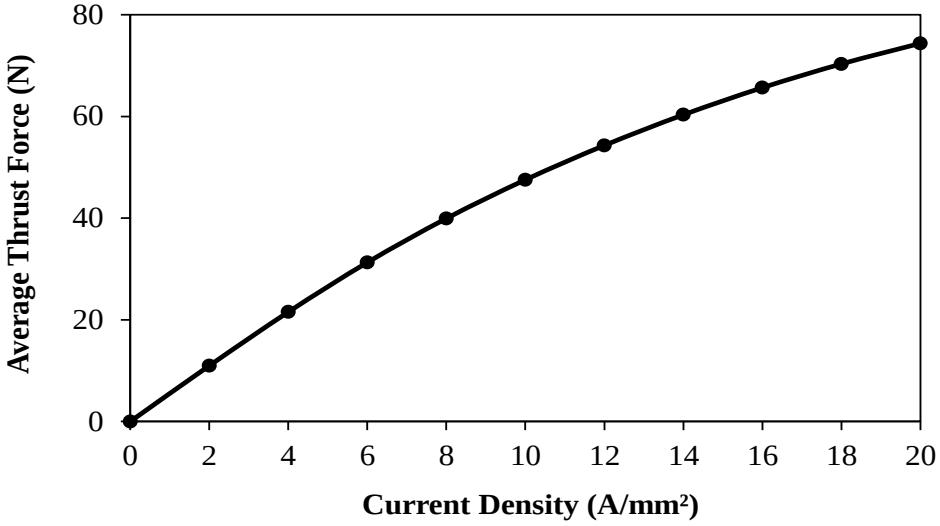

Fig. 2.21 Thrust force variation with current density.

2.4 Comparison of Electromagnetic Performance of SFPM and FRPM Linear Machines

The electromagnetic performance of both aforementioned machines will be compared in terms of flux linkage, back-EMF, open circuit force, thrust force capability, self- and mutual-inductances, and finally the demagnetization withstand capability for both machines will be investigated and compared.

2.4.1 Open Circuit Performance

Phase A flux linkages for both SFPM and FRPM linear machines are compared in Fig. 2.22. Higher flux linkage can be achieved by the SFPM linear machine because of the higher airgap flux density results from better flux focusing as well as higher amount of PM usage. On the other hand, FRPM linear machine shows almost symmetrical flux linkage, while SFPM linear machine exhibits asymmetric flux linkage waveform. Hence, it can be concluded that the longitudinal end effect has more influence on the SFPM linear machine performance compared to the FRPM linear machine. Fig. 2.23 compares phase A back-EMFs for both machines at 1 m/s velocity. Evidently, SFPM has higher back-EMF than that of FRPM linear machine due to the higher flux linkage. Although the low order harmonics, i.e. the 2^{nd}, 3^{th} and 4^{th} harmonics, exist in the back-EMF waveform of the SFPM linear machine, such harmonics are nearly eliminated in the FRPM linear machine because of low longitudinal end effect impact, as it will be seen in Chapter 3. Moreover, the open circuit forces, i.e. cogging forces, for both understudying machines are shown in Fig. 2.24. Lower undesirable cogging force can be obtained by the FRPM linear machine, leading to less thrust force ripple.

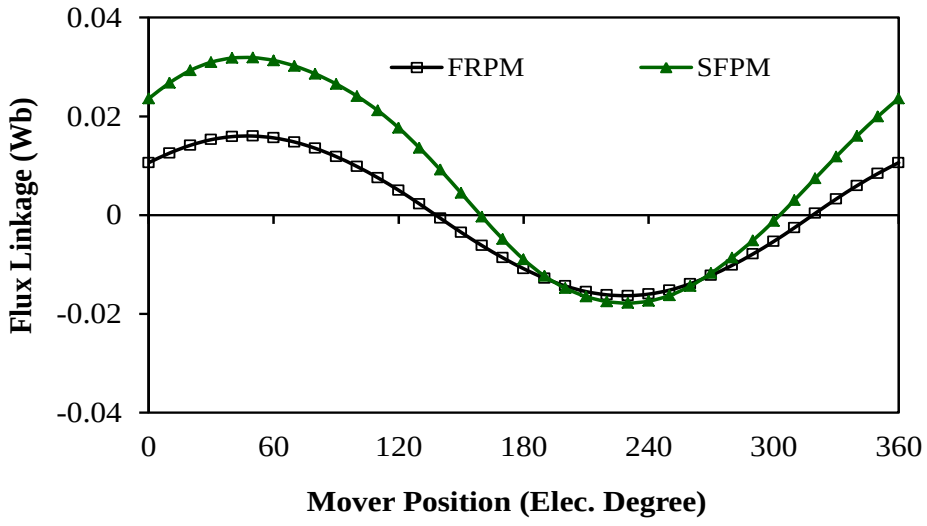

(a) Waveform

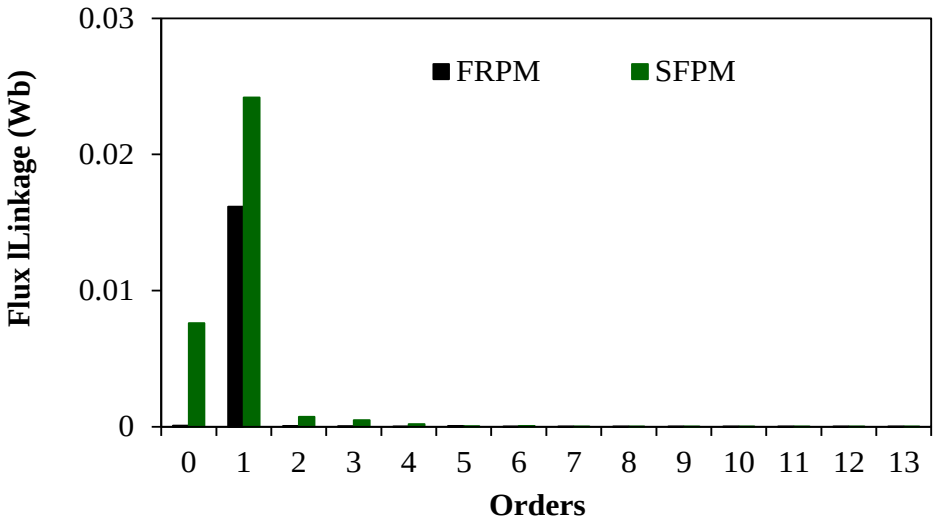

(b) Spectrum

Fig. 2.22 Flux linkage comparison.

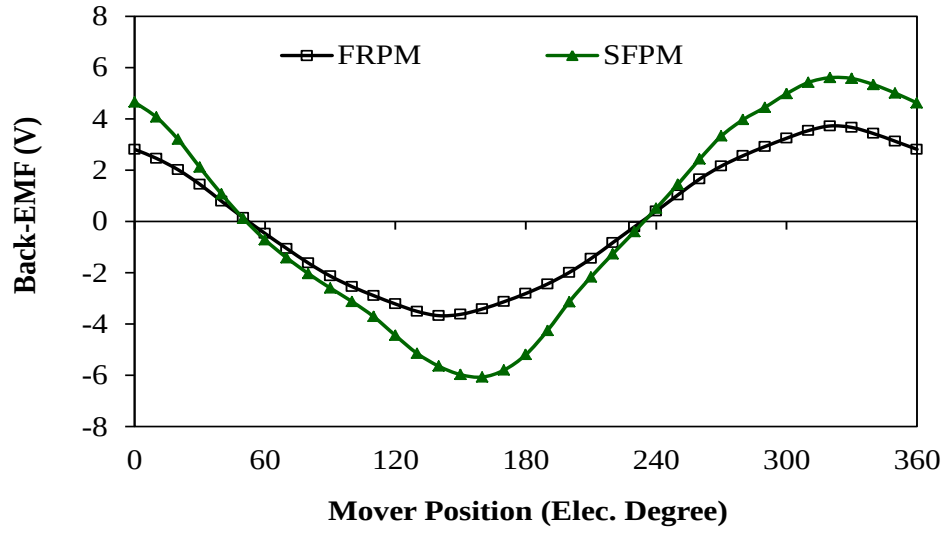

(a) Waveform

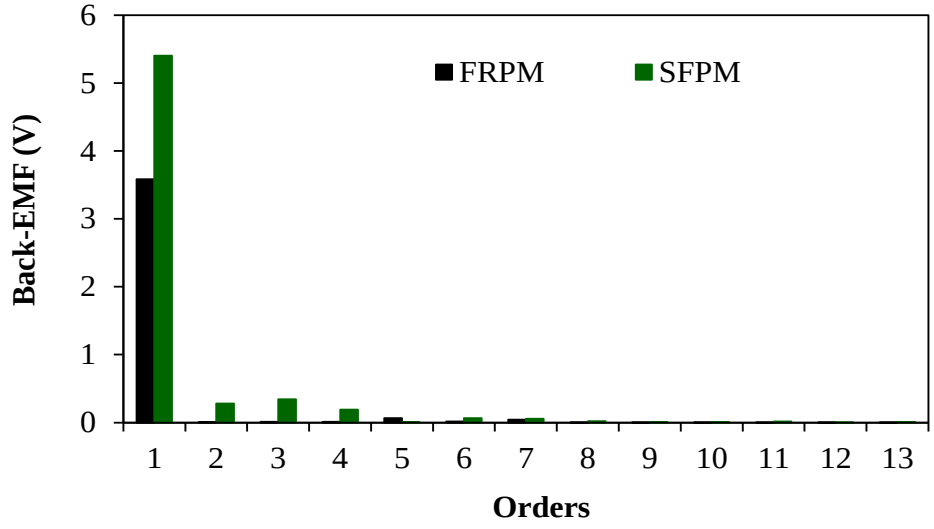

(b) Spectrum

Fig. 2.23 Back-EMF comparison.

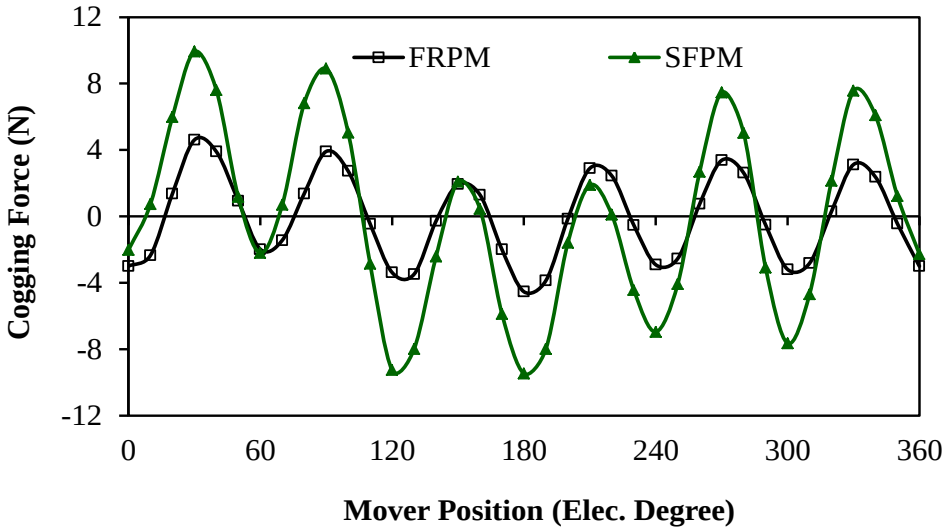

Fig. 2.24 Cogging force comparison.

2.4.2 Load Performance

Thrust forces of both machines are compared in Fig. 2.25. Obviously, the SFPM linear machine can achieve about 40% higher thrust force than that of the FRPM linear machine due to higher back-EMF. However, the FRPM linear machine has lower thrust force ripple compared to the SFPM linear machine because of lower cogging force, Fig. 2.26. In addition, the average thrust force with different current density for the analysed machines is illustrated in Fig. 2.27. Furthermore, the variation of self and mutual inductances with the mover position of the two machines are shown in Fig. 2.28. Both machines exhibit almost the same self-inductances. However, the variation of self-inductance with mover position of the FRPM topology is less than that one of the SFPM topology. On the other hand, in terms of mutual coupling the SFPM linear machine possesses slightly lower mutual coupling. It is worth mentioning that, self and mutual inductances of phase A of the understudying machines are calculated by [MIN11].

$$L_{AA} = \frac{\varphi_A(I_a = I, I_b = I_c = 0) - \varphi_A(I_a = I_b = I_c = 0)}{I} \tag{2.2}$$

$$L_{AB} = \frac{\varphi_B(I_a = I, I_b = I_c = 0) - \varphi_B(I_a = I_b = I_c = 0)}{I} \tag{2.3}$$

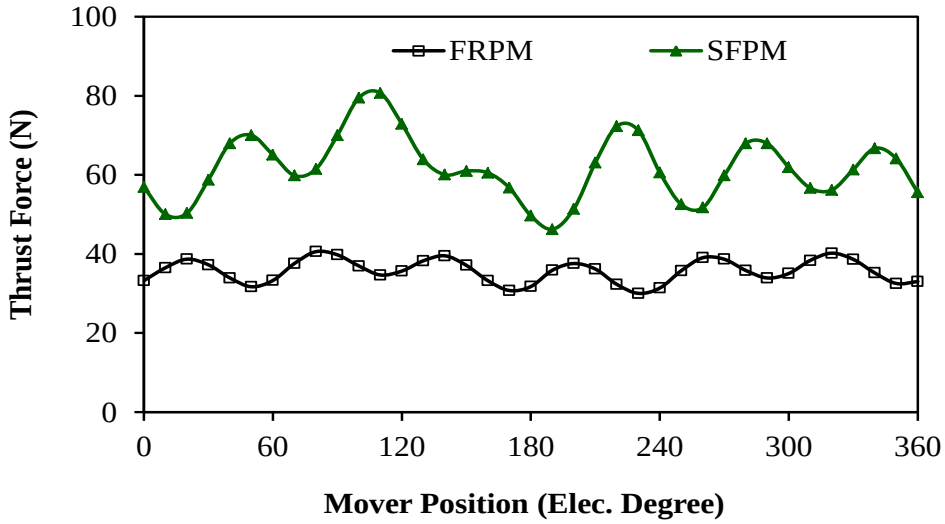

Fig. 2.25 Thrust force (current density = 7A/mm^2 rms).

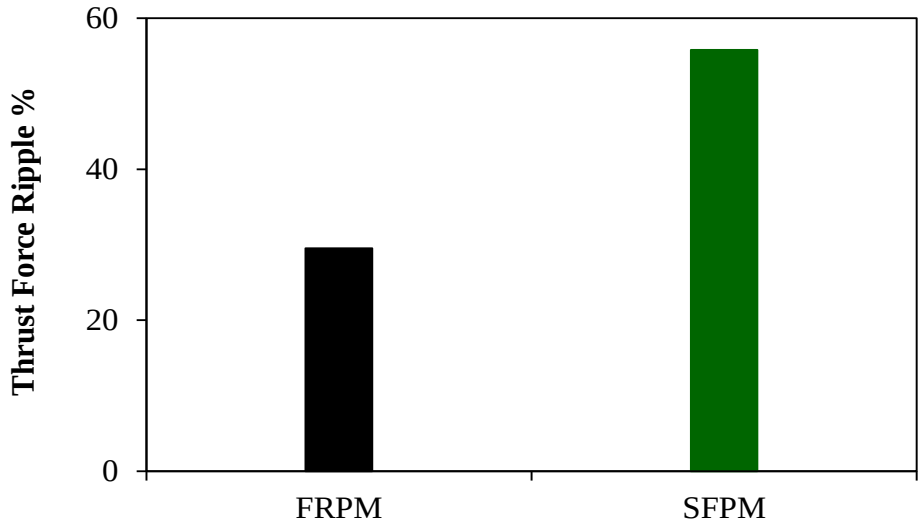

Fig. 2.26 Thrust force ripple comparison.

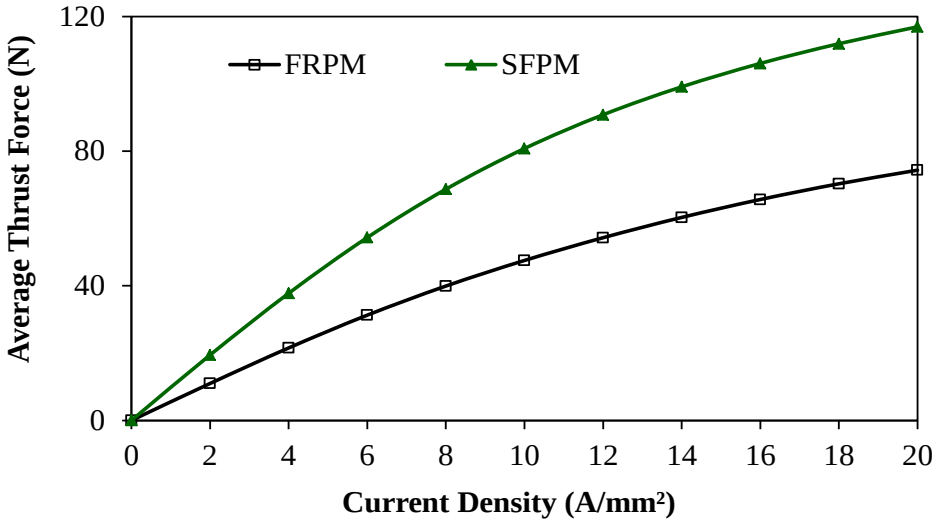

Fig. 2.27 Average thrust force variation with current density of both machines.

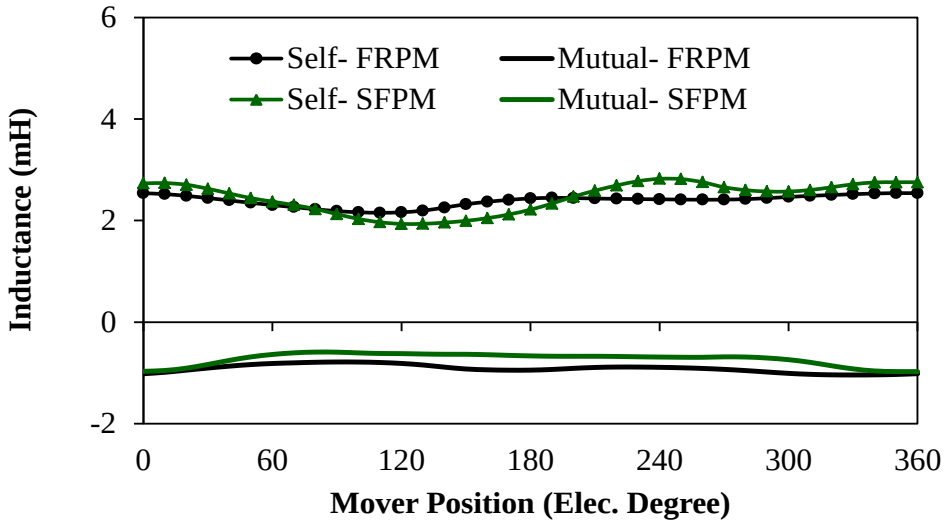

Fig. 2.28 Self- and mutual-inductances for both machines.

2.4.3 Investigation of Demagnetization Withstand Capability

Permanent magnets are vulnerable to demagnetization risk. Generally, rare earth NdFeB magnets, which are commonly used in many PM machines, would be partially or entirely demagnetized, if the magnet temperature or the armature reaction is very high [ZHO12b] [NAI16]]. High demagnetization withstand capability is a vital characteristic for reliable operation of the PM machines since magnet demagnetization negatively affects the PM machine performance. Hence, in this section the demagnetization withstand capabilities for both FRPM and SFPM linear machines will be investigated. An exemplary of PM demagnetization characteristic is shown in Fig. 2.29. It can be seen that due to the influence of the external demagnetization field, the PM working point would be moved from point P_1 to point P_2, which leads to reduction of the PM residual flux density, and subsequently, the PM demagnetization occurs [SHI12]. It should be mentioned that the demagnetization analysis has been conducted under the following conditions:

- PM temperature is 120^0C.
- Pure demagnetization current excitation.
- The PM knee point at 120^0C has been considered as the minimum flux density reference to avoid irreversible PM demagnetization.
- Four locations have been identified in each PM pole, i.e. on each corner of the PM in order to evaluate the flux density in the PMs.

Fig. 2.30 (a) and (d) show flux densities for north and south PMs of the FRPM linear machine, respectively, while Fig. 2.31, (a) and (c) illustrate flux densities for north and south PMs, of the SFPM linear machine, respectively. It can be noted that some PMs of both FRPM and SFPM linear machines lose their magnetizations and also some have flux densities equal to knee point. Therefore, it can be concluded that such topologies have the potential risk of irreversible PM demagnetization.

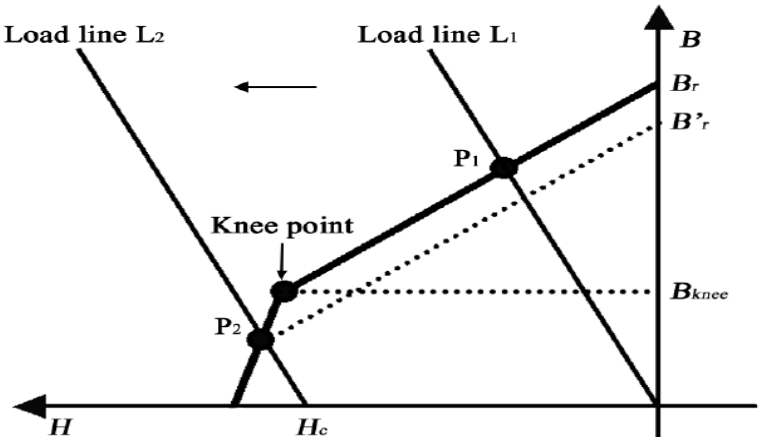

Fig. 2.29 Typical B-H curve of NdFeB magnet.

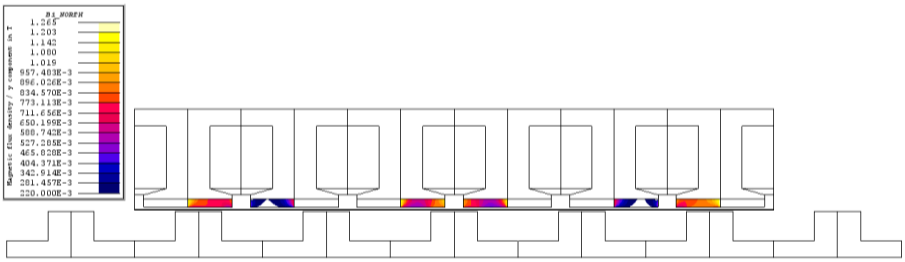

(a) North-pole PMs flux density distributions of FRPM linear machine

(b) Zoom in of PM no.3

(c) Zoom in of PM no.10

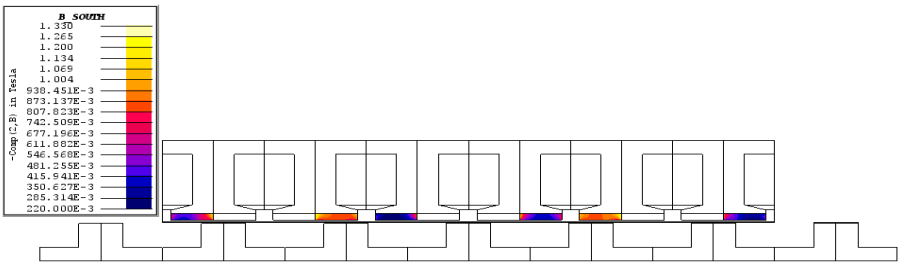

(d) South-pole PMs flux density distributions of FRPM linear machine

(e) Zoon in of PM no.5

(g) Zoon in of PM no.12

Fig. 2.30 FRPM linear machine PM flux density distributions at 120^0C.

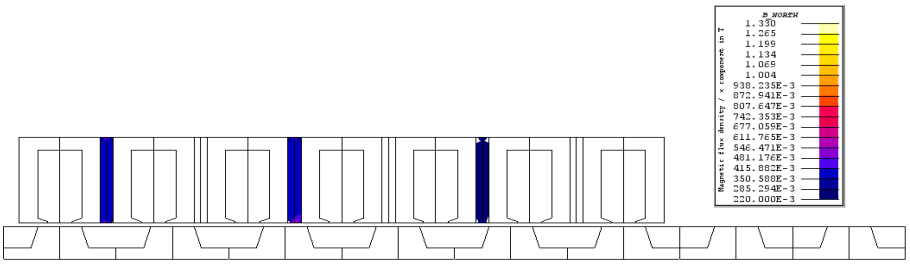

(a) North-pole PMs flux density distributions of SFPM linear machine

(b) Zoom in of PM no.5

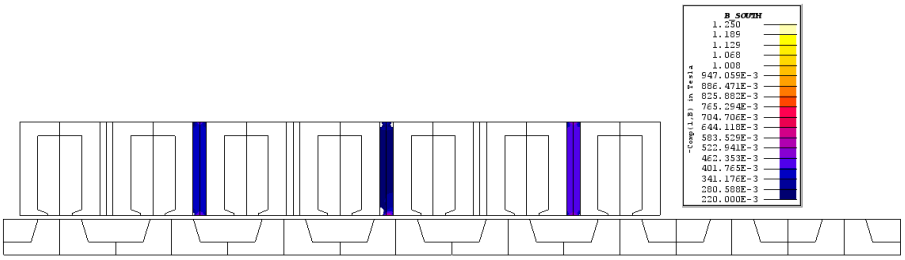

(c) South-pole PMs flux density distributions of SFPM linear machine

(d) Zoom in of PM no.4

Fig. 2.31 SFPM linear machine PM flux density distributions at 120^0C.

Table 2.5 summarises the electromagnetic performances of both machines. It shows that the SFPM linear machine possesses the advantage of flux focusing resulting in higher airgap flux density compared to the FRPM linear machine. In terms of flux linkage, back-EMF, and subsequently thrust force capability the SFPM linear machine has better performance than those of the FRPM linear machine. On the other hand, owing to less influence of the longitudinal end effect, the FRPM linear machine exhibits symmetrical flux linkage waveforms, less low order harmonics in the back-EMF waveforms and less thrust force ripples compared to the SFPM linear machine. Moreover, both machines have almost the same fault tolerant capability, and also both of them show the potential risk of irreversible PM demagnetization.

Table 2.5 Performance comparison of FRPM and SFPM linear machines

Items	FRPM	SFPM
Flux linkage fundamental	0.016	0.024
Back-EMF fundamental	3.6	5.4
Peak cogging force	4.6	10
Average thrust force (current density 7A/mm^2 rms)	35.7	61.7
Thrust force ripple	29.5%	55.8%
Longitudinal end effect	Very small	Significant
Mutual coupling	Low	Low
Demagnetization risk	Existing	Existing
Mover mass (kg)	0.5317	0.636

2.5 Summary

Two PM linear machines, i.e. SFPM and FRPM linear machines, are designed, optimized and compared in this chapter. It should be mentioned that both machines have the same design specifications and their optimizations are carried out under the same conditions. It is shown that the longitudinal end effect has a significant influence on the SFPM linear machine performance. In contrast, the FRPM linear machine is slightly affected by such feature. Despite the fact that the SFPM linear machine has higher thrust force compared to the FRPM linear machine, the later possess the advantage of low thrust force ripple and almost symmetrical flux linkage waveforms. Moreover, both machines have almost similar fault tolerance capability. Additionally, PM demagnetization risk presents in both analysed machines.

Chapter3. Novel Partitioned Stator (PS) Flux Reversal Permanent Magnet (FRPM) Linear Machines

3.1 Introduction

The demand for linear machines has significantly increased throughout the last two decades. Such machines have the characteristics of robustness and reliability, due to the omission of the conversion mechanism from rotary to linear motion [WAN08]. Hence, linear machines are being applied in numerous applications including, transportation, airspace, military, etc. [ZOU12]. PM linear machines are distinguished by the advantages of high thrust force and efficiency [BOL99] [ABB08].

FRPM linear machines belong to the PM linear machines topologies in which both exciting sources are being in one machine part (either mover or stator) and the second part is passive (made of iron only). Although FRPM linear machines possess the merits of a simple and robust mover (stator) structure, having both permanent magnets and armature windings in one machine part leads to magnetic and electrical loading limitations, which represent their main demerits, as is shown in Chapter 2 Thereby, to overcome such disadvantages, PS- FRPM linear machine topology in which the concept of dual active stators and one passive mover is adopted will be designed in this chapter. The machine configuration and operation principle are introduced. In addition, the force production mechanism for the proposed machine is analysed. The major design parameters of the proposed machine are optimized to achieve maximum thrust force. Furthermore, the influence of the longitudinal end effect on the machine performance is investigated. Moreover, the optimal stator/mover combination for the highest back-EMF and consequently the highest thrust force capability is determined. Additionally, the effect of the cross-coupling on the machine performance, particularly on flux linkage and d- and q-axis inductances, is highlighted. The machine losses and efficiency are obtained. Finally, machine demagnetization withstand capability is evaluated.

3.2 Machine Structure and Operation Principle

Fig. 3.1 shows a cross-section of the proposed PS-FRPM linear machine. It can be seen that the machine consists of one passive mover and two active stators. The mover is made of iron only, with segmental structure. On the other hand, the excitation sources, i.e. the PMs and the windings, are located on separate stators. Thus, the proposed machine has the feature of a larger slot area, which leads to reduce winding

resistance and copper loss, and consequently enhances the thrust force and efficiency. Furthermore, the demagnetization risk of the PMs can be reduced since the magnets are separated from the armature reaction. It is worth mentioning that concentrated windings have been used, since they have the merit of short end winding. As a result, the copper consumption is reduced, and hence less copper loss can be achieved [HUA05]. The specifications of the machine parameters are listed in Table 3.1. It is worth mentioning that the design parameters in Table 3.1 are the same to those in Table 2.1.

The operation principle of the PS-FRPM linear machine is based on flux switching where the amplitude as well as the direction of the flux linkage is varied with the motion of the mover.

Similar to the rotational PS-FRPM machine [ZHU15], the mover position in electrical degree can be determined by

$$\theta_e = N_m \theta_m \tag{3.1}$$

where θ_e, θ_m and N_m , and are respectively the mover position in electrical degree, the mover position in mechanical degree and the number of mover pole.

According to Fig. 3.2 when the mover moves 50 electrical degrees from its initial position in Fig. 3.1, the flux linkage of the armature winding due to PM will reach its maximum positive value, whilst with 90 electrical degrees displacement of the mover from point A the flux linkage becomes zero. Then the flux linkage will be on its negative maximum value at point C when the mover moves another 90 electrical degrees, and finally becomes zero again at point D.

Table 3.1 Main design parameter of PS-FRPM linear machine

Items	Value
Number of phases	3
Number of mover poles	5
Number of stator slots	6
Stator 1 slot pitch	23.6mm
Stator 2 pole pitch	23.6mm
Mover pole pitch	28.32mm
Air gap 1 length	1mm
Air gap 2 length	1mm
Total machine height	35mm
Machine length Z-direction	25mm
Current density (rms)	7A/mm^2
velocity	1m/s

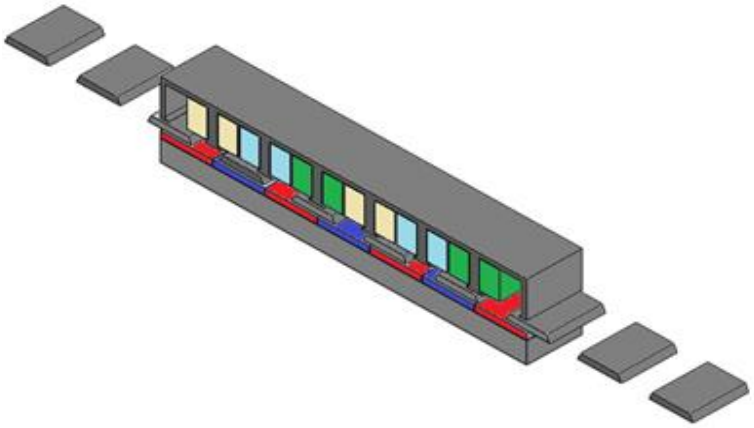

(a) 3D-View

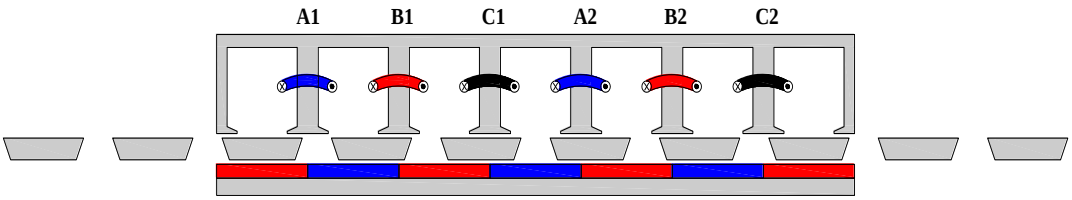

(b) Cross-section

Fig. 3.1 Proposed machine configuration.

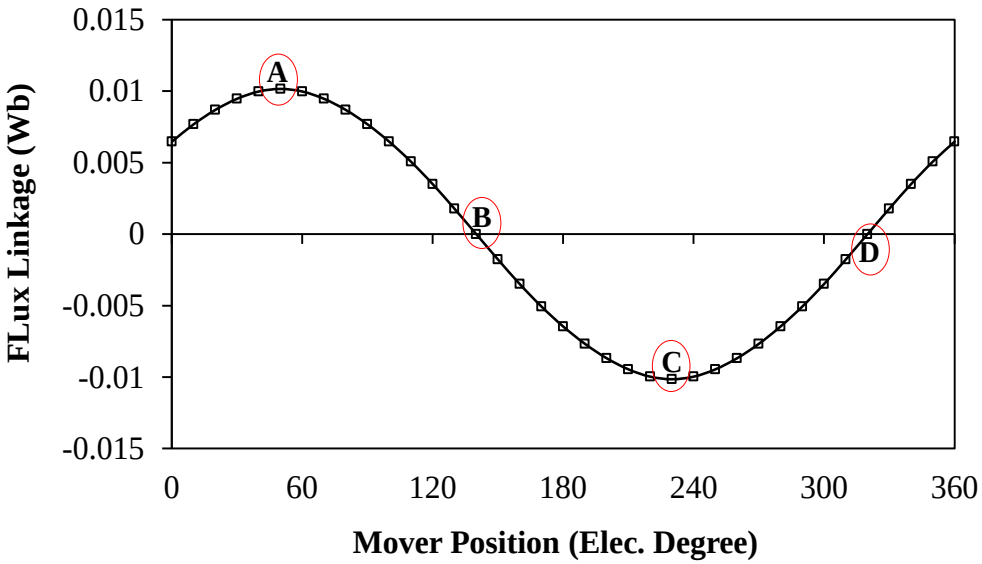

Fig. 3.2 Typical phase flux linkage of proposed machine.

3.3 Analysis of Force Production Mechanism for PS-FRPM Linear Machine

In the following section, the force production mechanism in the PS-FRPM linear machine will be investigated. As was mentioned, the proposed machine has both armature windings and the PMs in one machine part and the other part is passive; thereby, the torque production mechanism in DSPM machine such as SFPM machine, is valid for such a machine.

Generally, in PM machines that have a negligible reluctance torque, the electromagnetic torque is directly proportional to the stator winding magneto motive force (MMF) and air gap flux density due to the PM [FAR15]. Hence, in order to analyse the force production in the PS-FRPM linear machine, the winding MMF will be firstly calculated, and then the air gap flux density due to the stator permanent magnet and the air gap permeance will be determined by considering both stator teeth and mover poles. It should be noted that the analysis will be carried out for 6/5 slot/pole PS-FRPM linear machine, with concentrated windings. The MMF winding function calculation is carried out under the following assumptions:

- Saturation effect is not considered.
- The permanent magnet permeability is unity.

MMF of phase A, as shown in Fig. 3.3, can be expressed by Fourier series [CHE14]

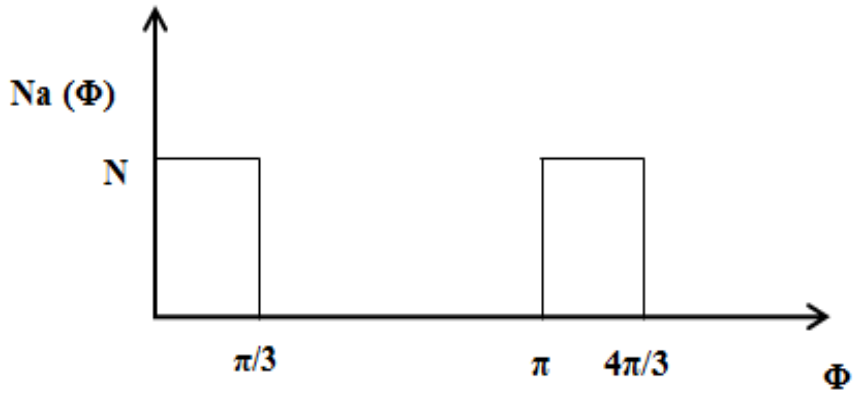

Fig. 3.3 MMF of phase A for the 6/5 PS-FRPM linear machine.

$$N_a(\phi) = \sum_n N_n \cos(n\phi) \tag{3.2}$$

where n is the harmonic order, N_n denotes the magnitude of the nth- order MMF harmonic and ϕ indicates the spatial angle. Similarly with proper phase shift the winding functions of both phases B and C can be obtained as follows:

$$N_b(\phi) = \sum_n N_n \cos(n\phi - n\theta_m) \tag{3.3}$$

$$N_c(\phi) = \sum_n N_n \cos(n\phi + n\theta_m) \tag{3.4}$$

where θ_m is the mechanical phase angle, which is equal to (π/3) for the analysed machine. The phase currents of the three phase set can be written as follows:

$$\begin{aligned} I_a &= I\cos(\omega t) \\ I_b &= I\cos(\omega t - \frac{2\pi}{3}) \\ I_c &= I\cos(\omega t + \frac{2\pi}{3}) \end{aligned} \tag{3.5}$$

where I is the current amplitude and ω represents the angular frequency.

The total MMF distribution of three phase windings is

$$\begin{aligned} F_s &= \sum_n (N_a I_a + N_b I_b + N_c I_c) \\ &= \sum_n N_n \cos(n\phi)\, I\cos(\omega t) \\ &\quad + \sum_n N_n \cos(n\phi - n\theta_m)\, I\cos(\omega t - \frac{2\pi}{3}) \\ &\quad + \sum_n N_n \cos(n\phi + n\theta_m)\, I\cos(\omega t + \frac{2\pi}{3}) \end{aligned} \tag{3.6}$$

$$= \sum_n \frac{N_n I}{2}[\cos(n\phi - \omega t) + \cos(n\phi + \omega t)]$$

$$+ \sum_n \frac{N_n I}{2}\left[\cos\left(n\phi - n\theta_m - \omega t + \frac{2\pi}{3}\right)\right.$$

$$\left. + \cos\left(n\phi - n\theta_m + \omega t - \frac{2\pi}{3}\right)\right]$$

$$+ \sum_n \frac{N_n I}{2}\left[\cos\left(n\phi + n\theta_m - \omega t - \frac{2\pi}{3}\right)\right.$$

$$\left. + \cos\left(n\phi + n\theta_m + \omega t + \frac{2\pi}{3}\right)\right]$$

$$= \sum_n \frac{N_n I}{2}[\cos(n\phi - \omega t) + \cos(n\phi + \omega t)]$$

$$+ \sum_n \frac{N_n I}{2}\left[\left\{\cos(n\phi - \omega t)\cos\left(n\theta_m - \frac{2\pi}{3}\right)\right.\right.$$

$$\left.\left. + \sin(n\phi - \omega t)\sin\left(n\theta_m - \frac{2\pi}{3}\right)\right\}\right.$$

$$\left. + \left\{\cos(n\phi + \omega t)\cos\left(n\theta_m + \frac{2\pi}{3}\right)\right.\right.$$

$$\left.\left. + \sin(n\phi + \omega t)\sin\left(n\theta_m + \frac{2\pi}{3}\right)\right\}\right]$$

$$+ \sum_n \frac{N_n I}{2}\left[\left\{\cos(n\phi - \omega t)\cos\left(n\theta_m - \frac{2\pi}{3}\right)\right.\right.$$

$$\left.\left. - \sin(n\phi - \omega t)\sin\left(n\theta_m - \frac{2\pi}{3}\right)\right\}\right.$$

$$\left. + \left\{\cos(n\phi + \omega t)\cos\left(n\theta_m + \frac{2\pi}{3}\right)\right.\right.$$

$$\left.\left. - \sin(n\phi + \omega t)\sin\left(n\theta_m + \frac{2\pi}{3}\right)\right\}\right]$$

$$= \sum_n \frac{N_n I}{2}[\cos(n\phi - \omega t)]$$
$$+ \sum_n \frac{N_n I}{2}\left[\cos(n\phi - \omega t)\cos\left(n\theta_m - \frac{2\pi}{3}\right)\right]$$
$$+ \sum_n \frac{N_n I}{2}\left[\cos(n\phi - \omega t)\cos\left(n\theta_m - \frac{2\pi}{3}\right)\right]$$
$$+ \sum_n \frac{N_n I}{2}[\cos(n\phi + \omega t)]$$
$$+ \sum_n \frac{N_n I}{2}\left[\cos(n\phi + \omega t)\cos\left(n\theta_m + \frac{2\pi}{3}\right)\right]$$
$$+ \sum_n \frac{N_n I}{2}\left[\cos(n\phi + \omega t)\cos\left(n\theta_m + \frac{2\pi}{3}\right)\right]$$

The forward and backward MMF equations can be expressed as:

$$F_f = \sum_n \frac{N_n I}{2}\cos\ (n\emptyset - \ \omega t)\left[1 + 2\cos\ (n\theta_m - \frac{2\pi}{3})\right] \quad (3.7)$$

$$F_b = \sum_n \frac{N_n I}{2}\cos\ (n\emptyset + \ \omega t)\left[1 + 2\cos\ (n\theta_m + \frac{2\pi}{3})\right] \quad (3.8)$$

The spatial harmonics of the stator winding MMF are illustrated in Fig. 3.4. It can be observed that the dominated harmonics are the 2nd order and its non-triple multiples. It has been found that for a SFPM machine the fundamental spatial harmonic of the MMF stator winding is equal to the ratio of stator slot number to the phase number. Thus, the obtained results are in a good agreement with those observed in [FAR15]. The MMF of the aforementioned machine and its spatial harmonic due to the PM are shown in Fig. 3.5. Obviously, the primary harmonic is equal to half of the stator slot number (6/2=3). The air gap permeance and corresponding harmonic accounting for the mover pole are depicted in Fig. 3.6. It can be clearly seen that main harmonic component is equal to the number of the mover pole (5th).

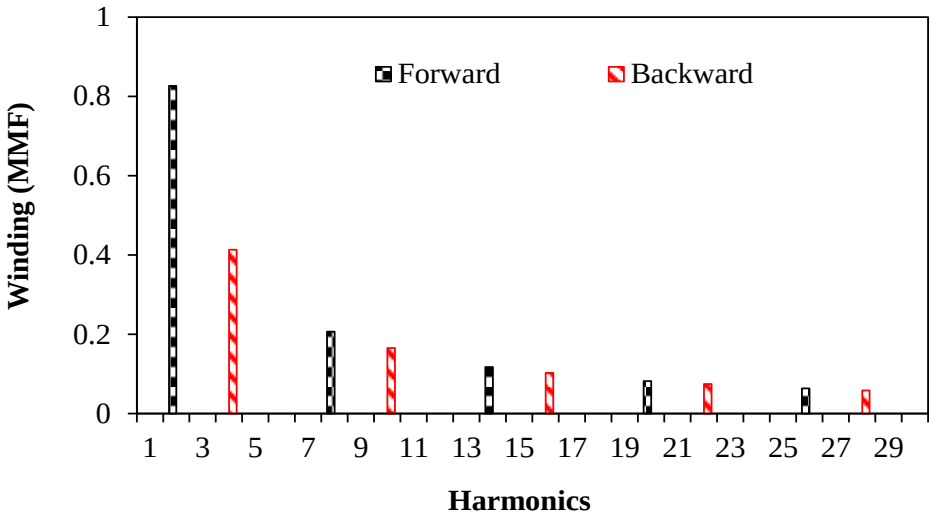

Fig. 3.4 Spatial harmonic of the stator winding MMF for 6/5 PS-FRPM linear machine.

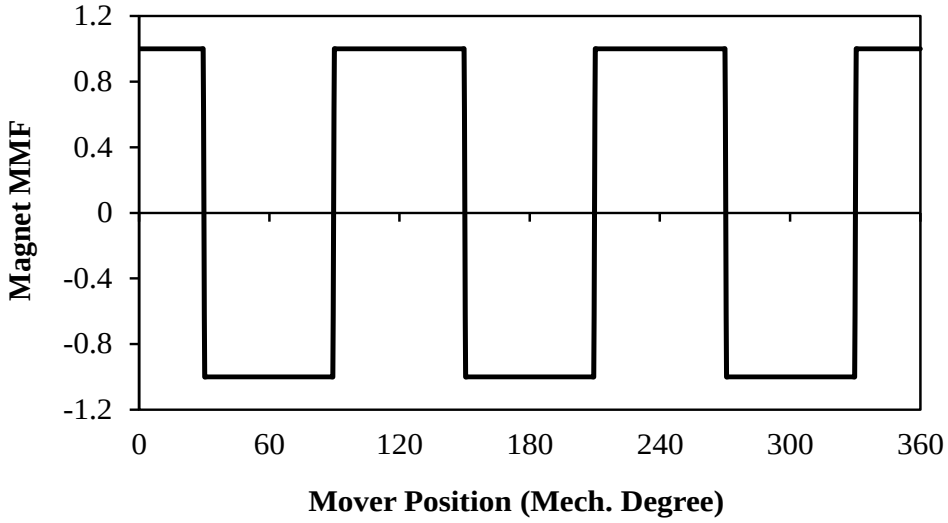

(a) Waveform

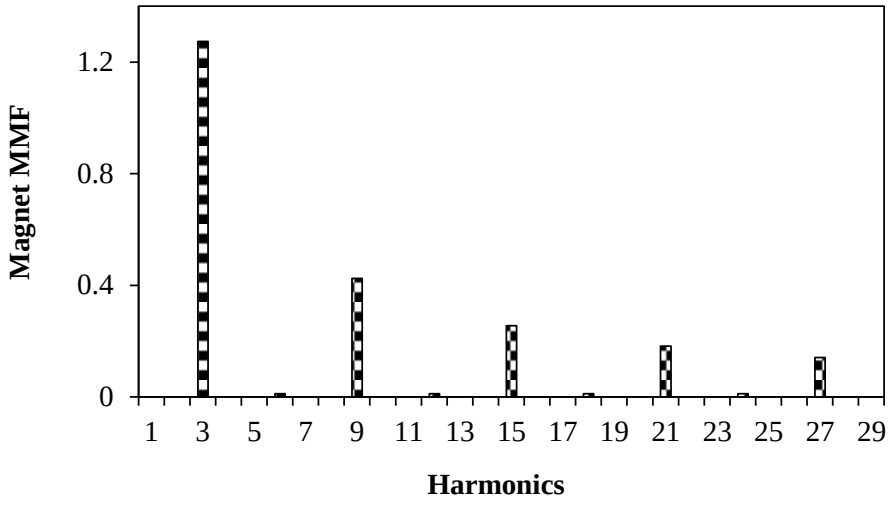

(b) Spectrum

Fig. 3.5 Magnet MMF for 6/5 PS-FRPM linear machine.

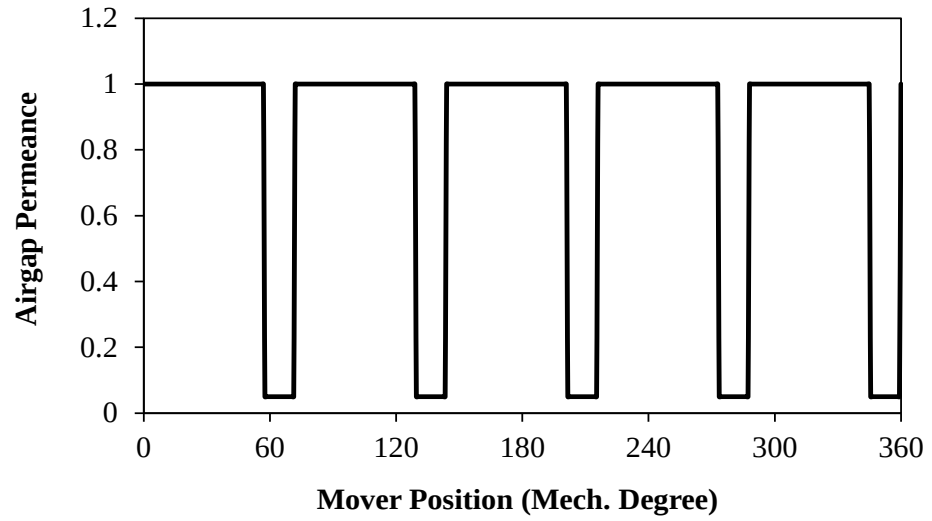

(a) Waveform

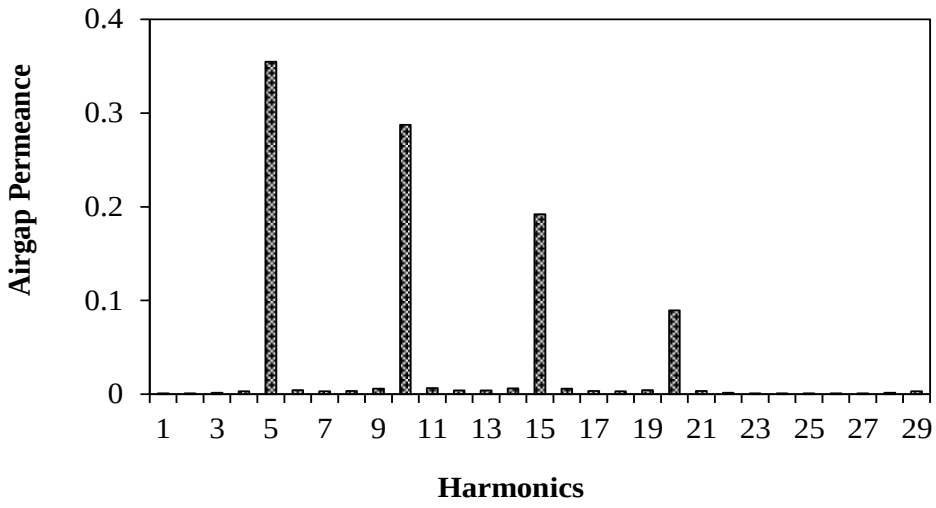

(b) Spectrum

Fig. 3.6 Airgap permeance accounting the mover pole for 6/5 PS-FRPM linear machine.

Flux density in the lower air gap, i.e. between the mover and stator one, which has the PMs, can be obtained by multiplying the magnet MMF and the air gap permeance considering the mover pole, Fig. 3.7. On the other hand, the open circuit flux density in the upper air gap located between the mover and stator two is equal to the product of the PM (MMF) and the air gap permeance accounting for both the mover pole and the upper stator teeth, Fig. 3.8. By comparing Fig. 3.4 and Fig. 3.8, it can be clearly seen that only the 2^{nd} and 8^{th} harmonic orders have the same direction and frequency. Hence, they interact to produce non zero average thrust force. It can be concluded that like SFPM machines, the force in a PS-FRPM linear machine is generated by many field harmonics (2^{nd}, 3^{th} and 8^{th}) [FAR15] [WU15].

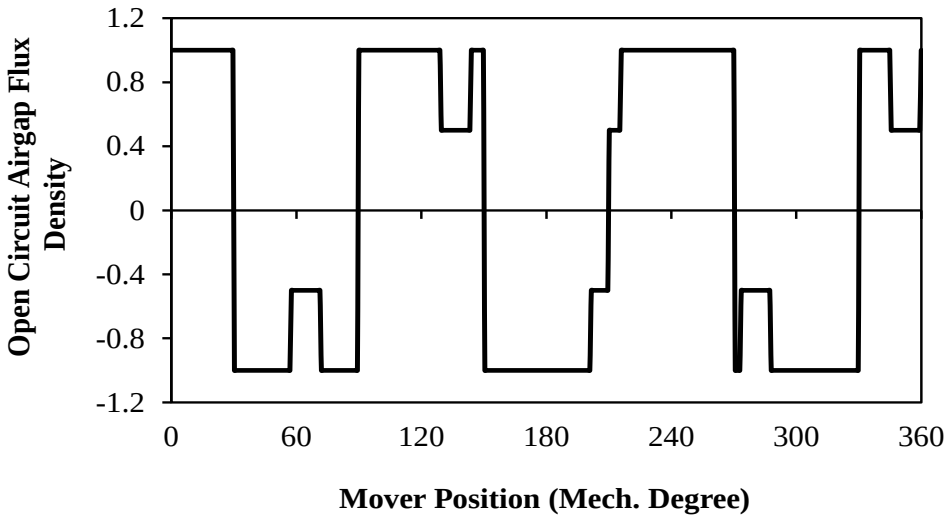

(a) Waveform

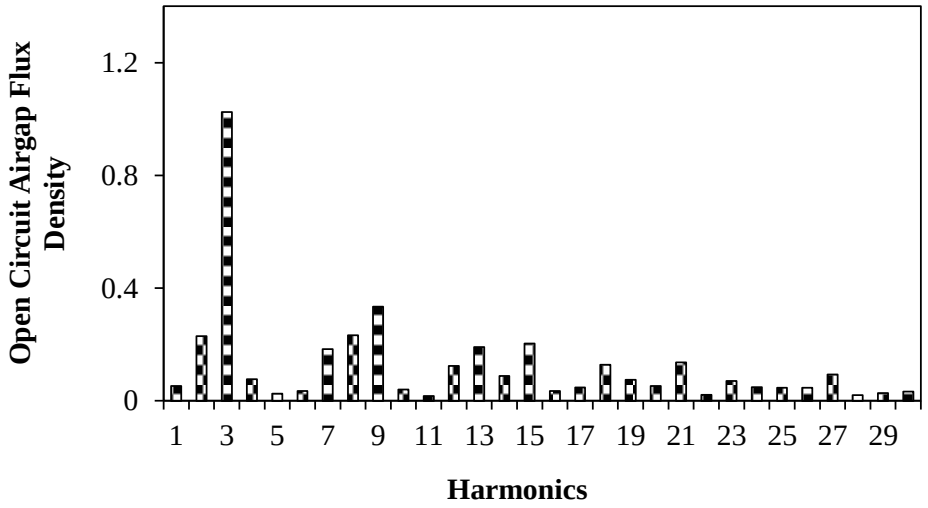

(b) Spectrum

Fig. 3.7 Open circuit lower air gap flux density for 6/5 PS-FRPM linear machine.

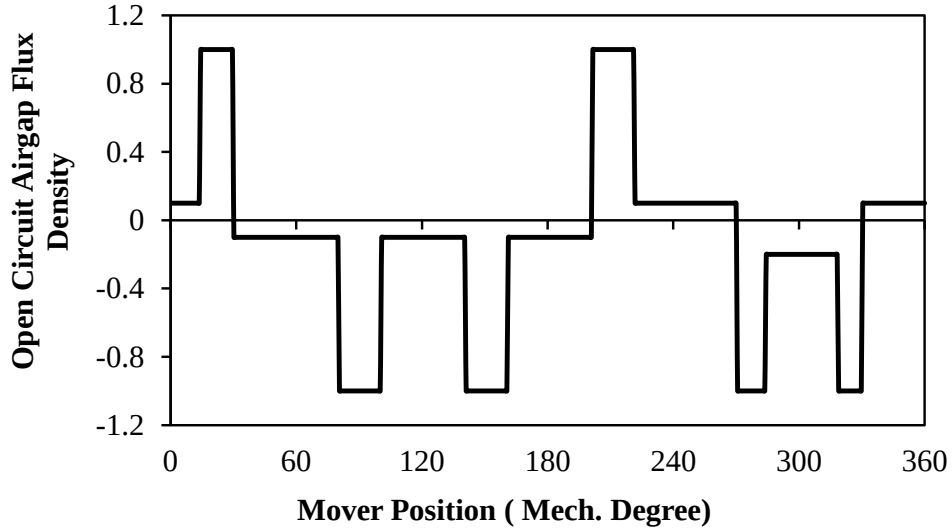

(a) Waveform

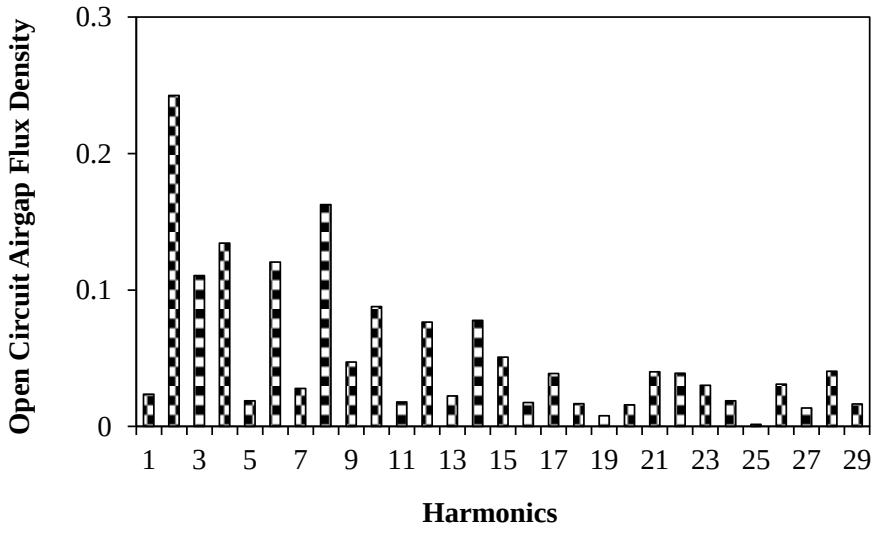

(b) Spectrum

Fig. 3.8 Open circuit upper air gap flux density for 6/5 PS-FRPM linear machine.

The open circuit flux densities and corresponding harmonics for both the lower and the upper air gaps, obtained from FE simulation, are illustrated in Fig. 3.9 and Fig. 3.10, respectively. It should be mentioned that the purpose of the simple analytical model is to determine the harmonic orders that contribute to force production in the PS-FRPM but not to precisely calculate air gap flux density. Therefore, differences in shape between the predictable and the simulated air gap can be clearly seen. However, the FFT results for open-circuit airgap flux density harmonics in both air gaps are in a good agreement, which is the main objective of this analysis.

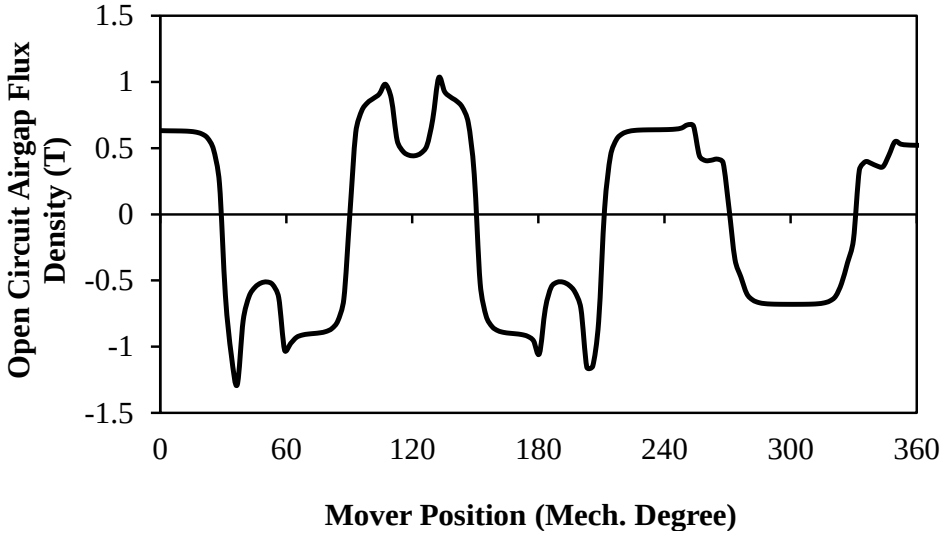

(a) Waveform

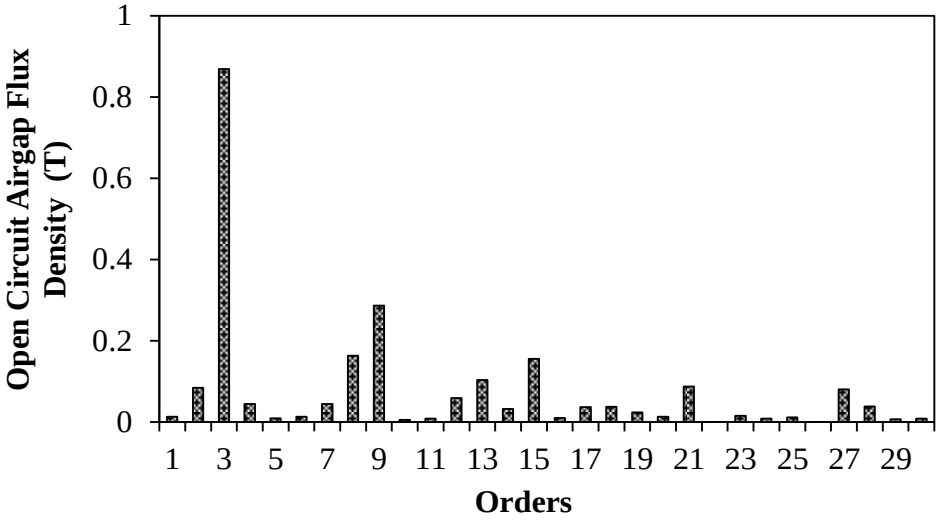

(b) Spectrum

Fig. 3.9 FE calculated lower air gap flux density.

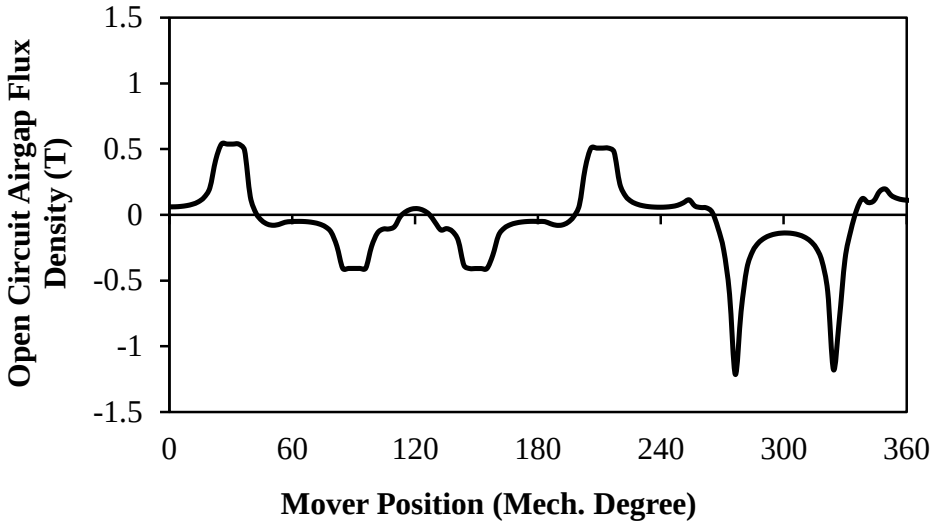

(a) Waveform

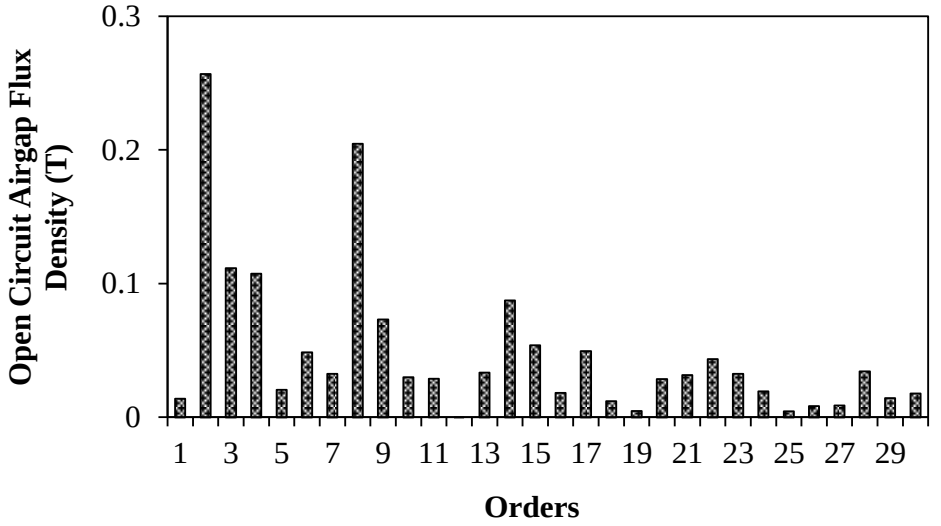

(b) Spectrum

Fig. 3.10 FE calculated upper air gap flux density.

3.4 Machine Optimization

3.4.1 Influence of Permanent Magnet Thickness

Since the stator teeth surfaces of the conventional FRPM machine are equipped by the PMs, the PM thickness has a considerable effect on the FRPM machine performance similar to that of a stator surface mounted brushless machine [DOR03], [HUA10]. However, the increase of the PM thickness of these machines results in the reduction of the difference in the reluctance variation. Consequently, the machine back-EMF would be reduced. Therefore, the PM thickness in the FRPM machine is restricted [DOR03]. Unlike the conventional FRPM, the electromagnetic performance of PS-FRPM machine would be improved with the increase of the PM thickness. Fig. 3.11shows the variation of the average thrust force with PM thickness. It should be noted that the average thrust force of the proposed machine increases with the increasing of PM thickness. By considering PM cost, the PM radial thickness of the proposed machine has been decided to be 3 mm.

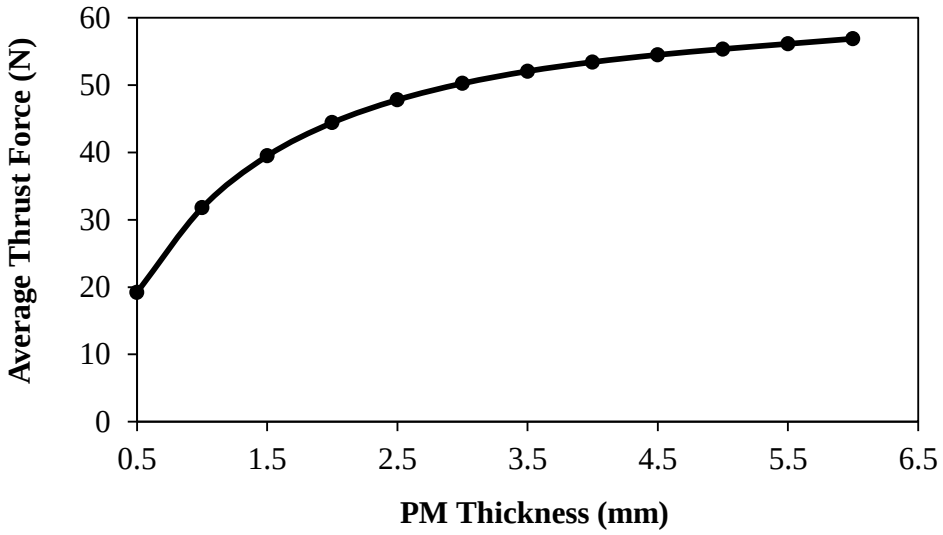

Fig. 3.11 Variation of the average thrust force with the PM thickness.

3.4.2 Individual and Global Optimizations

In order to achieve maximum thrust force, the PS-FRPM machine will be optimized. The parameters, which are kept constant during the optimization, are listed in Table 3.1. The current density is fixed at 7A/mm^2. The machine total height and its length in Z-direction are kept at 35mm and 25mm, respectively. The machine active stroke length is 165.2 mm. In order to simplify the discussion the number of mover poles is defined as the number of mover poles within the active stator.

The definitions of the parameters which are varied during the optimization process including *SR* = split ratio, *TMPWR* = top mover piece width ratio, *BMPWR* =bottom mover piece width ratio, *S1TWR* = stator one tooth width ratio, *S1SOR* = stator one slot opening ratio and *S1BITHR* = stator one back iron thickness ratio, are given as follows

$$SR = \frac{MGO}{TMH} \tag{3.9}$$

$$TMPWR = \frac{TMPW}{MPP} \tag{3.10}$$

$$BMPWR = \frac{BMPW}{MPP} \tag{3.11}$$

$$S1TWR = \frac{S1TW}{S1SP} \tag{3.12}$$

$$S1SOR = \frac{S1SO}{S1SP} \tag{3.13}$$

$$MGO = S2TH + G2 + MTH + 0.5G1 \tag{3.14}$$

$$S1BITHR = \frac{S1BITH}{S1TH} \tag{3.15}$$

where *TMH*,*TMPW*, *BMPW* and *MPP* are the total machine height, top mover piece width, bottom mover piece width and mover pole pitch respectively. *S1TW*, *S2TH*, *MTH*, *S1SO* , *S1BITH*, *S1TH* and *S1SP* indicate stator 1 teeth width, stator 2 height, mover thickness, stator 1 slot opening, stator 1 back iron thickness, total stator 1 height and stator1 slot pitch, respectively, while *G1* and *G2* represent the air-gap 1 and air-gap 2 length. Fig. 3.12 describes the leading design parameters of PS-FRPM linear machine

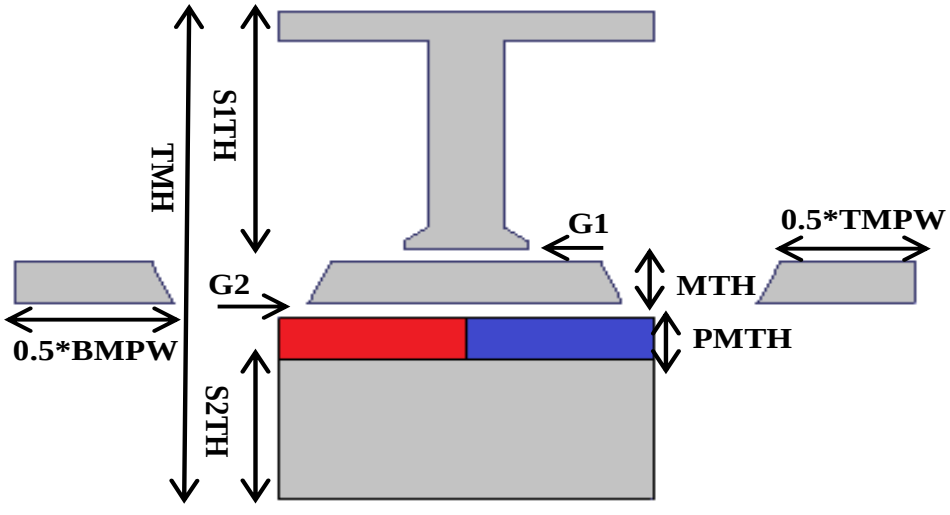

Fig. 3.12 Schematic of the machine parameters, which are varied during optimization process.

The main design parameters of the proposed machine are individually optimized for maximum thrust force. The optimization was conducted with the following sequence, split ratio, mover radial thickness, top mover piece width ratio, bottom mover pole piece ratio, stator one tooth width ratio, stator one back iron thickness ratio and stator one slot opening ratio.

The variation of the average thrust force with *SR* is illustrated in Fig. 3.13. It can be seen that the average thrust force increases dramatically with the increase of *SR*, and reaches the maximum value with *SR* equal to 0.3. After this value the average thrust force decreases sharply. Hence, the optimal *SR* value for the proposed machine is 0.3.

The influence of the mover dimensions, which include mover thickness, top mover piece width ratio and bottom mover piece width ratio on the machine thrust force, are shown in Fig. 3.14, Fig. 3.15 and Fig. 3.16, respectively. It is obvious that the thrust force is more sensitive to *MTH* and *TMPWR* than *BMPWR*. When *MTH* is small the machine has low thrust force due to saturation. On the other hand, a very high mover thickness results in low thrust force due to the increase of the flux leakage. Similarly, the thrust force increases with the increase of the top mover piece width ratio, and then after 0.7, which is the optimal value of this ratio, the thrust force reduces. It is worth mentioning that the optimal *BMPWR* is 0.6.

Finally, the variations of the average thrust force with stator one tooth width ratio, back iron thickness ratio and slot opening width ratio are depicted in Fig. 3.17, Fig. 3.18 and Fig. 3.19, respectively. It should be noted that the average thrust force increases significantly when S1TWR is varied from 0.1-0.23. After this value, it will be decreased due to the slot area decreasing, which consequently reduces the electrical machine loading. For the same mentioned reason the variation of the average thrust force with *S1BITHR* is similar to that with *S1TWR*.

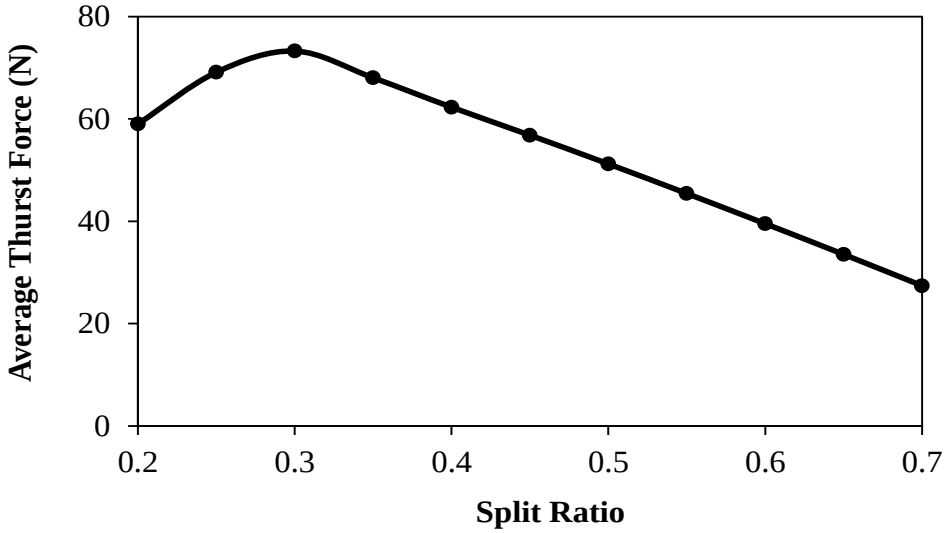

Fig. 3.13 Variation of the average thrust force with split ratio.

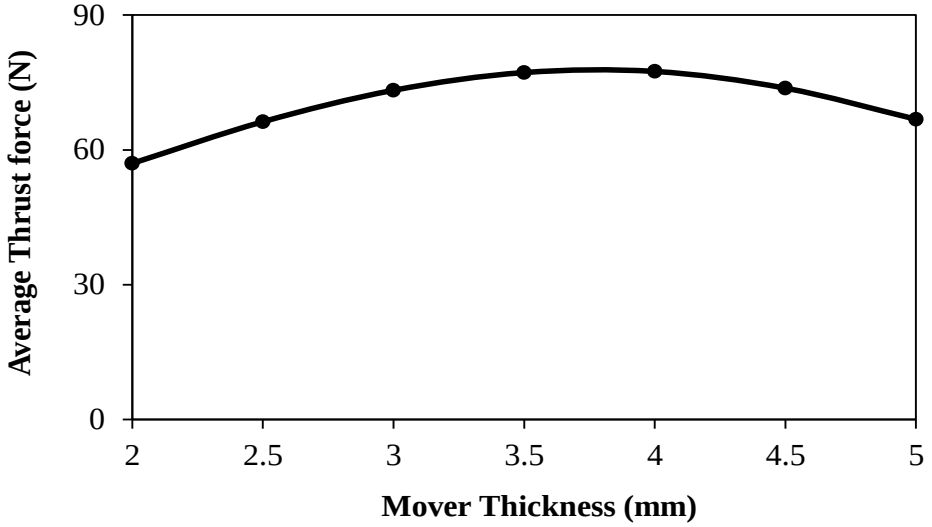

Fig. 3.14 Variation of the average thrust force with mover thickness.

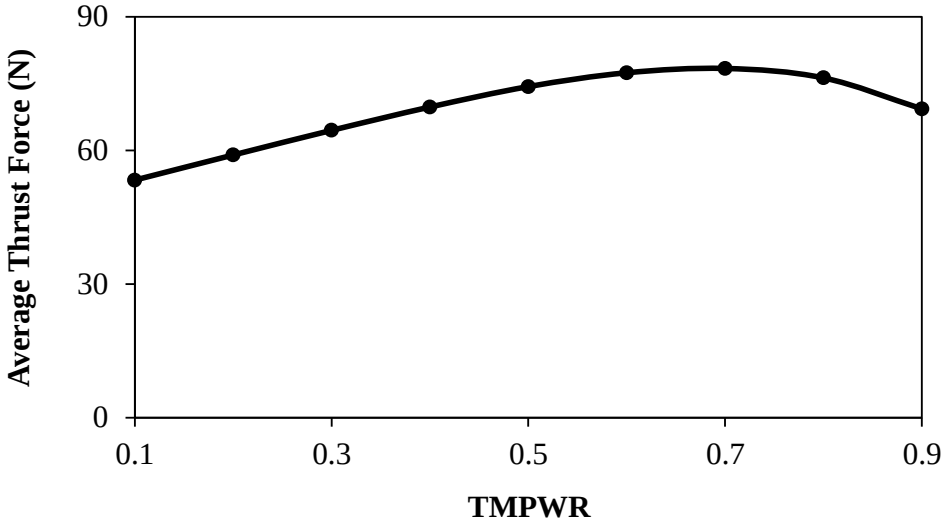

Fig. 3.15 Variation of the average thrust force with top mover piece width ratio.

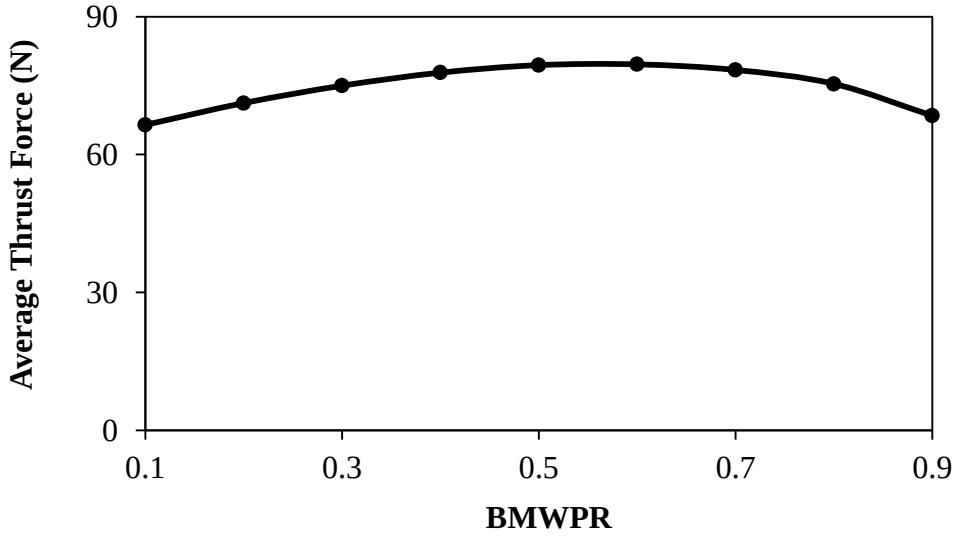

Fig. 3.16 Variation of the average thrust force with bottom mover piece width ratio.

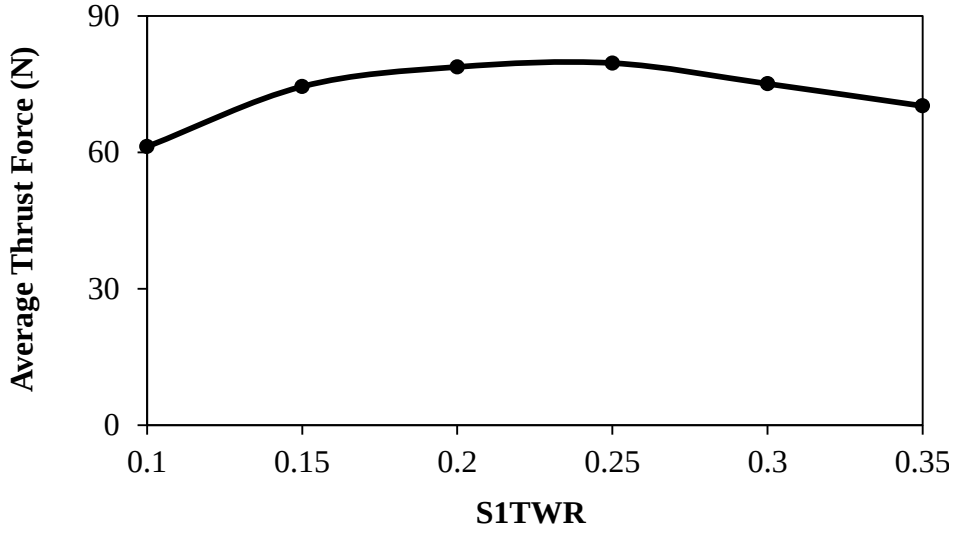

Fig. 3.17 Variation of the average thrust force with stator 1 teeth width ratio.

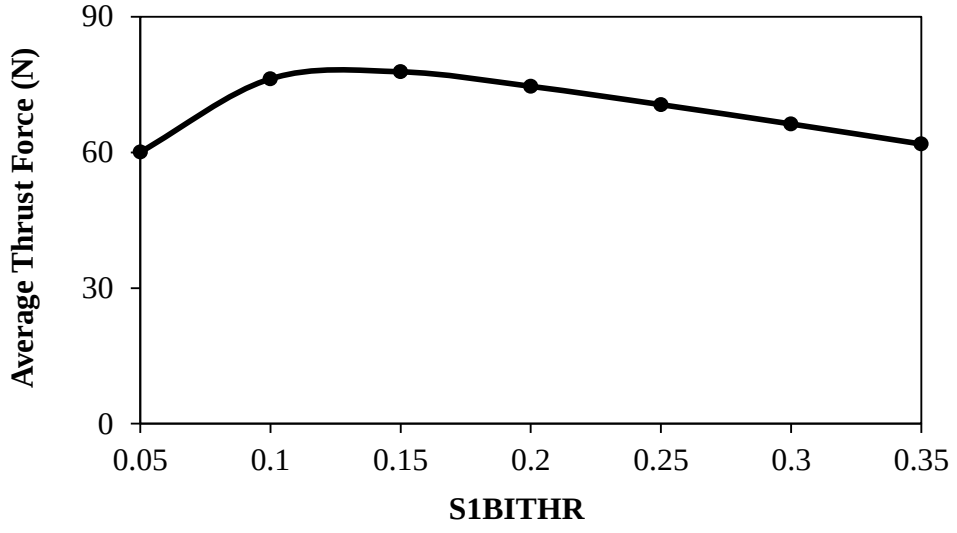

Fig. 3.18 Variation of the average thrust force with stator 1 back iron thickness width ratio.

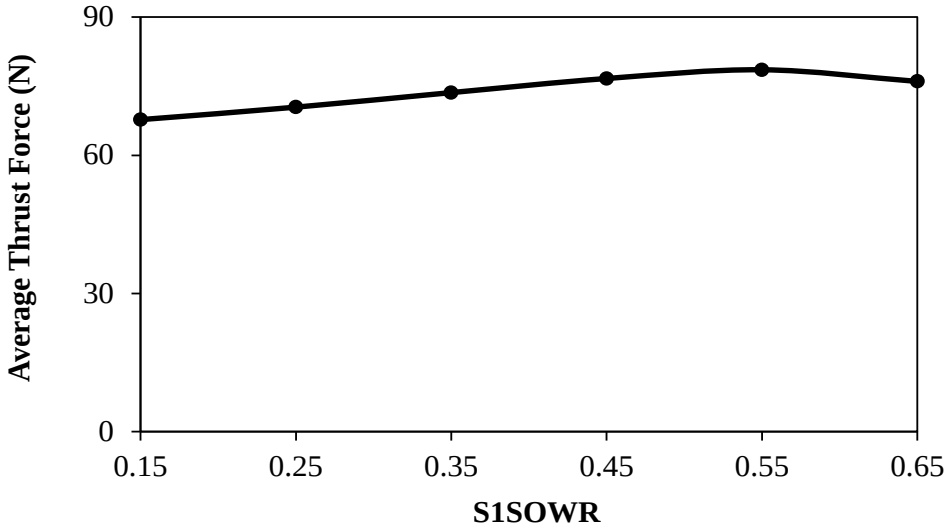

Fig. 3.19 Variation of the average thrust force with stator 1 slot opening width ratio.

Global optimization has been implemented by utilizing GA and FE in order to evaluate the individual optimization. The parameters of the GA are adjusted as follows: the size of population and the maximum generation are 20; crossover type is simulated binary crossover; individual crossover probability, variable crossover probability and Mu have the value of 1; variable exchange probability has the value of 0; mutation type is chosen to be polynomial mutation; the uniform mutation probability takes 0; variable mutation probability and individual mutation probability are 1; and standard deviation is 0.05. Table 3.2 lists initial, constrain and optimal values of the design parameters, which are varied during the optimization process.

Table 3.2 Initial, constraint and optimal values of variable parameters for optimization

Item	Initial	Constrain	Individual	Global
SR	0.5	[0.3,0.7]	0.3	0.37
MTH	3	[2,5]	4.5	4.7
TMPWR	0.6	[0.1,0.9]	0.7	0.732
BMPWR	0.7	[0.1,0.9]	0.6	0.6
S1TWR	0.2	[0.05,0.35]	0.25	0.23
S1SOR	0.64	[0.67,0.17]	0.55	0.55
S1BITHR	0.125	[0.05,0.3]	0.15	0.13

The electromagnetic performances of the proposed machine with individual and global optimal parameters are compared using FE. Three phase flux linkage and back-

EMF of both individually and globally optimized machines are compared in Fig. 3.20 and Fig. 3.21, respectively. It can be seen that the globally optimized machine exhibits about 30% higher flux linkage compared to that with the individually optimized machine, and consequently it has higher back-EMF. Similar to their rotational counterpart, PM linear machines suffer from the existence of open-circuit cogging force. However, PM linear machines usually exhibit higher cogging force compared to the rotating corresponding due to the longitudinal end effect [LI13] [ZHU97]. Fig. 3.22 shows open circuit cogging force for both machines. It is obvious that both individually and globally optimized machines have similar cogging force. Moreover, the variations of average thrust force with current density for the aforementioned machines are shown in Fig. 3.23. It should be noted that the globally optimized machine exhibits higher thrust force compared to the individually optimized machine due to the higher back-EMF. The predicted thrust force waveforms for one electrical period, when three phase sinusoidal currents in phase with the back-EMFs are applied to the machines are presented in Fig. 3.24. Apparently, higher thrust force can be obtained by globally optimized machine. Thus, it can be concluded that although both individual and global optimization are good approaches to determine the machine optimal parameter values for maximum thrust force, the global optimization is more efficient and can obtain higher machine performance.

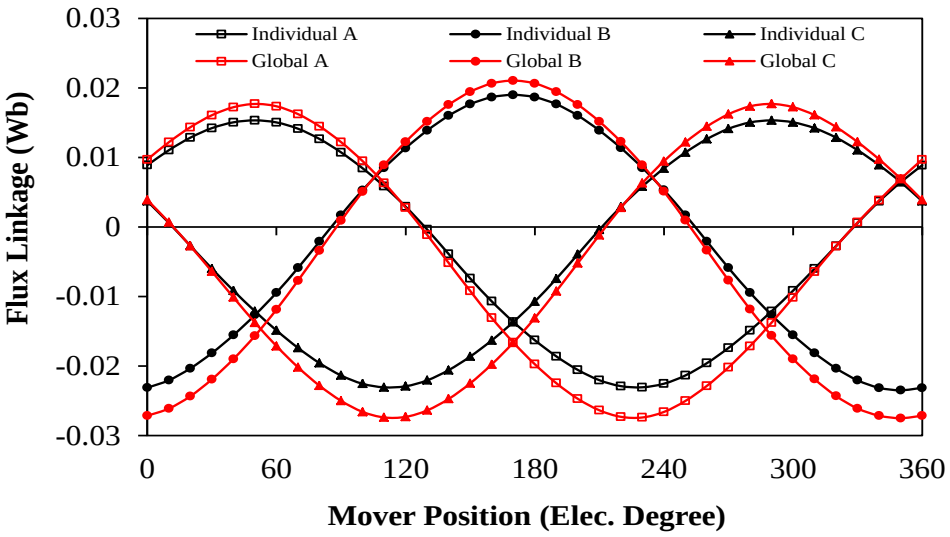

(a) Waveform

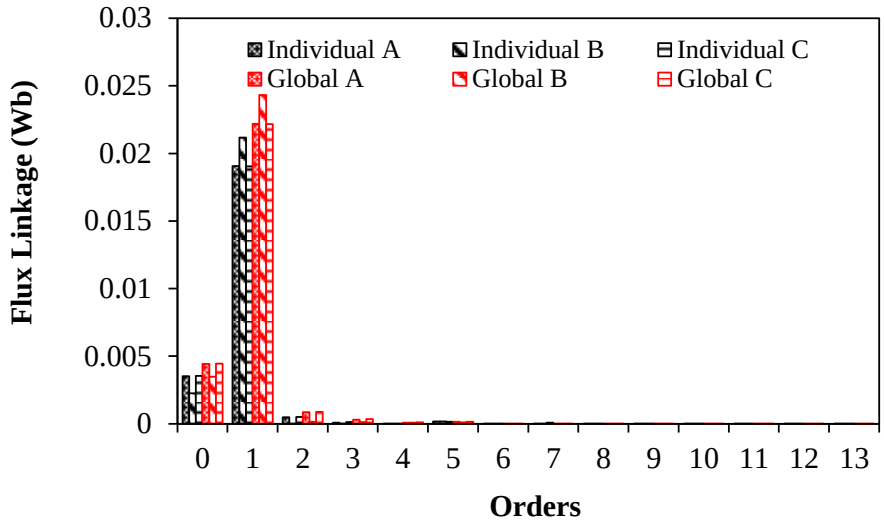

(b) Spectrum

Fig. 3.20 Comparison of flux linkages in individually and globally optimized machines.

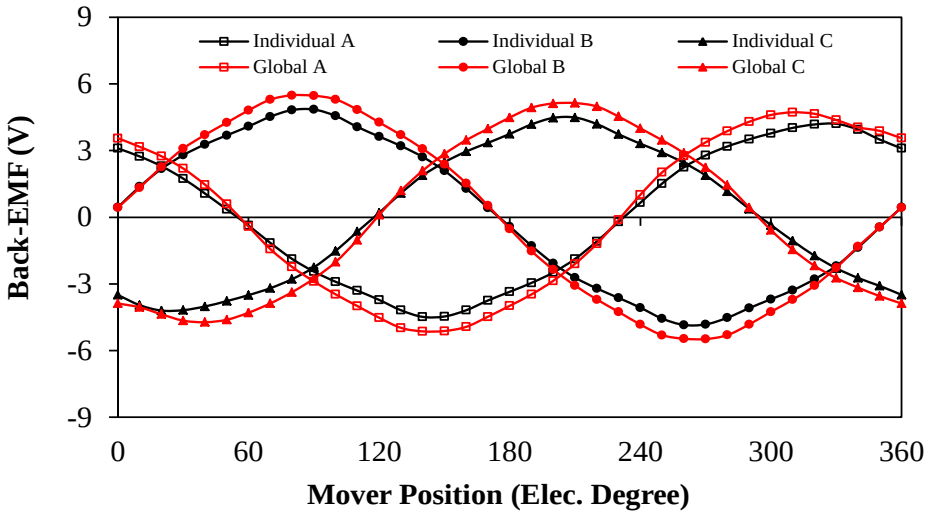

(a) Waveform

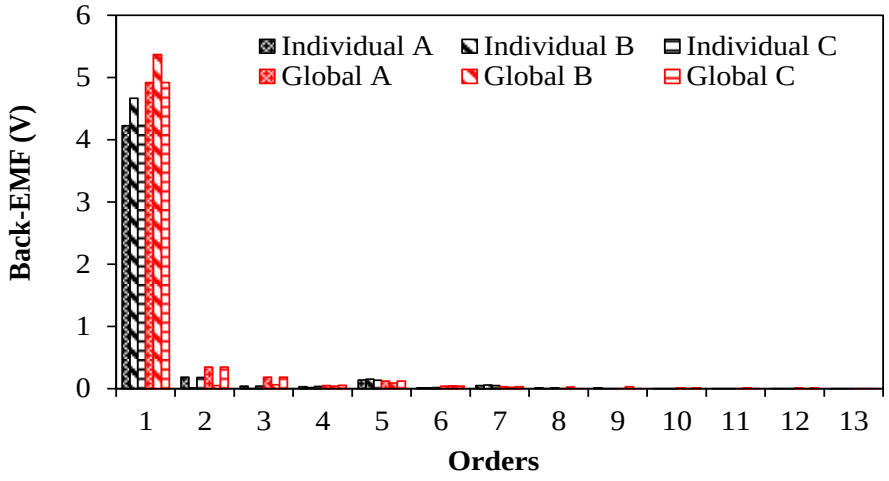

(b) Spectrum

Fig. 3.21 Comparison of back-EMF in individually and globally optimized machines.

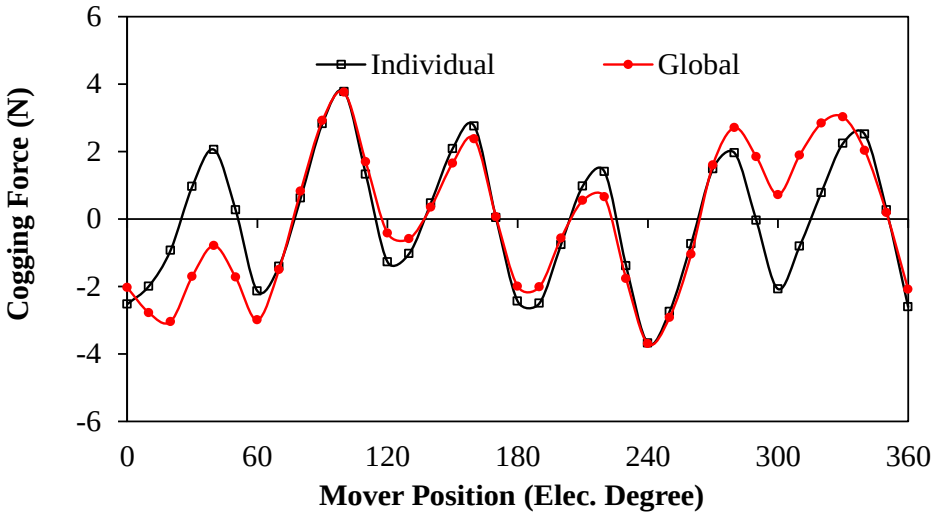

Fig. 3.22 Comparison of cogging force in individually and globally optimized machines.

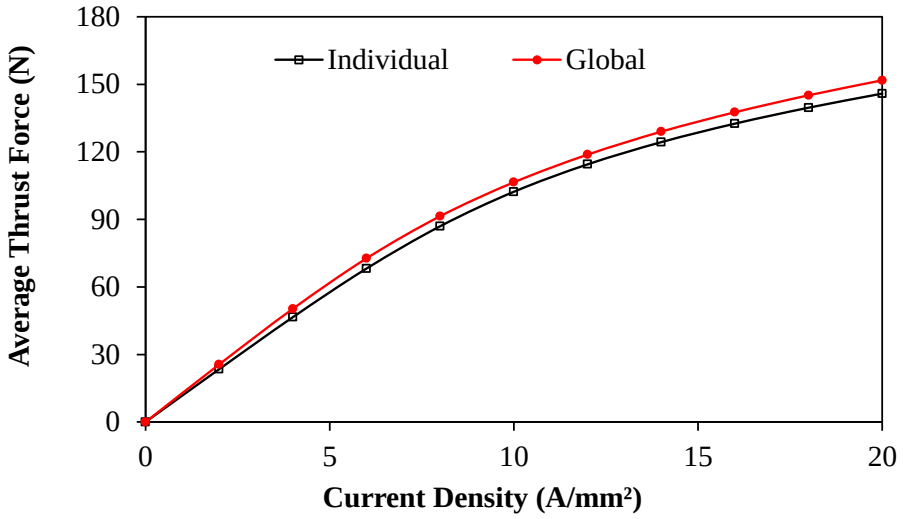

Fig. 3.23 Comparison of average thrust force-current density characteristics in individually and globally optimized machines.

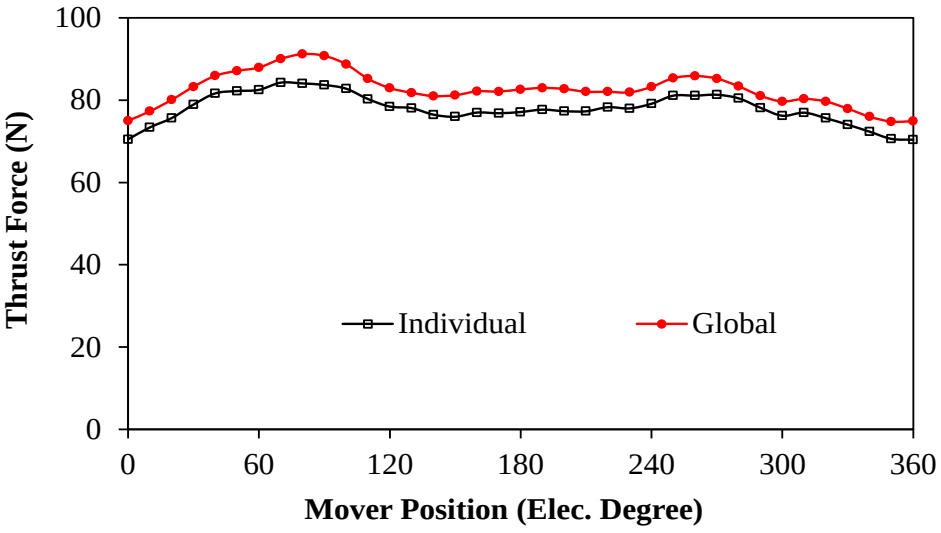

Fig. 3.24 Comparison of thrust force in individually and globally optimized machines (current density = 7A/mm^2 rms) .

3.5 Influence of Longitudinal End Effect on Machine Performance

To highlight the effect of longitudinal end effect on the electromagnetic performance of the proposed machine, a periodic model, i.e. without the longitudinal end effect, is employed. The cross-section of this model is depicted in Fig. 3.25. It is worth mentioning that the periodic model uses the same global optimized parameters of the practical model.

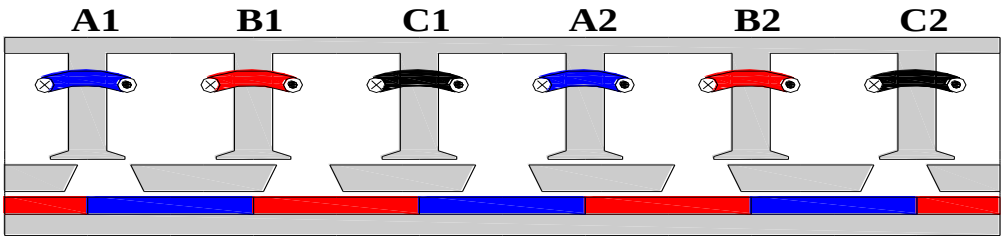

Fig. 3.25 Periodic model cross-section.

The electromagnetic performances of both practical and periodic models are compared by FE, the flux linkage waveforms and their spectrums are shown in Fig. 3.26. It can be seen that the periodic machine has almost symmetrical and balanced flux linkages. In contrast, due to the longitudinal end effect, the practical model exhibits asymmetric and unbalanced flux linkages [DAN07].

Fig. 3.27 compares the three-phase back-EMFs of both models. Apparently, phases A and C are more affected by the longitudinal end effect than phase B since both phases A and C have coils at the end of the stator. The 2^{nd} and 3^{th} harmonic orders are almost diminished on the periodic machine. The results agree with that obtained in [LI13].

To investigate the impact of the longitudinal end effect on the proposed machine cogging force, cogging forces of both models have been compared. The cogging force of the periodic model is analogous to the slot effect since the longitudinal end effect does not exist in this model, while the cogging force due to the longitudinal end effect can be obtained by

$$F_{end\ effect} = F_{cog} - F_{slot} \tag{3.16}$$

where F_{cog} and F_{slot} are cogging forces of the practical model and periodic model, respectively, as compared in Fig. 3.28. It is clear that the periodic model has less peak-peak cogging force than that of the practical one, and also it will be seen that the main ripple of the machine thrust force results from the longitudinal end effect cogging force.

Fig. 3.29 illustrates the thrust force of both practical and periodic models. It is obvious that the practical machine shows less thrust force with high ripples compared to the periodic machine. Hence, it can be confirmed that the cogging force due to the end effect has the major contributions in the thrust force ripple.

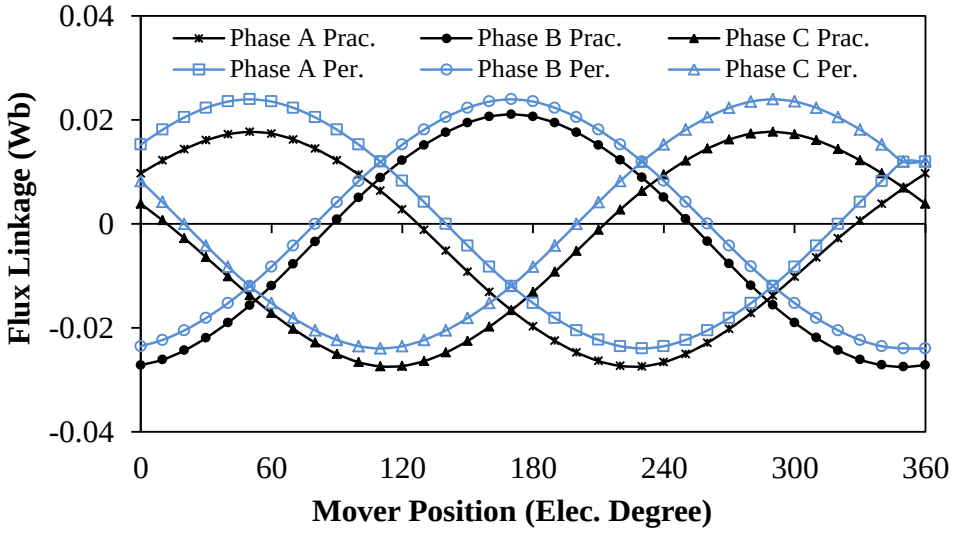

(a) Waveform

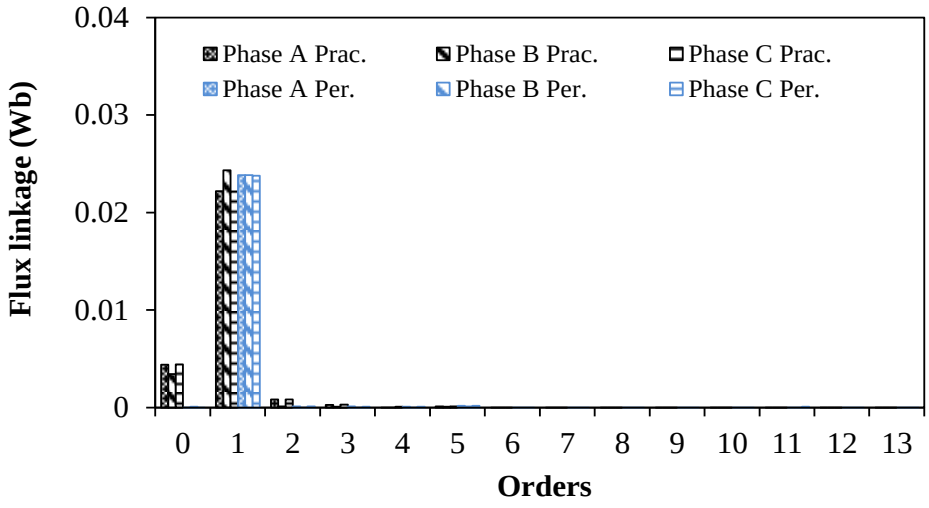

(b) Spectrum

Fig. 3.26 Comparison of flux linkage in periodic and practical machines.

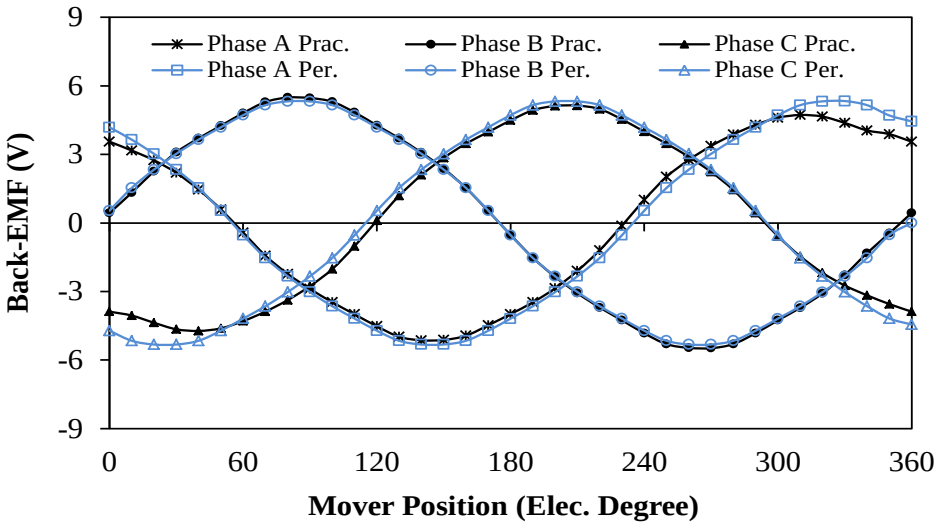

(a) Waveform

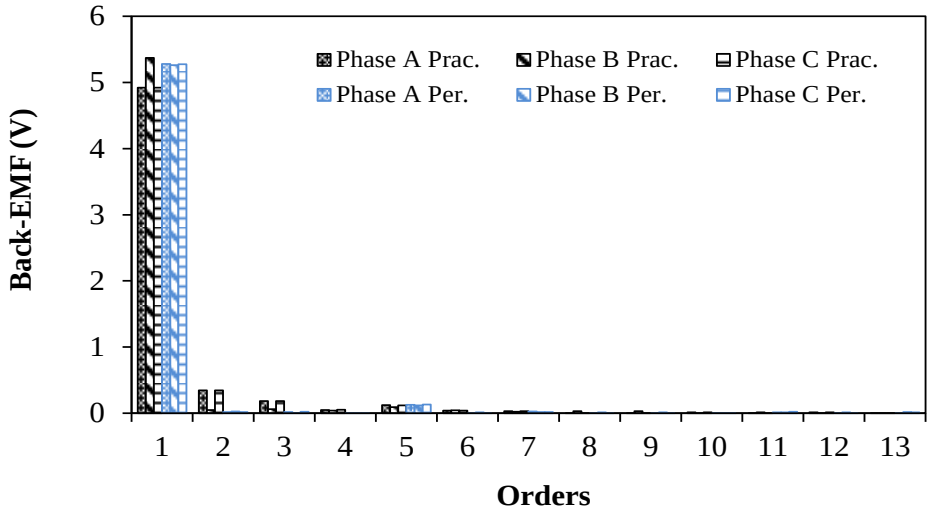

(b) Spectrum

Fig. 3.27 Comparison of back-EMF in periodic and practical machines.

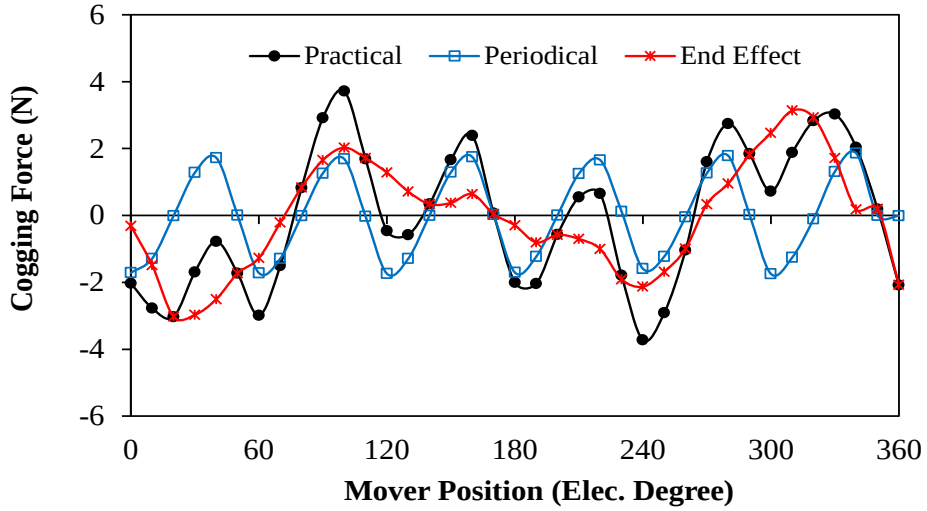

(a) Waveform

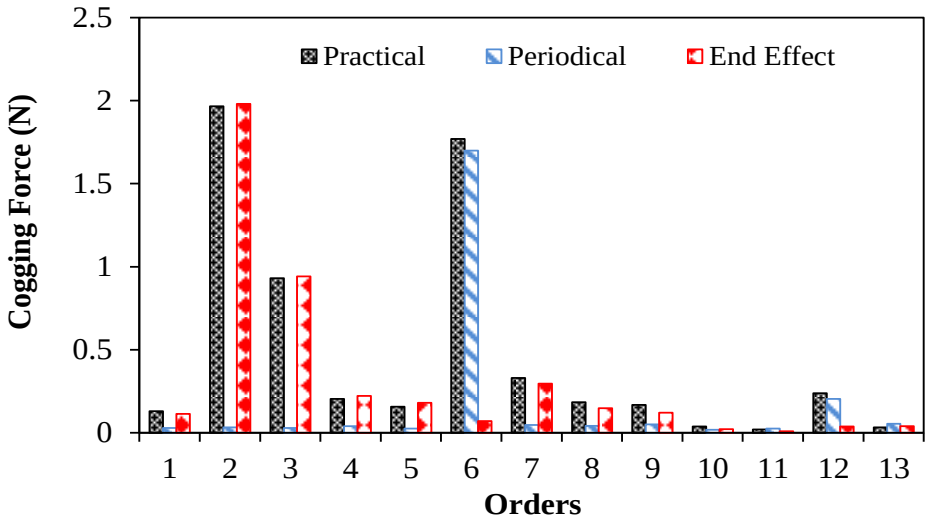

(b) Spectrum

Fig. 3.28 Comparison of cogging force in periodic and practical machines.

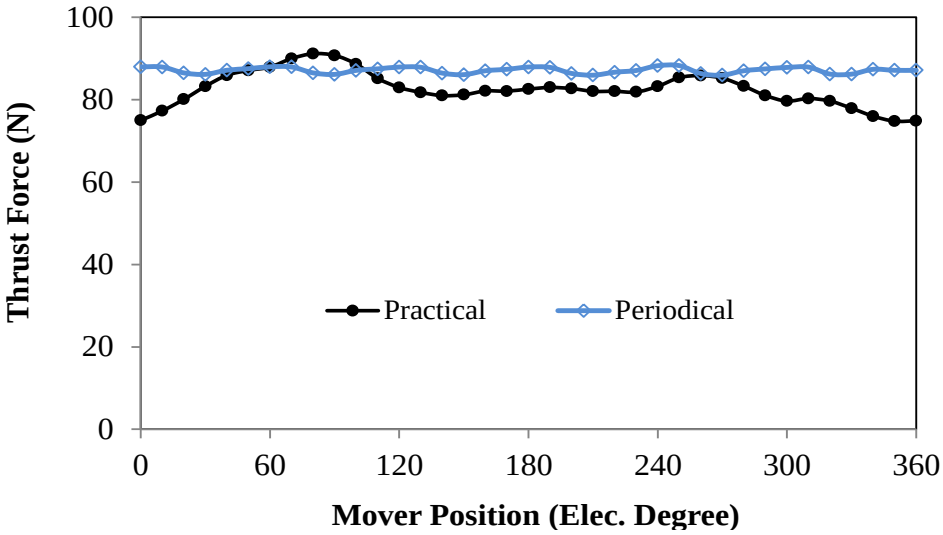

Fig. 3.29 Comparison of thrust force in periodic and practical models (current density = 7A/mm^2 rms)..

3.6 Influence of Mover Pole Numbers on PS-FRPM Linear Machine Performance

Since the proposed machine has same operation principle as that of the SFPM machine, many feasible stator/mover pole number combinations of the PS-FRPM linear machines can be obtained by applying the following relationships [CHE10].

$$Ns=2k_1m \quad (k_1=1, 2, 3....) \tag{3.17}$$

$$N_m=Ns \pm k_2 \quad (k_2=1, 2, 3....) \tag{3.18}$$

where *Ns*, N_m and *m* are stator slot number, mover pole number within the active stator and the phase number, respectively. k_1 and k_2 are integers. It should be noted that for the three-phase machine k_2 must not be a multiple of 3. It is worth mentioning that three phase PS-FRPM linear machines with k_1 equals one, and different k_2 will be designed, analysed and compared, to investigate the influence of the mover pole number on the proposed machine electromagnetic performance.

3.6.1 Coil Configuration

The winding configuration of the understudying machines can be achieved by using coil-EMF vectors [CHE10]. Stator coil positions in mechanical degree and their corresponding coil-EMF vectors in electrical degree are illustrated in

Fig. 3.30. It is worth mentioning that n' has been used to indicate the opposite polarity of the coil. Obviously, n' does not exist in machines with odd mover pole number, i.e. 6/5, 6/7, and 6/11. Hence, it can be concluded that all coils of these machines have the same connection polarity. In contrast, n' coil is presented in the coil-EMF vector configurations of the even mover pole number machines, which means that one phase coils for such machines are in different polarity.

(I) (II) (III)

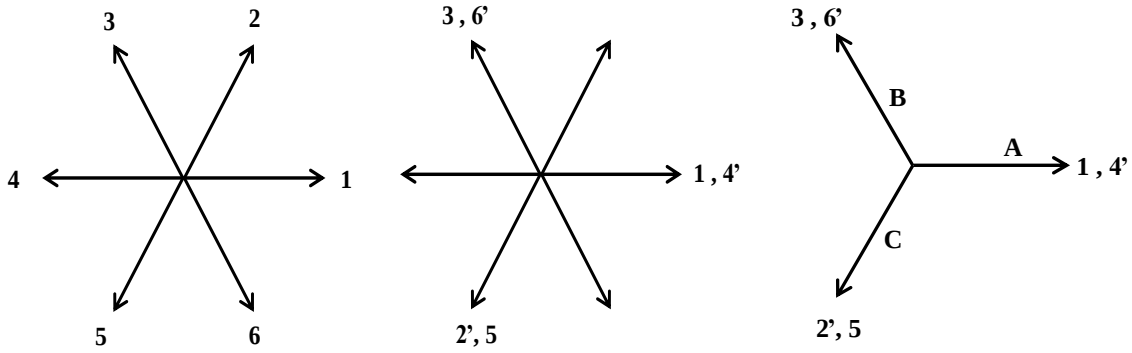

(a) 6/4

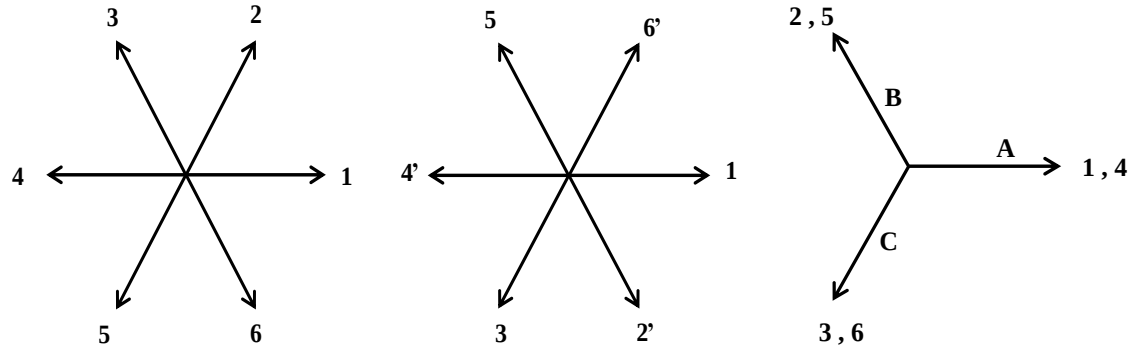

(b) 6/5

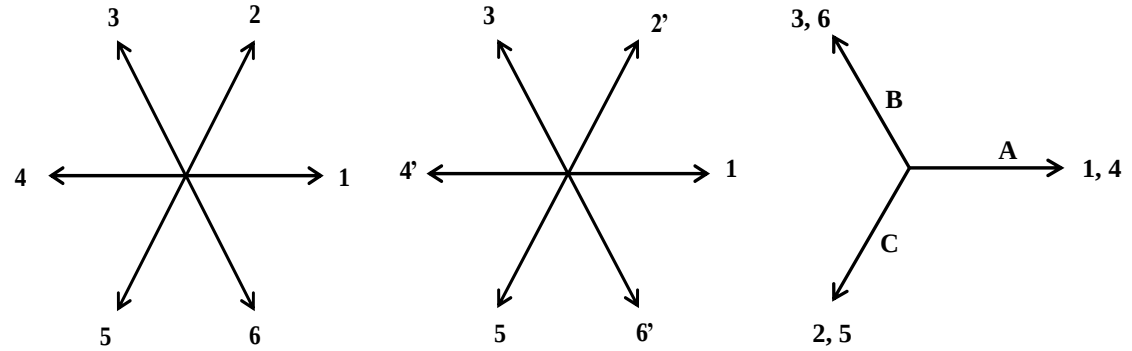

(c) 6/7

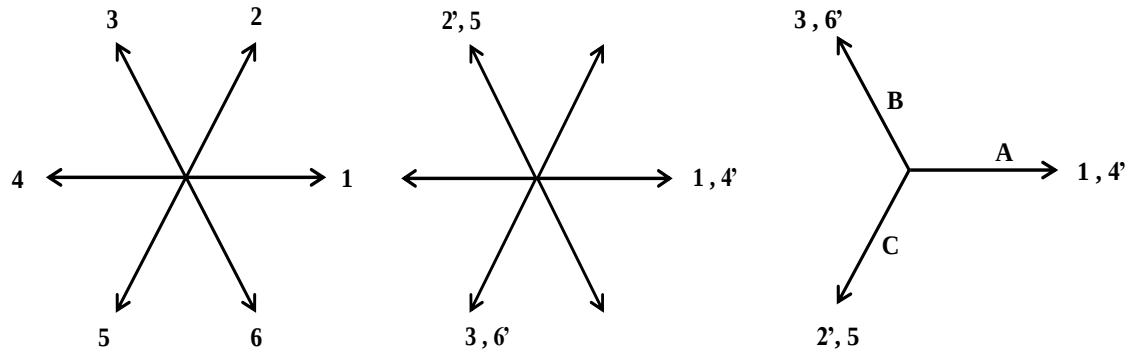

(d) 6/8

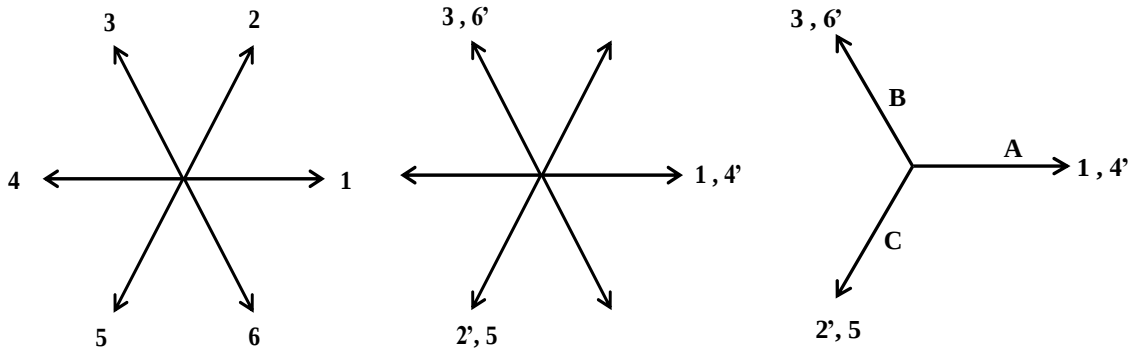

(e) 6/10

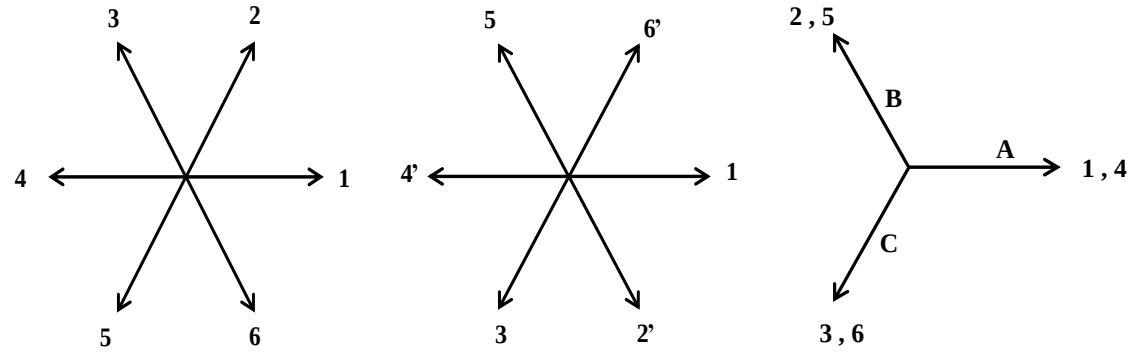

(f) 6/11

Fig. 3.30 Back-EMF vectors of PSFRPM linear machines, (I) Stator coils (mech. Degree), (II) Back-EMF vectors, (III) Phase coils.

3.6.2 Design Optimization

For quantitative comparison, the optimization constraints and the parameters of the global optimization are kept similar for all the designed machines. The definition, constraint, and initial values of the design variables for the optimization are setup to be similar to those which were used with 6/5 machine optimization in section 3.4.2. Initial and optimal values of the optimized variables are listed in Table 3.3. It can be seen that the optimal split ratio for the machines with odd mover pole number ranges between 0.35 and 0.38, while it is about 0.4 for those with an even mover pole number. Although all machines have the same stator slot number, they have different optimal values for their stator parameters, which include *S1TWR*, *S1SOR* and *S1BITHR*.

Table 3.3 Initial and optimal values of PS-FRPM linear machines

Optimization variables	Symbol	Initial value	Optimal values					
			6/4	6/5	6/7	6/8	6/10	6/11
Split ratio	*SR*	0.5	0.36	0.37	0.38	0.41	0.4	0.35
Mover thickness	*MTH*	3	4.8	4.7	4.7	3.33	3.39	3.65
Top mover pieces width ratio	*TMPWR*	0.6	0.649	0.732	0.782	0.771	0.716	0.649
Bottom mover pieces width ratio	*BMPWR*	0.7	0.85	0.6	0.433	0.529	0.45	0.55
Stator1 teeth width ratio	*S1TWR*	0.2	0.23	0.23	0.21	0.2	0.11	0.15
Stator1 slot opening ratio	*S1SOR*	0. 64	0.55	0.55	0.57	0.61	0.64	0.67
Stator1 back iron thickness ratio	*S1BITHR*	0.125	0.15	0.13	0.14	0.2	0.2	0.15

3.6.3 Electromagnetic Performance Comparison

The electromagnetic performances of the machines have been analysed and compared. Open circuit flux line distributions for all machines when their movers move one pole pitch are plotted in Fig. 3.31.

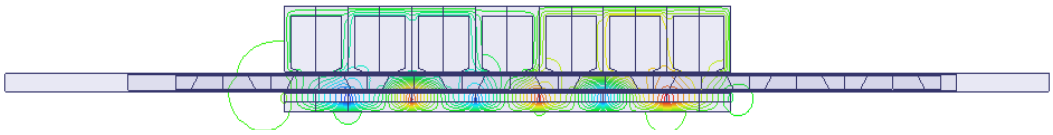

(a) 6/4

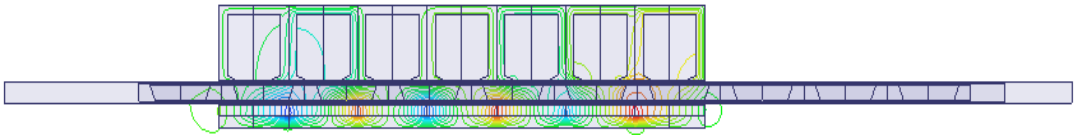

(b) 6/5

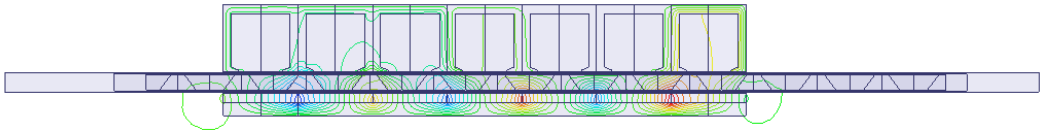

(c) 6/7

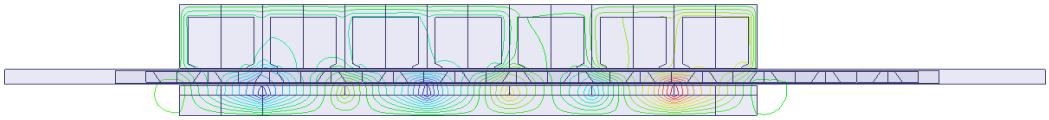

(d) 6/8

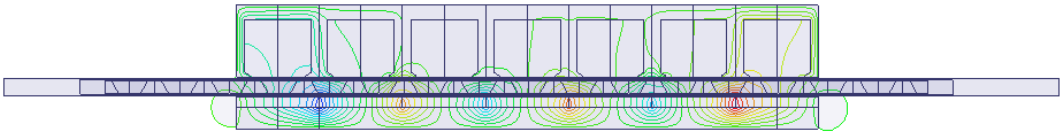

(e) 6/10

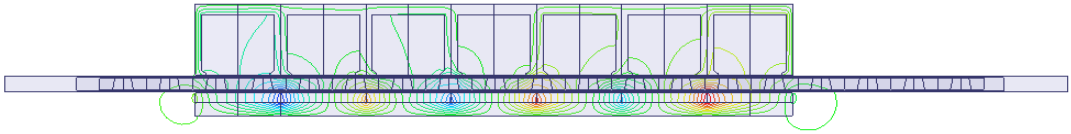

(f) 6/11

Fig. 3.31 Open circuit flux line distribution of the PS-FRPM linear machines.

Phase A flux linkage waveforms and corresponding spectrums of all machines are shown in Fig. 3.32. It is clear that the highest flux linkage can be obtained by 6/5 machine. The flux linkage decreases as the mover pole number increases due to the increasing of flux leakage, which is compatible to the PS-FRPM rotational machines, since they share the same operation principle and structure. However, 6/4 machine has about 22.5% less flux linkage than 6/5 due to the saturation.

Fig. 3.33 shows phase A back-EMF waveforms and their spectrums for the analysed machines. It can be noted that the highest back-EMF is obtained by 6/5 machine, which has the highest flux linkage. On the other hand, although 6/7 machine exhibits 40% less flux linkage than 6/5 machine, the difference between the back-EMF of two machines is about 8% since 6/7 machine has a higher frequency. For the same reason, the 6/10 machine has just 3% higher back-EMF than that of the 6/11 machine, however the former has a higher flux linkage.

Cogging force waveforms are compared in Fig. 3.34. It can be seen that the machines with even mover pole numbers exhibit higher cogging force than those with odd mover pole numbers, since the former have higher goodness factor than the latter.

As has been found in [ZHU00] the smaller the goodness factor the lower the cogging force amplitude. The goodness factor can be obtained by:-

$$C_T = \frac{N_S N_m}{N_C} \tag{3.19}$$

where C_T and N_C are the goodness factor and the least common multiple between N_S and N_m, respectively.

Thrust forces of the PS-FRPM machines are compared in Fig. 3.35. Obviously, the shape of thrust force and cogging force for each machine is similar. Hence, it can be concluded that the major components of the thrust force ripples are mostly caused by the cogging force. Furthermore, the machine with 6/5 stator/mover has the highest thrust force, as it exhibits the highest back-EMF among the other machines, and the lowest average thrust force is produced by the 6/10 machine. However, the 6/7 machine produces about 7% less average thrust force than that of the 6/5 machine, it has less thrust force ripple.

Moreover, the variations of the average thrust force with current density under id=0 control and packing factor of 0.6 are shown in Fig. 3.36. However, 6/4, 6/8, 6/10 and 6/11 machines exhibit similar average thrust force under low current density values, while the machine with 6/10 combination has the lowest average thrust force at high current density. The highest average thrust force is achieved by the 6/5 machine.

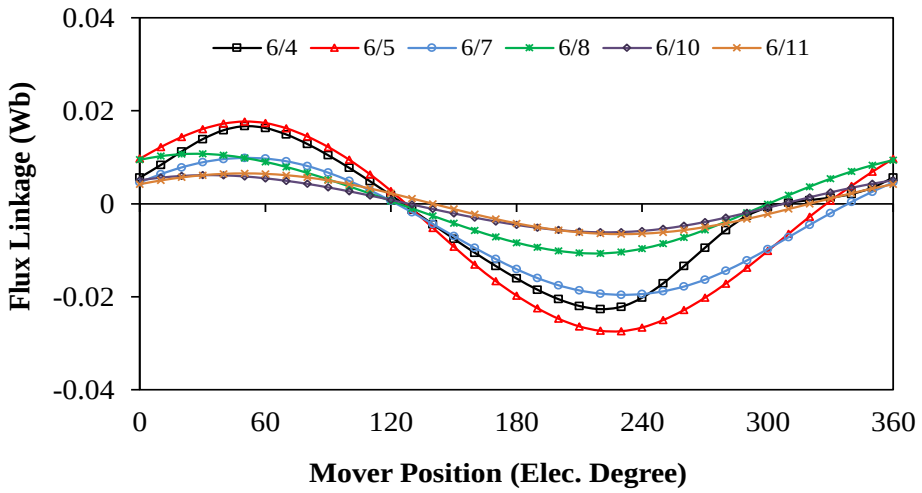

(a) Waveform

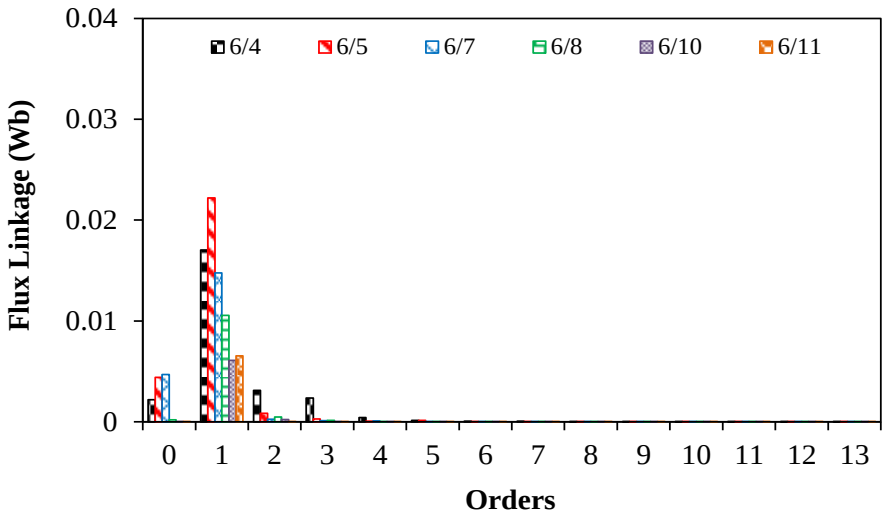

(b) Spectrum

Fig. 3.32 Phase A flux linkage comparison.

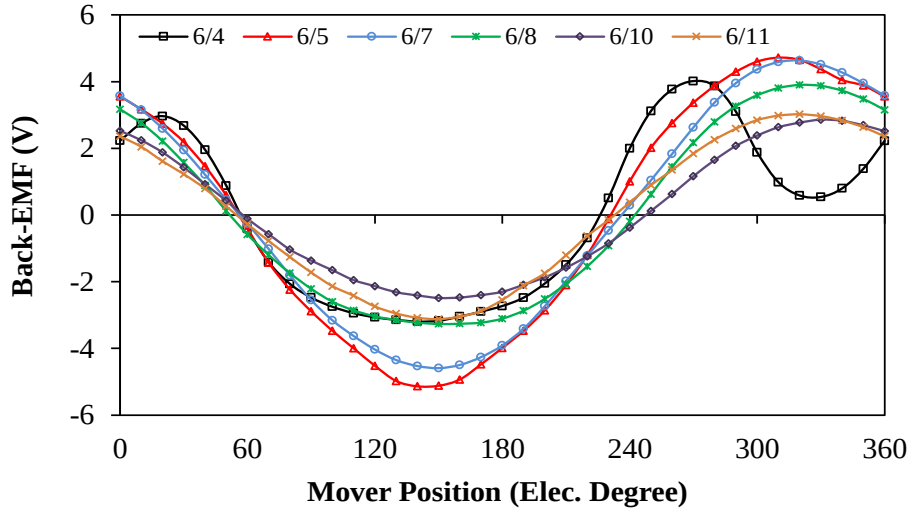

(a) Waveform

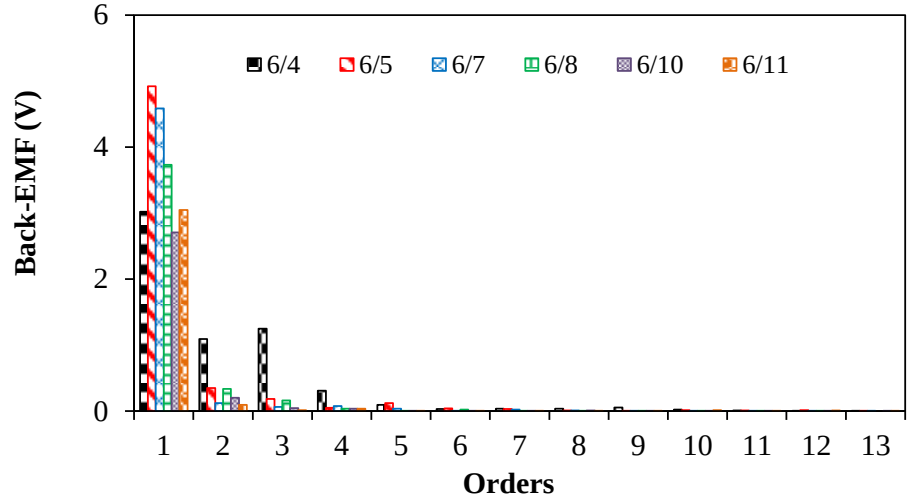

(b) Spectrum

Fig. 3.33 Phase A back-EMF comparison.

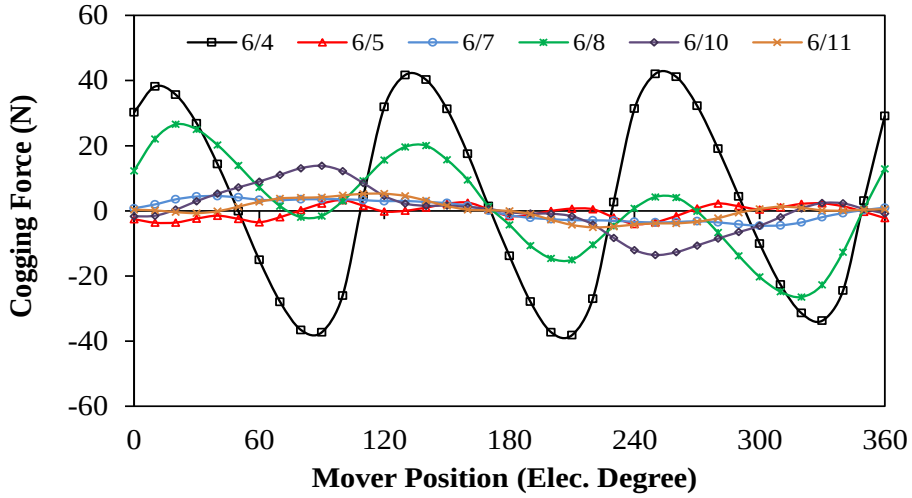

Fig. 3.34 Cogging force comparison.

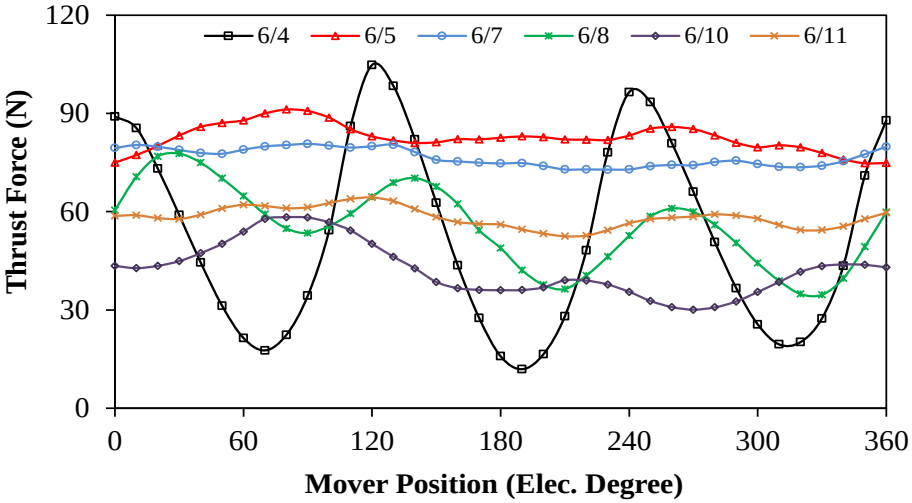

Fig. 3.35 Thrust force comparison (current density = 7A/mm^2 rms).

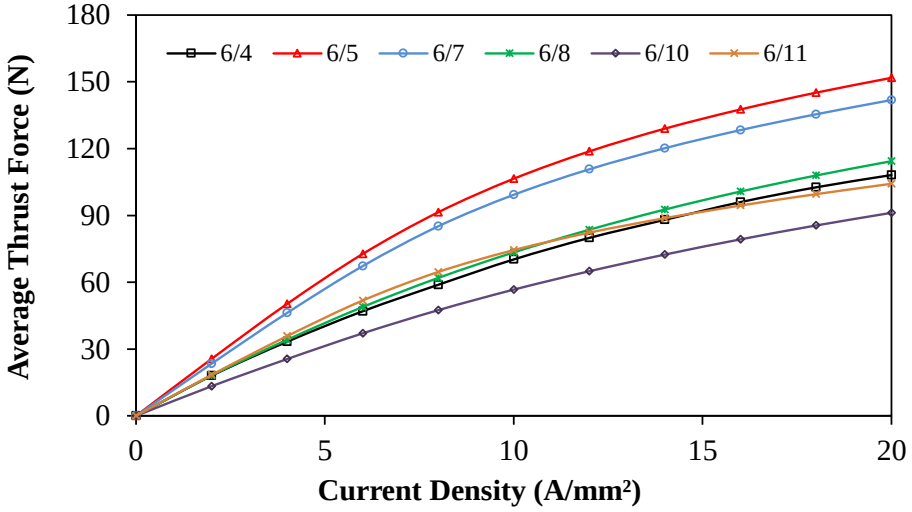

Fig. 3.36 Average thrust force variation with current density.

3.7 Effect of Cross-coupling on Machine Performance

The influence of cross-coupling on the PS-PFRPM linear machine performance, particularly on the PM flux linkage and d-q axis inductances, will be investigated by utilizing the method that has been proposed in [QI09], which can be summarised as follows:

$$\psi_{PM}(I_q) = \psi_d(I_d = 0, I_q) \tag{3.20}$$

$$L_d(I_d, I_q) = \frac{\psi_d(I_d, I_q) - \psi_{PM}(I_q)}{I_d} \tag{3.21}$$

$$L_q(I_d, I_q) = \frac{\psi_q(I_d, I_q)}{I_q} \tag{3.22}$$

where ψ_{PM} indicates flux linkage due to the PM, while ψ_d, L_d and I_d represent d-axis flux linkage, inductance and current, respectively. ψ_q, L_q and I_q are q-axis flux linkage, inductance and current, respectively. In such method, d- and q-axis flux linkages are obtained for different values of both d- and q-axis currents by FE. Then, use (3.21) and (3.22) to calculate d- and q-axis inductances from these values.

Fig. 3.37 shows the PM flux linkage with different I_q. It is obvious that the flux linkage due to the permanent magnet reduces with the increasing of q-axis current due to the saturation.

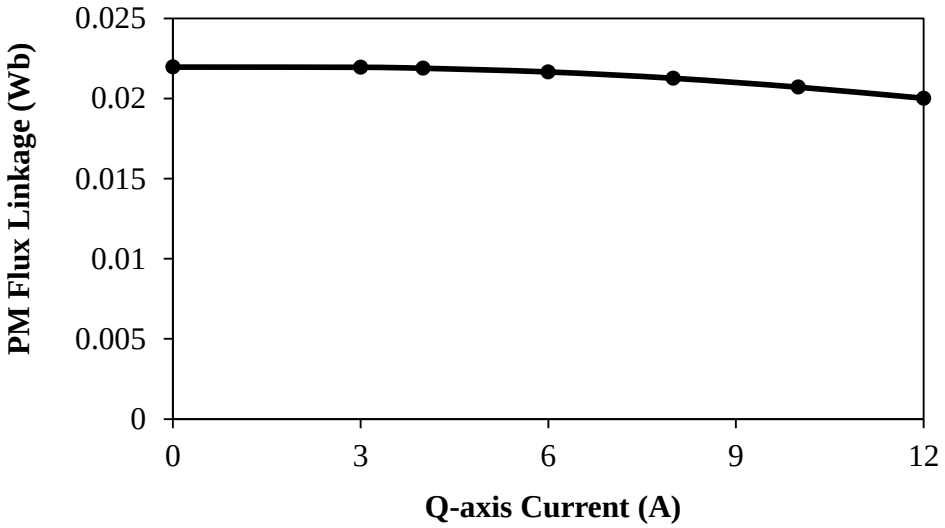

Fig. 3.37 Variation of PM flux linkage with q-axis current.

Inductances in both d- and q-axes with different d- and q-axis currents are illustrated in Fig. 3.38 and Fig. 3.39 , respectively. It can be seen that L_d increases with the

increasing of d-axis current. On the other hand, it reduces with the increasing of the q-axis current. However, the effect of the q-axis current on the d-axis inductance is less than that on the q-axis inductance, which sharply decreases with the increasing of the q-axis current, particularly at low values of I_q. It should be mentioned that q-axis inductance is less sensitive to I_d compared to d-axis inductance although both increase as d-axis current increases.

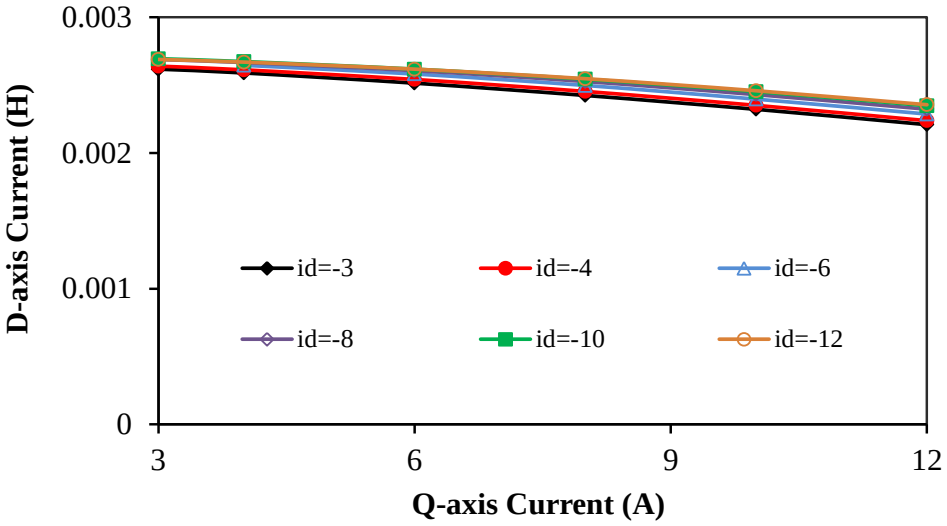

(a)

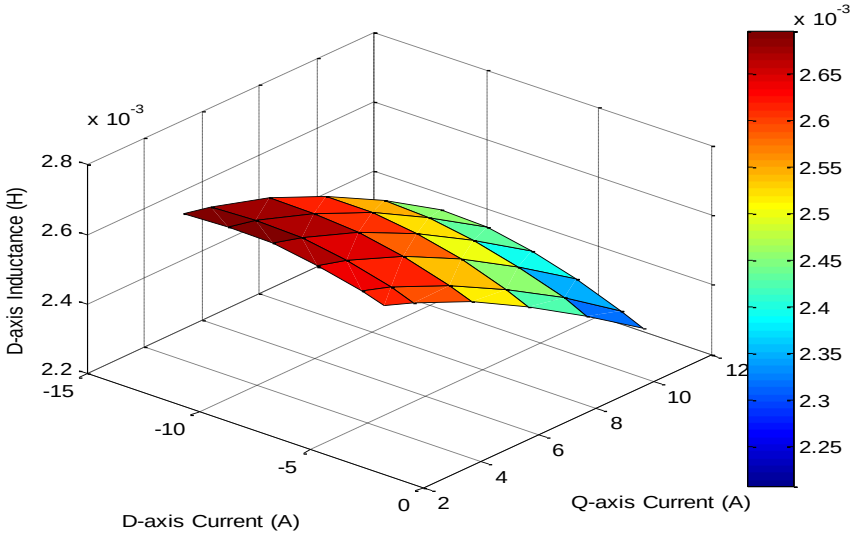

(b)

Fig. 3.38 D-axis inductance accounting cross-coupling.

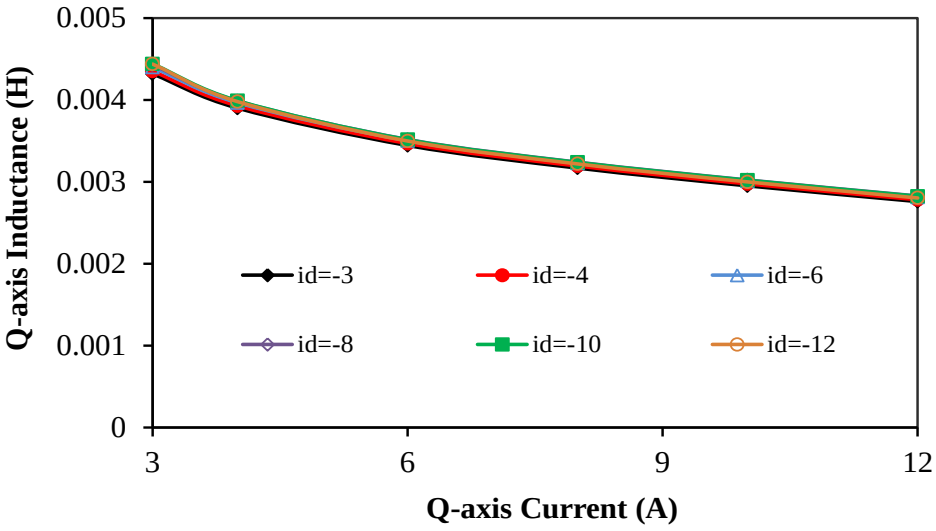

(a)

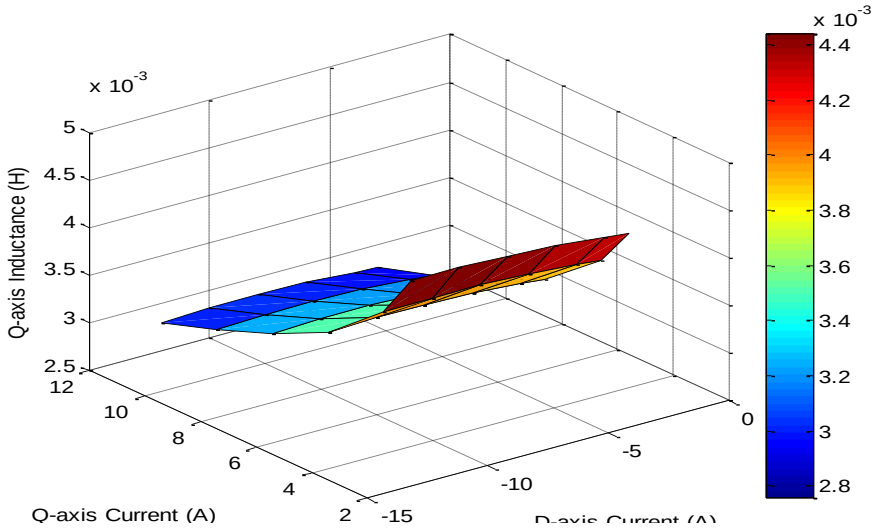

(b)

Fig. 3.39 Q-axis inductance accounting cross-coupling.

In order to implement a suitable position control for the machine, its dynamic performance is required. Thanks to the introduction of rare earth permanent magnet materials that are distinguished by a linear demagnetisation performance, flux weakening control approach in which I_d is utilized to weaken the permanent magnet flux without magnet demagnetization risk, has been applied to control the PM machine. Similar to their rotating counterparts, PM linear machines can be driven by the flux weaken control method [SAN97].

Voltages in d-and q-axes for PM linear machines can be expressed as follows [CAO12]:

$$V_d = \frac{d\psi_d}{dt} - \omega_e \psi_q + RI_d \tag{3.23}$$

$$V_q = \frac{d\psi_q}{dt} + \omega_e \psi_d + RI_q \tag{3.24}$$

$$\omega_e = \frac{2\pi V}{\tau} \tag{3.25}$$

where V_d and V_q, indicate d- and q-axis voltage, respectively. ω_e represents electrical angular frequency, V is the velocity. τ is the pole pitch.

Due to the constraints of both voltage and current, the terminal voltage V_a and current I_a would be limited and determined as [SAN97]

$$I_a = \sqrt{{I_d}^2 + {I_q}^2} \leq I_{max} \tag{3.26}$$

$$V_a = \sqrt{{V_d}^2 + {V_q}^2} \leq v_{max} \tag{3.27}$$

Output thrust force can be calculated by [CAO12]

$$F_{o/p} = \frac{3\pi}{\tau}\left[\psi_{PM} i_q + I_d I_q (L_d - L_q)\right] \tag{3.28}$$

The force-velocity curve can be obtained by utilising the method, which was described in [QI09]. Fig. 3.40 shows the force-velocity curve of the PS-FRPM linear machine. It can be seen that the machine has a good flux weakening capability. On the other hand, the power-velocity curve is illustrated in Fig. 3.41. It is obvious that the machine exhibits a wide constant power region.

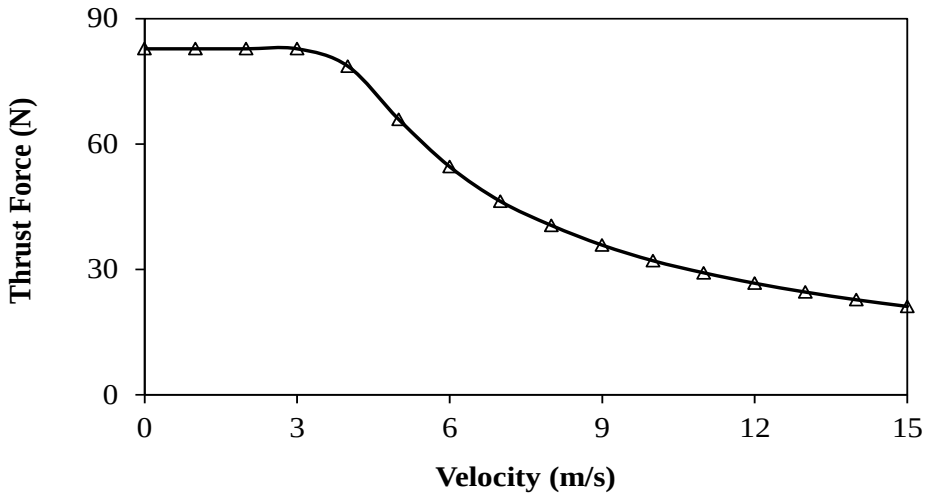

Fig. 3.40 Force-velocity curve.

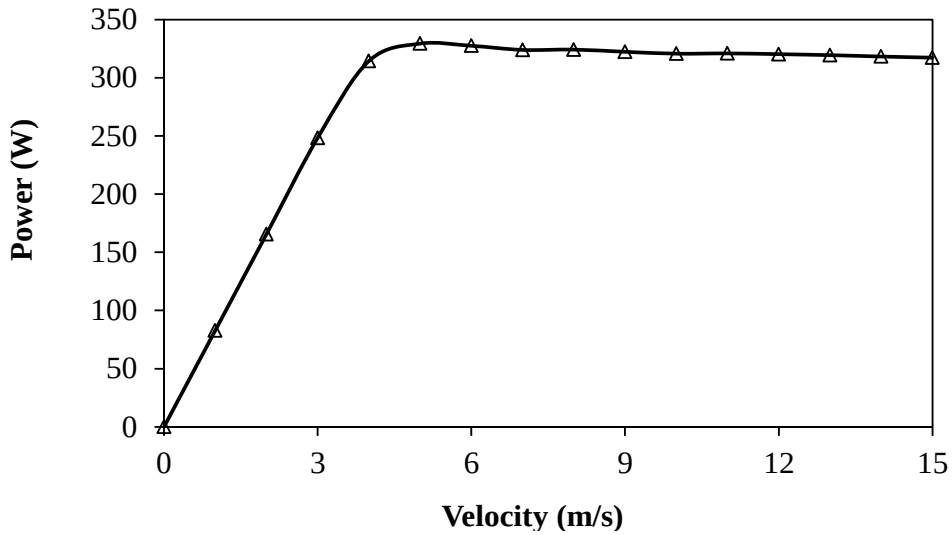

Fig. 3.41 Power-velocity curve.

3.8 Machine Losses and Efficiency

3.8.1 Copper Loss

When machine windings are supplied by currents, copper loss will be produced. Generally, copper loss is calculated by

$$P_{cu}=3\, I_{rms}\, R \tag{3.29}$$

where P_{cu}, I_{rms} and R indicate copper loss, RMS value of the current, and phase resistance, respectively.

The machine phase resistance is expressed as

$$R = N_a^2 l_a \rho / S_a k_{pf} \tag{3.30}$$

where N_a, S_a, l_a, ρ and k_{pf} represent the number of turns per phase, slot area, the active length, the copper resistivity and packing factor, respectively.

By applying (3.29) and (3.30), the copper loss of the proposed machine can be determined.

3.8.2 Iron Loss

Usually, ferromagnetic materials exhibit three loss components when they are exposed by an AC magnetic field. These components are explained [ATA92]

$$P_{iron} = P_{hyst} + P_{class} + P_{excess} \tag{3.31}$$

where P_{iron}, P_{hyst}, P_{class}, P_{excess} are iron loss, hysteresis loss, classical and excess eddy-current losses, respectively. The hysteresis loss, classical and eddy-current losses can be determined by [PAN08]

$$P_{hyst} = K_h F B_{max}^{a_h + b_h + B_{max}} \tag{3.32}$$

$$P_{class} = \frac{d_{iron}^2}{12 m_v \rho_{iron}} \frac{1}{T_{cycle}} \int_0^{T_{cycle}} \left(\frac{dB}{dt}\right)^2 dt \tag{3.33}$$

$$P_{excess} = \frac{K_e}{T_{cycle}} \int_0^{T_{cycle}} \left|\frac{dB}{dt}\right|^2 dt \tag{3.34}$$

where K_h, K_e, a_h and b_h represent material coefficients, which can be decided from experiment. On the other hand, B_{max} refers to the flux density amplitude (T). Whilst d_{iron}, ρ_{iron}, and m_v are iron lamination thickness (m), iron lamination resistance (Ωm) and iron lamination mass density, respectively. In addition, T_{cycle} is the time cycle of the flux density variation (s). It should be noted that the values of the material coefficient which are used for core loss calculation are given in Table 3.4.

Table 3.4 Parameters for iron loss calculation

Items	Values
K_h	0.0179
K_e	0.0002
a_h	0.841
b_h	1.023

The origin of eddy current loss components is referred to the Joule loss because of the eddy currents, which are generated by the variation of the magnetization [ROS07]. 2DFE can be employed to calculate the iron loss of the proposed machine. For each mesh element the flux density which varies with the time is predicated by FE and the iron loss can be determined by (3.32). The summation of the iron losses of all the elements is the total iron loss [PAN08].

The predicted no load and load iron losses of the PS-FRPM linear machine are shown in Fig. 3.42. It can be seen that loss increases with the increase of the velocity due to the frequency increasing.

3.8.3 Magnet Eddy Current Loss

Due to the variation of the magnet flux with the rotor position, eddy current loss is produced in the magnet of the machine under open circuit and load operation conditions [ATA92]. Fig. 3.43 presents magnet eddy current loss distributions of the PS-FRPM

linear machine. It should be mentioned that the mover position has been selected based on the highest magnet eddy current loss. On the other, the magnet eddy current losses as a function of the velocity under no-load and full-load for the mentioned machine are shown in Fig. 3.44. Since the current leads to the increase of the permanent magnet flux variation [ZHU08], the load loss is about 10 times higher than the open circuit loss.

Fig. 3.45, Fig. 3.46 and Fig. 3.47 display the copper loss map, the iron loss map and the efficiency map of the understudy machine, respectively. The efficiency map can be obtained by calculating iron and magnet losses for different velocities and d- and q-axis currents using FE. The copper loss is calculated at different d- and q-axis currents with assumed fixed phase resistance. Furthermore, it can be seen that the maximum efficiency for the PS-FRPM linear machine is 95%, and is located in the flux weakening region due to the reduction of the rated current, which results in reduced copper loss that is the highest amount of PS-FRPM linear machine loss of all the losses, i.e. iron and magnet eddy losses.

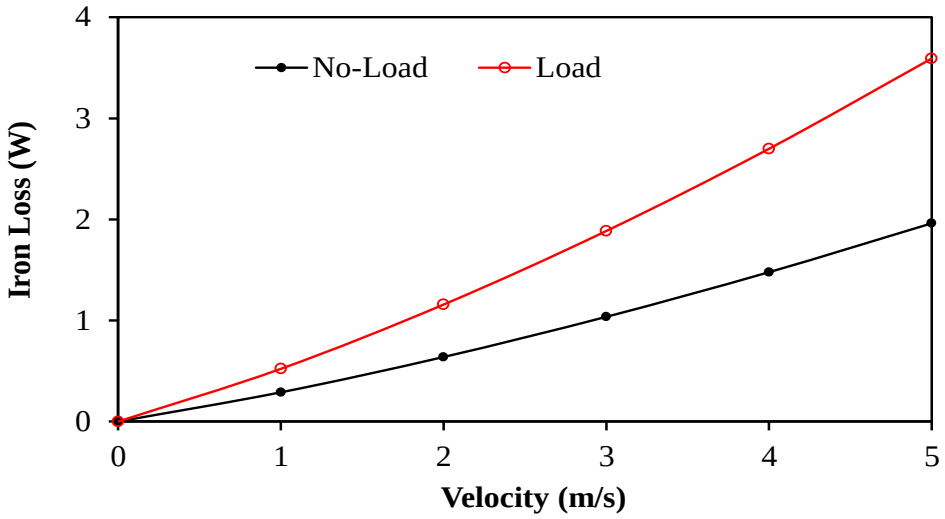

Fig. 3.42 PS-FRPM linear machine no-load and load iron loss variation with velocity.

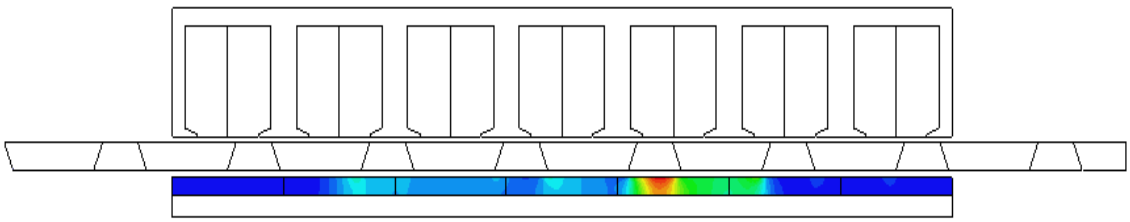

Fig. 3.43 Magnet eddy current loss distribution.

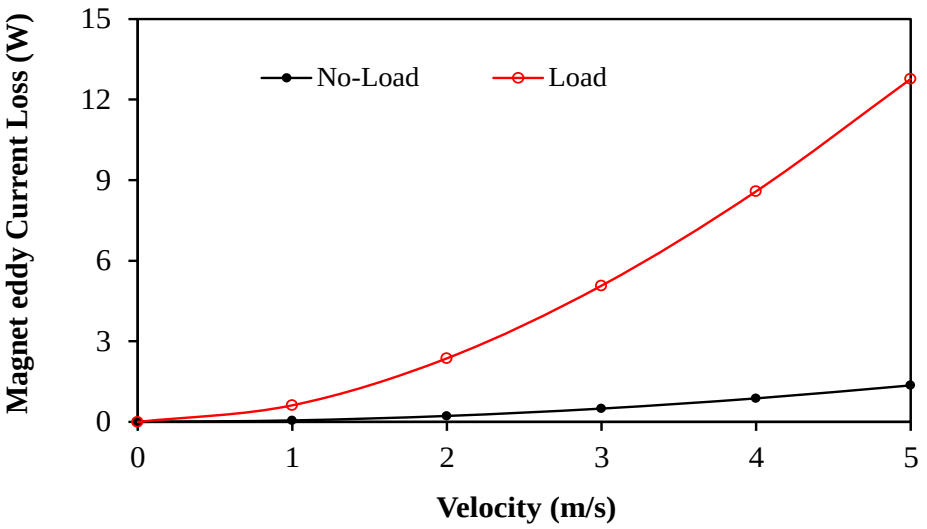

Fig. 3.44 Variation of magnet eddy current loss with velocity at no-load and load conditions for PS-FRPM linear machine.

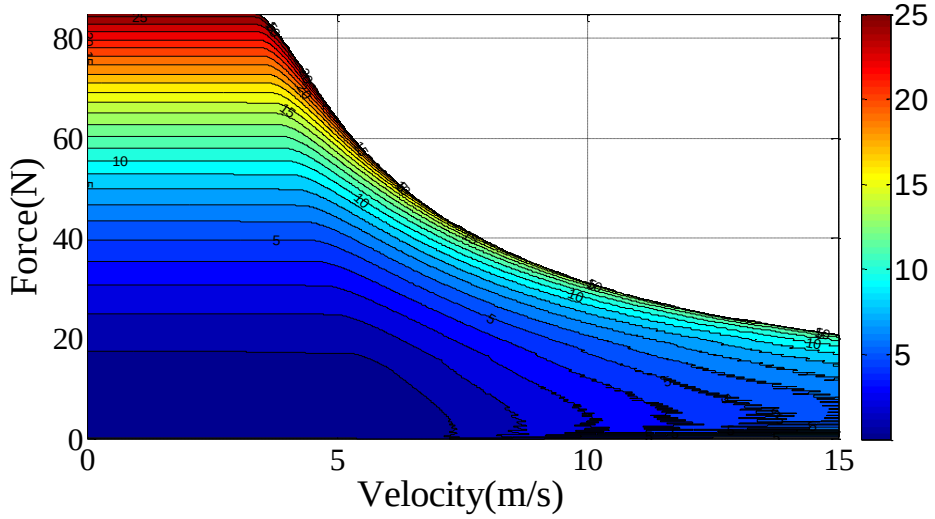

Fig. 3.45 Copper loss map of the PS-FRPM linear machine.

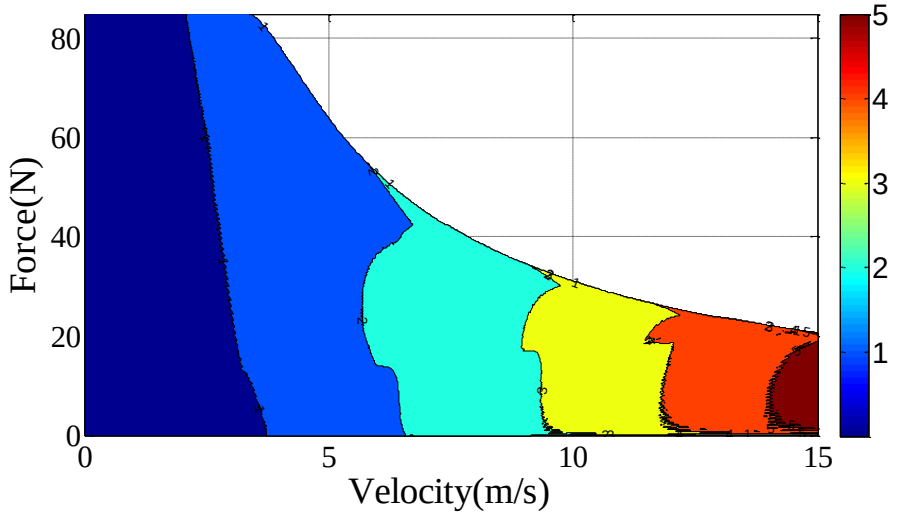

Fig. 3.46 Iron loss map of the PS-FRPM Linear machine.

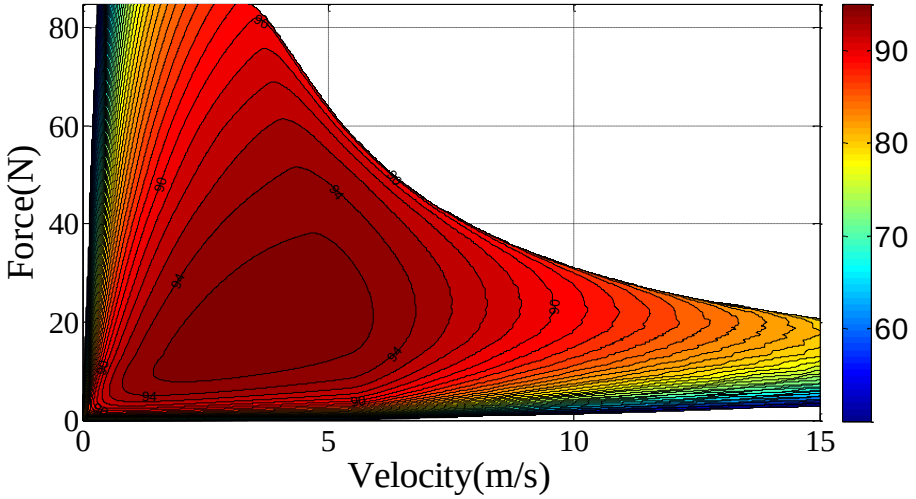

Fig. 3.47 Efficiency map of the PS-FRPM linear machine.

3.9 Demagnetization Withstand Capability

PM demagnetization phenomenon would be presented in a PM machine when the load current is applied, particularly with the demagnetisation current, and becomes worse when the PM temperature increases. It has been confirmed that when such a phenomenon exists, the PM machine performance would deteriorate [ROS05] [ZHA10]. Therefore, a PM machine with high capability to withstand irreversible demagnetization is required for high reliability. Hence, this section highlights the PM demagnetization risk of the proposed machine. It should be underlined that the method, which was explained in Chapter 2, will be utilized to evaluate the PS-FRPM linear machine ability to withstand the demagnetization. Fig. 3.48 (a) and (b) show the machine flux density distributions for the north and the south PM poles, respectively. It can be noted that the proposed machine has a good capability to withstand demagnetization since the lowest flux density in its PMs is higher than the PM knee point at 120^0C, i.e. higher than 0.22T.

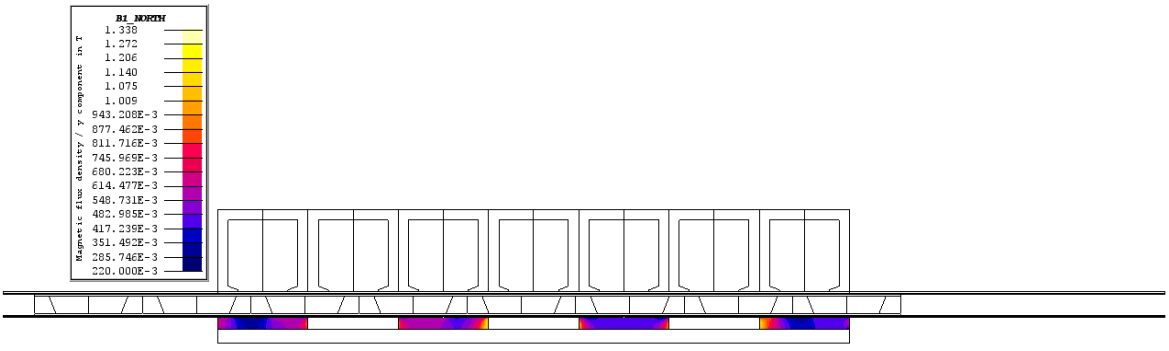

(a) North-pole PMs flux density distributions PS-FRPM linear machine.

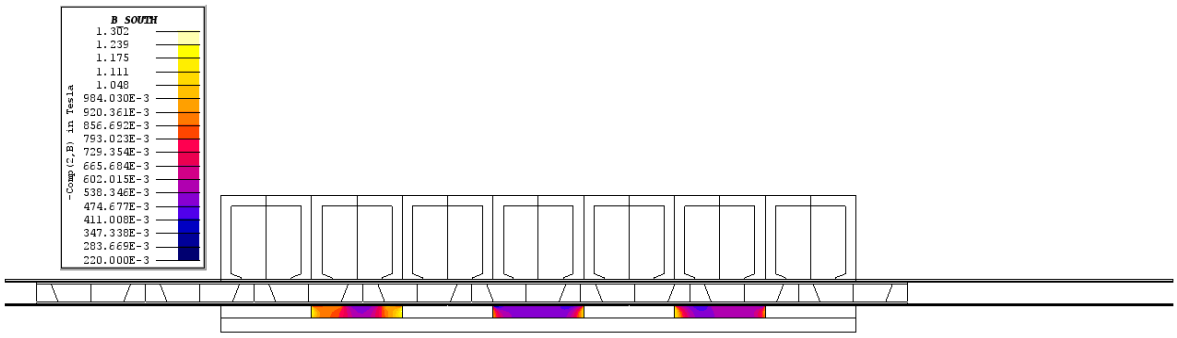

(b) South-pole PMs flux density distributions PS-FRPM linear machine.

Fig. 3.48 PM flux density distributions at 120^0C.

3.10 Experimental Validation

To validate the FE results of the PS-FRPM linear machine, a prototype, Fig. 3.49, has been built and tested at the company and Zhejiang University in China. Stator 1 in which the armature windings are located is made of laminations of steel 50W470, while the back-iron of the PM and the rotor iron pieces are made of steel Q235-A. The mover pieces are connected by a bridge made of a non-ferromagnetic material. It should be mentioned that both stators are connected together by a bridge made of a non-ferromagnetic material. The drawings and material BH curves of the prototype are illustrated in Appendix B. On the other hand, Fig. 3.50 and Fig. 3.51, show 2D and 3D FE models of the mentioned machine with the optimal and prototype dimensions, respectively. A comparison between the dimensions of the optimal and prototype FE models is given in Table 3.5.

The back-EMF test that was carried out in the company was done for each phase with the mover moved by hand. The test results for both phases A and B are illustrated in Fig. 3.52 and Fig. 3.53, respectively. It can be noted that the velocities of the back-EMF waveforms for both phases A and B are not constant. Fig. 3.54 and Fig. 3.55 show the variations of the velocities of the back-EMF waveforms of phases A and B, respectively. It can be clearly seen that the middle parts of the back-EMF waveforms for both phases are more stable compared with those at the beginning and the end. Hence, all the cycles of phase A back-EMF waveform will be converted to be equal to that of cycle No.6, whilst those for phase B back-EMF waveform will be converted to be equal to that of cycle No.4. It should be mentioned that the method used to unify the velocities of the cycles is as follows.

- Firstly, the velocity of each cycle in the waveform has been determined by

$$V = M_{pp} * Fre \tag{3.36}$$

$$Fre = \frac{1}{Time} \tag{3.37}$$

where V, M_{pp}, Fre, and *Time* are the average velocity over one cycle, the mover pole pitch, the frequency, and the time period of one cycle, respectively.

- Afterwards, the ratio of the velocity of cycle No.6 (for phase A test results) to the velocity of each cycle is obtained.

- The new cycles with constant velocities over each cycle can be determined by dividing the time by the obtained ratio, and meanwhile the amplitude of each cycle is multiplied by the corresponding ratio.

Fig. 3.56 and Fig. 3.57 illustrate the converted Phases A and B back-EMF waveforms, respectively. Moreover, Fig. 3.58 shows the measured three-phase back-EMFs, which were measured at Zhejiang University. It can be noted that the velocities of the back-EMF waveforms are not constant, Fig. 3.59. Therefore, the velocities of all back-EMF cycles are converted to be equal to the velocity of 500 mm/s, Fig. 3.60. The back-EMFs of phases A and B for both tests, i.e. carried out at the company and Zhejiang University, are compared, as shown in Fig. 3.61 and Fig. 3.62, respectively. Obviously, there is a very good agreement between both tests. Furthermore, a comparison between three phase back-EMF waveforms and their corresponding 2D and 3D FE results is depicted in Fig. 3.63. Although 3D FE predicted results agree well with the test results, the difference between the 2D FE results and the test results is about 35%, due to the end effect as well as the difference in axial lengths of the stator 1, the stator 2 and the mover, which cannot be considered in the 2D FE simulation. In order to investigate the influence of the unequal axial length of the machine parts, a comparison between 2D and 3D FE models with the prototype and globally optimised dimensions, as illustrated in Fig.3.50 and Fig.3.51, is conducted. It should be mentioned that

- 2D and 3D optimal models refer to the models with global optimized dimensions.
- 2D prototype model represents the model with prototype parameters with even axial length.
- 3D prototype model is the model which has the same prototype dimensions (considering the difference in the axial length of the stator 1, stator 2 and the mover).

Fig. 3.64 compares the phase A back-EMFs of the 2D and 3D FE models with the globally optimised and the prototype dimensions. It can be observed that the difference between the globally optimised 2D and 3D models is about 7.7% which is reasonable due to the end effect. In addition, the 3D model with optimal dimensions has about 34% higher back-EMF compared to the 3D model according to the prototype dimensions. This is occurred since the model with prototype dimensions has larger air gap lengths and also extended axial lengths of the mover and the stator 2 back-iron, which lead to

the reduction of flux linkage. Consequently, the back-EMF is reduced. Furthermore, cogging forces of the mentioned models are compared in Fig. 3.65. Although the models exhibit almost the same trace, a slight change can be found in their peak. Static force capabilities of the mentioned models are shown in Fig. 3.66. It should be mentioned that the static thrust force refers to the electromagnetic thrust force, when the machine is fed by a constant current under the relationship of (I_a= - 2I_b= - 2I_c). On the other hand, the variation of the maximum value of the static force with current is depicted in Fig. 3.67. The difference between the dimensions of the optimal and prototype models results in higher thrust force capability for both 2D and 3D FE models with optimal dimensions compared to that of the corresponding prototype dimensions. In addition, due to the end effect and iron saturation, the 2D FE model with optimal dimensions has about (5-8) % higher thrust force capability than that of the 3D FE counterpart. Owing to the above-mentioned reasons of back-EMF reduction, the 2D FE model with the prototype dimensions exhibits about (23-37) % higher thrust force capability than that of the corresponding 3D FE model. The measured cogging force is compared with the 2D and 3D FE predicted results, as shown in Fig. 3.68. The peak to peak value of the FE result is slightly lower than the measured one, due to high sensitivity to manufacturing tolerance as it has been found in [LU16]. Moreover, the measured and predicted FE static thrust forces are shown in Fig. 3.69, while the variation of thrust force with the current for both FE and measured results is illustrated in Fig. 3.70. The variance between both results is sensible by taking into consideration of assembling tolerance and measuring error.

Fig. 3.49 Prototype PS-FRPM linear machine.

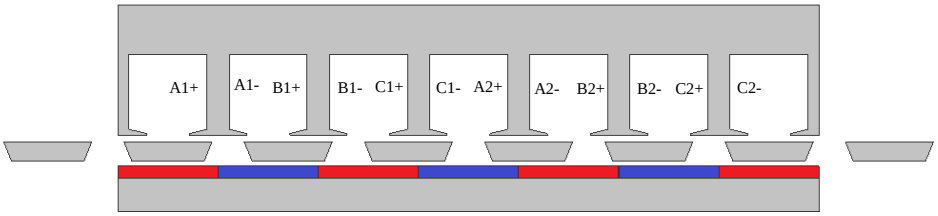

(a) 2D-model

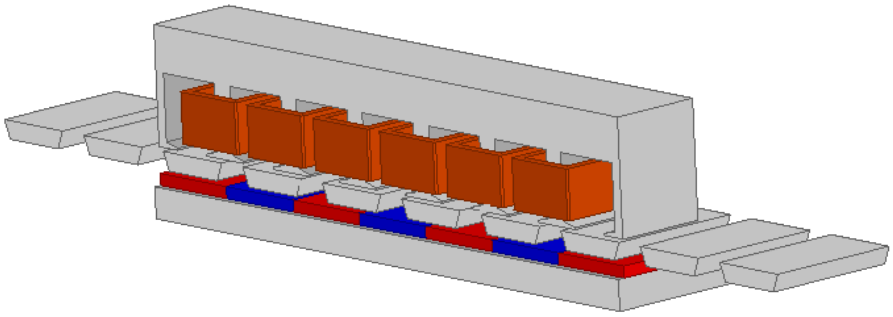

(b) 3D-model

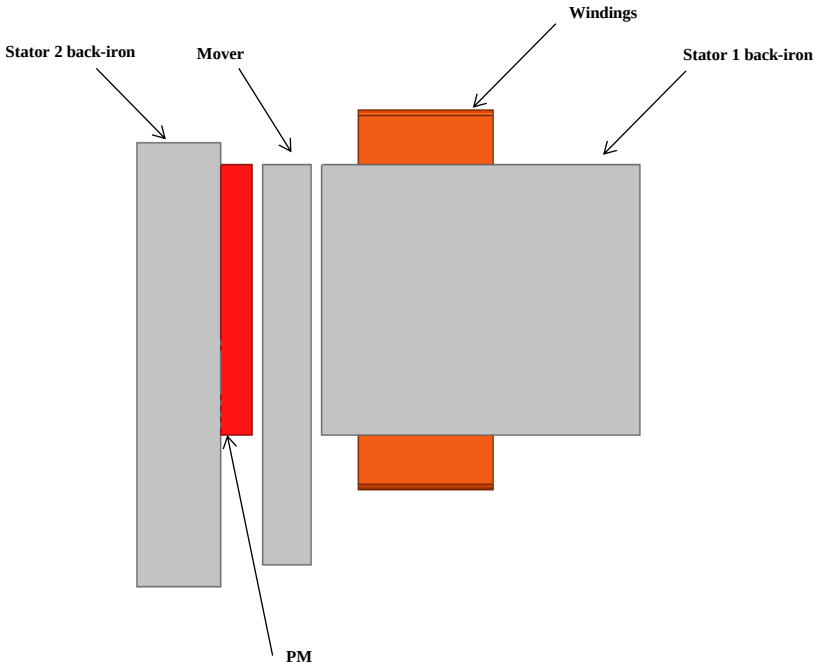

(c) Side-view

Fig. 3.50 FE models with prototype dimensions.

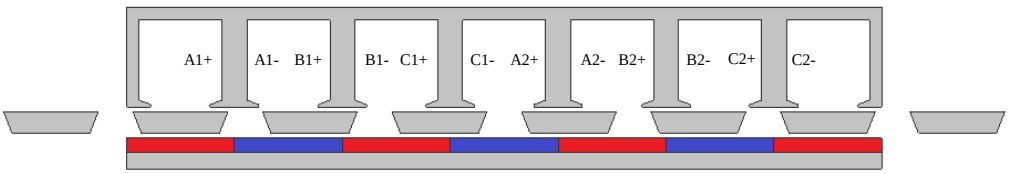

(a) 2D-model

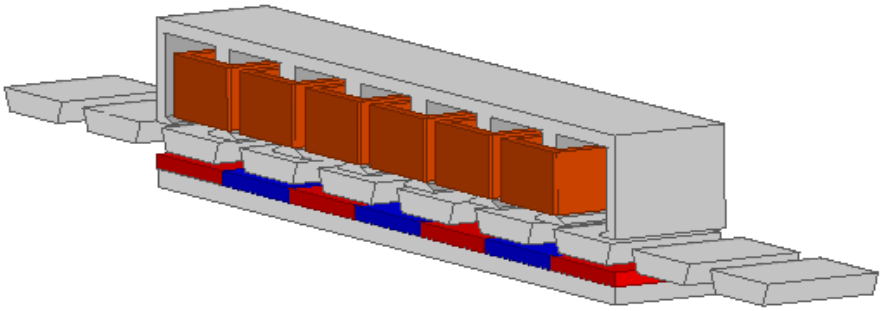

(b) 3D-model

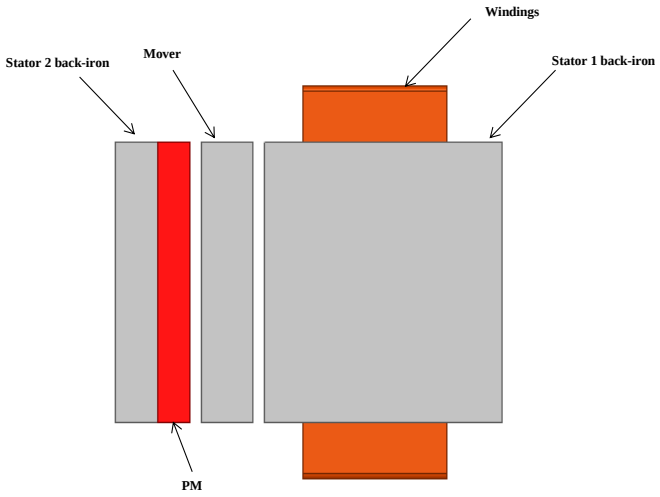

(c) Side-view

Fig. 3.51 FE models with optimal dimensions.

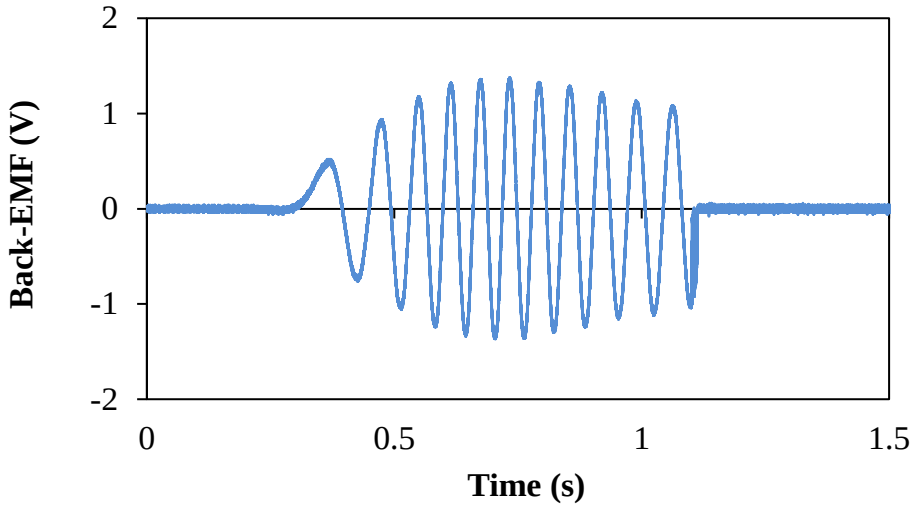

Fig. 3.52 Original Phase A back-EMF test result.

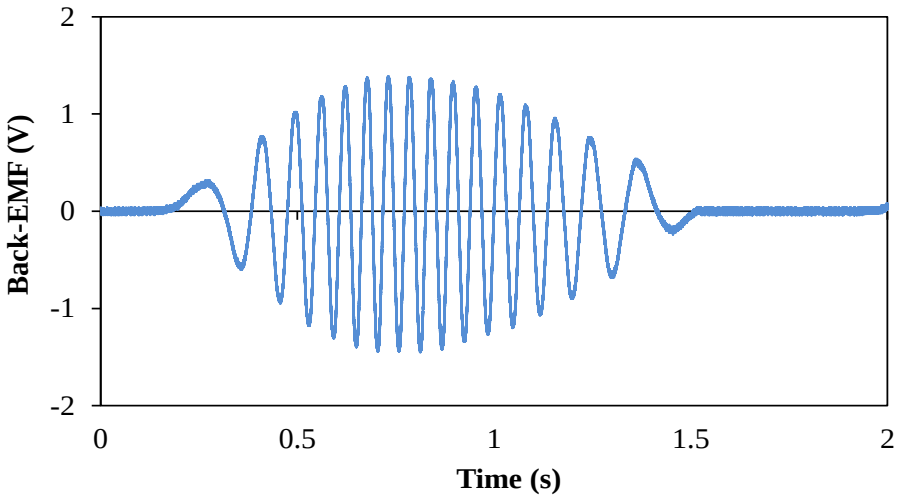

Fig. 3.53 Original Phase B back-EMF test result.

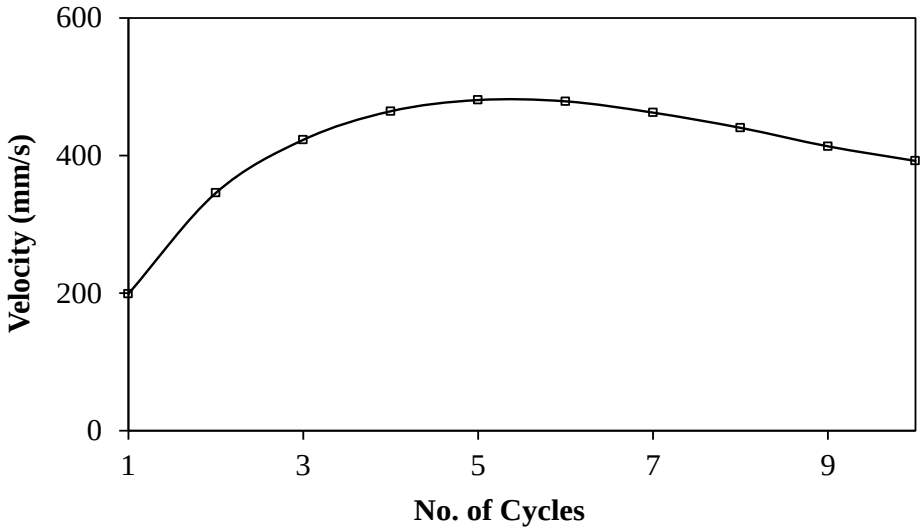

Fig. 3.54 Variation of velocities of phase A back-EMF waveform test result.

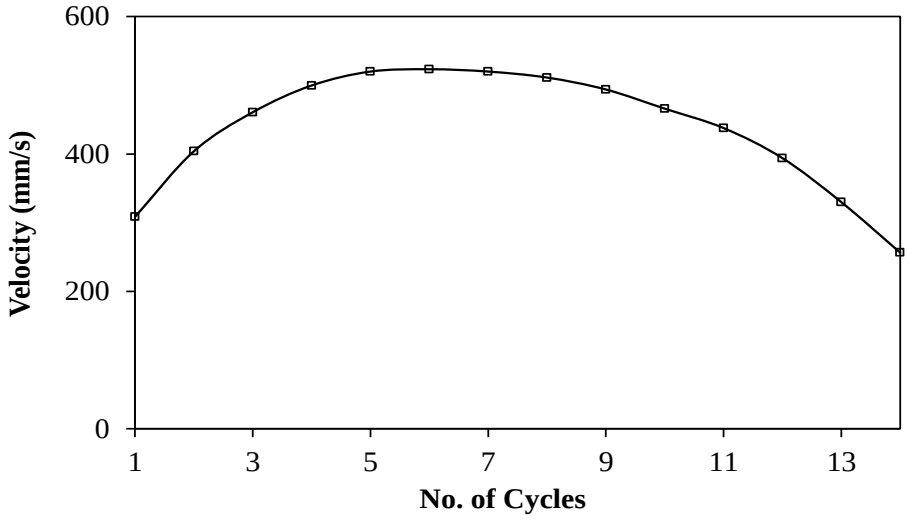

Fig. 3.55 Variation of velocities of phase B back-EMF waveform test result.

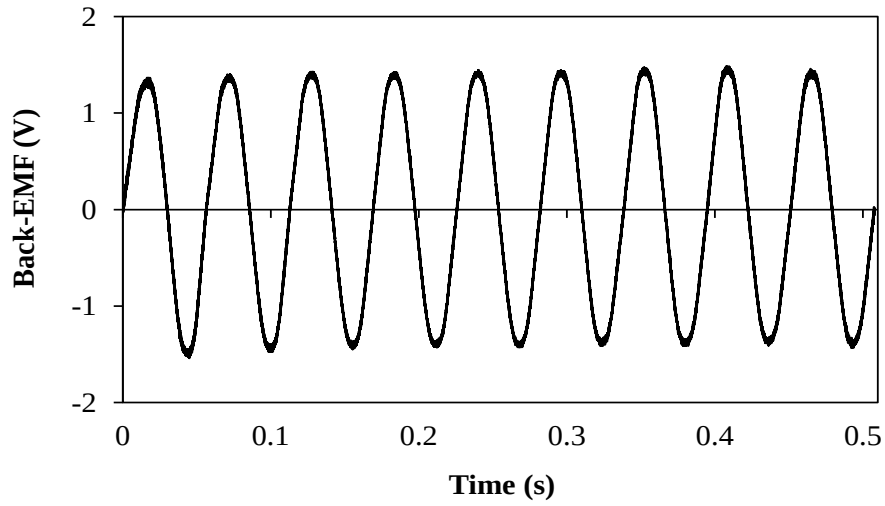

Fig. 3.56 Converted Phase A back-EMF test result at velocity of 500 mm/s.

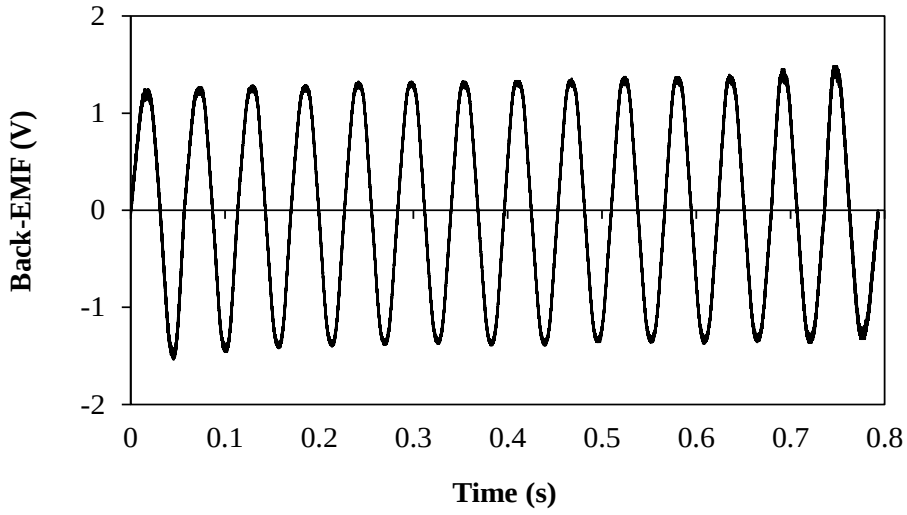

Fig. 3.57 Converted Phase B back-EMF test result at velocity of 500 mm/s.

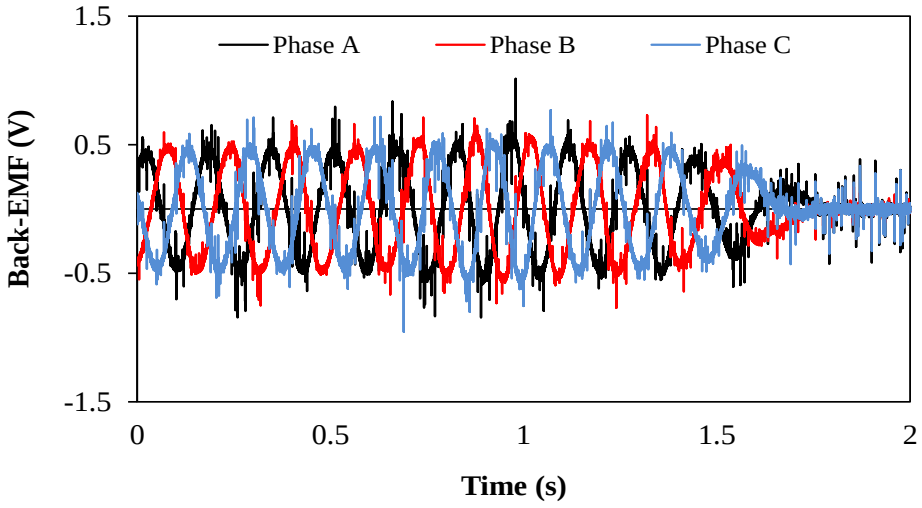

Fig. 3.58 Original 3-phase back-EMF test results made at Zhejjang University.

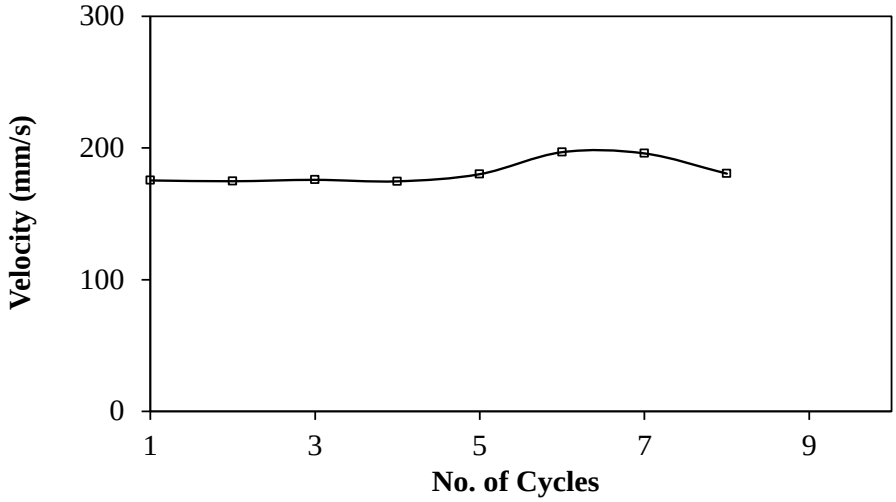

Fig. 3.59 Variation of velocity of 3-phase back-EMF waveform test.

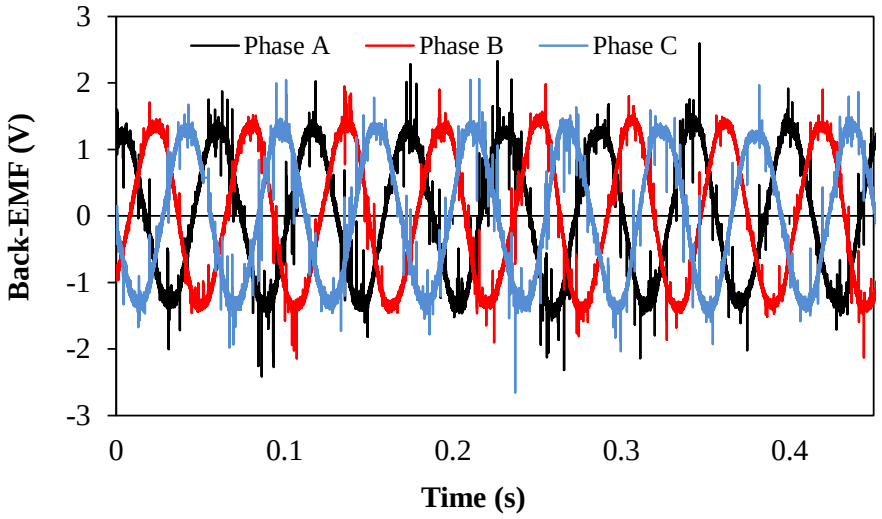

Fig. 3.60 Converted 3-phase back-EMF test results at velocity of 500 mm/s.

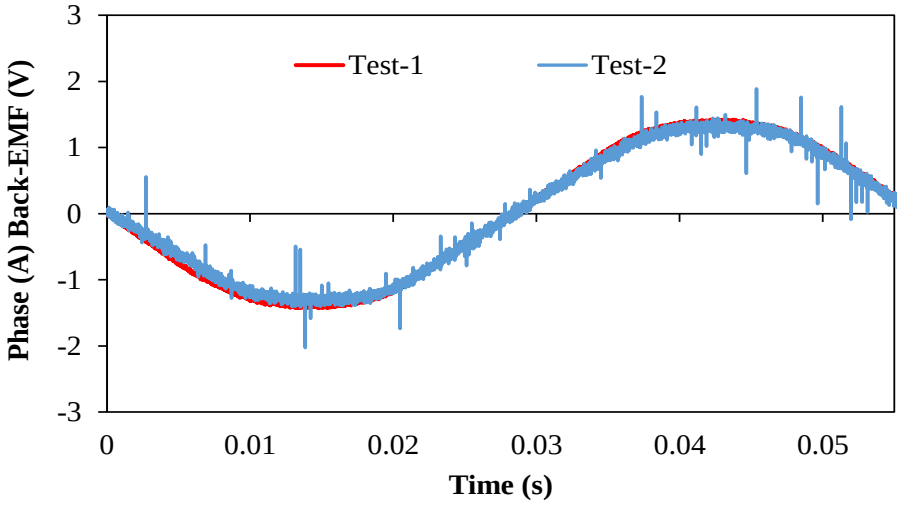

Fig. 3.61 Comparison of measured phase A back-EMFs at velocity of 500 mm/s (Test-1: company test, Test-2: University test).

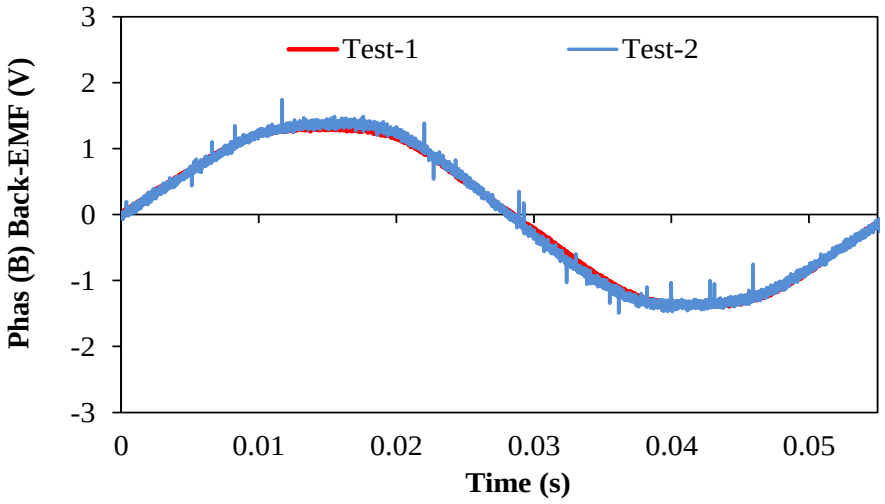

Fig. 3.62 Comparison of measured phase B back-EMF at velocity of 500 mm/s (Test-1: company test, Test-2: University test).

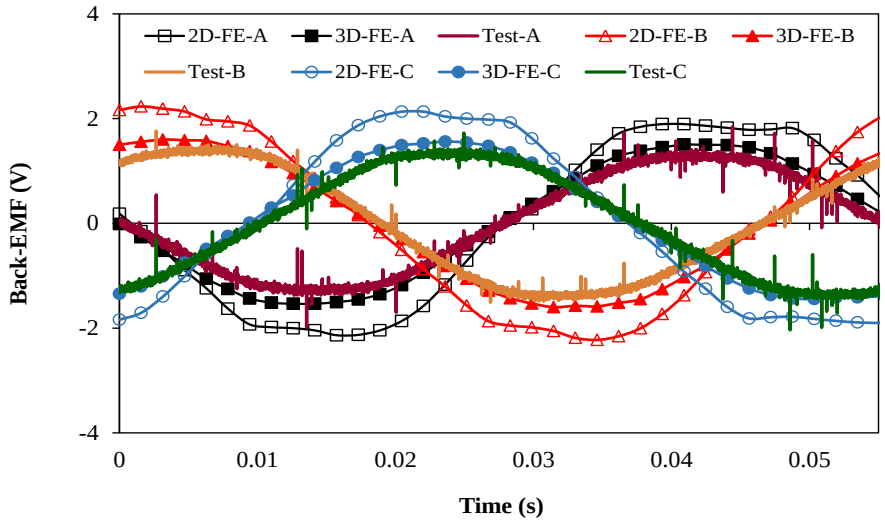

Fig. 3.63 Comparison of 2D-3D FE and test results at velocity of 500 mm/s.

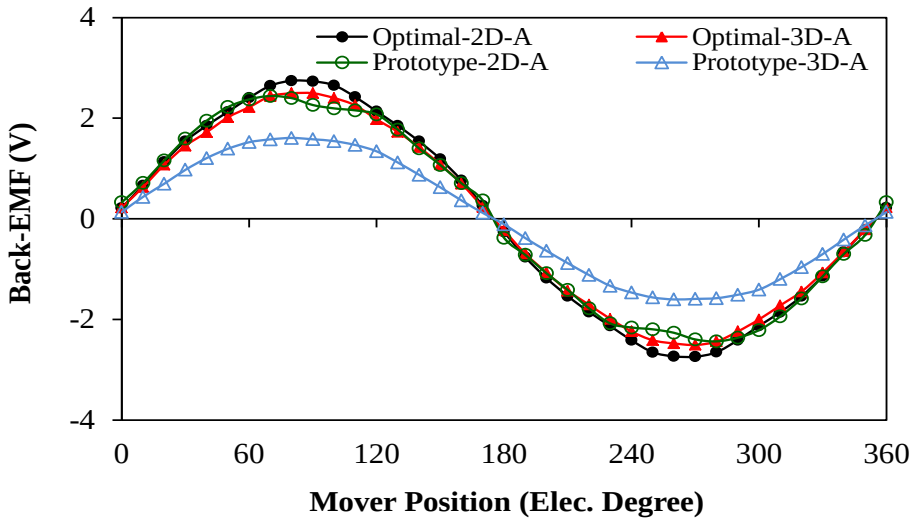

Fig. 3.64 Comparison of phase A back-EMFs at velocity of 500 mm/s.

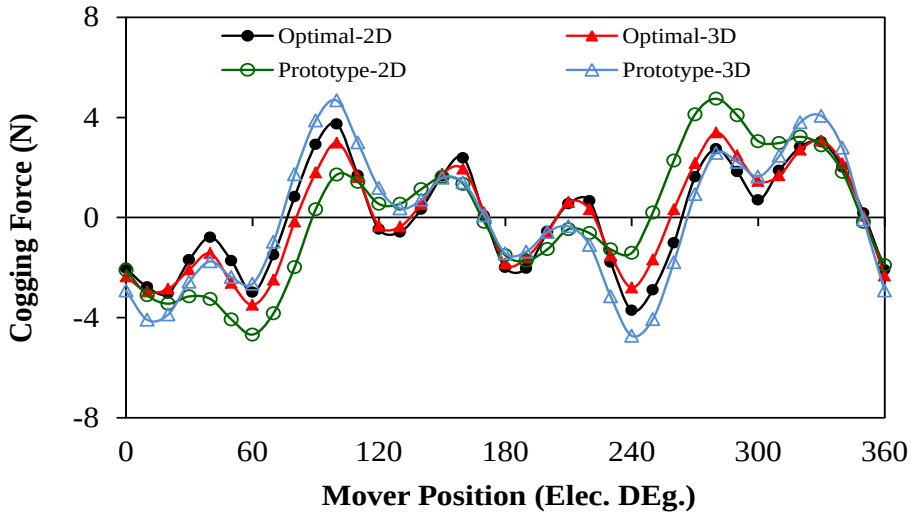

Fig. 3.65 Comparison of cogging forces.

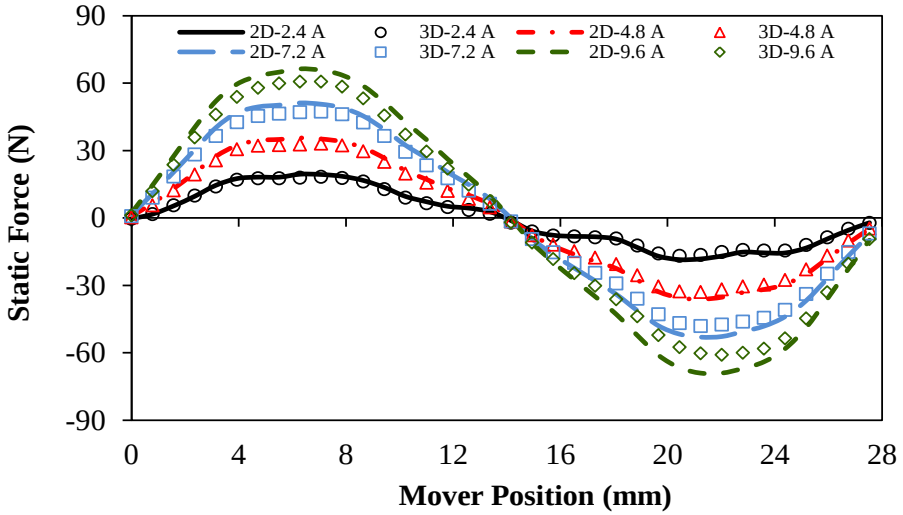

(a) Comparison of static forces (2D-3D models, optimal dimensions)

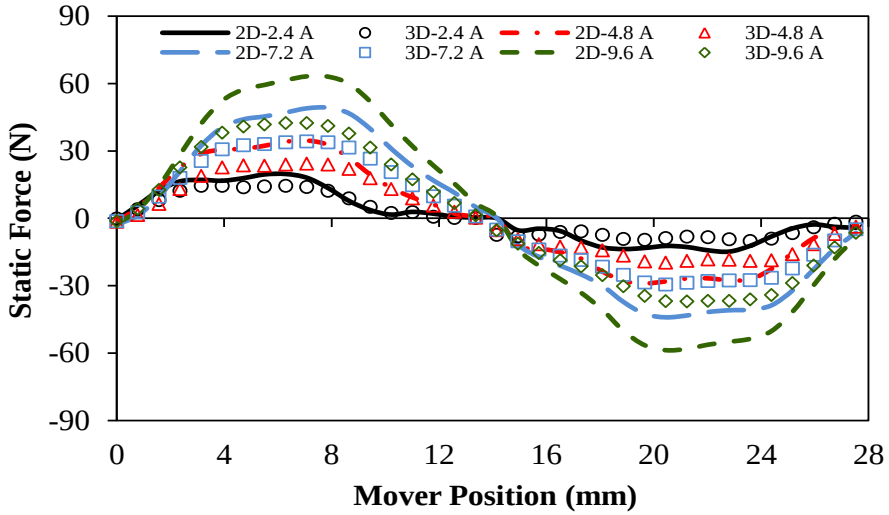

(b) Comparison of static forces (2D-3D models, prototype dimensions)

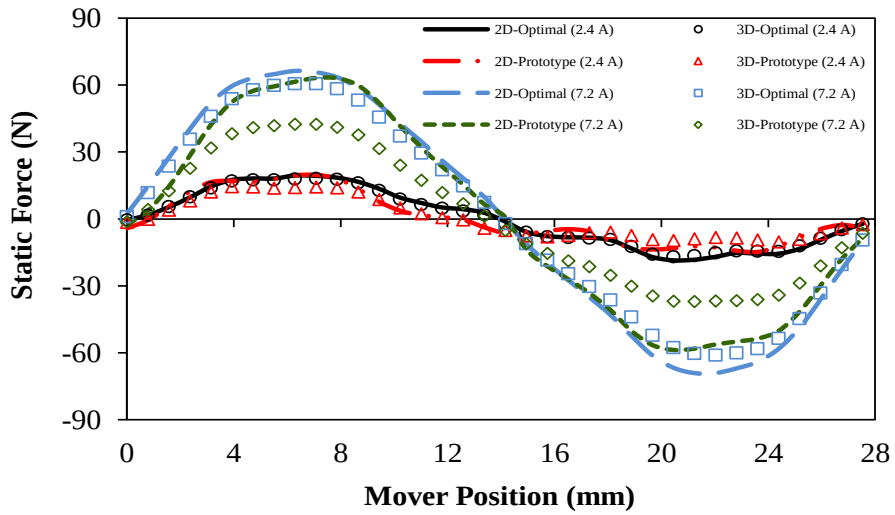

(c) Comparison of static forces (2D-3D models with optimal and prototype dimensions).

Fig. 3.66 Comparison of static forces.

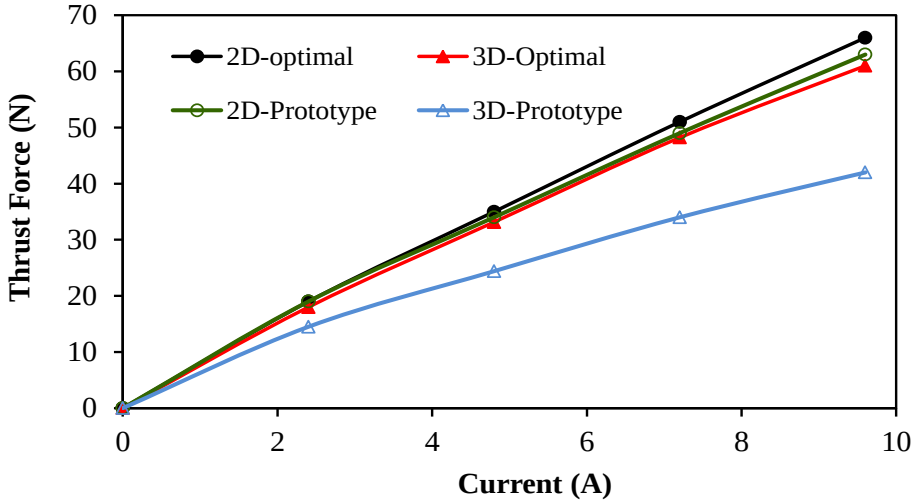

Fig. 3.67 Variation of thrust forces with current.

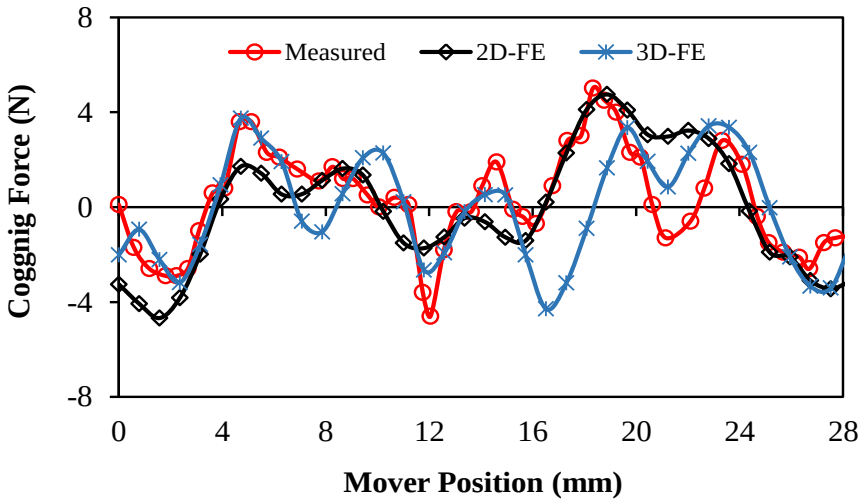

Fig. 3.68 Comparison of measured and FE predicted cogging forces.

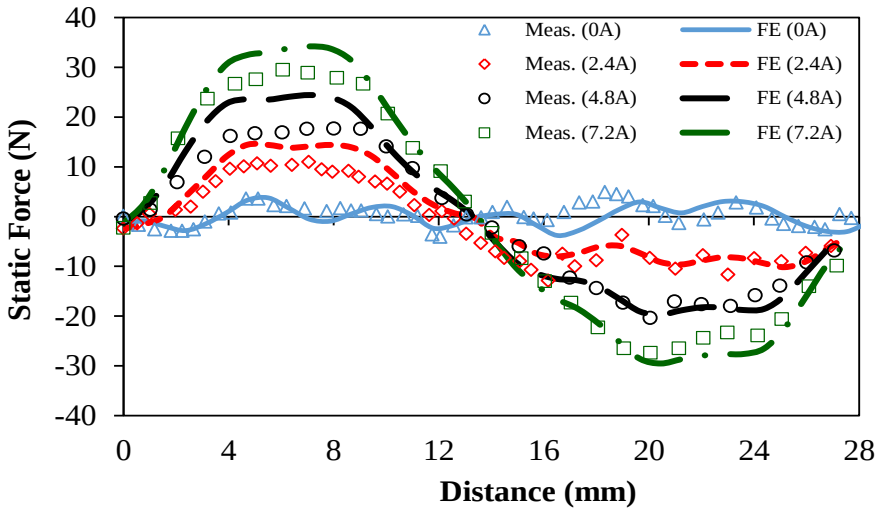

Fig. 3.69 Comparison of measured and 3D FE predicted static thrust forces.

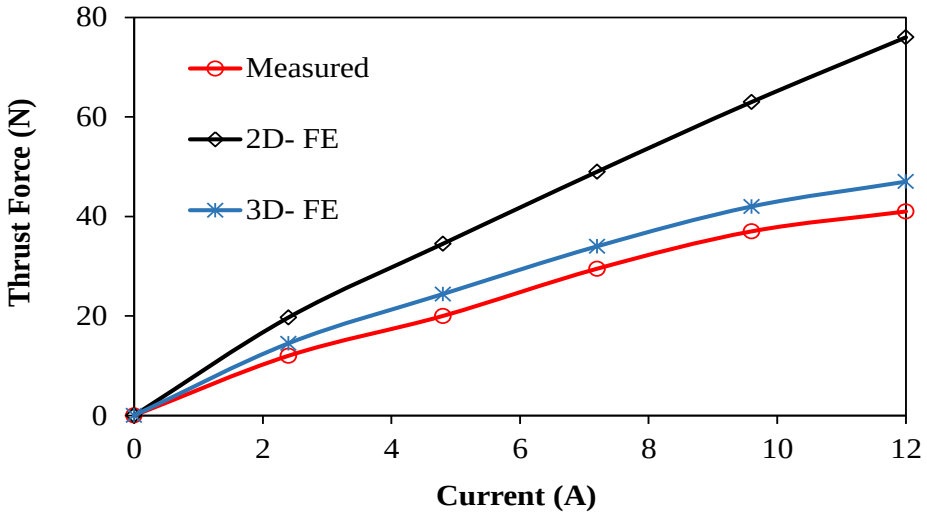

Fig. 3.70 Comparison of measured and FE predicted thrust force variations with current.

Table 3.5 Optimal and prototype dimensions (mm)

Items	Optimal	Prototype
Air gap 1 length	1	1.1
Air gap 2 length	1	1.35
Stator 1 back-iron thickness	2.8	11.635
Tooth tip	10.6	13.48
Tooth width	5.43	5.22
PM width	23.6	23.55
PM height	3	2.9
Stator 2 back-iron thickness	3.8	7.8
Stator 1 axial length	25	25
Mover axial length	25	52
Stator 2 back-iron axial length	25	41
PM axial length	25	25

3.11 Summary

A novel PS-FRPM linear machine has been developed in this chapter. With constant current density, total machine height and active length conditions, the machine optimization is carried out. In order to investigate the influence of the longitudinal end effect on the electromagnetic performance of the PS-FRPM linear machine a virtual periodic model has been employed to compare with the practical model. It is shown that the longitudinal end effect has an obvious impact on the machine performance, particularly on the cogging force and the asymmetries of magnet circuit and associated parameters. Furthermore, PS-FRPM linear machines with different mover pole numbers were designed, optimized, and compared. It is found that the highest back-EMF and thrust force capability can be obtained when the mover pole number is less than the stator slot number by one. Additionally, the impact of the cross-coupling on the PM flux linkage and d- and q-axis inductances has been highlighted. Moreover, flux weakening control strategy is applied to the proposed machine. It is observed that the machine has a wide constant power region. Moreover, the risk of PM demagnetization is assessed. It is realised that the proposed machine has the advantage of good demagnetization withstand capability. Finally, a prototype of the machine is built and tested to validate the FE results.

Chapter4. Novel Partitioned Stator (PS) Permanent Magnet (PM) Tubular Machines

4.1 Introduction

PM linear machines have been introduced with three main topologies, i.e. planar machines including single- and double-sided, three phase and single phase short stroke tubular machines, as mentioned in Chapter 1. However, among these topologies, PM tubular machines have become the most prevalent in literature, since end-winding effect and net attractive force between the stator and the mover do not exist in such topologies [WAN12], [WAN05], [ZYL99]. With regard to the mover construction, tubular PM machines could have either iron movers or magnet movers [KAN12]. Considering the position of magnets, SPM with radial magnetization and IPM with axial magnetization in tubular PM machines have been manufactured [WAN99], [WAN04], [ASH10], [CLA95]. Moreover, SPM tubular machines can be constructed as external or internal PM tubular machine [WAN01].

The interest of applying the idea of SFPM machines to tubular machines has been emerged during the last decade. Due to the fact that SFPM machines have both excitation sources on the stator with a rotor being made of iron only. Thus, with this structure, the heat dissipate problem, which exists in the mover-magnet PM tubular machines can be eliminated [WAN08a], [WAN08b], [AMA05].

The SFPM tubular machines have the advantage of a simple mover structure. However, the slot area would be reduced when having both magnets and windings on the stator. Thus, the machine electrical loading will be restricted, and consequently, the machine force density will be limited. Also, the permanent magnet demagnetization withstand capability will be reduced. Hence, in order to overcome this compromise between the magnets and the windings, the idea of the partitioned stator permanent magnet (PS-PM) machine has been proposed in [ZHU14], [DAV15], [WU15], [ZHU16], [WU16], in which the windings are located in one stator and the magnets are placed on the other stator, while the mover is made only of iron. In Chapter 3 such idea has been adapted to planner linear machine. It has been found that the proposed machine has the merit of high electrical and magnetic loading leading to high thrust force capability. Hence, in order to investigate the advantage of the PS-PM machine with tubular configuration, PM tubular machines based on the concept of the PS-PM machine are developed in this chapter. Two novel partitioned stator PS-PM tubular

machines, i.e. partitioned stator interior permanent magnet (PS-IPM) and partitioned stator surface permanent magnet (PS-SPM) tubular machines are designed. The machine structures and operation principles are described. In addition, both machines have been optimized for maximum thrust force. Besides, the influence of leading design parameters on the machine performances is investigated. Moreover, PS-SPM and PS-IPM tubular machines having different mover pole number are designed, analysed and compared, in order to investigate the effect of rotor pole number on the machines performances.

4.2 Machines Configurations and Operation Principles

Fig. 4.1 shows cross-sections of the two proposed machines, while 3D-views are illustrated in Fig. 4.2. It can be observed that the machines have one mover made of iron only and two stators. The outer stator comprises the phases windings (A1, A2, B1, B2, C1 and C2), while the magnets are placed on the inner stator (i.e. mounted on the inner stator surface for SPM topology and buried in the inner stator iron for IPM topology). The machine specifications are listed in Table 4.1. The operation principle of the introduced machines can be demonstrated based on Fig. 4.3. It should be mentioned that although the PMs provide constant flux the value and the direction of this flux would vary with the mover position. When the mover is on position (a), the flux linkage will reach its maximum positive value, and it becomes zero after 90 electrical degrees movement, position (b). Then, the flux linkage reaches the maximum negative value on position (c), i.e. when it moves an additional 90 electrical degrees. On position (d), which indicates 240 electrical degrees mover displacement from position (a), the flux linkage of the armature windings is zero. The interaction between the PM flux and the armature current flux on load condition produces thrust force.

Table 4.1 Design parameters of proposed tubular machines

Items	PS-SPM/PS-IPM
Number of phases	3
Number of mover poles within the stator	5
Number of stator slots	6
Outer stator slot pitch	23.6mm
Inner stator slot pitch	23.6mm
Mover pole pitch	28.32mm
Outer air gap radial length (*GO*)	1 mm
Inner air gap radial length (*GI*)	1 mm
Outer stator radius (*OSR*)	35mm
Inner stator radius (*ISR*)	13.5mm
Mover radius (*MR*)	19.5mm

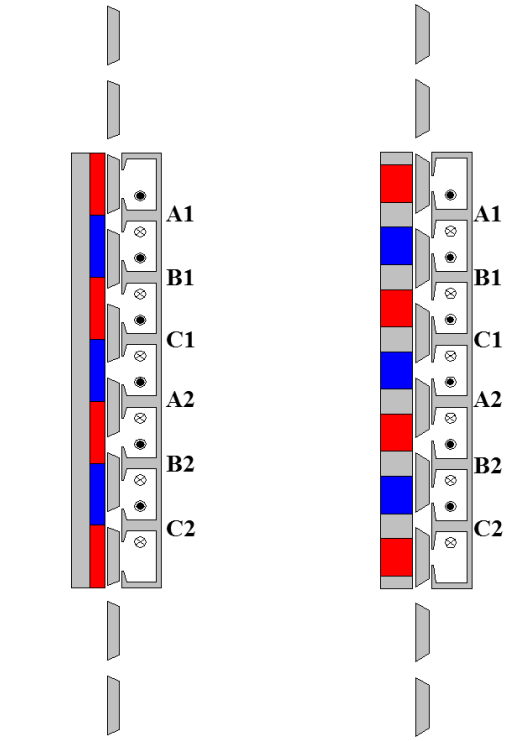

Fig. 4.1 Axisymmetric cross-sections of proposed tubular machines.

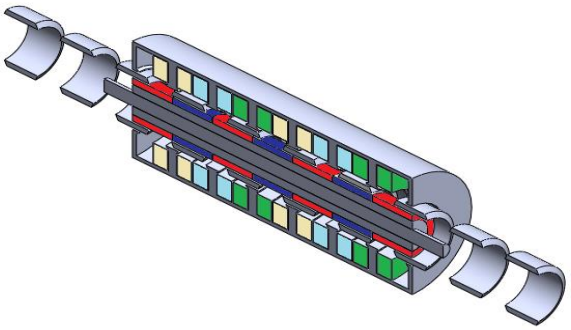

(a) Tubular PS-SPM

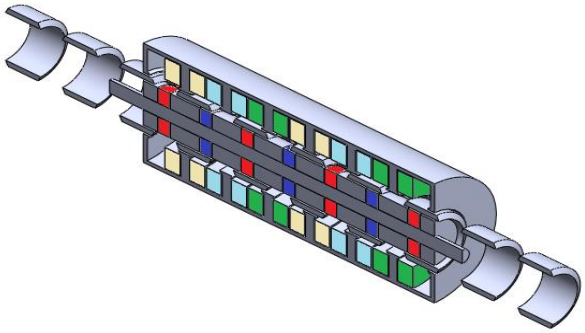

(b) Tubular PS-IPM

Fig. 4.2 3-D views of proposed tubular machines.

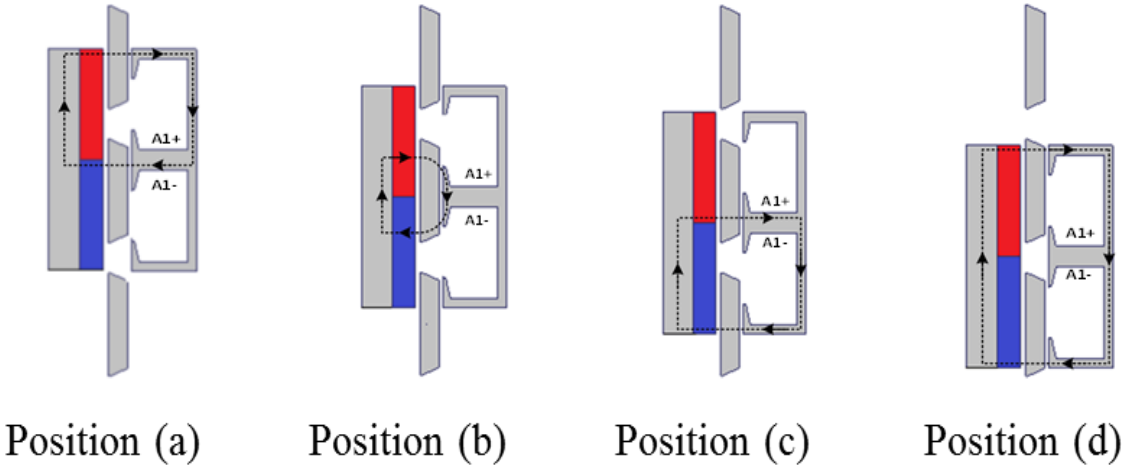

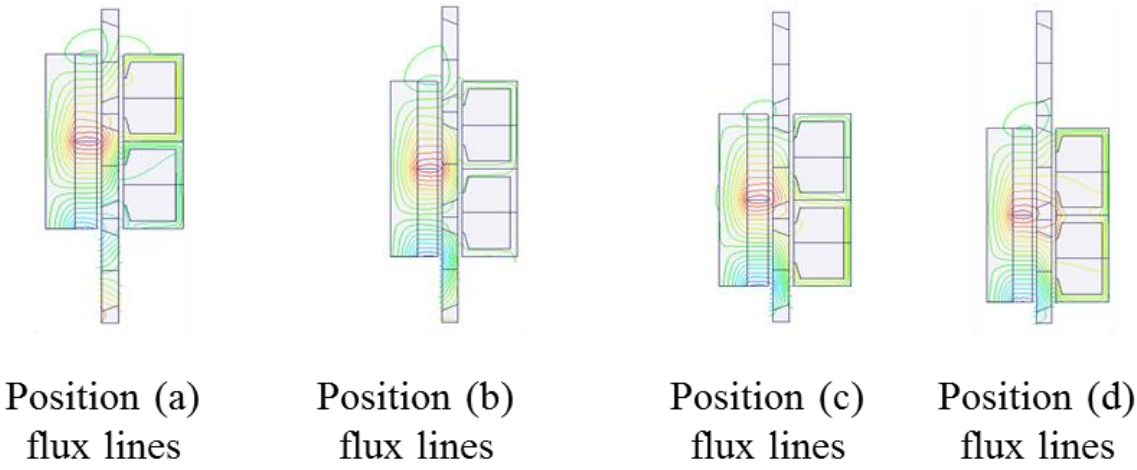

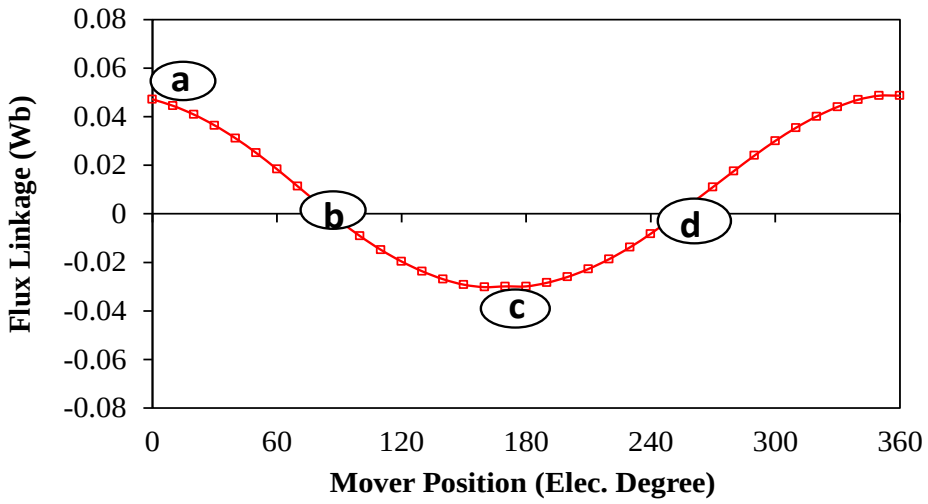

Fig. 4.3 Schematics of operation principle for proposed tubular machines, and phase A flux linkage.

4.3 Machine Optimizations

With the aim of maximum thrust force, both proposed machines have been optimized by utilizing FE method based on GA. It should be mentioned that the outer stator radius, the machine active length and the current density are kept to be fixed for both proposed machines during the optimization process. The definitions of the optimization variables, which include the split ratio (*SR*), the mover radial thickness (*MTH*), the outer mover width ratio (*OMWR*), the inner mover pieces width ratio (*IMWR*), the outer stator tooth width ratio (*OSTWR*), the outer stator slot opening ratio (*OSSOR*), the magnet width ratio (*PMWR*) and the outer stator back iron thickness ratio (*OSBITHR*) for both machines, and the inner stator back iron thickness ratio (*ISBITHR)* for PS-SPM machine topology, are detailed in Table 4.2 and shown in Fig. 4.4

Table 4.2 Varied parameters for optimization in PS-SPM and PS-IPM

Symbol	Definition
SR	$\frac{MGO}{TMH}$
MGO	$ISR + GI + MTH + 0.5GO$
PMWR	$\frac{PMW}{ISPP}$
ISBITHR	$\frac{ISBITH}{ISR}$ $(for\ SPM\ only)$
OSBITHR	$\frac{OSBITH}{OSTH}$
OSTWR	$\frac{OSTW}{OSSP}$
OMWR	$\frac{OMW}{MPP}$
IMWR	$\frac{IMW}{MPP}$

In Table 4.2, *MTH, OMW, IMW* and *MPP* represent the mover radial thickness, outer mover width, inner mover width, and the mover pole pitch, respectively. *OSTW, ISR, OSSOW, OSBITH, ISBITH, OSTH and OSSP* refer to the outer stator tooth width, the inner stator radius, the outer stator slot opining, the outer stator back iron thickness, the inner stator back iron thickness, the outer stator total height and the outer stator slot

pitch, respectively. *PMW* and *ISPP* are the magnet width and the inner stator pole pitch, *GI* and *GO* are denoted as the inner and the outer air-gap radial lengths, respectively.

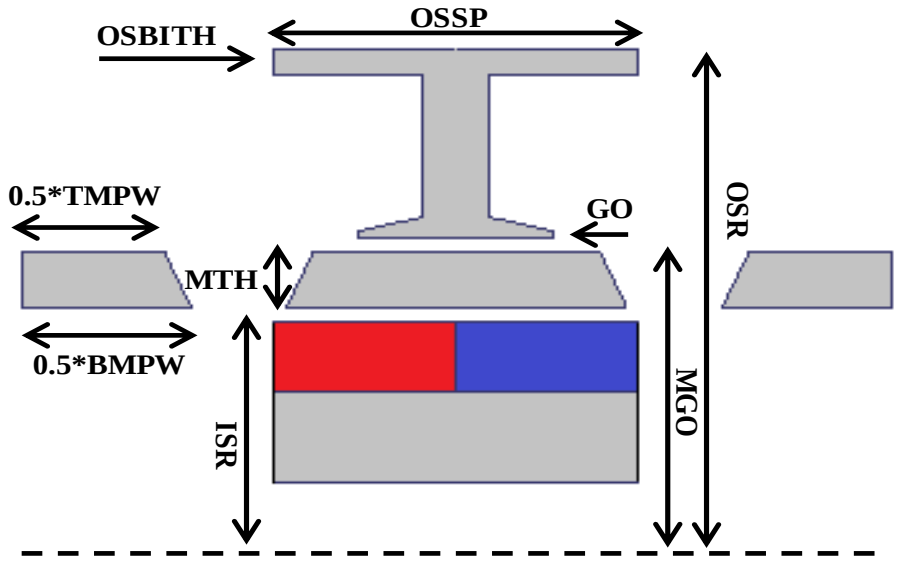

(a) Tubular PS-SPM

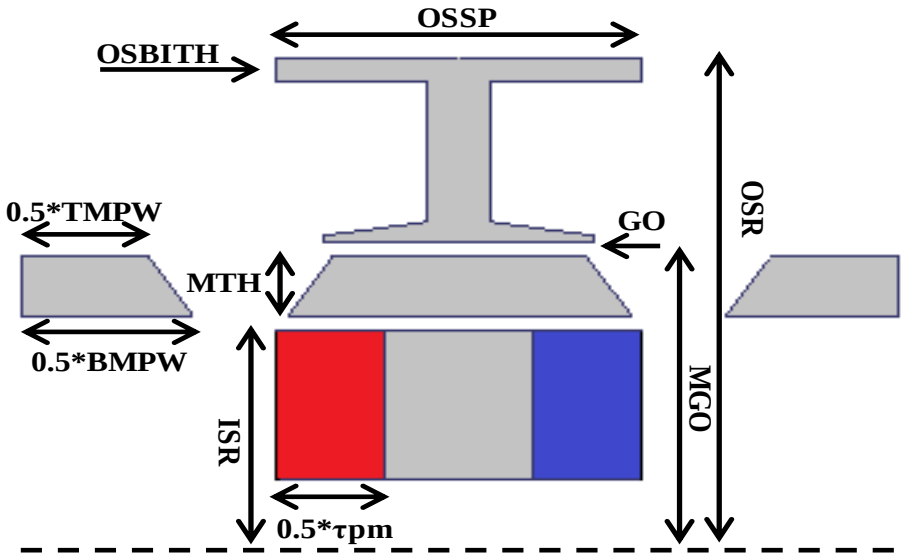

(b) Tubular PS-IPM

Fig. 4.4 Leading design parameters of both proposed machines.

The initial, restriction and optimal values of the optimization variables for both machines are listed in Table 4.3.

Table 4.3 Initial, restriction and optimal values of optimization parameters

	Initial		Restriction		Optimal	
	PS-SPM	PS-IPM	PS-SPM	PS-IPM	PS-SPM	PS-IPM
SR	0.5		[0.3, 0.7]		0.6	
OMWR	0.6		[0.1, 0.9]		0.657	0.557
IMWR	0.7		[0.1, 0.9]		0.783	0.785
OSTWR	0.2		[0.1, 0.35]		0.18	
OSSOR	0.75		[0.05, 0.3]		0.464	0.261
OSBITHR	0.125		[0.1, 0.3]		0.13	0.12
ISBITHR	0.7	-	[0.2, 0.8]	-	0.68	-
PMWR	1	0.3	[0.6,1]	[0.1, 0.8]	1	0.6
MTH	3 mm		[2, 5]		4mm	4.5mm

4.4 Influence of Main Design Parameters on Machines Performances

The effect of the major design parameters on the proposed machine performances has been investigated by utilizing 2D-axisymmetry FE based on the globally optimized designs shown in Table 4.3. Fig. 4.5 depicts the variation of the average thrust force as a function of the split ratio. It is obvious that the average thrust force for both machines increases as the split ratio increases from 0.35 to 0.6, and then it will gradually decrease. The optimal value of the split ratio which results in maximum thrust force is 0.6 for both machines.

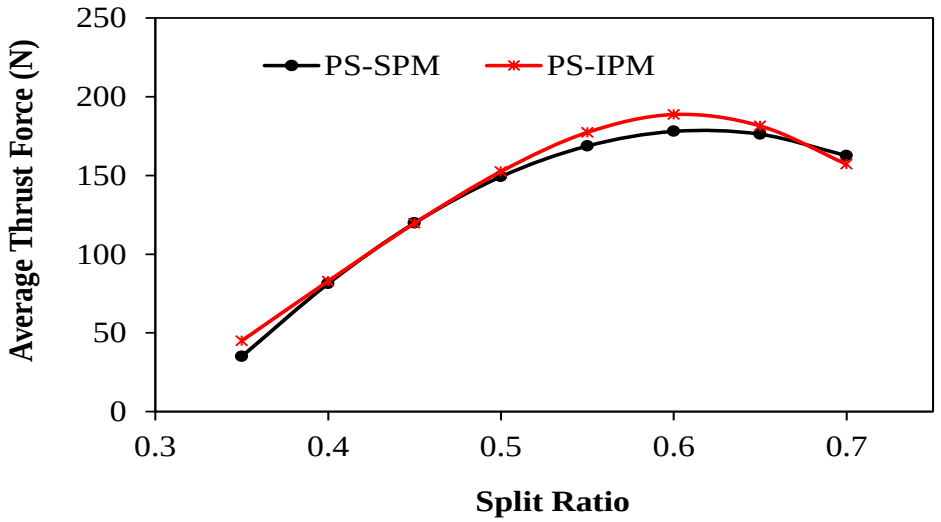

Fig. 4.5 Average thrust force vs. split ratio.

The characteristics of the average thrust force versus the mover radial thickness for both machines are plotted in Fig. 4.6. It is apparent that each machine has its own optimal radial mover thickness for maximum average thrust force. The optimal radial

mover thickness for the PS-IPM is 4.5mm, while it is 4mm for the PS-SPM. The PS-IPM topology is more sensitive to the mover radial thickness than the PS-SPM.

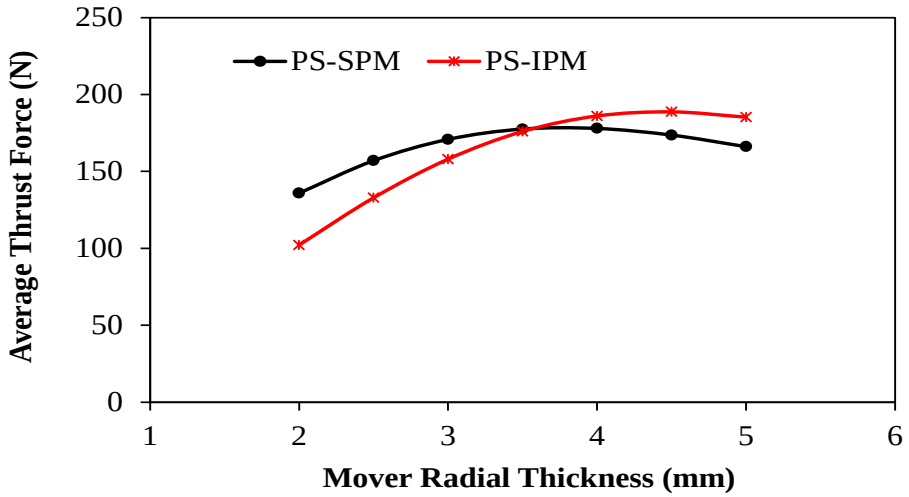

Fig. 4.6 Average thrust force variation vs. mover radial thickness.

According to [WAN99], the magnet width to pole pitch (*PMW/ISPP*) ratio is one of the main design parameters, which has a significant influence on the tubular PM machine performance. Hence, the variation of the average thrust force of the proposed machines as a function of *PMW/ISPP* ratio is shown in Fig. 4.7. It can be noted that the capability of the PS-SPM machine for maximum thrust force increases with the increase of the *PMW/ISPP* ratio which agrees reasonably with [WAN99]. On the other hand, the average thrust force of the tubular PS-IPM machine increases firstly with the increase of this ratio and then decreases due to the saturation. The optimal *PMW/ISPP* ratio of the PS-IPM machine is much smaller than that of the PS-SPM machine.

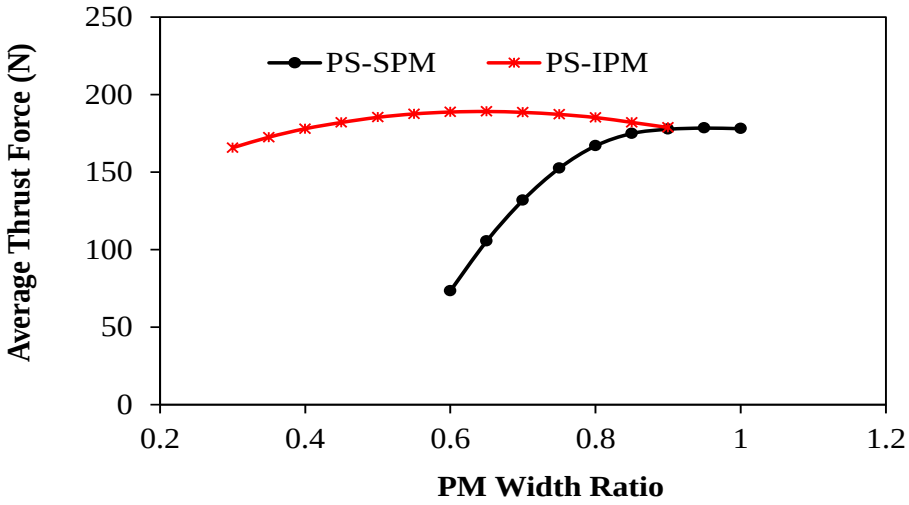

Fig. 4.7 Variation of the average thrust force with magnet width to pole pitch ratio (current density = 6A/mm^2 rms).

As a function of *OMWR* and *IMPR*, the variation of the average thrust force for both proposed machines is displayed in Fig. 4.8 and Fig. 4.9, respectively. It can be seen that although both machines exhibit almost the same sensitivity to these ratios, the optimal *OMWR* and *IMWR* of the PS-SPM are 0.657 and 0.783, and for PS-IPM are 0.557 and 0.785, respectively.

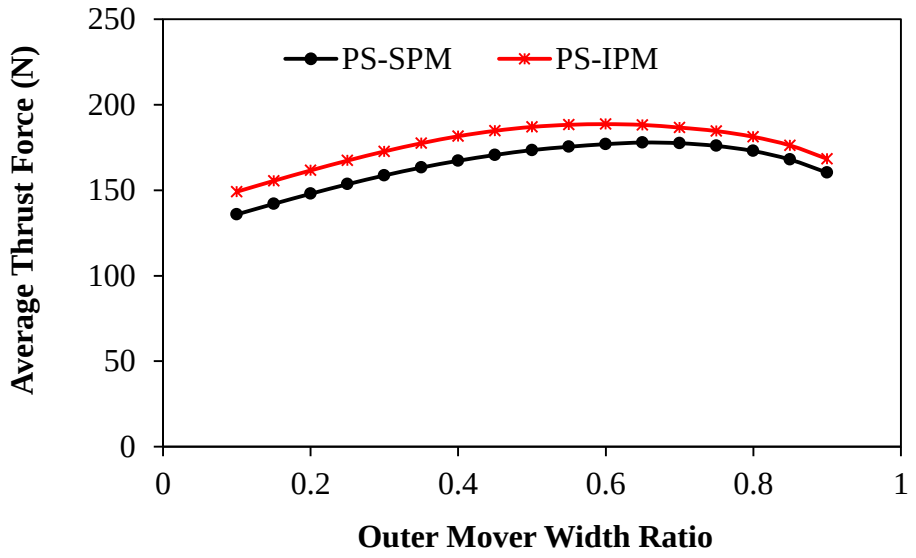

Fig. 4.8 Average thrust force vs. outer mover width ratio.

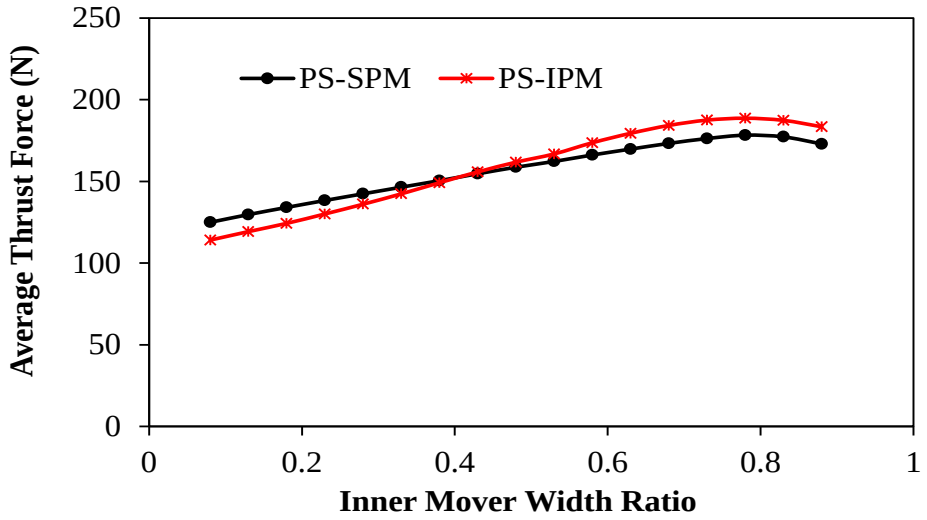

Fig. 4.9 Average thrust force vs. inner mover width ratio.

Fig. 4.10, Fig. 4.11 and Fig. 4.12 show the variations of the average thrust force versus *OSTWR*, *OSBITHR* and *OSSOR*, for both machines, respectively. It is evident that the average thrust force for both machines increases as the *OSTWR* varies from 0.08 to 0.18 where the machines have the maximum thrust force. After that the capability of

the thrust force for both machines will be decreased with the increase of *OSTWR*. This is due to the slot area being decreased, which consequently diminishes the machine electrical loading. Similarly, the average thrust forces of the proposed machines increase when *OSBITHR* is changed from 0.05 to 0.14, and after that, the machine thrust force capabilities will be decreased with the increase of this ratio, for the same reason mentioned above. On the other hand, the average thrust force for both machines changes slightly with the variation of *OSSOR*, although each machine has its optimal ratio in which the machine exhibits its maximum average thrust force.

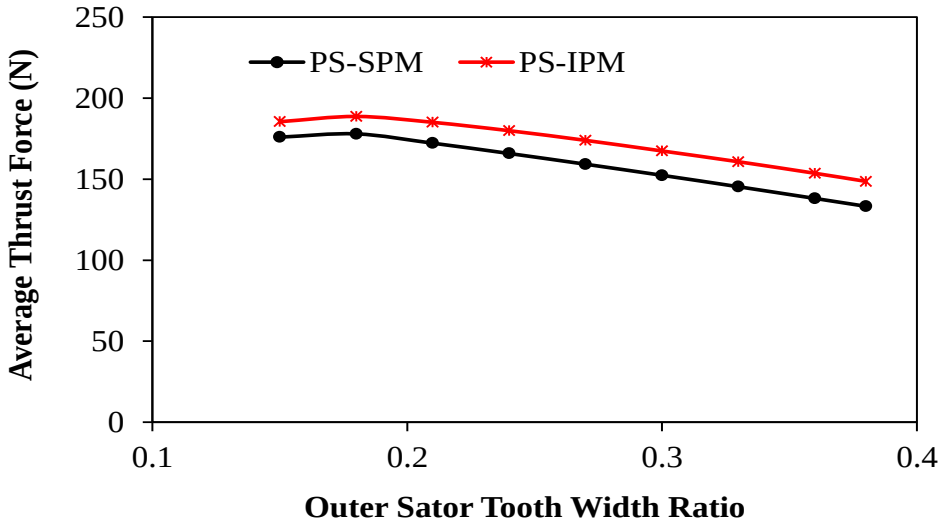

Fig. 4.10 Average thrust force vs. outer stator tooth width ratio.

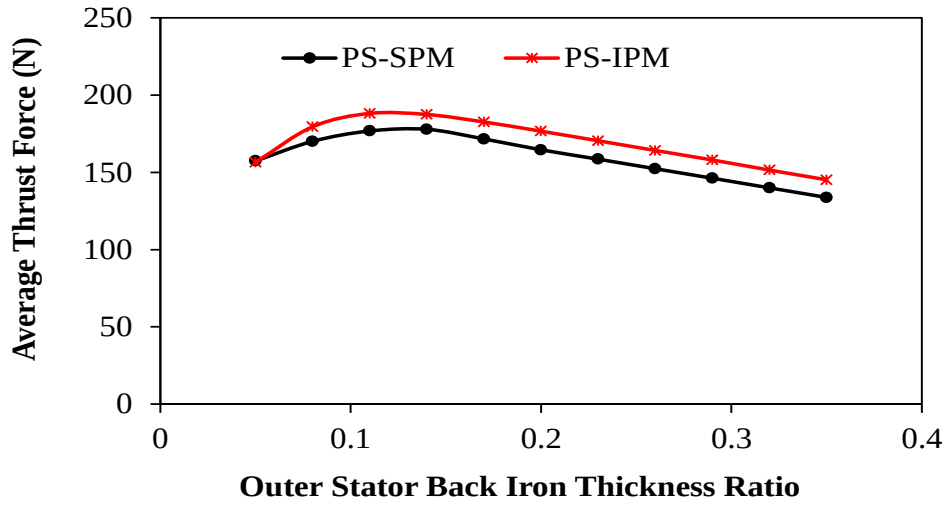

Fig. 4.11 Average thrust force vs. outer stator back iron thickness ratio.

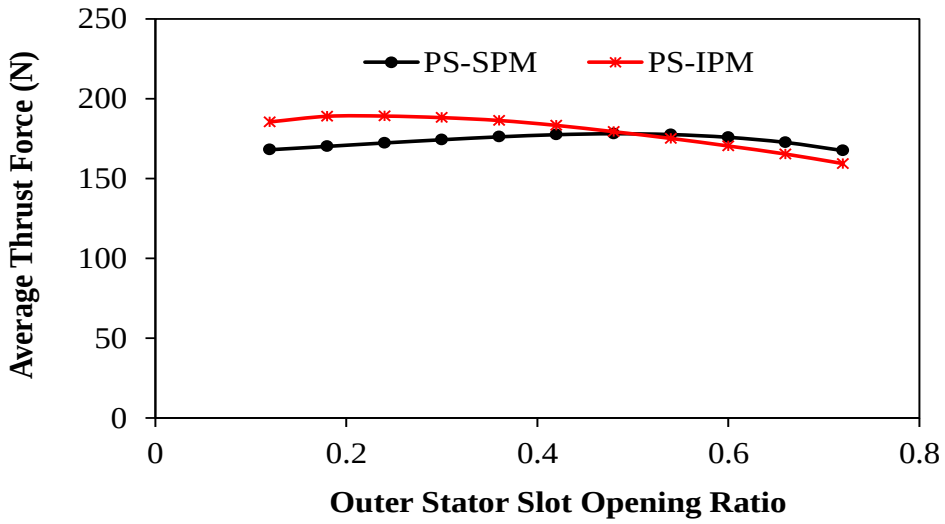

Fig. 4.12 Average thrust force vs. outer stator slot opening ratio.

4.5 Influence of Magnet Width to Pole Pitch Ratio on Cogging Force

In this section, the effect of *TPM/ISPP* ratio on the cogging force of two proposed machines is investigated. The variation of cogging force with TPM/ISPP ratio for PS-SPM and PS-IPM tubular machines is shown in Fig. 4.13. It can be seen that when the ratio changes from 0.3 to 0.8, the cogging force of the PS-IPM tubular machine will be increased, and when the ratio is larger than 0.9 the cogging force will be sharply reduced. For the PS-SPM tubular machine the optimal value of the TPM/ISPP ratio for minimum cogging force is 0.9. Fig. 4.14 and Fig. 4.15 display the cogging force versus mover position when the mover moves one pole pitch with different TPM/ISPP ratios for PS-SPM and PS-IPM tubular machine, respectively.

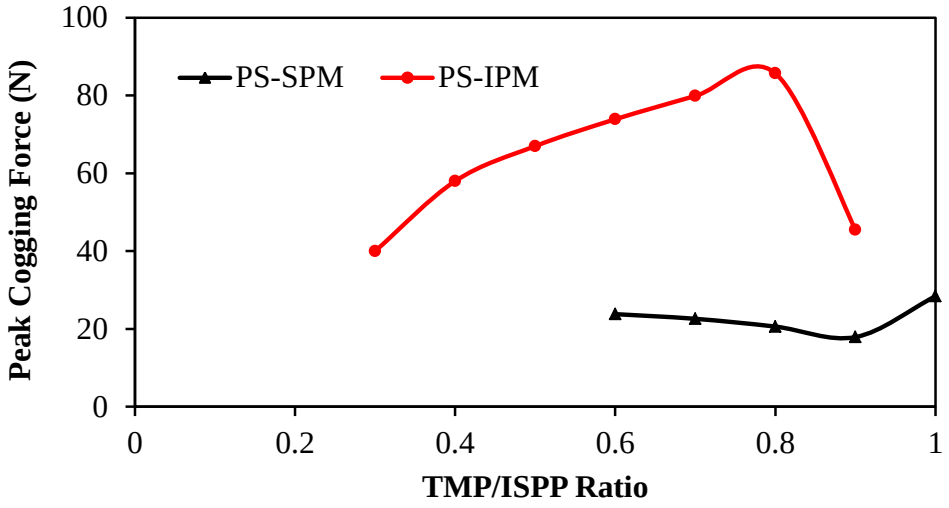

Fig. 4.13 Peak cogging force vs. magnet width to pole pitch ratio.

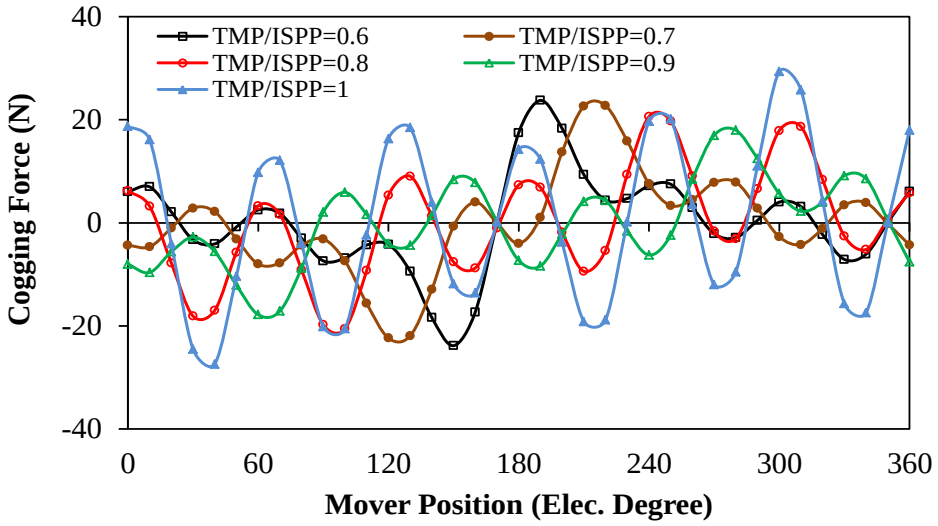

Fig. 4.14 Cogging force waveforms of PS-SPM tubular machine with different TPM/ISPP ratios.

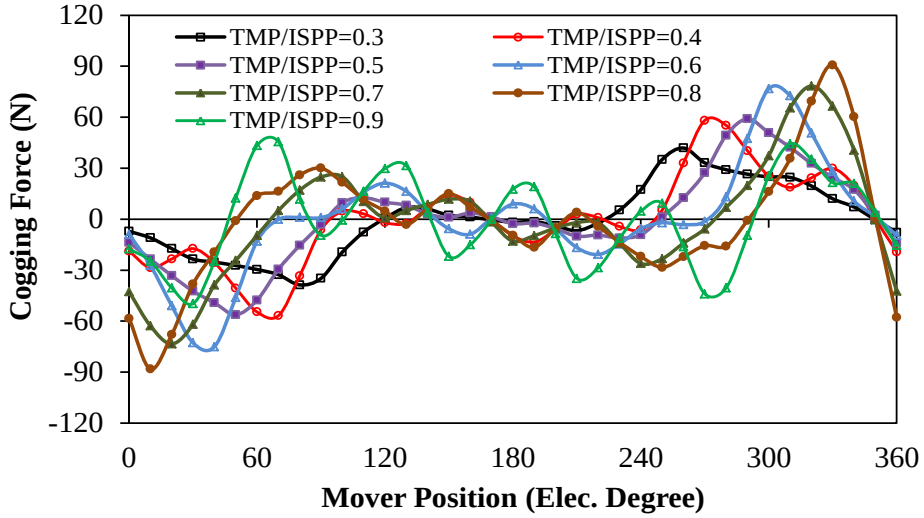

Fig. 4.15 Cogging force waveforms of PS-IPM tubular machine with different TPM/ISPP ratios.

4.6 PS-PM Tubular Machines Having Different Mover Pole Number

The influence of stator/mover pole number combination of the proposed machines in terms of back-EMF and thrust force will be investigated. It is worth noting that by applying (3.17) and (3.18) many stator/mover pole number combinations can be obtained. However, in this investigation, the stator slot number is considered to be fixed to 6, while the mover pole number will be determined by (3.18). It should be mentioned that winding configurations of the designed machines can be determined by coil-EMF vectors as explained in Chapter 3. The combinations of the designed machines for both proposed machines are 6/4, 6/5, 6/7, 6/8, 6/10, 6/11, 6/13, 6/14. It should be emphasized that all leading design specifications, which are given in Table 4.1, except the mover pole number, are kept the same for all designed machines. Moreover, all machines have been globally optimized for maximum thrust force with the same optimization conditions that were detailed in section 4.3. The initial and the optimal values of the varied parameters during the optimization for PS-SPM tubular machines are listed in Table 4.4, whilst Table 4.5 lists those for PS-IPM tubular machines. It can be noted that all PS-SPM tubular machines have similar SR and OSBITHR. Additionally, 6/11, 6/13 and 6/14 have almost the same MTH and OSTWR. On the other hand, MTH decreases as the mover pole increase, while OSSOR increases with the higher mover pole number. Furthermore, SR of all PS-IPM tubular machines is 0.6, except that of 6/11, which equals to 0.58. In addition, TMPWR of all PS-IPM decreases with the increase of the mover pole number, however 6/11, 6/13 and 6/14 have the same value, about 0.22.

Table 4.4 Initial and optimal values of the all PS-SPM machines

Optimization variables	Symbol	Initial value	Optimal values							
			6/4	6/5	6/7	6/8	6/10	6/11	6/13	6/14
Split ratio	*SR*	0.5	0.59	0.6	0.6	0.6	0.6	0.58	0.59	0.59
Mover thickness	*MTH*	2.5	4.46	4	3.3	3.2	3.1	3	3	3
Top mover pieces width ratio	*TMPWR*	0.6	0.474	0.657	0.775	0.77	0.71	0.56	0.64	0.53
Bottom mover pieces width ratio	*BMPWR*	0.7	0.78	0.783	0.549	0.47	0.54	0.775	0.64	0.53
Outer stator teeth width ratio	*OSTWR*	0.2	0.11	0.12	0.11	0.1	0.1	0.1	0.1	0.1
Outer stator slot opening ratio	*OSSOR*	0.75	0.45	0.464	0.64	0.65	0.65	0.7	0.7	0.7
Outer stator back iron thickness ratio	*OSBITHR*	0.15	0.113	0.13	0.11	0.12	0.12	0.11	0.11	0.12
Inner stator back iron thickness ratio	*ISBITHR*	0.6	0.7	0.68	0.76	0.82	0.84	0.8	0.8	0.88

Table 4.5 Initial and optimal values of the all PS-IPM machines

Optimization variables	Symbol	Initial value	Optimal values							
			6/4	6/5	6/7	6/8	6/10	6/11	6/13	6/14
Split ratio	*SR*	0.5	0.6	0.6	0.6	0.6	0.6	0.58	0.6	0.6
Mover thickness	*MTH*	2.5	4.5	4.5	3.4	3.2	4.4	4.3	3.6	3.8
Top mover pieces width ratio	*TMPWR*	0.6	0.6	0.58	0.51	0.44	0.23	0.22	0.22	0.22
Bottom mover pieces width ratio	*BMPWR*	0.7	0.8	0.79	0.82	0.84	0.89	0.85	0.87	0.87
Outer stator teeth width ratio	*OSTWR*	0.2	0.13	0.18	0.17	0.13	0.12	0.14	0.14	0.13
Outer stator slot opening ratio	*OSSOR*	0.75	0.3	0.26	0.57	0.76	0.75	0.76	0.76	0.74
Outer stator back iron thickness ratio	*OSBITHR*	0.15	0.13	0.12	0.12	0.12	0.11	0.11	0.12	0.1
Inner stator back iron thickness ratio	*ISBITHR*	0.6	0.47	0.6	0.58	0.44	0.78	0.8	0.76	0.6

4.6.1 Comparison of PS-SPM Tubular Machines Performances

The electromagnetic performance of all PS-SPM tubular machines will be compared in terms of open circuit and on load performances. Open circuit flux distributions for all PS-SPM machines, when the mover moves over one pole pitch, are shown in Fig. 4.16. Flux linkages of phase A for the PS-SPM tubular machines are compared in Fig. 4.17. The highest flux linkage can be achieved by the 6/5 machine, while the lowest one is obtained by the 6/14 machine. It should be mentioned that all machines exhibit asymmetric flux linkage because of the longitudinal end effect. Fig. 4.18 shows the phase A back-EMF for the aforementioned machines. Obviously, the 6/5 machine has the highest back-EMF among the other machines. However, the 6/4 machine shows higher flux linkage than the 6/7 machine, the latter has higher back-EMF, due to the higher frequency and higher winding factor. Owing to the same reasons above, the 6/11 machine exhibits higher back-EMF than the 6/10 machine. The open circuit forces for

the PS-SPM tubular machines are illustrated in Fig. 4.19. It can be seen that the machines with odd mover pole numbers produce less cogging force than the machines with even mover pole numbers, since they have a smaller goodness factor. It can be noted that the 6/4 machine exhibits the highest cogging force among all the machines. On the contrary, the 6/13 machine shows the lowest cogging force.

Thrust forces as a function of mover position are illustrated in Fig. 4.20. Apparently, the 6/5 machine produces the highest thrust force due to the highest back-EMF. The variations of the average thrust force with different q-axis current values for PS-SPM tubular machines are compared in Fig. 4.21. It is obvious that the highest thrust force capability is obtained by the 6/5 machine. In contrast, the lowest thrust force is shown by the 6/14 machine, since it has the lowest back-EMF compared to other machines. In order to investigate the magnet utilisation for all PS-SPM tubular machines, the average thrust force per total magnet volume as a function of q-axis current for each machine is shown in Fig. 4.22. It is clear that both the 6/5 and 6/7 machines have the best magnet utilisation compared to other machines. On the other hand, the lowest magnet utilisation is shown by the 6/13 machine.

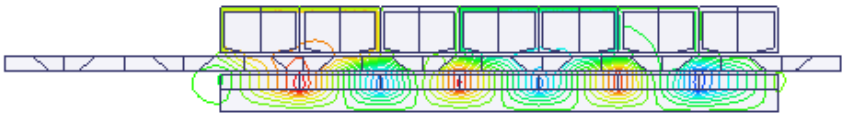

(a) 6/4

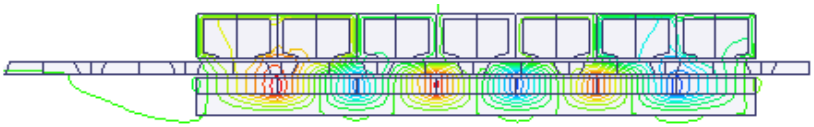

(b) 6/5

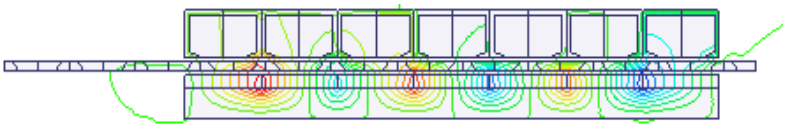

(c) 6/7

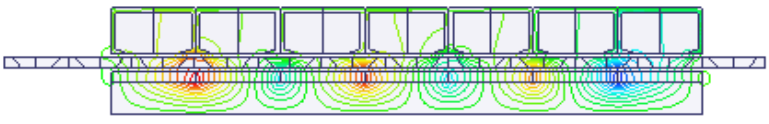

(d) 6/8

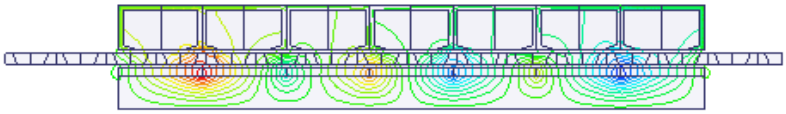

(e) 6/10

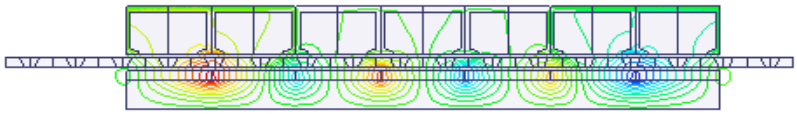

(f) 6/11

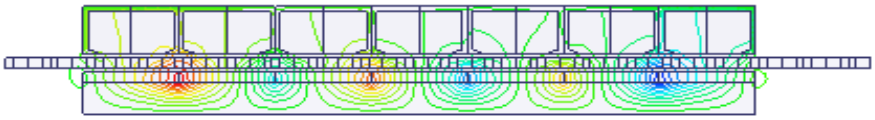

(g) 6/13

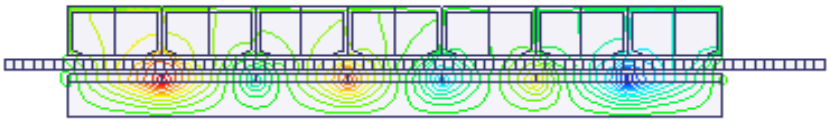

(h) 6/14

Fig. 4.16 Open circuit flux lines distributions in PS-SPM tubular machines having different stator/mover pole number combinations.

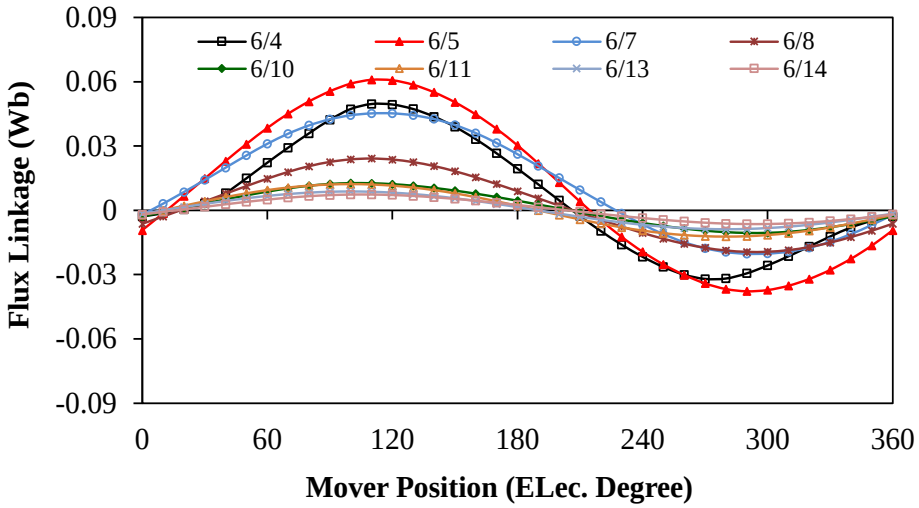

(a) Waveform

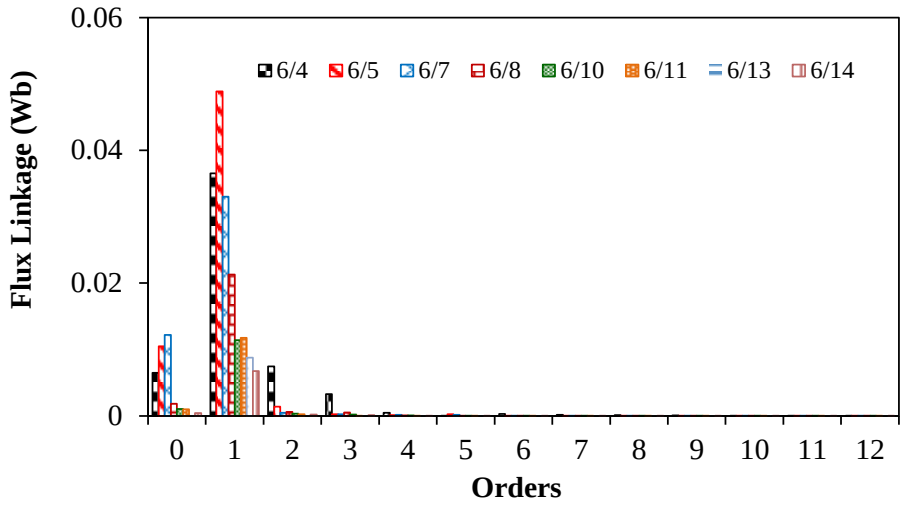

(b) Spectrum

Fig. 4.17 Flux linkage comparison for different stator/mover pole number combinations.

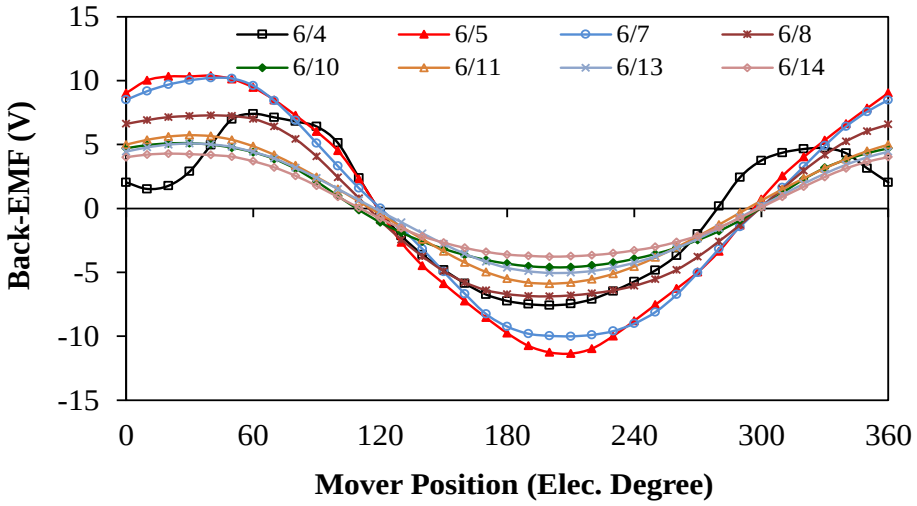

(a) Waveform

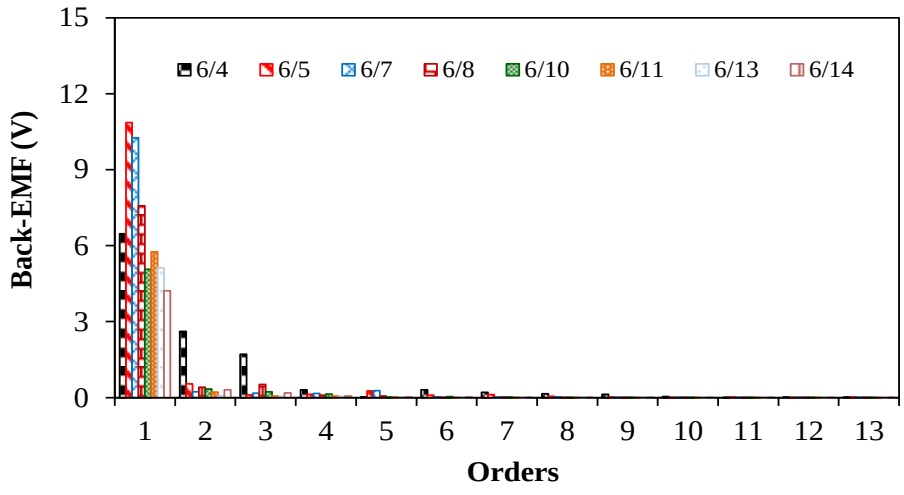

(b) Spectrum

Fig. 4.18 Back-EMF comparison for different stator/mover pole number combinations.

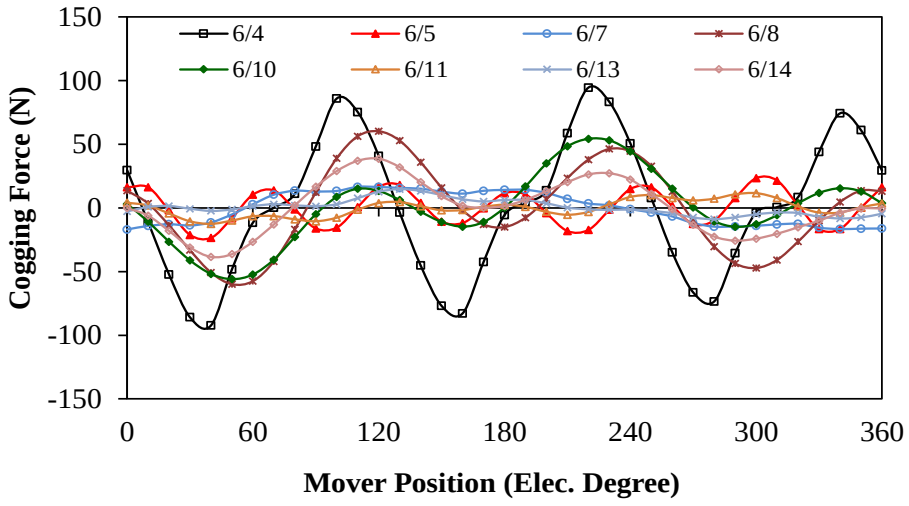

(a) Waveform

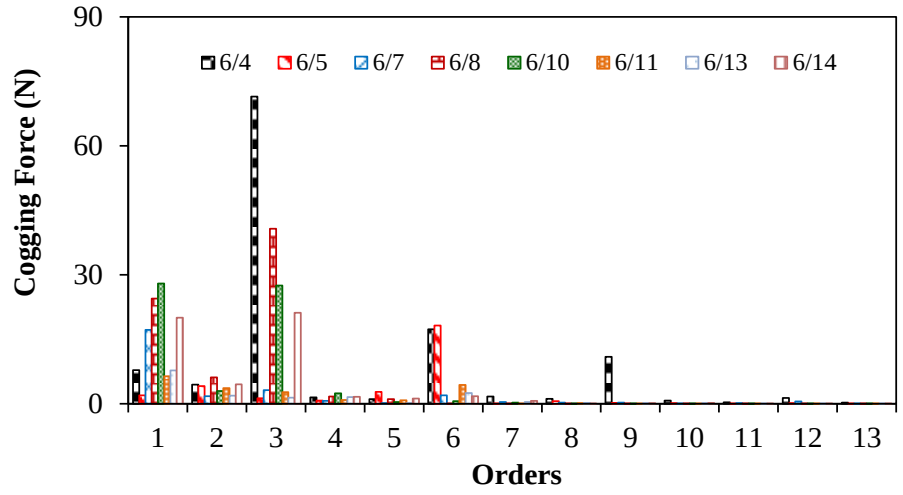

(b) Spectrum

Fig. 4.19 Cogging force comparison for different stator/mover pole number combinations.

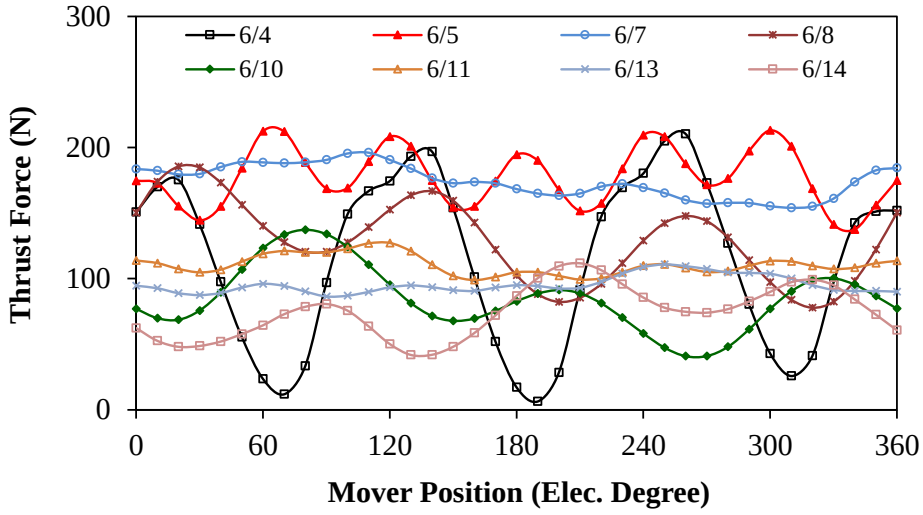

Fig. 4.20 Thrust force comparison for different stator/mover pole number combinations (current density = 6A/mm^2 rms).

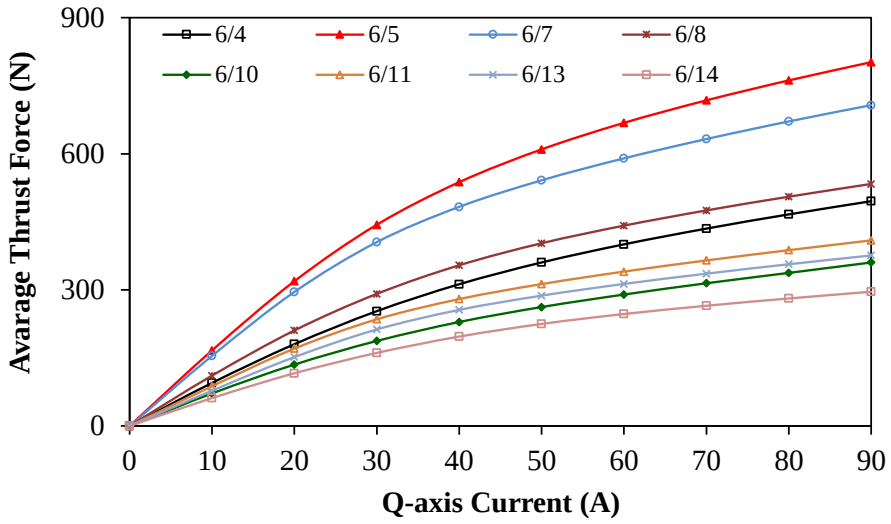

Fig. 4.21 Average thrust force variation with q-axis current for different stator/mover pole number combinations.

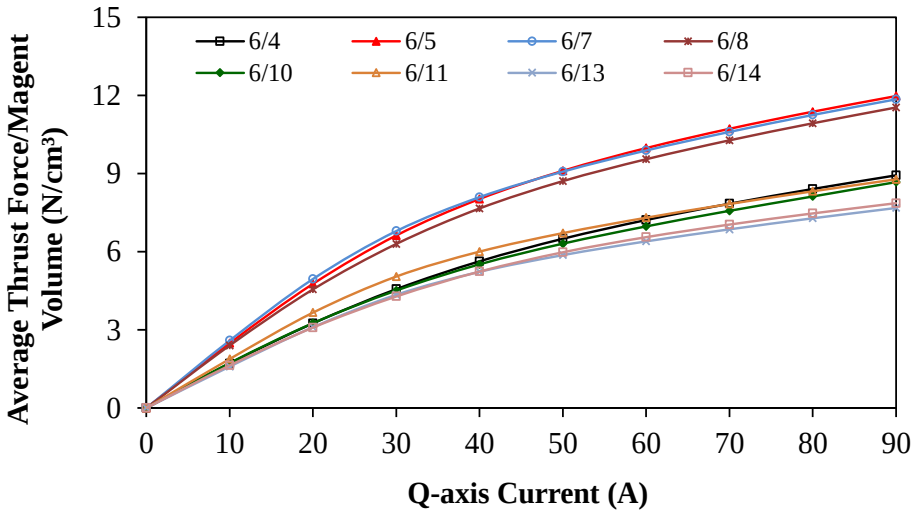

Fig. 4.22 Comparison of magnet utilization for different stator/mover pole number combinations.

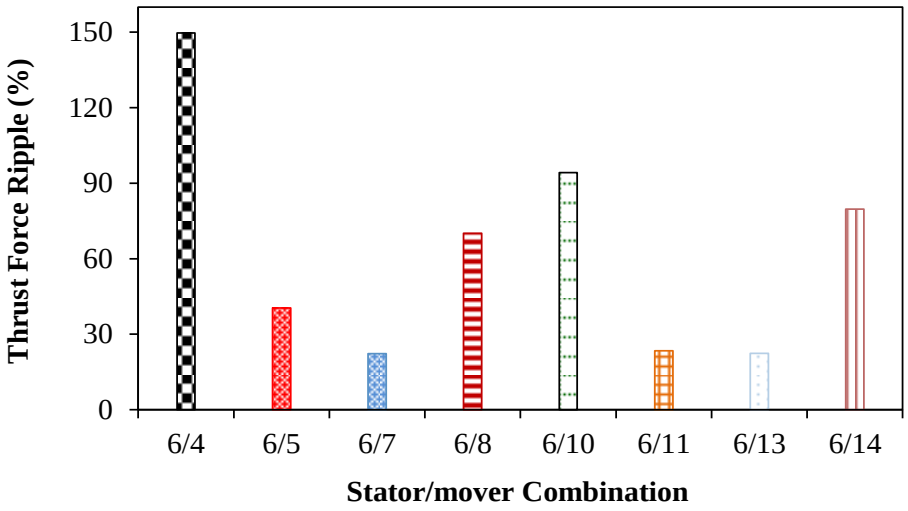

Fig. 4.23 Thrust force ripple for different stator/mover pole number combinations.

Table 4.6 compares the performances of the PS-SPM tubular machines. It can be noted that in term of back-EMF and thrust force, the 6/5 machine exhibits the highest capability among the other machines. However, in terms of force ripple, the 6/7 machine has the lowest thrust force ripple. On the other hand, both the 6/5 and 6/7 machines have similar magnet utilization. Furthermore, even mover pole machines possess higher cogging force, and subsequently higher thrust force ripple compared to the machines with odd mover pole numbers. This is because such machines, i.e. with even mover pole numbers, have a higher goodness factor. Moreover, the odd mover pole number machines have higher winding factor than the even mover pole number machines due to higher pitch factor.

Table 4.6 Summary of PS-SPM tubular machine performances

Items	Stator/ mover combinations							
	6/4	6/5	6/7	6/8	6/10	6/11	6/13	6/14
Flux linkage (fundamental) (Wb)	0.036	0.049	0.033	0.021	0.011	0.011	0.008	0.007
Back-EMF(fundamental) (V)	6.5	10.9	10.3	7.57	5.1	5.75	5.11	4.22
Winding factor	0.5	0.867	0.867	0.5	0.5	0.867	0.867	0.5
Cogging force (peak) (N)	94.56	23.4	16.58	60.3	54.4	11.65	15	38.7
Average thrust force (N)	114.4	178	174.5	129.6	85	111	95.4	74.4
Thrust force ripple	147%	40%	22%	70%	94%	24%	22.4%	79%
Total magnet volume (cm^3)	55.5	66.99	60.7	46.26	41.57	46.61	48.97	37.65

4.6.2 Comparison of PS-IPM Tubular Machines Performances

The electromagnetic performances of the PS-IPM tubular machines with different mover pole numbers are compared. Fig. 4.24 displays the equipotential flux distributions at no load condition. It can be noted that all machines have similar flux line distribution pattern. Phase A flux linkages of all PS-IPM tubular machines are compared in Fig. 4.25. It is obvious that the 6/5 machine has the highest flux linkage, whilst the 6/14 machine exhibits the lowest flux linkage. Furthermore, it should be mentioned that for both odd and even mover pole number machines, the flux linkage decreases with the increase of mover pole number. Fig. 4.26 compares phase A back-EMFs for all analysed machines. It is worth mentioning that the odd mover pole number machines have higher back-EMF compared to the even mover pole number machines due to the higher winding factor. Moreover, cogging forces of the aforementioned

machines are illustrated in Fig. 4.27. It can be seen that the machines with even mover pole number show higher cogging forces compared to those with odd mover pole numbers because such machines have higher goodness factor. Fig. 4.28 depicts the average thrust force versus the current angle for all PS-IPM tubular machines. It can be seen that the 6/5, 6/11 and 6/13 machines have the highest average force with current angle equals to 10^0 , while the 6/4 machine has its maximum average thrust force when the current angle equal to 20^0. On the other hand, the 6/7, 6/8, 6/10 and 6/14 machines show the maximum thrust force with zero current angle. Thrust forces with mover position for the understudying machines are shown in Fig. 4.29. Apparently, the shape of thrust force for each machine is similar to the cogging force waveform. Hence, it can be concluded that the main thrust force ripple of such machines is caused by the cogging force. As a function of q-axis current the average thrust forces for all machines are illustrated in Fig. 4.30. Obviously, the highest thrust force capability can be achieved by the 6/5 machine, while the 6/14 machine produces the lowest thrust force capability. Moreover, the odd mover pole number machines have higher thrust force capability than the even mover pole number machines. Fig. 4.31 introduces the variation of the average thrust force per total magnet volume with q-axis current. It should be mentioned that the 6/5 machine has the best magnet utilization of all machines. The 6/4 and 6/8 machines show better magnet utilization compared to the 6/11 and 6/13 machines. Finally, in order to investigate the influence of the mover pole number on the PS-IPM machine thrust force ripple, the thrust force ripple percentage, which is calculated by (2.1) for all PS-IPM machines is demonstrated in Fig. 4.32. The lowest thrust ripple can be obtained by 6/11 machine because of the lower cogging force, while the highest thrust force ripple is for the 6/4 machine since it has the highest cogging force.

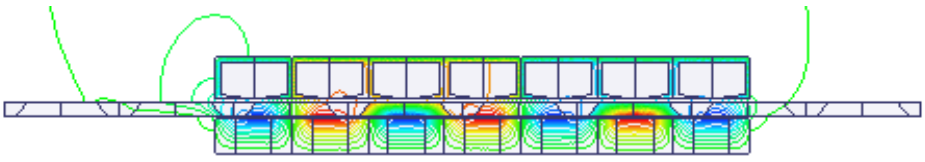

(a) 6/4

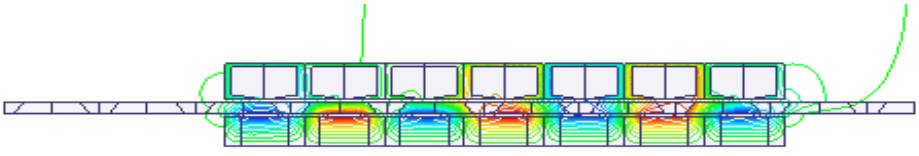

(b) 6/5

(c) 6/7

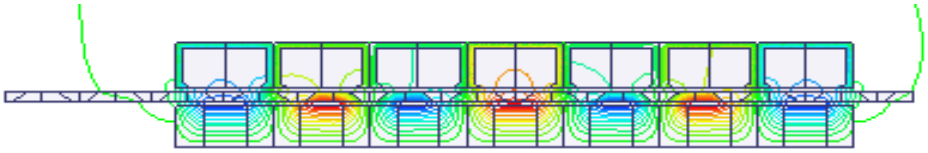

(d) 6/8

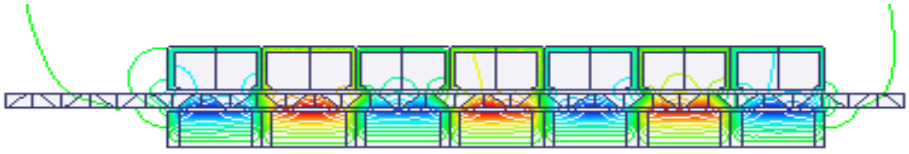

(e) 6/10

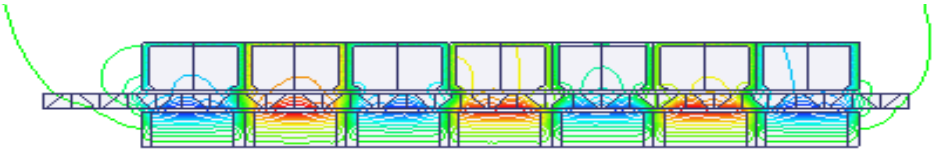

(f) 6/11

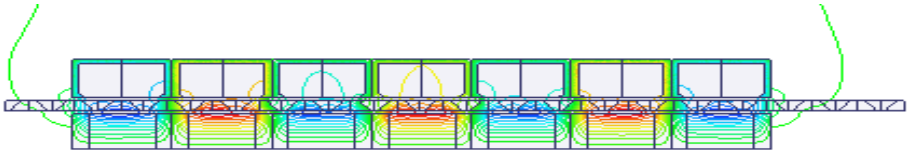

(g) 6/13

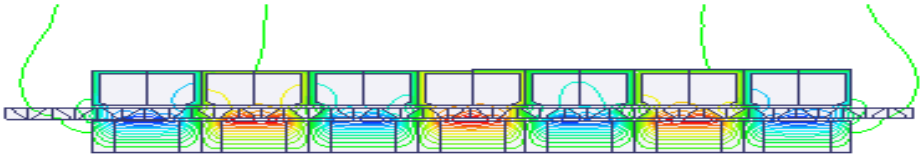

(h) 6/14

Fig. 4.24 Open circuit equipotential flux distribution in PS-IPM tubular machines having different stator/mover pole number combinations.

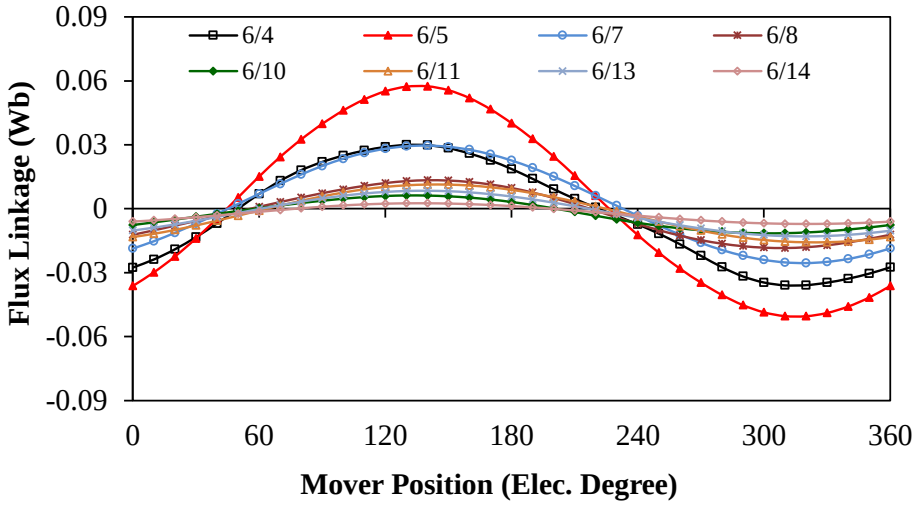

(a) Waveform

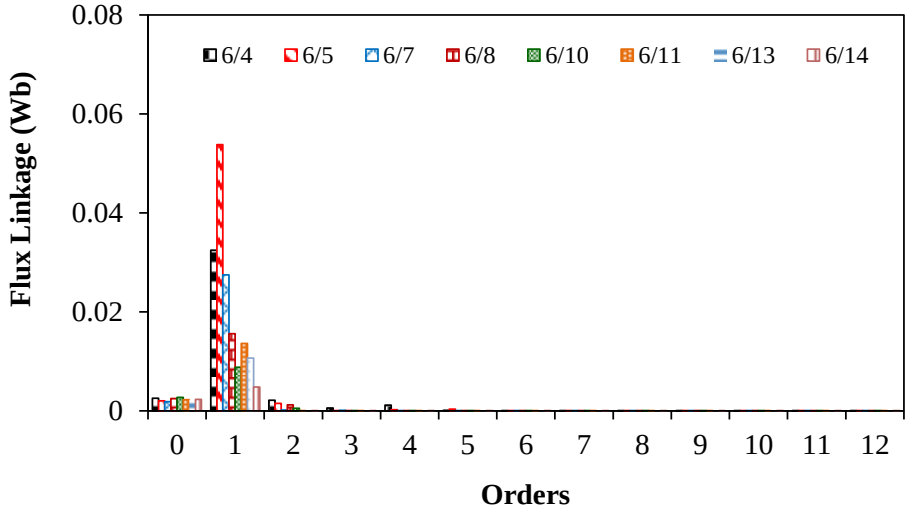

(b) Spectrum

Fig. 4.25 Flux linkage comparison for different stator/mover pole number combinations.

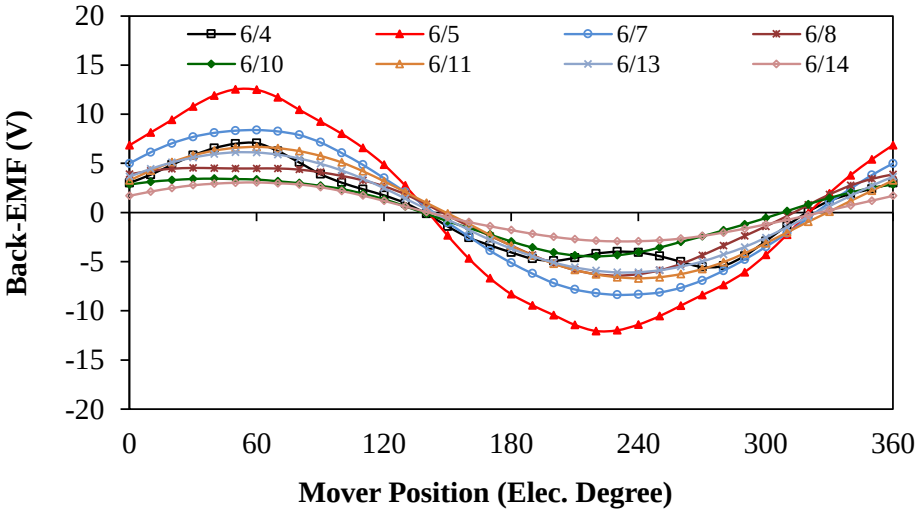

(a) Waveform

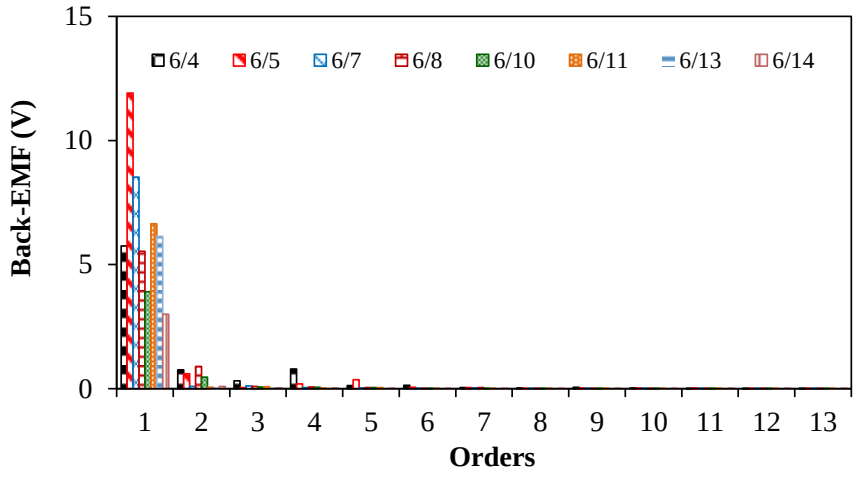

(b) Spectrum

Fig. 4.26 Back-EMF comparison for different stator/mover pole number combinations.

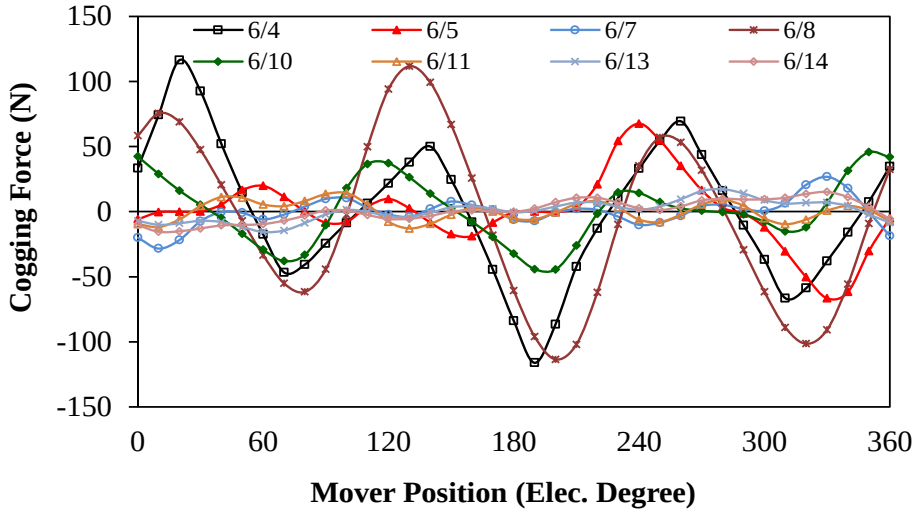

(a) Waveform

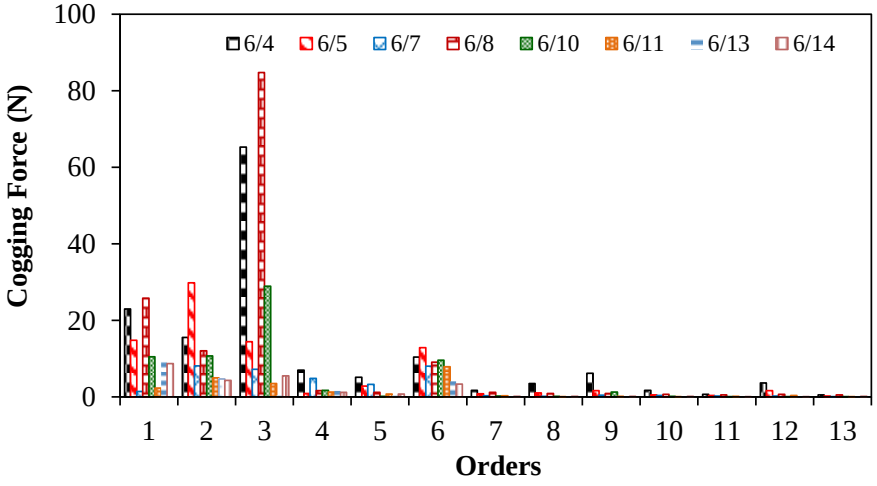

(b) Spectrum

Fig. 4.27 Cogging force comparison for different stator/mover pole number combinations.

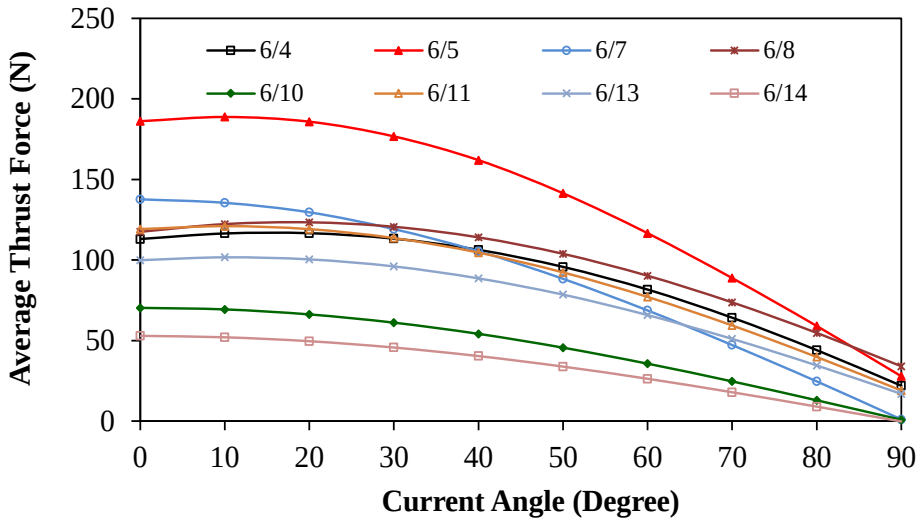

Fig. 4.28 Average thrust force variation with current angle for different stator/mover pole number combinations.

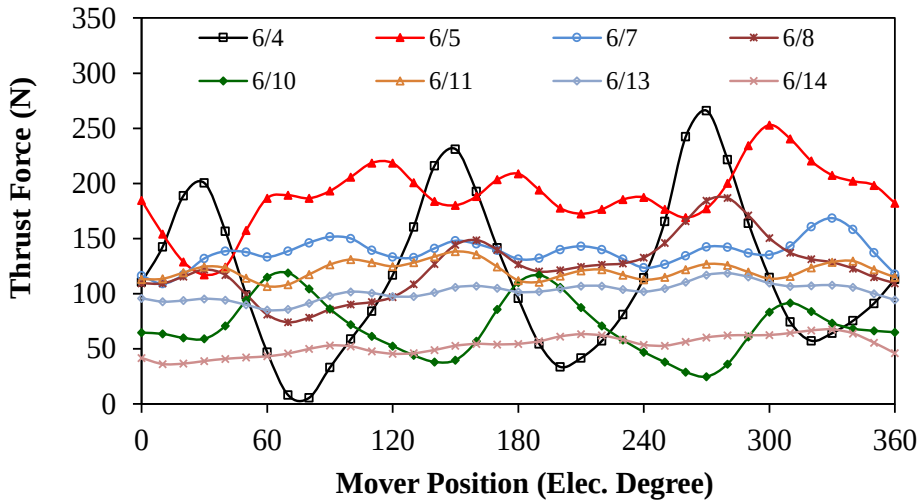

Fig. 4.29 Thrust force comparison for different stator/mover pole number combinations (current density = 6A/mm^2 rms).

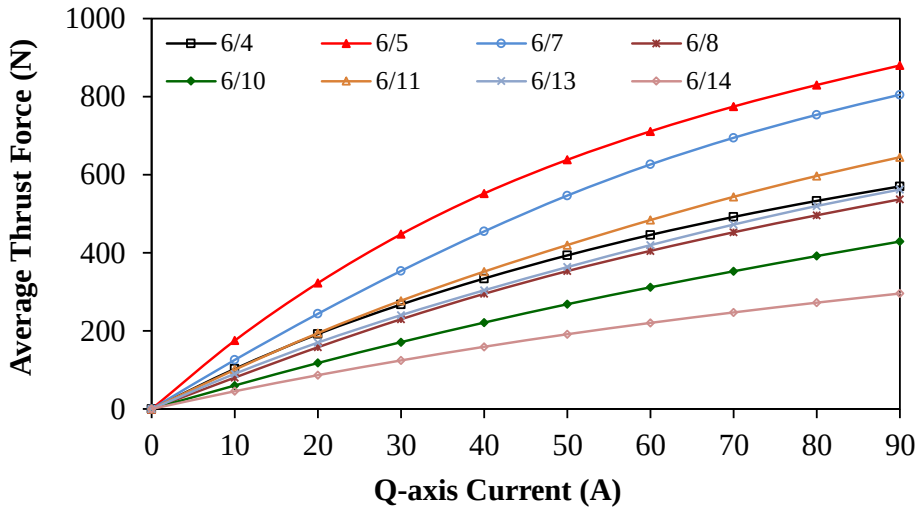

Fig. 4.30 Average thrust force variation with q-axis current for different stator/mover pole number combinations.

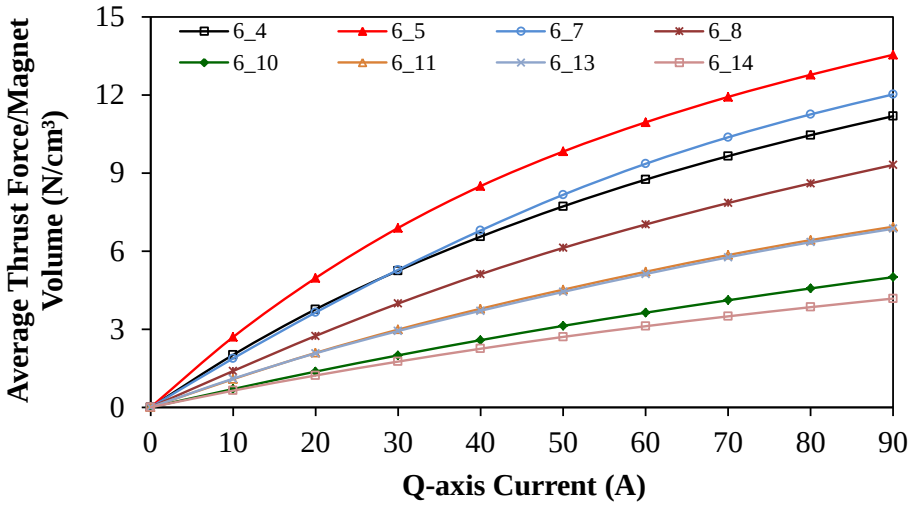

Fig. 4.31 Magnet utilization comparison for different stator/mover pole number combinations.

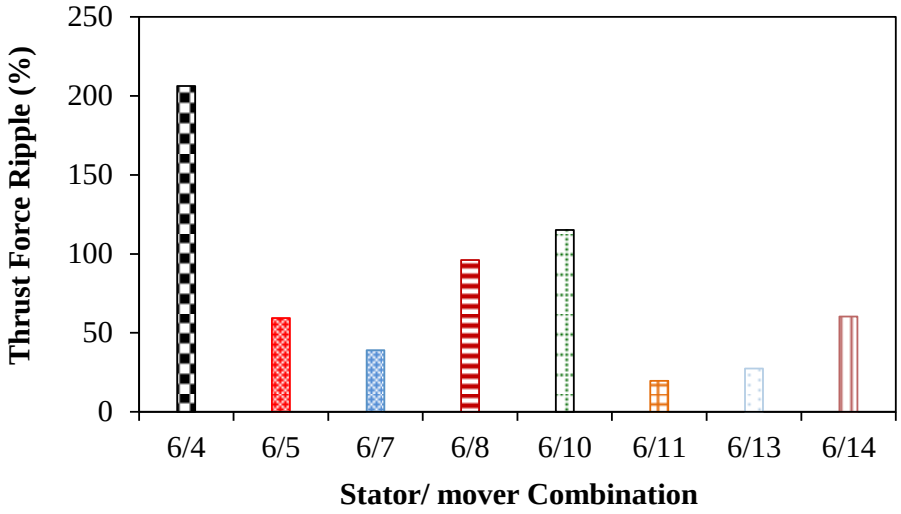

Fig. 4.32 Thrust force ripple comparison for different stator/mover pole number combinations.

The performances of the understudying machines are compared in

Table 4.7. It can be clearly seen that the worst thrust force capability is found in the 6/14 machine followed by the 6/10 machine, since they have the lowest back-EMF of the other machines, about 3V and 3.9V, respectively. On the other hand, the 6/5 machine exhibits the best thrust force capability compared to other combinations. The 6/4 and 6/11 combinations show a compatible thrust force, however the 6/11 machine has the lowest thrust force ripple, whilst the 6/4 machine possesses the highest. All odd mover pole machines exhibit higher back-EMF and lower cogging force compared to their even counterparts due to a higher winding factor and lower goodness factor, respectively.

Table 4.7 PS-IPM tubular machines performances comparison

Items	Stator/ mover combinations							
	6/4	6/5	6/7	6/8	6/10	6/11	6/13	6/14
Flux linkage (fundamental) (Wb)	0.032	0.053	0.027	0.016	0.009	0.015	0.011	0.005
Back-EMF(fundamental) (V)	5.75	11.91	8.5	5.54	3.9	6.64	6.13	3.01
Winding factor	0.5	0.867	0.867	0.5	0.5	0.867	0.867	0.5
Cogging force (peak) (N)	116.4	67.6	26.76	53.7	45.66	14.2	17.25	15.1
Average thrust force (N)	116.7	188.7	137.6	123.4	70.0	121.0	101.7	52.9
Thrust force ripple	206%	60%	39%	96%	115%	19.7%	27%	61%
Total magnet volume (cm^3)	51	65	67	57.7	85.8	93	82	70.8

4.7 Summary

Two novel PM tubular machines are introduced by adopting the idea of partitioned stator PM machines. The machine structures as well as operation principles are described. Moreover, both machines have been globally optimized for maximum thrust force based on GA, and the influence of leading design parameters on both machine performances is investigated. In addition, in terms of back-EMF and thrust force capability, the influence of mover pole number for both machines is examined. It is found that the odd mover pole number machines have a higher winding factor than those with a corresponding even mover pole number. Furthermore, it is noted that machines with a mover pole number equals to (stator slot number ±1) have the best performances. However, the optimal mover pole number for both machines is (stator slot number -1).

Chapter5. Comparison of Electromagnetic Performance of PS-SPM and PS-IPM Tubular Machines

5.1 Introduction

This chapter introduces a quantitative comparison of PS-SPM and PS-IPM tubular machines based on their global optimization models. In Chapter 4, it has been found that in terms of the highest back-EMF and the highest average thrust force, the optimal stator/mover combinations is 6/5 for both machines. Thus, the electromagnetic performances of 6/5 SP-SPM and 6/5 PS-IPM tubular machines will be compared. The electromagnetic performances involve open circuit flux linkage and back-EMF, thrust force capability as well as thrust force ripple, PM utilizations, inductances, losses, and magnet demagnetization withstand capability. Furthermore, the influence of cross-coupling on the performance of both machines is investigated and compared. Additionally, in order to highlight the impact of the winding configuration on the PS-PM tubular machines, single-layer winding PS-SPM and PS-IPM tubular machines have been designed, and compared with their double-layer winding counterparts.

5.2 No-load and On-load Performances Comparison of PS-SPM and PS-IPM Tubular Machines

The 6/5 PS-SPM and PS-IPM tubular machines are optimized in the previous chapter under the same optimization conditions for the highest thrust force. Their main design parameters are listed in Table 5.1. The 2D-axisymmetry FE will be employed to analyse and compare the electromagnetic performances of the two machines. Flux linkages due to the PMs for phase A of both machines are compared in Fig. 5.1 (a). It can be noted that higher flux linkage can be obtained by the PS-IPM tubular machine, thanks to the flux focusing. On the other hand, both machines exhibit asymmetric flux linkage waveforms due to the longitudinal end effect [DAN07], which is an inherent feature of the linear machines. In order to illustrate the effect of the longitudinal end effect on both machines, periodical models, i.e. without longitudinal end effect, have been designed, and phase A flux linkages for both models are compared in Fig. 5.1 (b). It can be seen that both periodical models for both machines have symmetrical flux linkage waveforms. The spectra of the periodical and practical (with longitudinal end effect) models for both machines are depicted in Fig. 5.1 (c). Clearly, the periodical models do not exhibit DC components.

Fig. 5.2 shows back-EMF for phase A of the PS-SPM and PS-IPM tubular machines. Obviously, the PS-SPM tubular machine has less back-EMF compared to the PS-IPM tubular machine since it has less flux linkage. For both machines, the open circuit cogging forces, which result from both slot effect and longitudinal end effect [ZHU97], are compared in Fig. 5.3. It can be seen that the PS-IPM tubular machine has a higher cogging force than the PS-SPM tubular machine. The result is in good agreement with that obtained in [BIA03] for the conventional tubular machines.

The variation of the average thrust force with current angle for both proposed machines is illustrated in Fig. 5.4. It can be observed that the PS-SPM has maximum thrust force with zero current angle. In contrast, the PS-IPM produces maximum thrust force when the current angle is equal to 10 degrees. As mentioned before, the interaction between the PM flux linkage and the armature current results in producing thrust force. Hence, thrust forces for both machines are predicted and compared in Fig. 5.5. Due to the contribution of both magnet and reluctance forces to the machine thrust force, the PS-IPM machine produces higher thrust force than the PS-SPM, which is similar to [BIA03], [WAN01]. The relation between the average thrust force and the current density for both machines are compared in Fig. 5.6. The two machines have good thrust force-current density characteristics. However, the PS-IPM tubular machine exhibits higher thrust than the PS-SPM tubular machine.

In order to determine the magnet utilization in both machines, average thrust forces per total magnet volume have been calculated for different current densities, Fig. 5.7. It is worth mentioning that the PS-IPM tubular machine also has better magnet utilization compared to the PS-SPM tubular machine.

Moreover, thrust ripples for PS-SPM and PS-IPM tubular machines, which are calculated by (3.20), are depicted in Fig. 5.8. It can be clearly noted that the PS-SPM tubular machine shows less thrust force ripple in comparison with the PS-IPM tubular machine, which is a preferable feature for better control characteristic since thrust force ripple results in noise and vibration and subsequently affect the control characteristic.

Fig. 5.9 shows self- and mutual-inductances for both machines, which are predicated by 2D-axisymmetry and (2.1) (2.2), for one electrical cycle. Although the PS-IPM tubular machine exhibits a slightly higher self-inductance compared to the PS-SPM tubular machine, both of them have similar mutual inductances. Thus, it can be concluded that both machines possess similar fault tolerance capability.

Table 5.1 Main design parameters of both machines

Items	PS-SPM	PS-IPM
No. of phase	3	
No. of stator slot	6	
No. of mover pole	5	
Rated velocity	1 m/s	
Current density (rms)	6 A/mm^2	
No. of turn/phase	90	
Packing factor	0.5	
Mover radial thickness	4 mm	4.5 mm
Outer stator back-iron	0.13	0.12
Outer stator tooth width		
PM volume	66.99 cm³	65 cm³

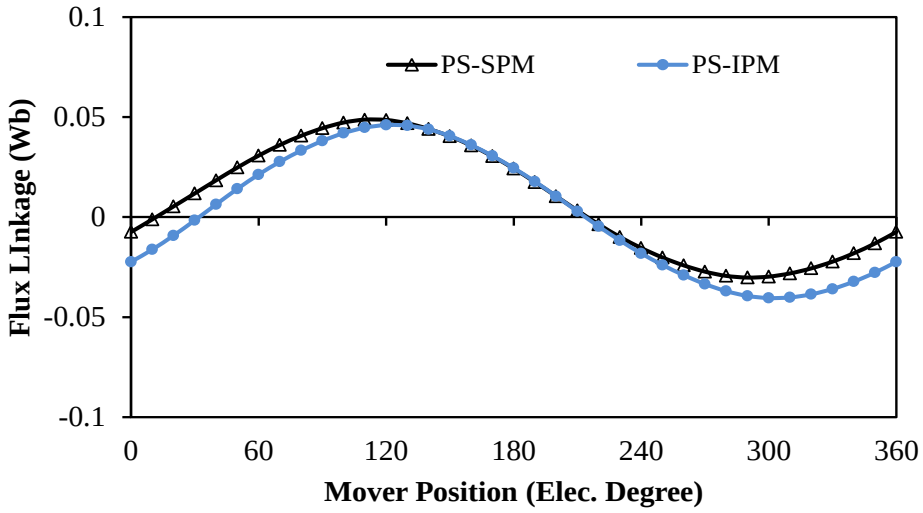

(a) Waveform practical models.

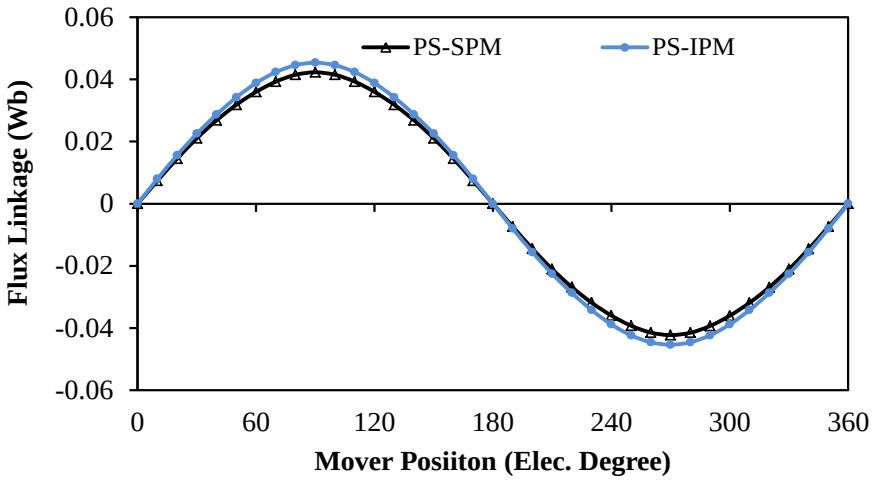

(b) Waveform periodical models.

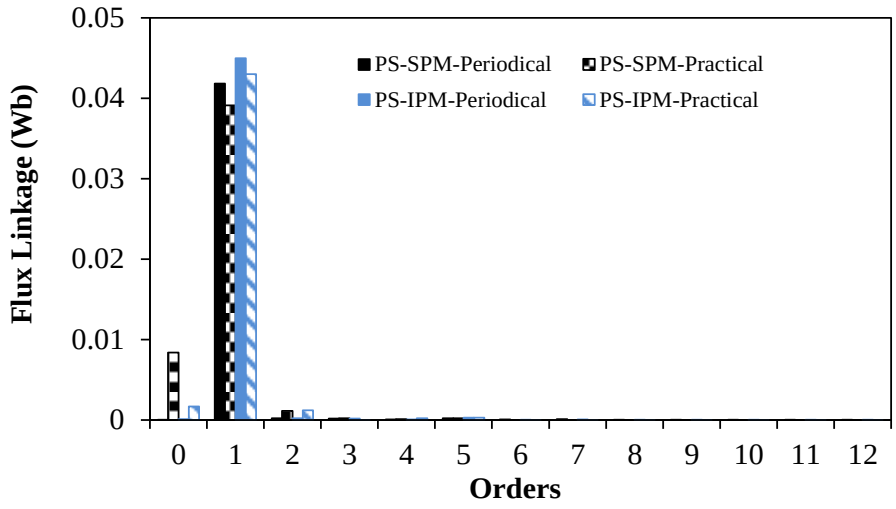

(c) Spectrum

Fig. 5.1 Flux linkage comparison.

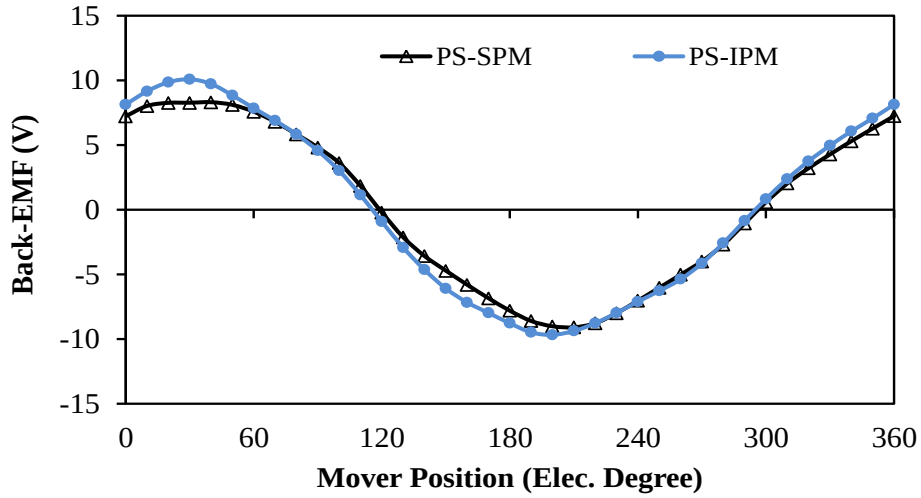

(a) Waveform

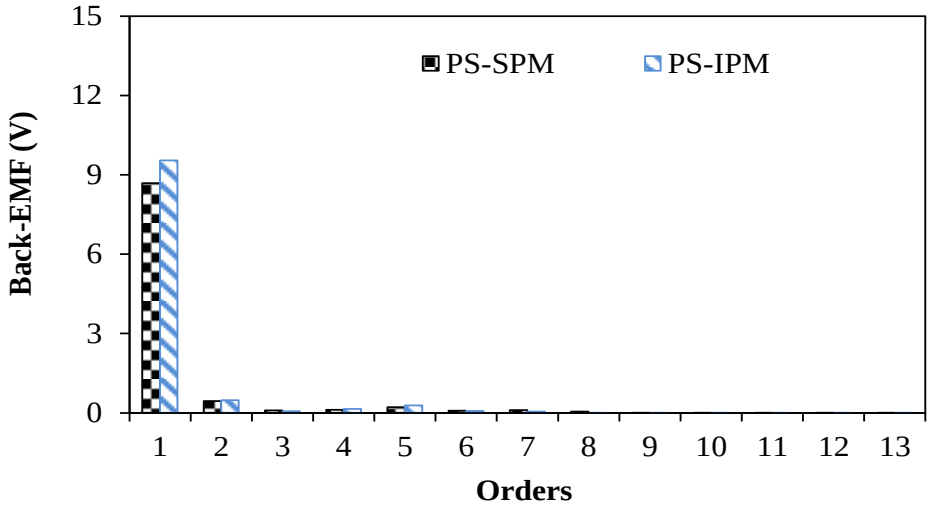

(b) Spectrum

Fig. 5.2 Back-EMF comparison.

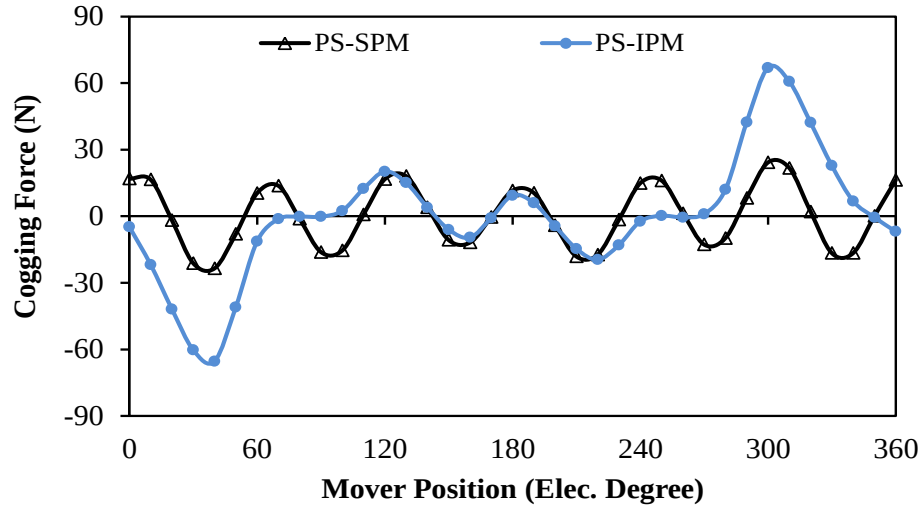

Fig. 5.3 Cogging force comparison.

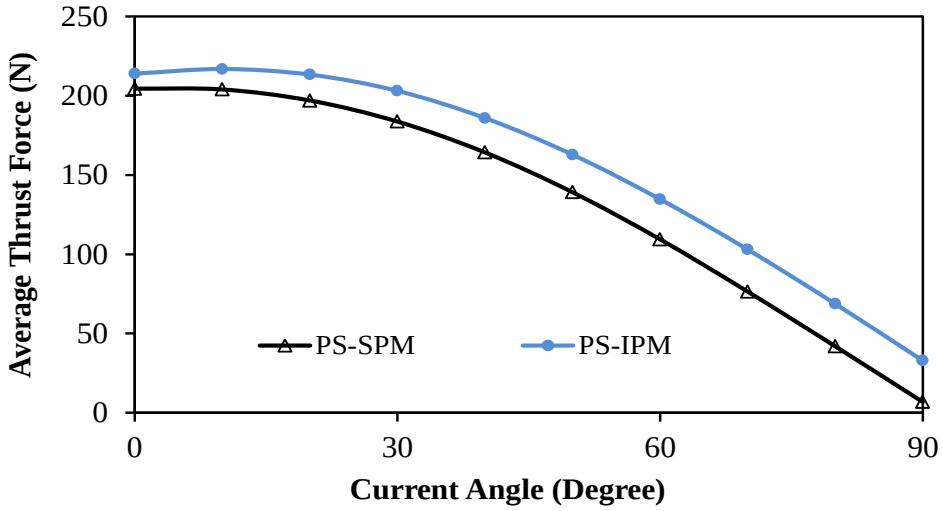

Fig. 5.4 Average thrust force variation with current angle.

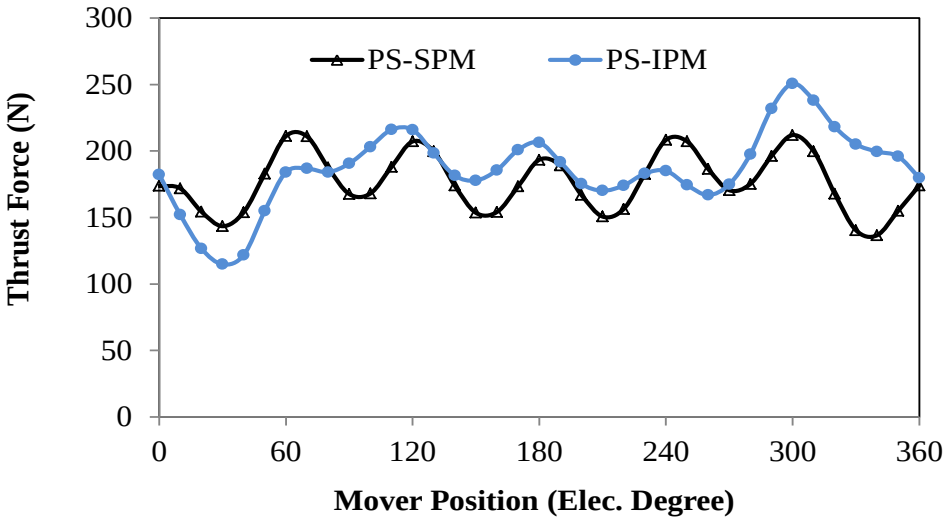

Fig. 5.5 Thrust force comparison (current density = 6A/mm^2 rms).

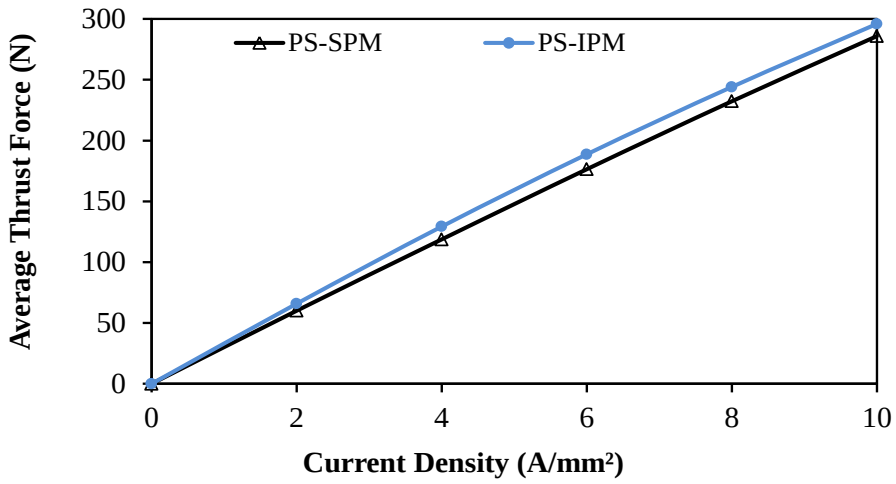

Fig. 5.6 Average thrust force variation with current density.

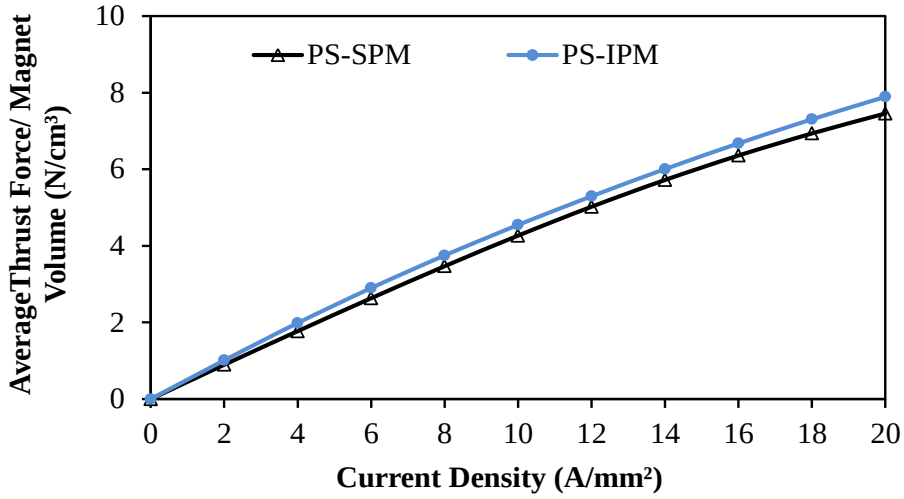

Fig. 5.7 PM utilization comparison.

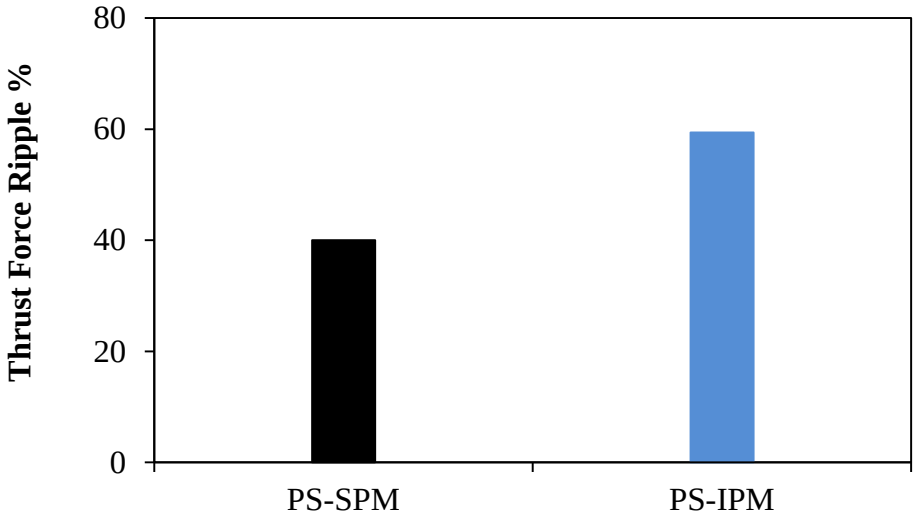

Fig. 5.8 thrust force ripple comparison.

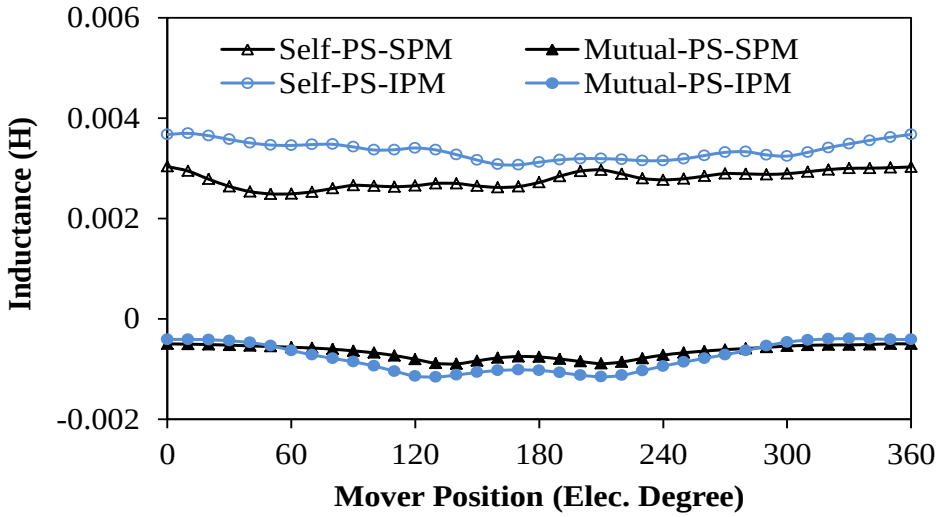

Fig. 5.9 Self- and mutual-inductances comparison.

5.3 Influence of Cross Coupling on Machine Performances

The method that was proposed in [QI09] and described in Chapter 3 will be utilized to highlight the effect of the cross-coupling and saturation on the performance of both machines, in terms of PM flux linkage and d- and q-axis inductances. The variations of flux linkage due to the PM with q-axis current for both machines are shown in Fig. 5.10. It can be observed that the flux linkages are slightly decreased with the increase of the q-axis current due to the saturation. However, the flux linkage reduction of PS-IPM tubular machine is more significant than that of the PS-SPM tubular machine. Hence, it can be concluded that the PS-IPM tubular machine is more sensitive to saturation compared to the PS-SPM tubular machine.

Fig. 5.11 and Fig. 5.12 demonstrate d-and q-axis inductances of the PS-SPM tubular machine with different d- and q-axis currents accounting for the fully cross-coupling, respectively. On the other hand, those for the PS-IPM tubular machine are illustrated in Fig. 5.13 and Fig. 5.14. Clearly, the variation of both L_d and L_q of the PS-SPM tubular machine with q-axis current is less than that of the PS-IPM one. Furthermore, the saliency ratio, which is defined as the ratio of q-axis inductance to d-axis inductance for the PS-IPM tubular machine is higher compared to the PS-SPM this is because of the difference between the d- and q-axis flux paths in the IPM machine. Moreover, it is obvious that the PS-IPM tubular machine suffers higher saturation as its d- and q-axis inductances decrease with the increase of the q-axis current.

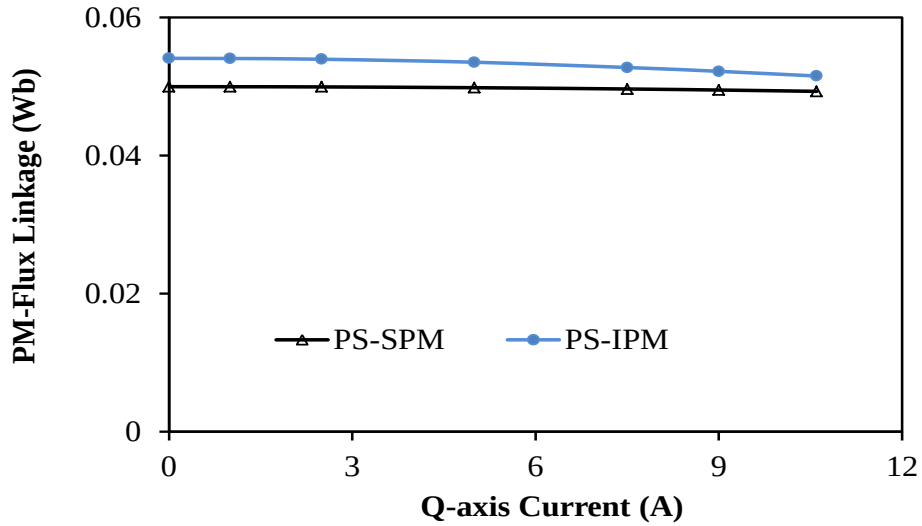

Fig. 5.10 Comparison of PM flux linkage variation with q-axis current in both machines.

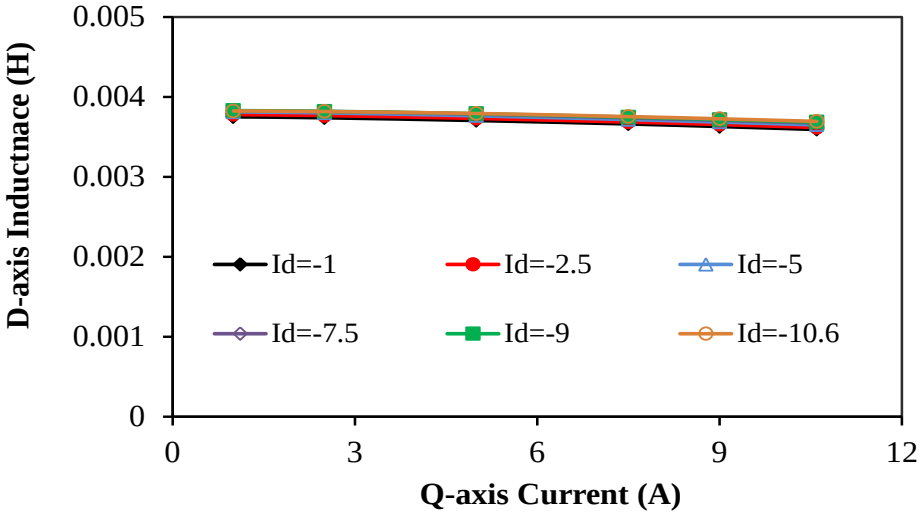

(a)

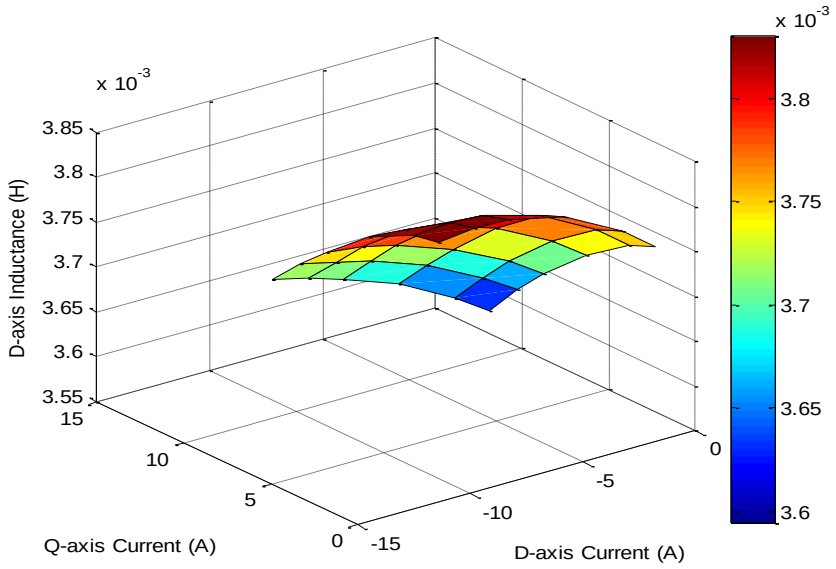

(b)

Fig. 5.11 D-axis inductance of PS-SPM tubular machine considering cross-coupling.

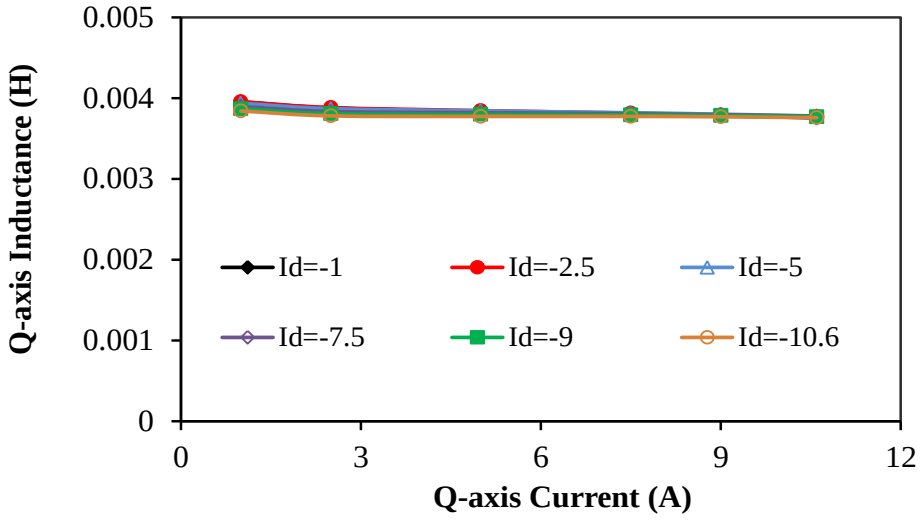

(a)

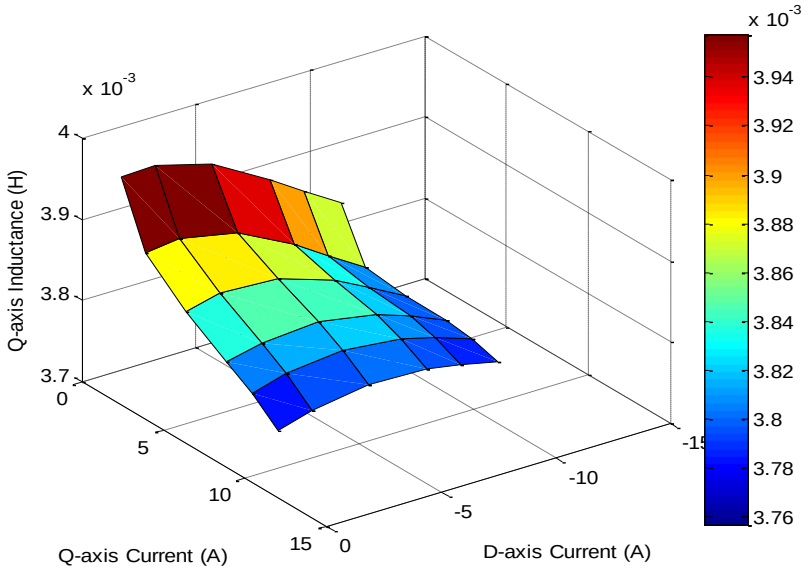

(b)

Fig. 5.12 Q-axis inductance of PS-SPM tubular machine considering cross-coupling.

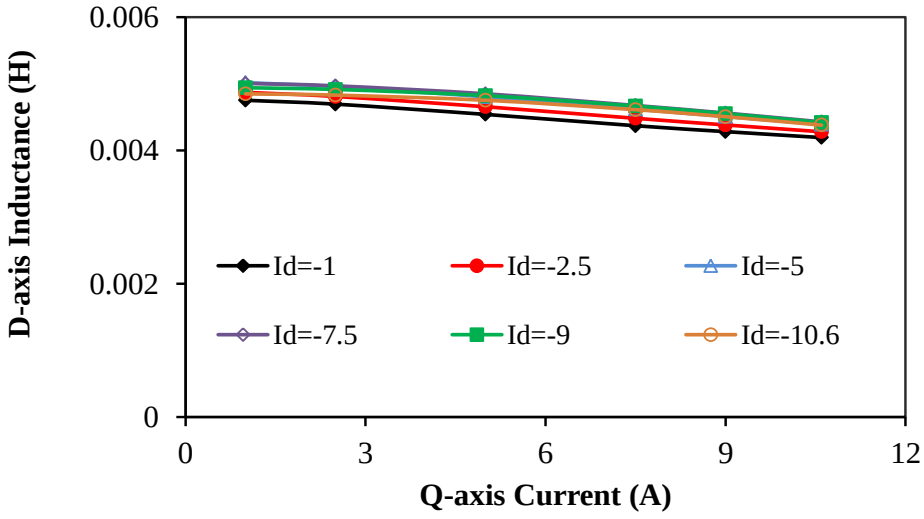

(a)

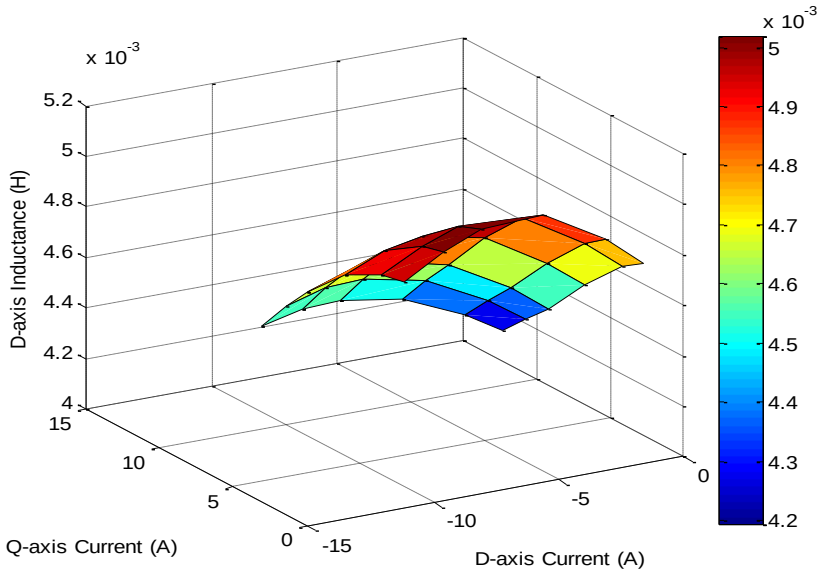

(b)

Fig. 5.13 D-axis inductance of PS-IPM tubular machine considering cross-coupling.

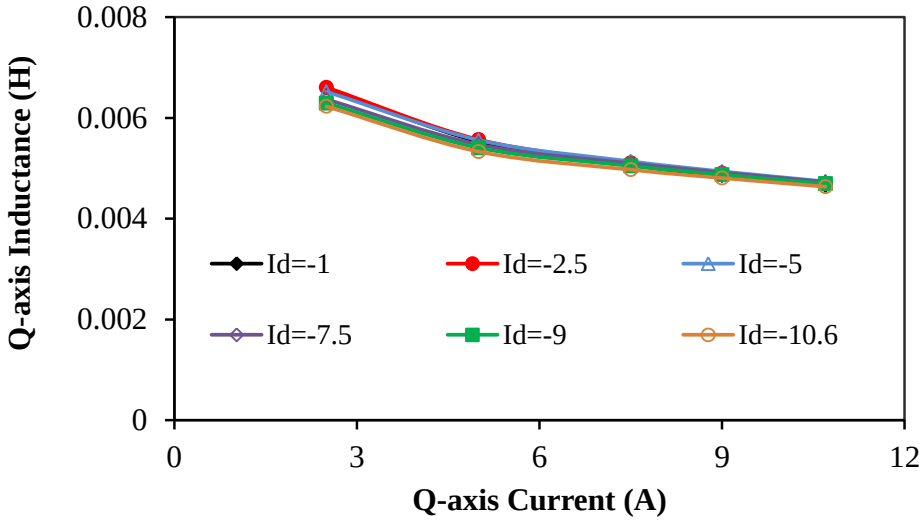

(a)

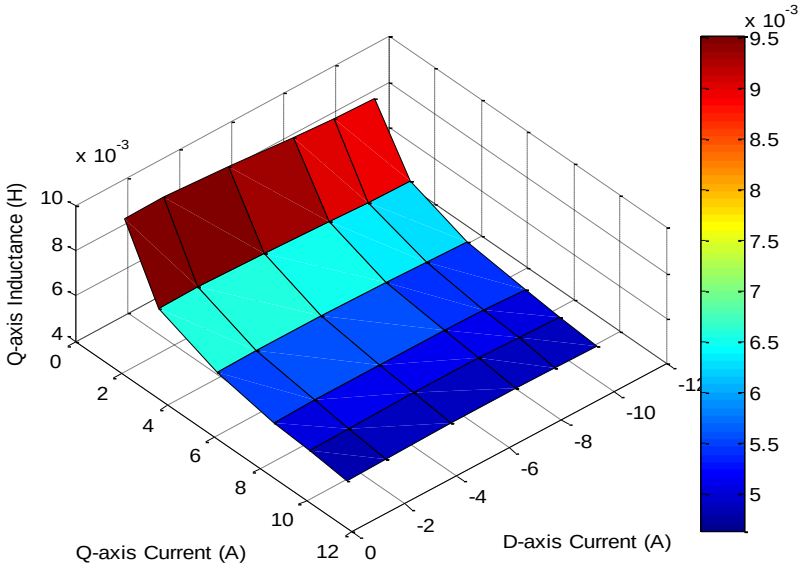

(b)

Fig. 5.14 Q-axis inductance of PS-IPM tubular machine considering cross-coupling.

5.4 Force-velocity Curve for PS-SPM and PS-IPM Tubular Machines

Force-velocity and output power-velocity curves for both machines can be obtained by using (3.21-3.26). The force-velocity curves of the understudying machines are compared in Fig. 5.15. Clearly, both machines exhibit similar performances. However, the PS-IPM tubular machine has a higher force capability in the constant force region compared to the PS-SPM tubular machine. In addition, beyond this region both machines have the same force capabilities and then, beyond (6 m /s) velocity, again the PS-IPM tubular machine shows higher thrust force than the PS-SPM tubular machine. Moreover, Fig. 5.16 presents the power-velocity curves of the aforementioned machines. It can be seen that PS-IPM tubular machine possesses a good constant power region compared to the PS-SPM tubular machine. Hence, it can be observed that the PS-IPM tubular machine offers a wider velocity operation region than that of the PS-SPM tubular machine, which is conformable to that found in [SAN97].

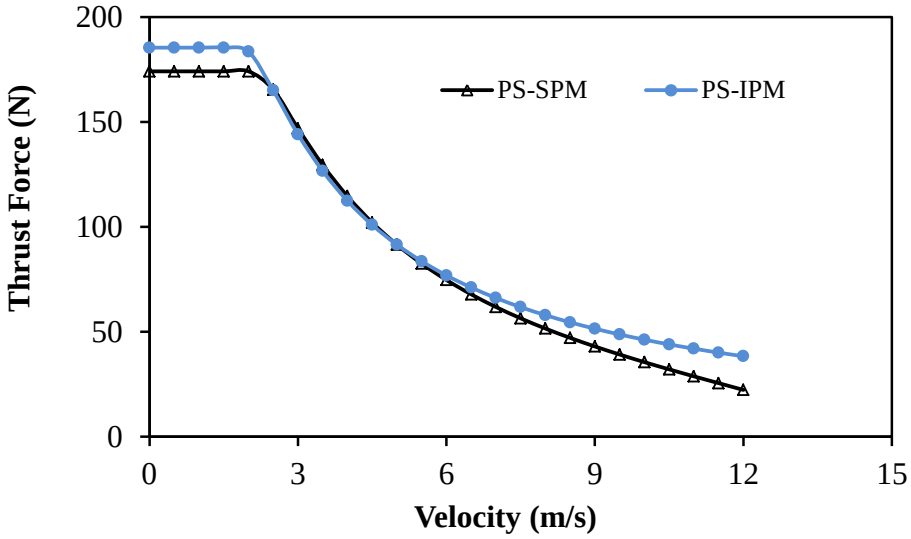

Fig. 5.15 Thrust force-velocity curve comparison.

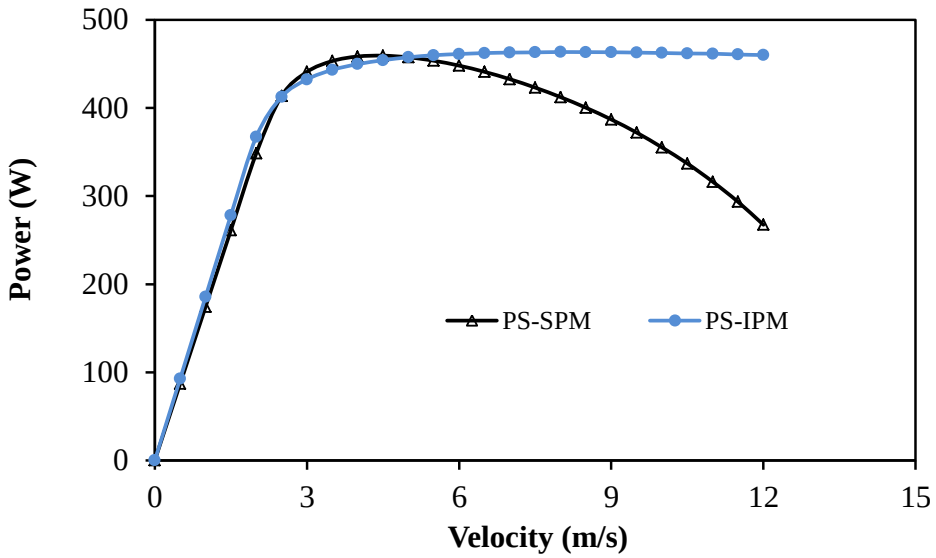

Fig. 5.16 Output power-velocity curve comparison.

5.5 Loss Comparison

5.5.1 Copper Loss

In PM linear machines, the highest amount of the loss is copper loss, particularly at low velocity operating condition. Copper loss is also known as winding loss, such loss is usually frequency independent, and it is caused when the current from an external source flows through the armature winding. Copper losses for both machines are calculated by (3.32). It is worth mentioning that the copper losses for both machines are equal to 70W.

5.5.2 Iron Loss

Iron losses for the understudying machines are predicted by 2D-axissymmetric FE. The variations of the average iron loss with the velocity for both no-load and load operating conditions for both machines are shown in Fig. 5.17 and Fig. 5.18, respectively. It can be seen that the PS-SPM tubular machine exhibits about 22% lower no-load as well as load iron losses compared to the PS-IPM tubular machine. On the other hand, the value of iron loss increases with the increasing of the velocity. This is because such loss is frequency dependent.

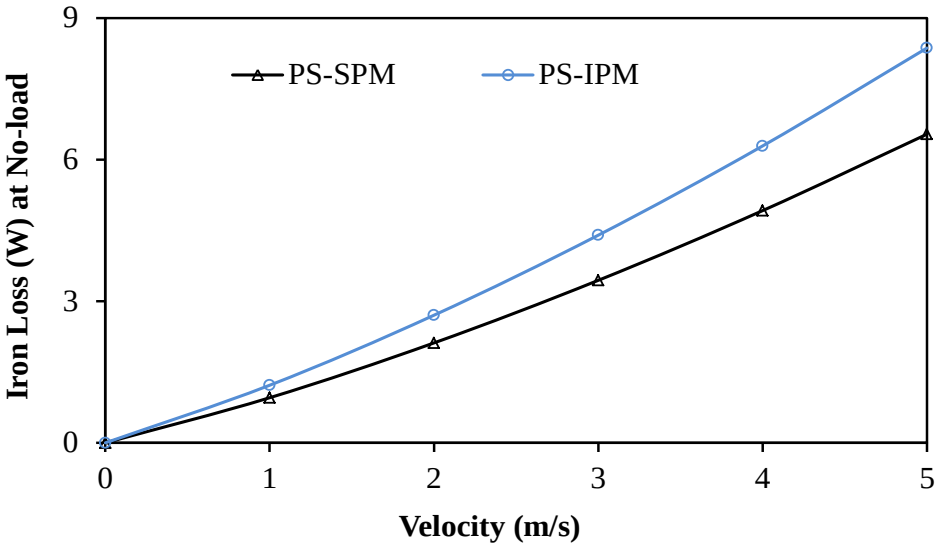

Fig. 5.17 No-load iron loss comparison.

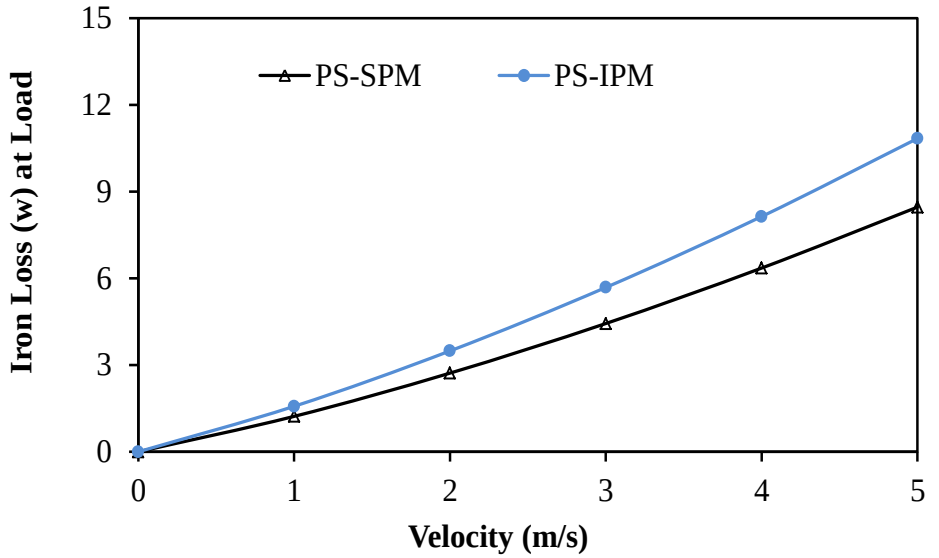

Fig. 5.18 On-load iron loss comparison.

5.5.3 Magnet Eddy Current Loss

Normally, in PM excitation electrical machines, eddy current loss would exist in the PMs, and consequently the PM temperature may be increased. Such phenomenon would be generated by the winding (MMF) harmonics, which have a different speed to that of the PM (MMF) harmonics. Fig. 5.19 compares both machines magnet eddy current losses, which are predicted for one electrical period at rated velocity (1m/s) as well as rated current density (6 A/mm^2).(rms) It should be noted that the PS-SPM tubular machine shows about 78% higher magnet eddy current loss than that of the PS-IPM tubular machine. This is because the PS-IPM tubular machine has lower air gap flux

density harmonic orders compared to the PS-SPM tubular machine as shown in Fig. 5.24

Magnet eddy current loss distributions in both machines are illustrated in Fig. 5.20. It is worth mentioning that the mover position for each machine was chosen with the highest value of magnet eddy current loss as shown in Fig. 5.19. Furthermore, average no-load and on-load magnet eddy current losses as functions of the velocity for the understudying machines are compared in Fig. 5.21 and Fig. 5.22, respectively. Moreover, Fig. 5.23 depicts the variation of such losses with the current at rated velocity. Obviously, those losses increase with the increasing of both velocity and current due to the increase of frequency and air-gap flux density.

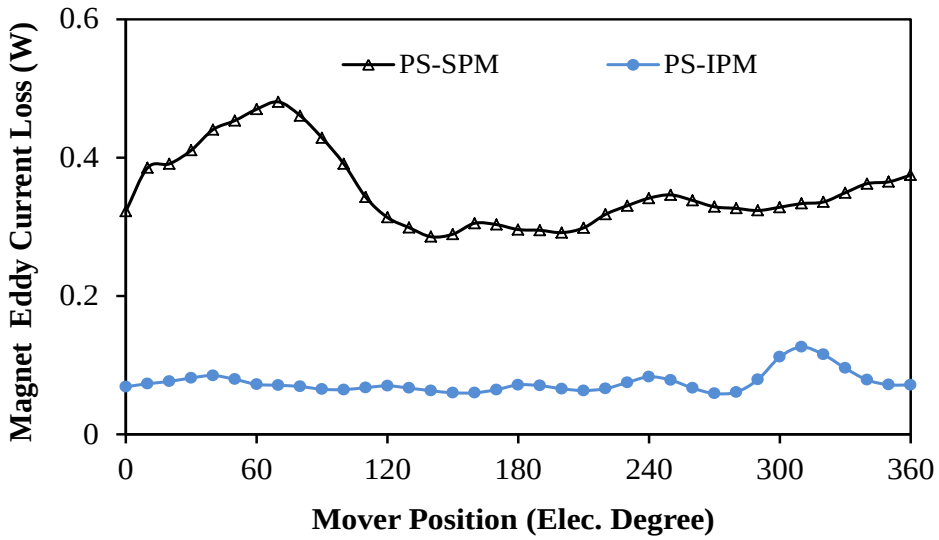

Fig. 5.19 Magnet eddy current loss variation with mover position (mover velocity of 1m/s).

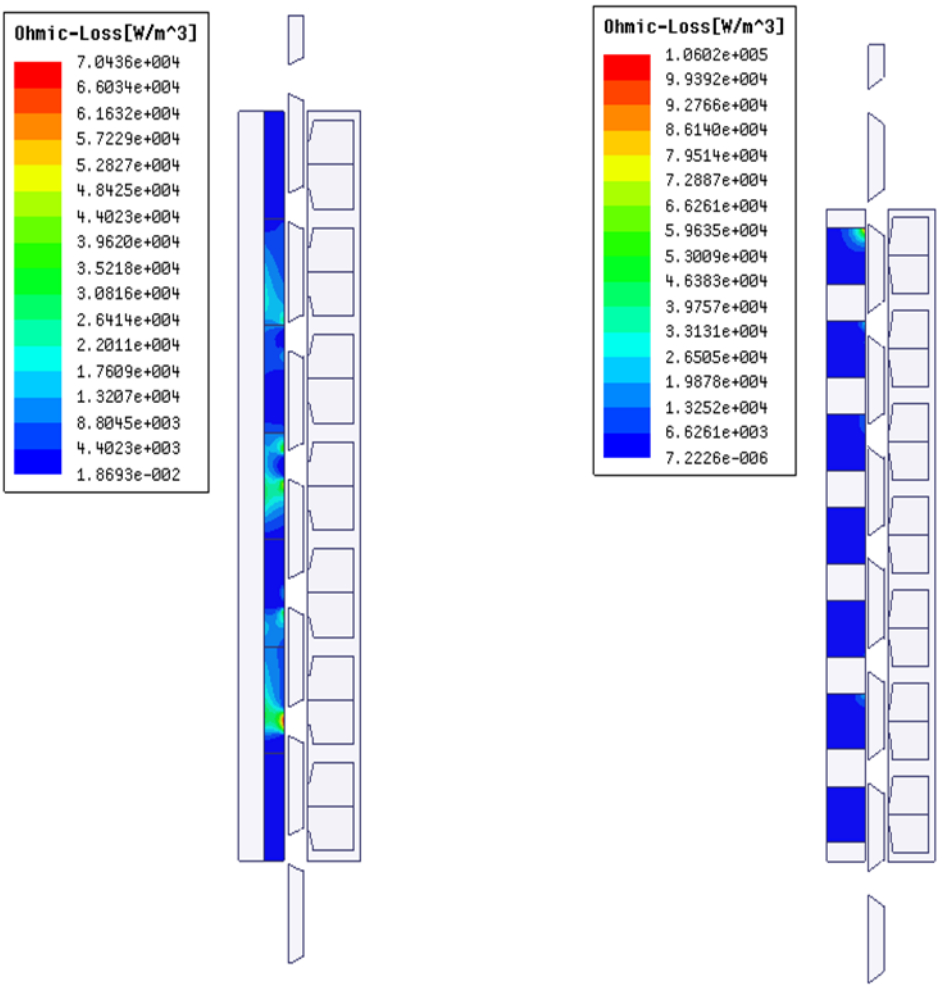

Fig. 5.20 Magnet eddy current distribution.

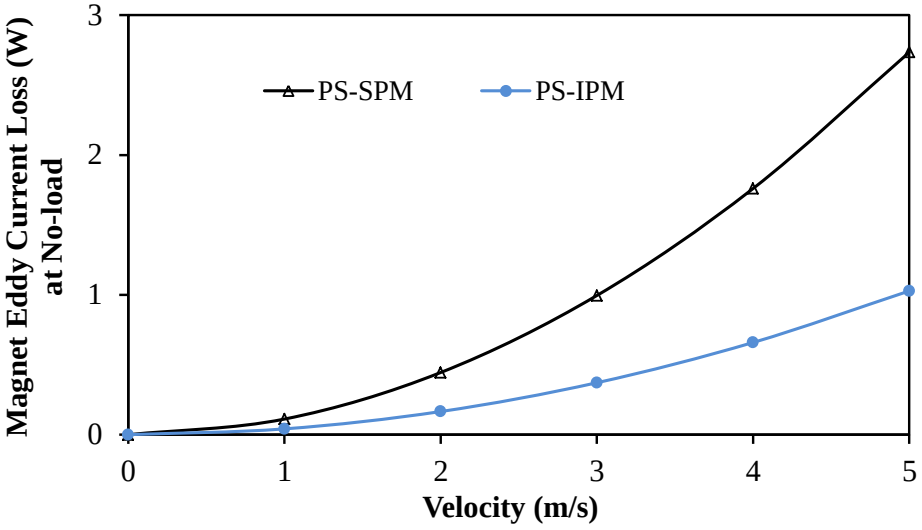

Fig. 5.21 No-load magnet eddy current loss variation with different velocity.

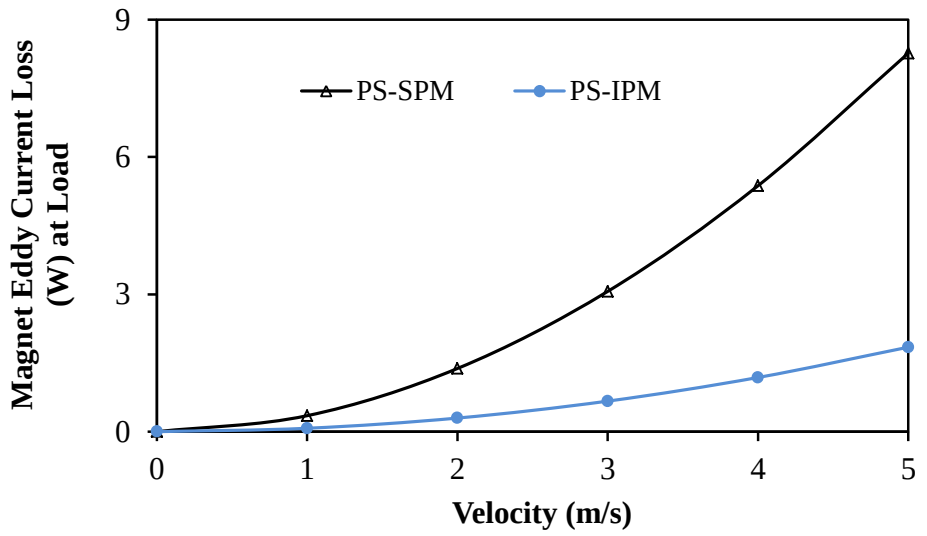

Fig. 5.22 On-load magnet eddy current loss variation with different velocity.

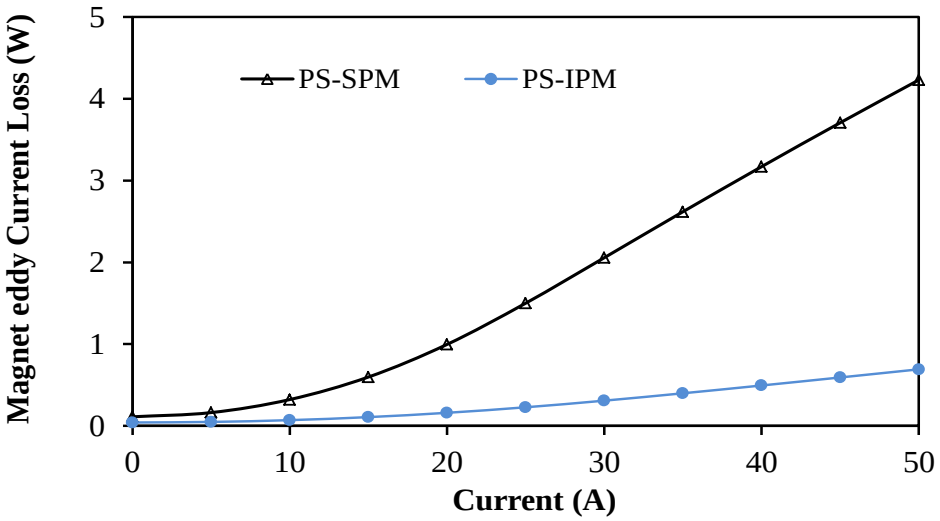

Fig. 5.23 Load magnet eddy current loss variation with different current.

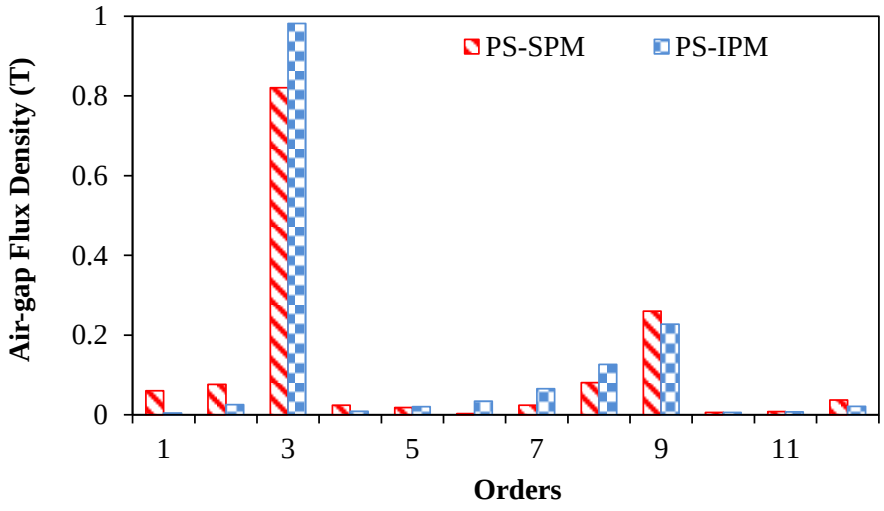

Fig. 5.24 Comparison of air gap flux density.

5.6 PM Demagnetization in PS-PM Tubular Machines

In PM machines, some of the PMs may lose their magnetization due to high current or/and high temperature, which may be occur under overload transient or faulty operating conditions. As this phenomenon results in degradation the PM machine performance, it is an important step to analyse PM demagnetization through the machine design process. Thus, in order to investigate the demagnetization withstand capabilities of understudying machines, the approach which was detailed in Chapter 2 will be employed.

Fig. 5.25 shows the flux density distributions for both north and south PM poles of the PS-SPM tubular machine. It should be mentioned that the mover position has been selected for the minimum flux density in the PMs in order to demonstrate the worst operating situation. It is obvious that the machine exhibits a good demagnetization withstand capability, as the permanent magnet flux densities are higher than the knee point.

Fig. 5.26 shows the flux density distributions for both north and south poles of the PS-IPM tubular machine. It can be seen that the machine has no PM demagnetization risk since the PM flux density is higher than the knee point. However, some edges of the PM of the PS-IPM tubular machine experience demagnetization because of the fringing and leakage flux.

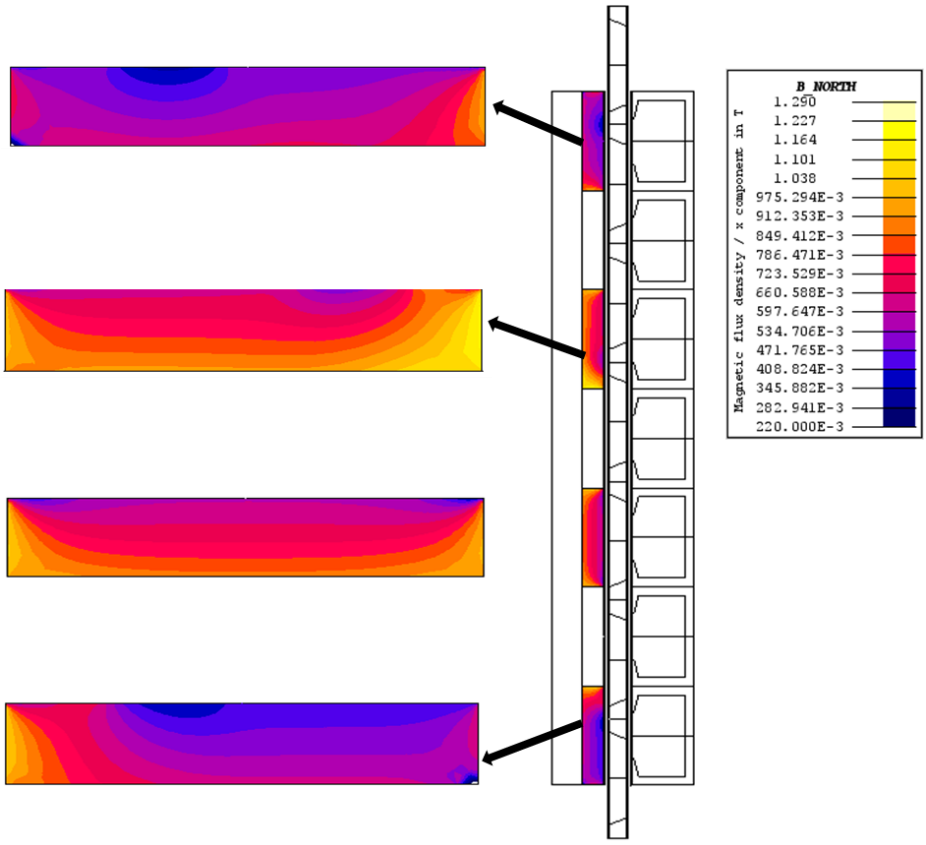

(a) North-pole

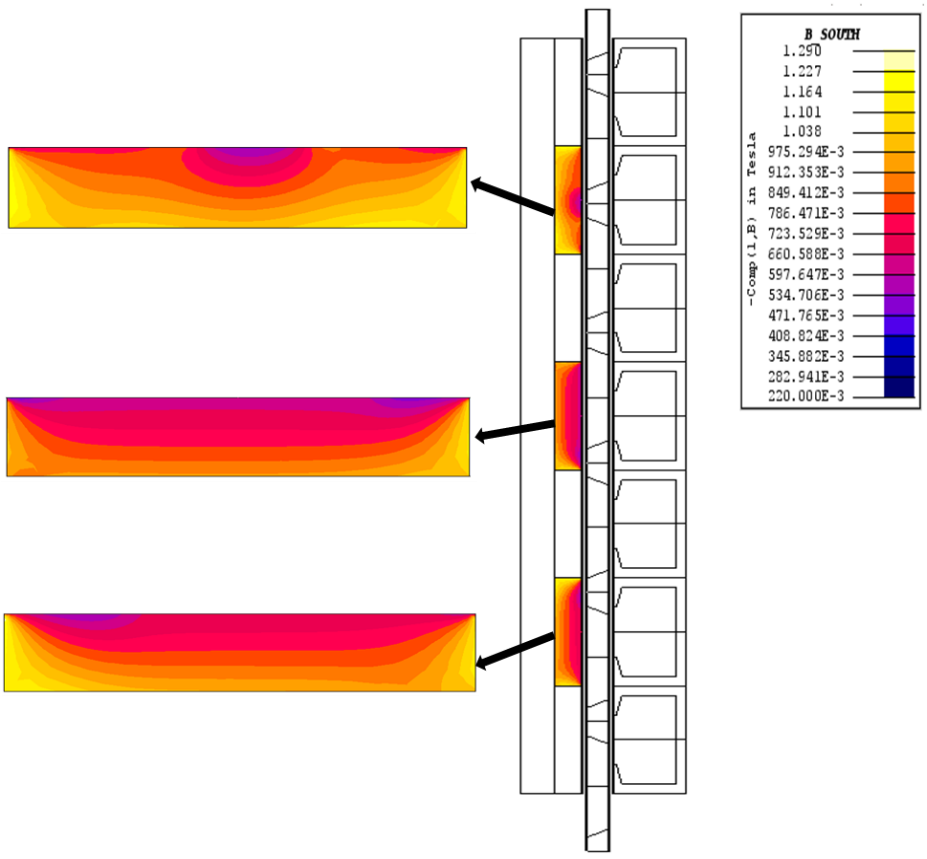

(b) South-pole

Fig. 5.25 PM flux density distributions PS-SPM tubular machine.

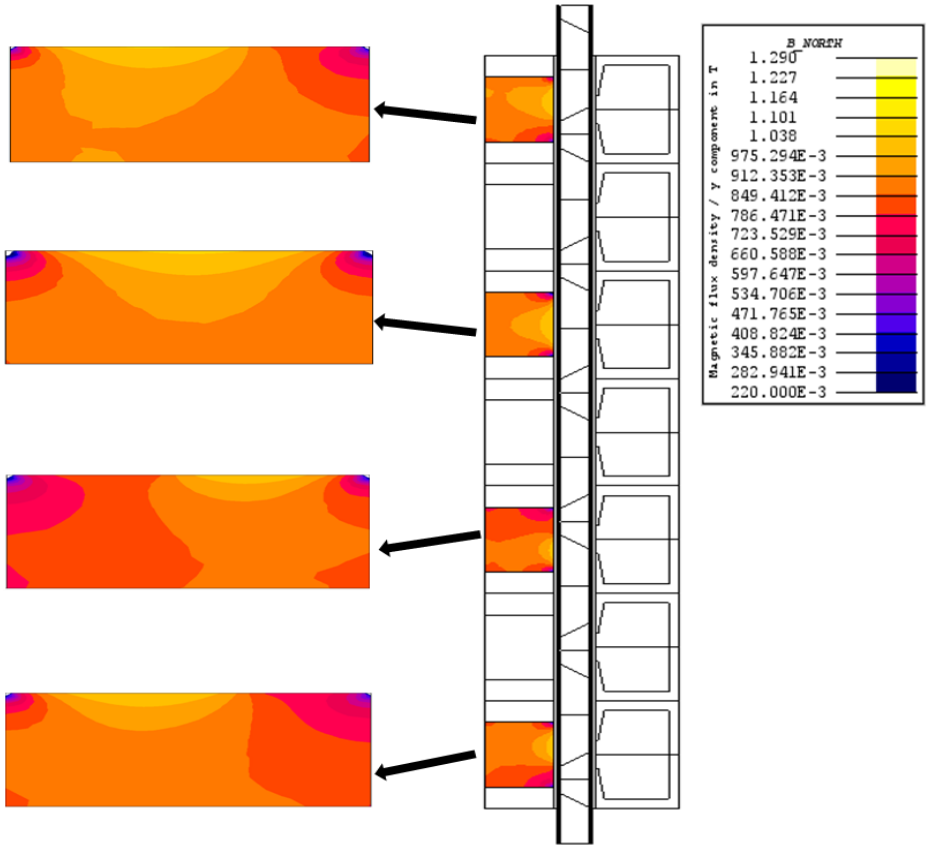

(a) North-pole

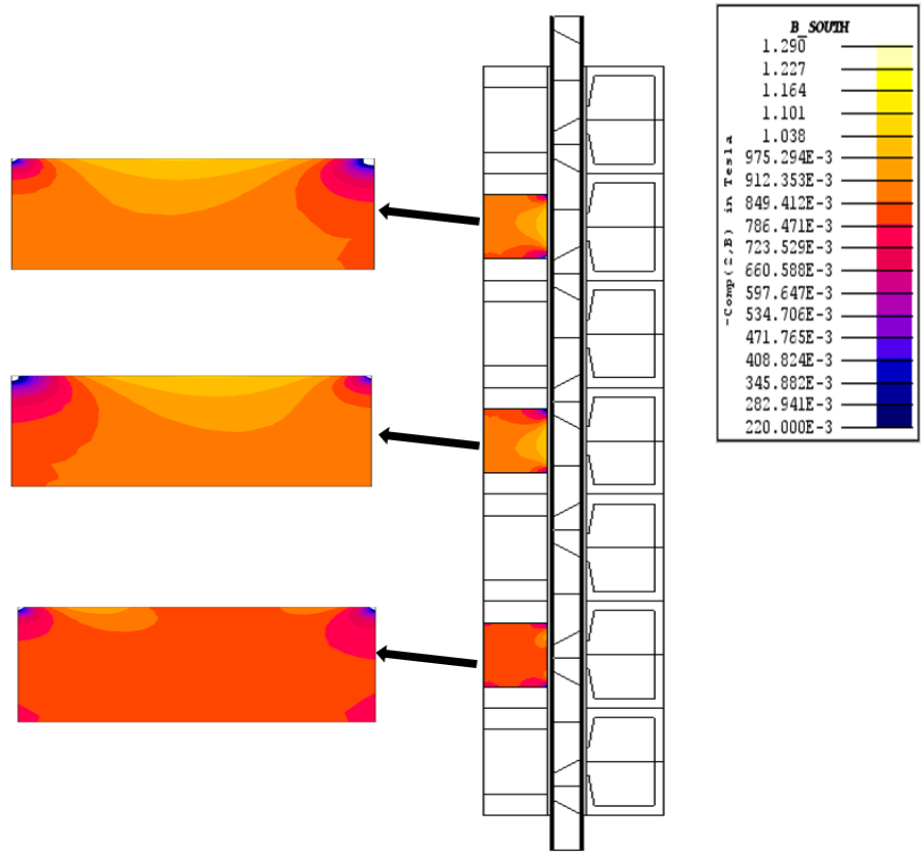

(b) South-pole

Fig. 5.26 PM flux density distributions PS-SPM tubular machine.

5.7 Comparison of PS-PM Tubular Machines Having Single- and Double-layer Windings

5.7.1 PS-SPM Tubular Machine

In this section, the performance of PS-SPM tubular machines with single- and double-layer windings will be compared. Firstly, in order to obtain a PS-SPM tubular machine with a single-layer winding configuration, the double-layer windings PS-SPM tubular machine has been redesigned. The construction difference between both machines can be clearly observed in Fig. 5.27. Obviously, the PS-SPM tubular machine with double-layer winding has an empty half slot at each end which is created by the assistance teeth. On the other hand, the configuration of single-layer tubular machine eliminates the need of such slots. Therefore, the single-layer tubular machine has been designed with one slot pitch less than that of its double-layer counterpart. Secondly, in order to carry out fair comparison between both machines, the single-layer machine is optimized with the same optimization conditions of the double-layer machine. The machine performances have been analysed using 2D-axi-symmetric FE.

Phase A flux linkages in both machines are compared in Fig. 5.28. However, both machines exhibit asymmetric flux linkage due to the presence of the longitudinal end, the single-layer machine has a higher DC component compared to the double layer machine. The impact of the longitudinal end effect can be explained by comparing the flux linkage of the practical model (with longitudinal end effect) with the periodic model (without longitudinal end effect), as is shown in Fig. 5.28. The periodic model of both single- and double- layer windings machines have symmetry flux linkage, while the practical models deliver asymmetry flux linkage. On the other hand, coil flux linkages can be employed to illustrate the difference between the flux linkages of two machines. Fig. 5.29 and Fig. 5.30 depict phase A coil flux linkages for single- and double-layer windings machines, respectively. It can be seen that four coils contribute to the phase flux linkage of the double layer-windings machine and only coil A1 has unipolar flux linkage. Thus, the DC component can be reduced when adding the coil flux linkages together. In contrast, the phase flux linkage of the single-layer windings machine comprises of two coils, i.e. coil A1 with unipolar flux linkage and coil A2 with bipolar flux linkage, which also has a DC component. Therefore, the DC component of the result in phase flux linkage would be increased when adding these coils together. Phase A back-EMFs for both machines are shown in Fig. 5.31. Considering the longitudinal end effect the double-layer winding machine has slightly higher back-EMF

compared to the single-layer windings machine; otherwise, the periodic model of the single-layer winding machine shows higher back-EMF than that of the double-layer winding machine.

Fig. 5.32 compares open circuit cogging forces for both machines. Generally, changing the winding configuration from single-layer to double-layer and vice versa does not have any impact on the machine cogging force/torque, if the machine structure is not changed. However, as mentioned above, the structures of the understudying machines are different. Thus, it is worth comparing the cogging force in both machines. Clearly, the single-layer winding machine has a lower cogging force compared to the double-layer winding machine.

The variations of average thrust force with copper loss for both machines are illustrated in Fig. 5.33. However, the amount of magnet usage in a single-layer machine is less than that of a double-layer machine. Both machines produce similar thrust force at lower copper loss value while at high copper loss value the single-layer winding machine exhibits slightly higher thrust force than the double-layer winding. Moreover, the variations of thrust forces with mover position and different copper losses for both machines are displayed in Fig. 5.34 and Fig. 5.35. Furthermore, the variations of average thrust force per total magnet volume with copper loss for both machines are illustrated in Fig. 5.36. It can be seen that the single layer-winding machine has better magnet utilization then the double-layer winding machine.

Self and mutual inductances for both machines are compared in Fig. 5.38. It can be observed the double-layer winding machine exhibits lower self-inductance compared with that of the single-layer winding. It should be mentioned that the ratio of mutual to self- inductance of the double-layer winding machine is less than that of the single-layer winding machine. Thereby, the single-layer winding machine can deliver more fault tolerance capability, since it possesses less coupling compared to the double-layer machine [BIA06].

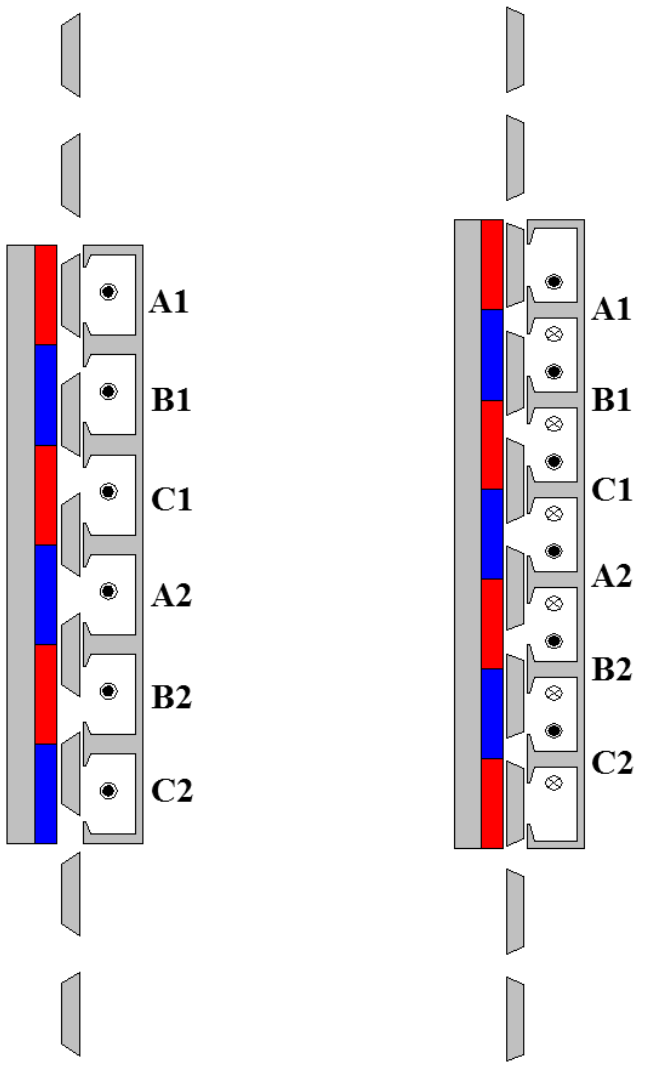

(a) Tubular SL- PS-SPM **(b) Tubular DL- PS-SPM**

Fig. 5.27 1 Cross-section of both single-and double-layer windings.

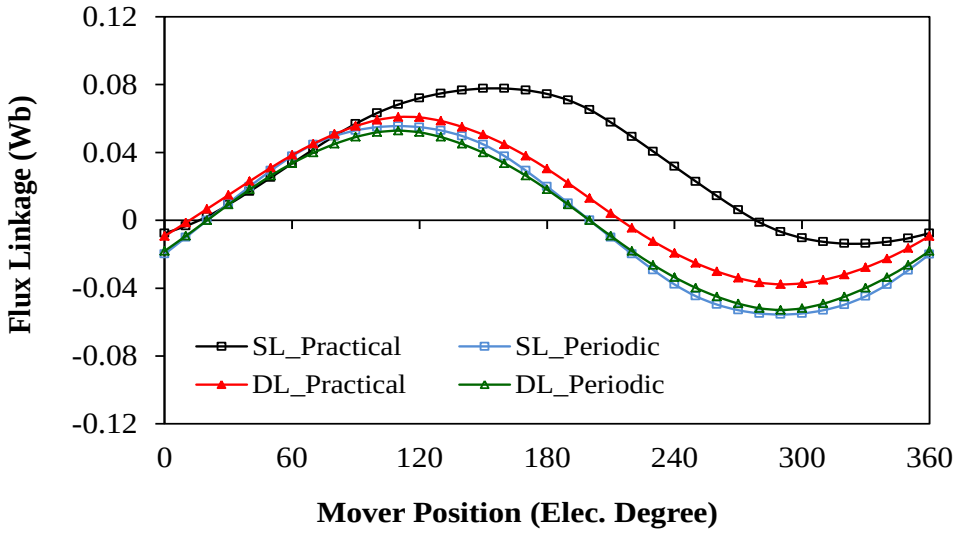

(a) Waveform

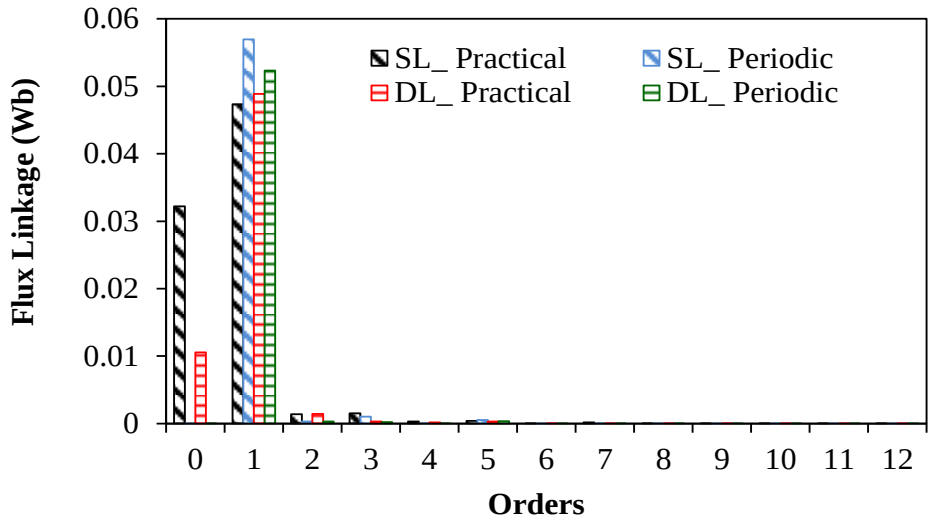

(b) Spectrum

Fig. 5.28 Phase A flux linkage comparison.

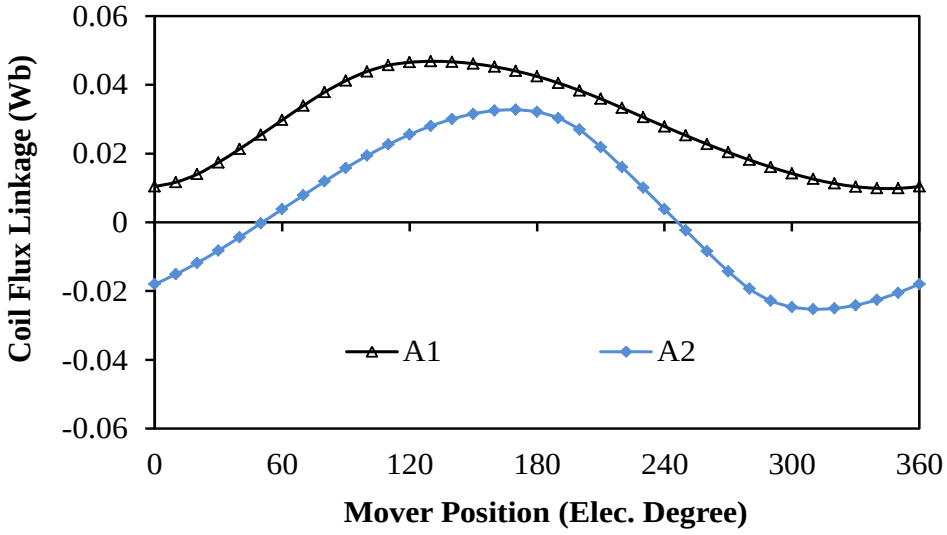

(a) Waveform

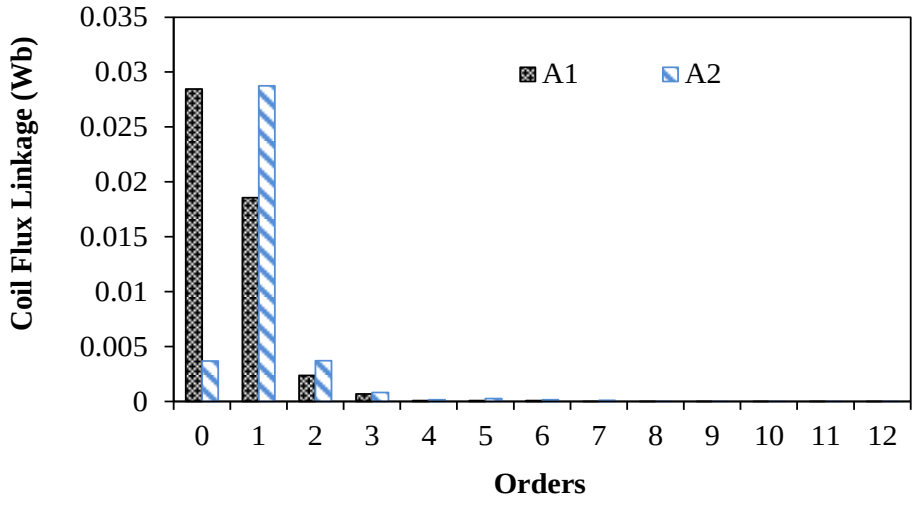

(b) Spectrum

Fig. 5.29 Coil flux linkage in single-layer winding machine.

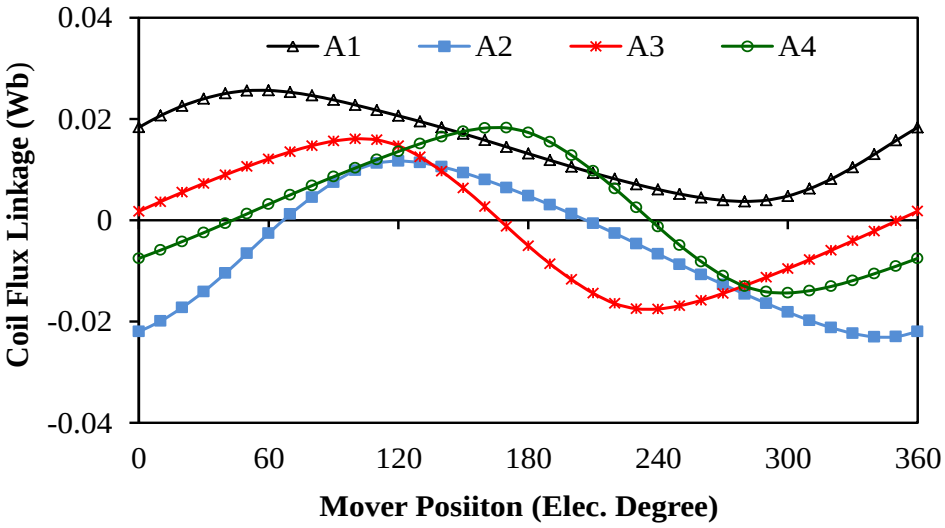

(a) Waveform

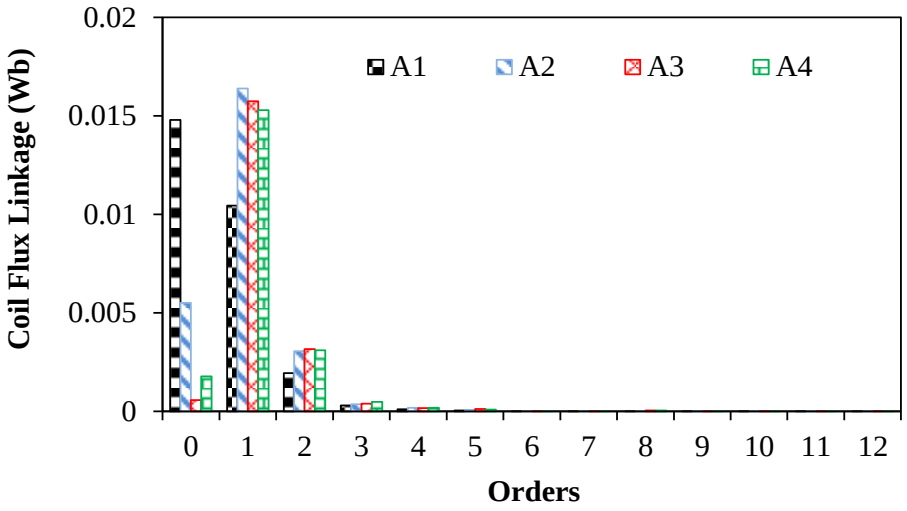

(b) Spectrum

Fig. 5.30 Coil flux linkage in double-layer winding machine.

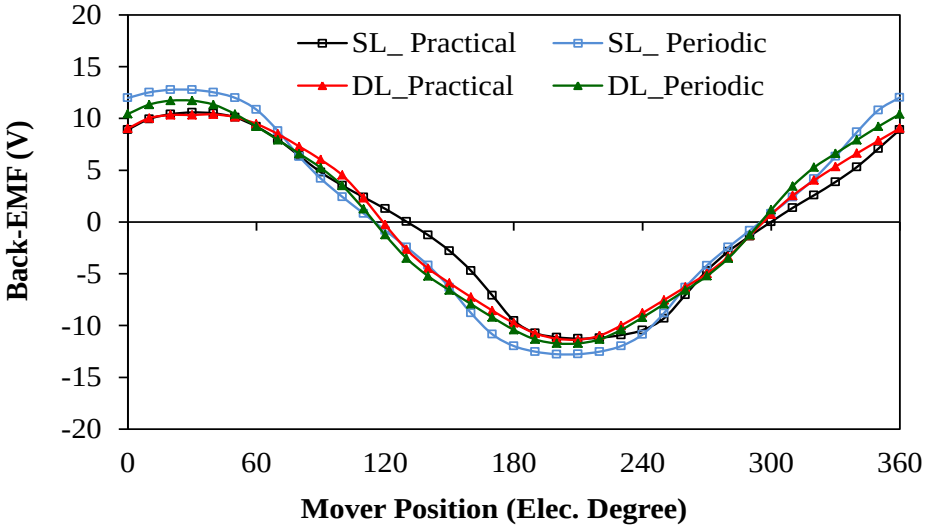

(a) Waveform

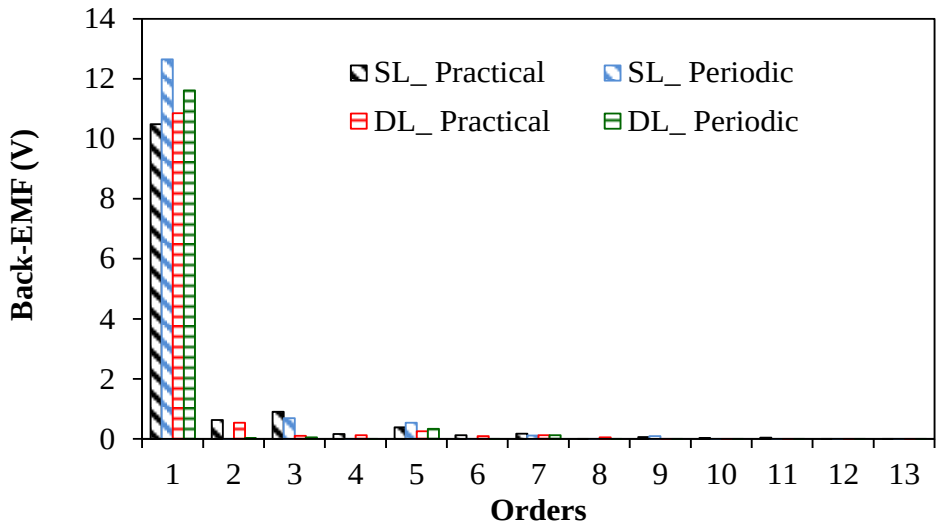

(b) Spectrum

Fig. 5.31 Phase A back-EMF Comparison.

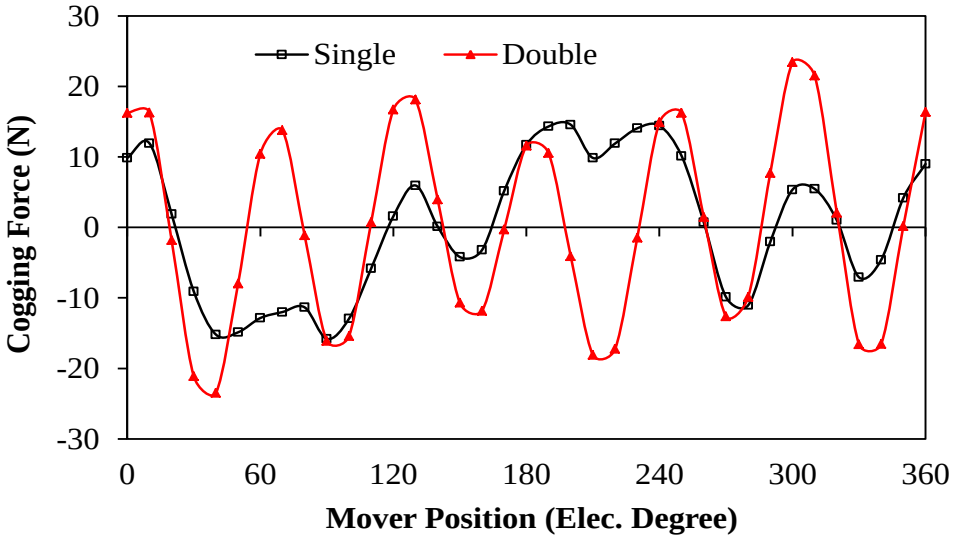

Fig. 5.32 Cogging force comparison.

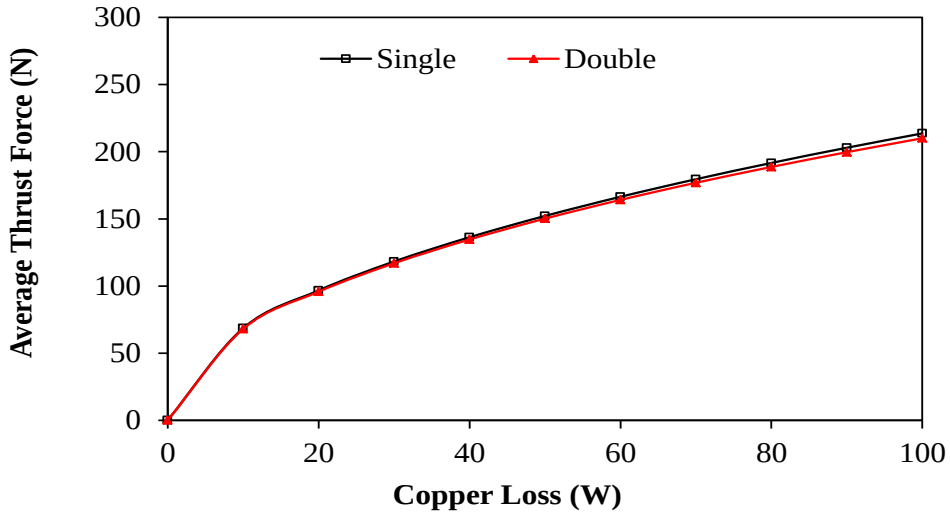

Fig. 5.33 Average thrust force variation with copper loss.

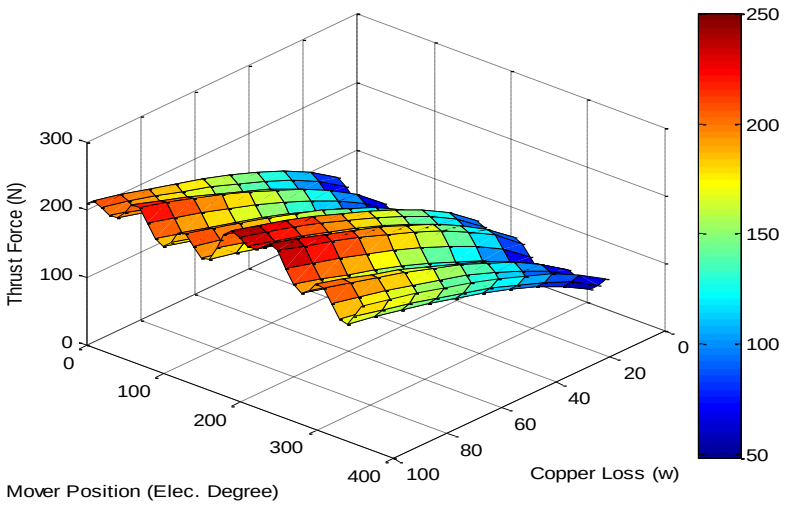

Fig. 5.34 Tubular SL- PS-SPM thrust force variation with mover position and copper loss.

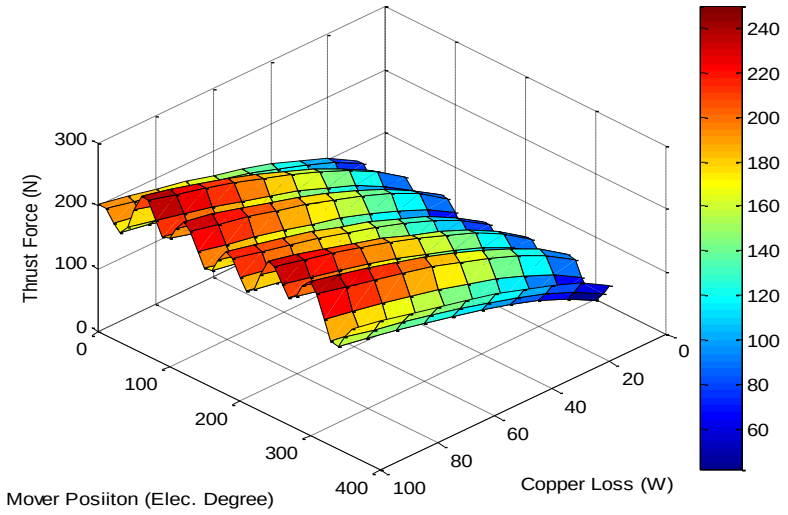

Fig. 5.35 Tubular DL- PS-SPM thrust force variation with mover position and copper loss.

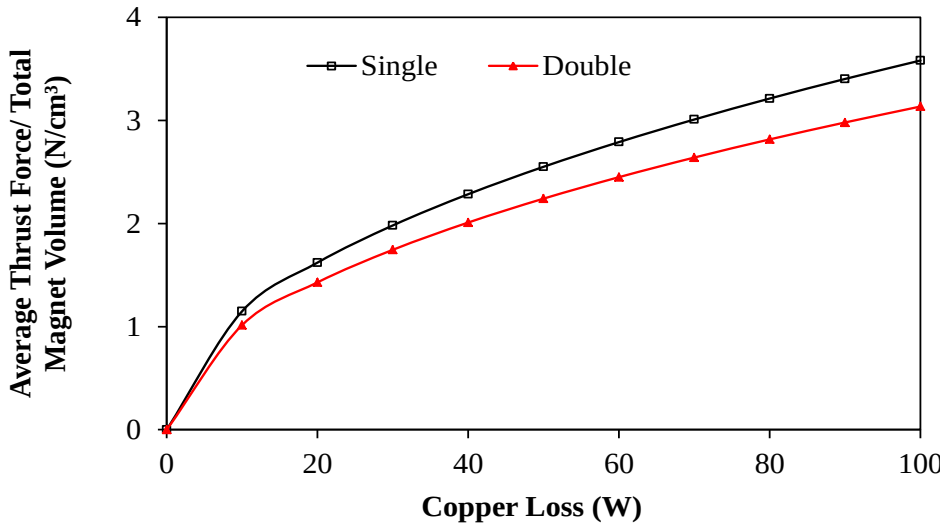

Fig. 5.36 PM utilization comparison.

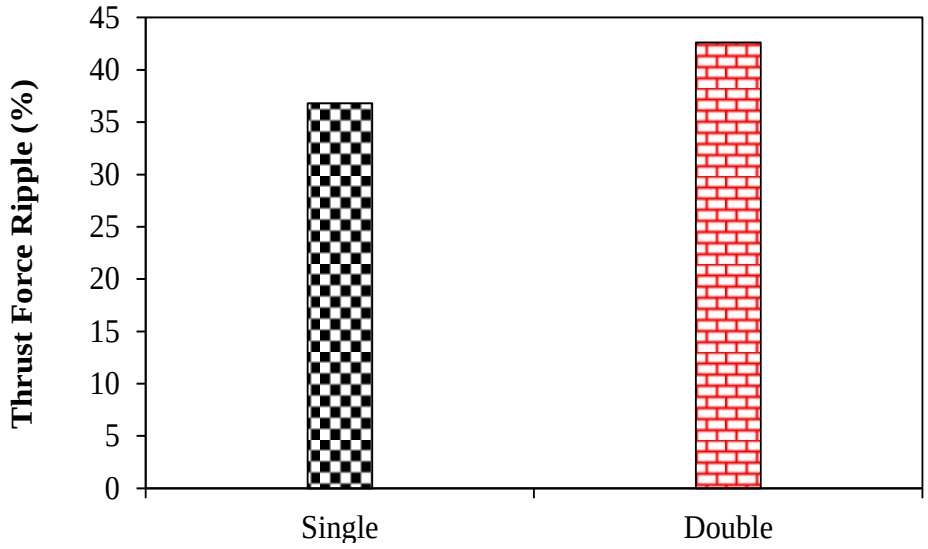

Fig. 5.37 Thrust force ripple comparison.

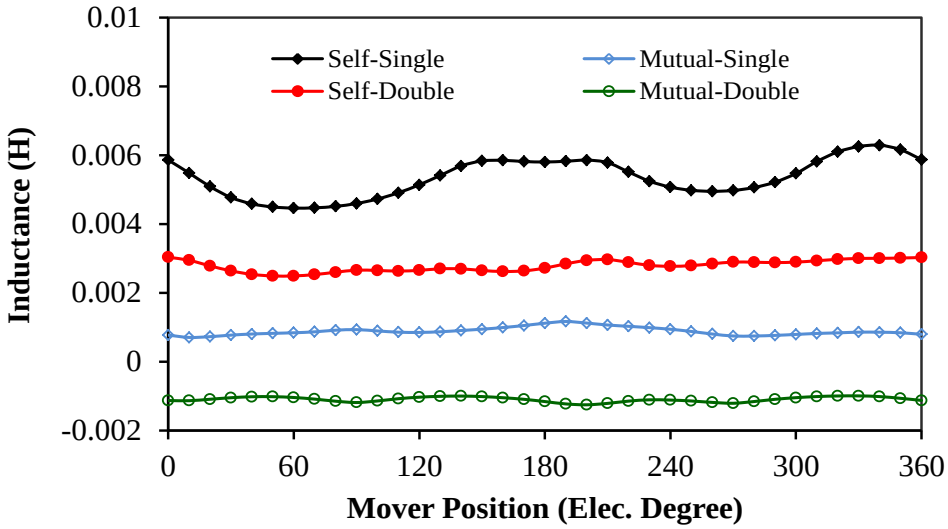

Fig. 5.38 Self- and mutual-inductnace comparison.

5.7.2 PS-IPM Tubular Machine

In the following section, PS-IPM tubular machines having double-layer and single-layer winding configurations will be compared in terms of no-load and load performance. It should be mentioned that the PS-IPM tubular machine with single-layer configuration has been designed and globally optimized with the same main design parameters and optimization conditions to that of the double-layer corresponding, respectively. Machine configurations are depicted in Fig. 5.39. Obviously, PS-IPM with single-layer winding has one coil per slot, whilst the doubly-layer winding counterpart has two coils which belong to different phases per one slot.

Phase A flux linkages and back-EMFs for both machines are compared in Fig. 5.40 and Fig. 5.41, respectively. It can be noted that the single-layer winding machine shows

about 8% higher flux linkage and back-EMF compared to the double-layer winding machine due to higher winding factor, which also has been confirmed for the rotatory PS-PM machine [AWA16]. Although the single-layer winding machine has higher back-EMF than that of the double-layer counterpart, the latter exhibits more sinusoidal back-EMF compared to the former, i.e. the back-EMF waveform of the single-layer machine exhibits lower order harmonic components.

Fig. 5.42 compares cogging force for both machines. Usually, winding configuration (single- and double-layers) has no effect on the machine cogging torque/force when the machine structure is not changed. As mentioned in the previous section, for tubular machines the structures of single- and double- layer windings are not the same, when an assistance teeth configuration is employed. Hence, it would be beneficial to compare the cogging force in both machines. It can be seen that the single-layer winding machine exhibits lower cogging force compared to its double-layer winding counterpart. Thereby, the double-layer winding machine shows higher thrust force ripple, as can be noted in Fig. 5.43. Furthermore, average thrust force variations with the copper loss for both machines are shown in Fig. 5.44. Apparently, the PS-IPM tubular machine with single-layer windings has slightly higher average thrust force than that with double-layer windings, due to higher back-EMF. Thrust force variation with mover position and different copper loss for both understudying machines is shown in Fig. 5.45 and Fig. 5.46. Additionally, thrust forces per magnet volume with different copper loss for the understudying machines are illustrated in Fig. 5.47. Higher average thrust force per magnet volume can be delivered by a single-layer winding machine, and thus, such configuration has better magnet usage compared to a double-layer winding machine. Moreover, the predicted winding inductances including self- and mutual inductances for the aforementioned machines are presented in Fig. 5.48. Notably, the PS-IPM tubular machine with single-layer configuration possesses higher self- inductance and lower mutual- to self-inductance ratio in comparison with its double-layer winding counterpart.

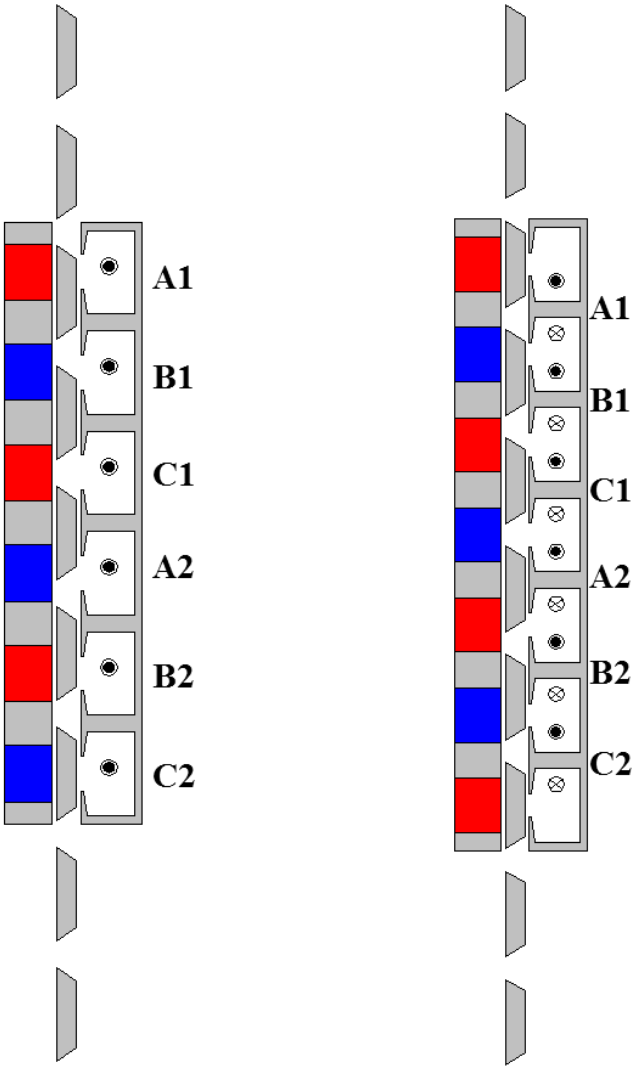

Fig. 5.39 Cross-section of both single-and double-layer winding PS-IPM tubular machines.

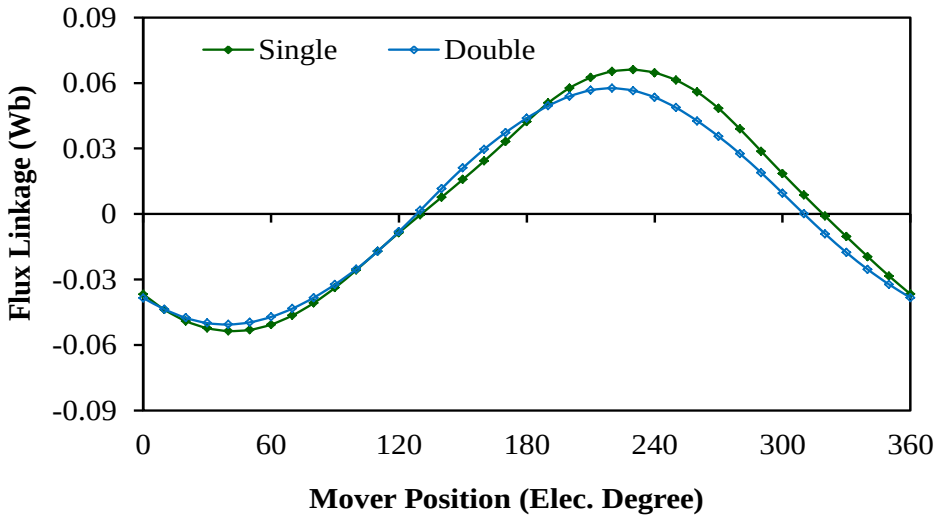

(a) Waveform

(b) Spectrum

Fig. 5.40 Phase A flux linkage comparison.

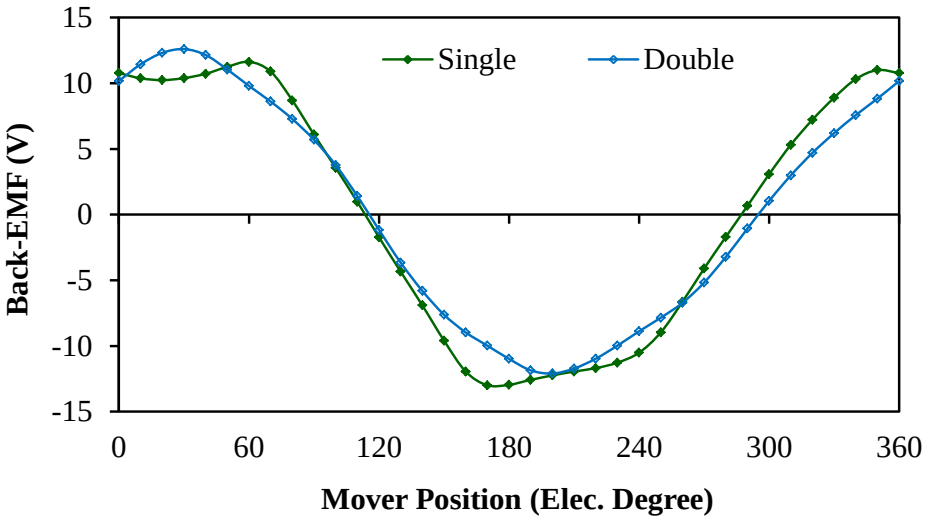

(a) Waveform

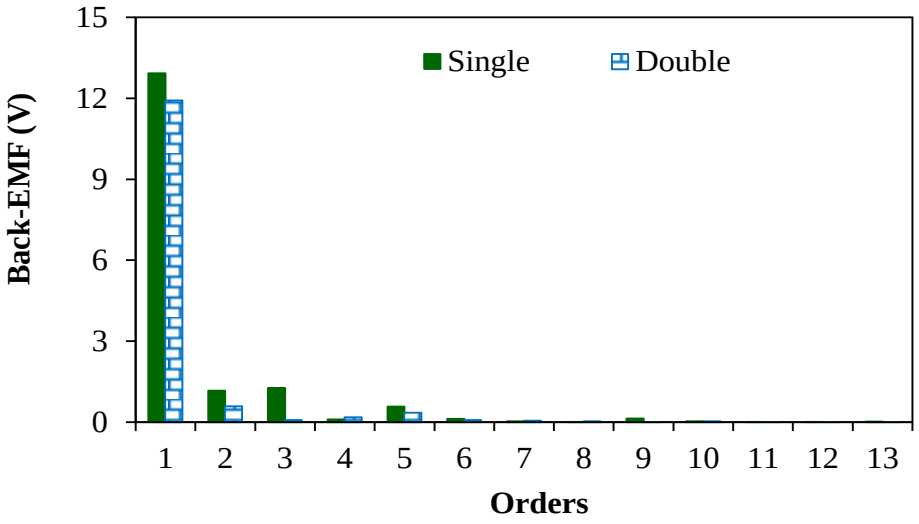

(b) Spectrum

Fig. 5.41 Phase A back-EMF comparison.

Fig. 5.42 Cogging force comparison.

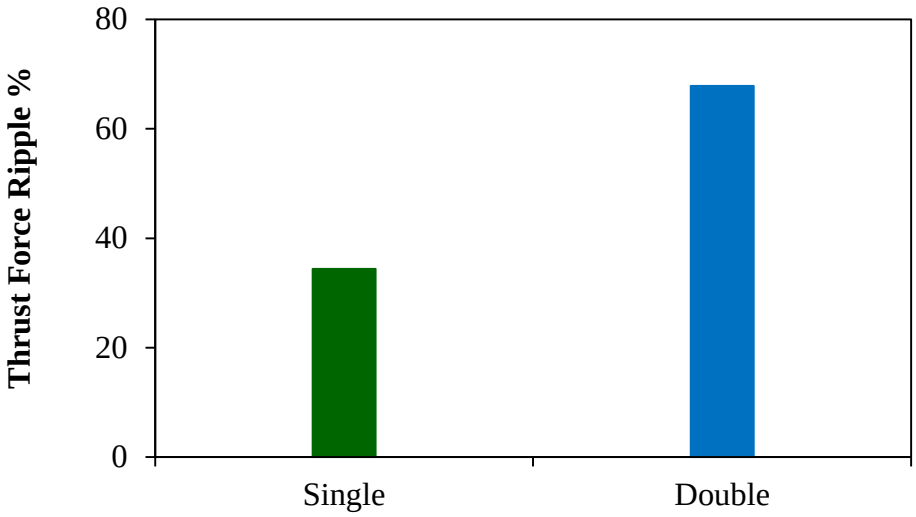

Fig. 5.43 Thrust force ripple comparison.

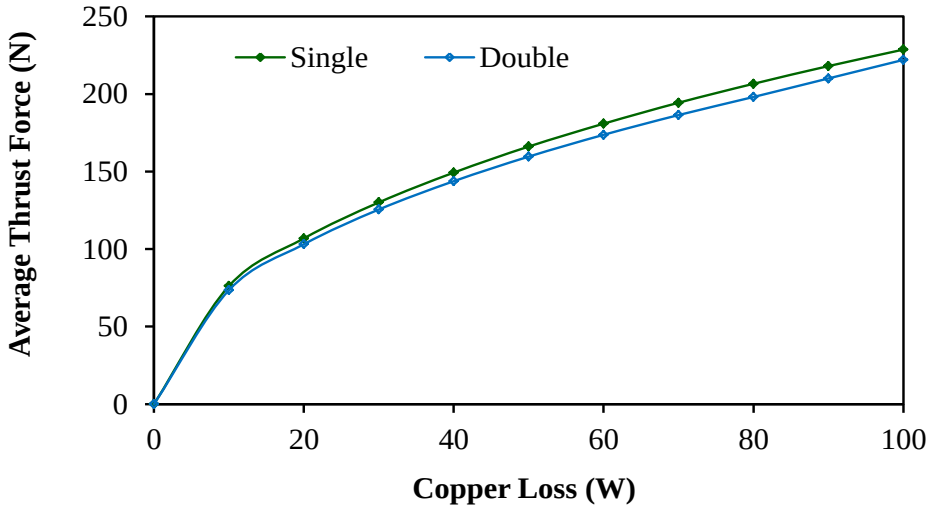

Fig. 5.44 Average thrust force variation with copper loss.

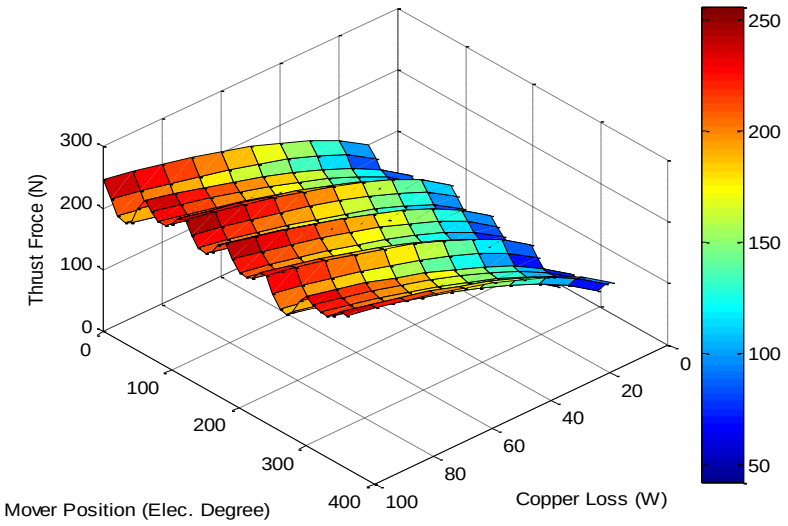

Fig. 5.45 Tubular SL- PS-IPM thrust force variation with mover position and copper loss.

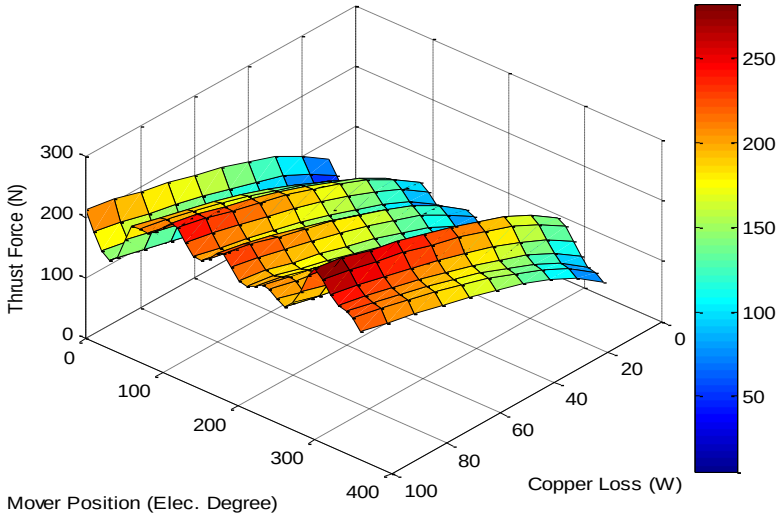

Fig. 5.46 Tubular DL- PS-IPM thrust force variation with mover position and copper loss.

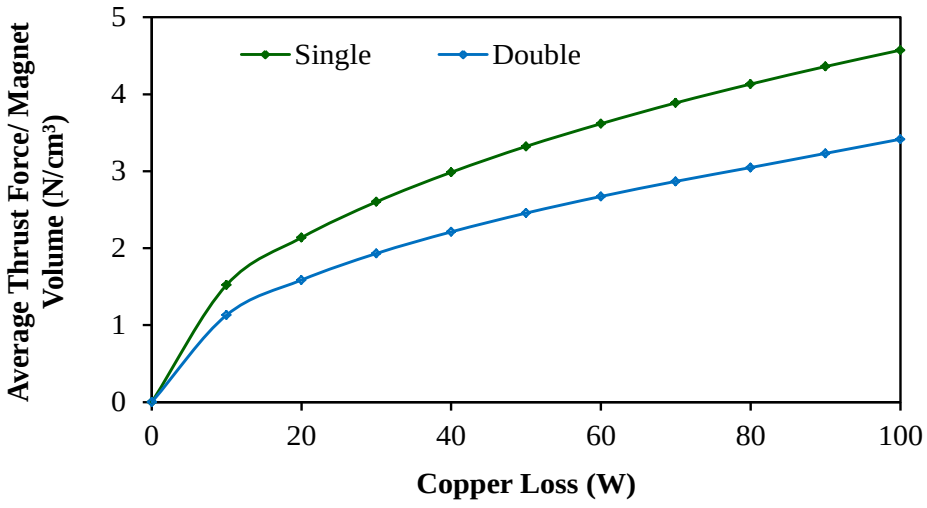

Fig. 5.47 PM utilization comparison.

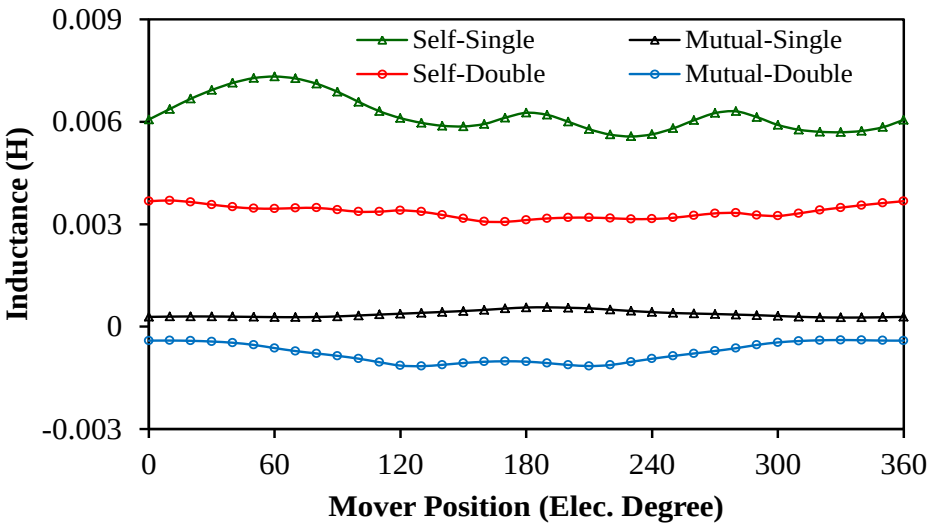

Fig. 5.48 Comparison of self- and mutual-inductnaces.

5.8 Summary

The electromagnetic performances of both 6/5 slot/pole PS-SPM and PS-IPM tubular machines are comprehensively compared based on their globally optimized configurations. It is revealed that the PS-IPM tubular machine exhibits higher thrust force, better magnet utilization and a wider constant power operation region compared to the PS-SPM tubular machine. On the other hand, the PS-SPM tubular machine has less cogging force and consequently less thrust force ripple than the PS-IPM tubular machine. Although the PS-IPM tubular machine shows higher iron loss in comparison with the PS-SPM tubular machine, it has about 78% lower magnet eddy current loss than that of the PS-SPM tubular machine. Moreover, both machines possess good PM demagnetization withstand capability. Finally, the influence of the winding layout, i.e. single- and double-layer windings, on the performances of both machines has been investigated. It is found that higher average thrust per magnet volume as well as less thrust force ripple can be obtained with a single-layer winding configuration for both machines compared to their double-layer winding counterparts.

Chapter6. Single-Phase Short Stroke Permanent Magnet Tubular Machines with Partitioned Stator

6.1 Introduction

Generally, PM tubular machines can be classified into short stroke and long stroke tubular machines by considering the mover travelling displacement [WAN01]. The interest of SPSS-PMTMs is considerably increased over last few years, and they have been applied in healthcare [JI13], wave energy extraction [AND13], and household appliance [WAN08d].

As a promising candidate for refrigerator compressor application a SPSS-SPMTM was presented in [WAN08d]. The machine comprises of C-core stator and two-pole PM Halbach magnetized mover. It has been demonstrated that the machine can offer good performance with efficiency about 93%. On the other hand, [WAN10] investigated the effect of main design parameters on the SPSS-SPMTM efficiency, and an approach to achieve the maximum machine efficiency was described. Furthermore, in order to reduce the eddy current loss and minimize the moving mass, the aforementioned machine has been redesigned with non-ferromagnetic back-iron mover in [IBR08]. Such a machine has the advantage of low mover mass which results in enhancement of the dynamic capability. However, it shows less efficiency than the machine with ferromagnetic back-iron mover. The influence of winding configuration on the performance of the aforementioned machine was introduced in [WAN07]. It has been concluded that the machine with C-core has a higher thrust force than that with distributed winding. Additionally, [ABD13] introduced a new magnet configuration of the existing machine. The magnet shape was changed to be trapezoidal instead of rectangular shape. The influence of the split ratio, the PM angle and the axial magnet width to pole pitch ratio, on the machine losses and efficiency was examined. E-core stator, Halbach magnet pattern mover SPSS-SPMTM has been designed and analysed in [ZHU08e]. The radial magnet width to pole pitch ratio was optimized for maximum thrust force, and the combination of stator tooth and mover pole numbers has been determined. It was confirmed that the difference between the stator tooth and mover pole numbers should be equal to one. In [CHE08], a comparison of E- and C-core SPSS-PMTM with radial, axial and Halbach magnetized PM movers has been presented. It was found that the E-core machine with axially magnetised magnet mover

produces similar peak thrust force to that with E-core Halbach magnetized mover with half amount of magnet usage.

Although all abovementioned machines exhibit high thrust force, such topologies suffer from thermal dissipation difficulty. Thereby, switched flux permanent magnet (SFPM) SPSS-PMTM was designed in [ZHE14], and the influence of leading design parameters on the machine performance has been investigated. The machine has simple and robust mover. However, it exhibits less power density compared to the conventional PM mover counterpart. Thus, [ZHE15] introduced dual stator SFPM-SPSSPMTM in order to enhance the power density of the single stator SFPM-SPSS-PMTM. The machine comprises of two stators having identical mechanical structures. Each stator consists of C-core with annular winding and two PMs that are oppositely magnetized in axial direction, while the mover is yokeless made of two iron pieces. It has been observed that better performance with lower mover mass can be obtained by the dual stator machine compared to the single stator machine. However, the magnet volume is increased.

Recently, a new topology so-called partitioned stator PM machine in which each excitation source is placed in separated stators has been designed in [ZHU15]. It was demonstrated that better inner space utilization can be achieved, and the PM heat dissipation as well as the conflict of electrical and magnetic loadings can be overcome. In this chapter, novel SPSS-PMTMs, known as partitioned stator (PS) SPSS-SPMTM and PS-SPSS-IPMTM are proposed in which the concept of partitioned stator is adopted. The structures of the machines are described, and the influence PM pole alignment with stator slot or stator tooth is investigated. In addition, the impact of the mover pole on the proposed machine performances is investigated, and the main design parameters of the proposed machines have been optimized. Moreover, the performance of the machines are analysed and compared.

6.2 Machine Configurations

The proposed machines consist of two stators and one mover. The outer stator is designed with E-core and two annular windings having opposite current direction. On the other hand, the PMs are located on the inner stator, while the iron pieces of the mover are sandwiched between the two stators. It is worth mentioning that the difference between the proposed machine configurations is the PM location, i.e. they are mounted on the surface of the inner stator with radial magnetization for PS-SPSS-

SPMTM, whilst the PMs are embedded on the inner stator iron with axial magnetization for the PS-SPSS-IPMTM. It should be emphasized that the PS-SPSS-IPMTM is designed with two configurations, i.e. PS-SPSS-IPMTM-1 with one magnet pole and PS-SPSS-IPMTM-2 with two magnet poles. Fig. 6.1 shows the machine configurations. The design specifications of the aforementioned machines are listed in Table 6.1.

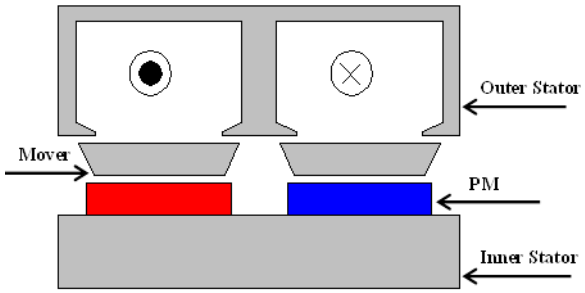

PS-SPSS-SPMTM

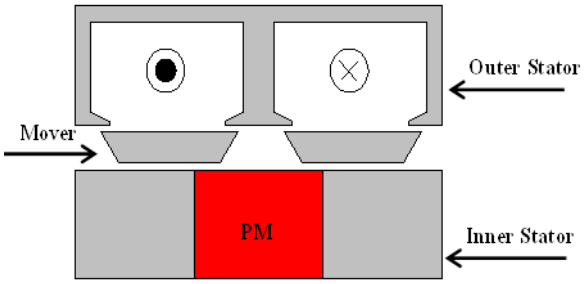

PS-SPSS-IPMTM-1

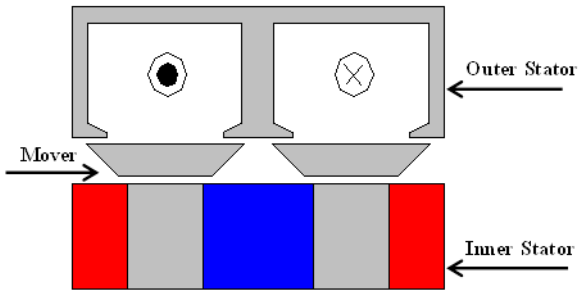

(c) PS-SPSS-IPMTM-2

Fig. 6.1 Machine configurations.

Table 6.1 Machine main design parameters

Items	PS-SPSS-SPMTM/ PS-SPSS-IPMTM
Outer radius	35 mm
Machine active length	47.2 mm
Inner air gap length	0.8 mm
Outer air gap length	0.8 mm
No. of slots	2 slots
No. of mover poles	2 poles
Current density (rms)	4 A/mm^2
No. of turns per coils	350
Slot pitch	23.6 mm
Pole pitch	23.6 mm
Stroke length	±4 mm

6.3 Influence of Permanent Magnet Alignment

In order to obtain a proper design of the proposed machines, which should be able to produce the oscillation, the influence of the PM pole alignment with either stator slot or stator tooth will be investigated. Hence, two configurations for each machine are designed as shown in Fig. 6.2. It is worth mentioning that model-1 is referred to the PS-SPSS-SPMTM where the PM poles are aligned with the stator teeth, while the PS-SPSS-SPMTM, in which the PM poles align with the stator slots, is known as model-2. On the other hand, model-3 and model-4 represent PS-SPSS-IPMTM where the PM poles are designed to be in alignment with stator teeth and stator slots, respectively. It has been proved that in order to achieve the oscillation, profile of the back-EMF with the mover displacement for the SPSS-SPMTM must not be in linear pattern [CHE12]. Therefore, the no-load performance of the aforementioned machines are analysed and compared. Flux linkage and back-EMF variations with the mover displacement of the two configurations of the PS-SPSS-SPMTM are compared in Fig. 6.3 and Fig. 6.4, respectively. It can be seen that the direction of the flux linkage of model-1 does not change with the mover position, resulting in approximately linear pattern of the back-EMF with the displacement. Thereby, according to [CHE12] such configuration is incapable of producing oscillation. In contrast, in model-2 both the direction and the amplitude of the flux linkage are varied with the mover displacement leading to non-linear back-EMF-displacement characteristic. Thus, oscillation can be achieved with this topology. Moreover, Fig. 6.5 and Fig. 6.6 show the variations of the flux linkage and the back-EMF with the mover displacement of model-3 and model-4, respectively. Obviously, model-3 is unable to achieve the oscillation due to the linearly profile of its back-EMF against the mover displacement. On the other hand, model-4 exhibits non-

linear back-EMF-displacement characteristic, and therefore oscillation production can be obtained with such a topology. According to above analysis it can be concluded that for PS-SPSS-SPMTM as well as PS-SPSS-IPMTM the PM poles should be aligned with stator slots.

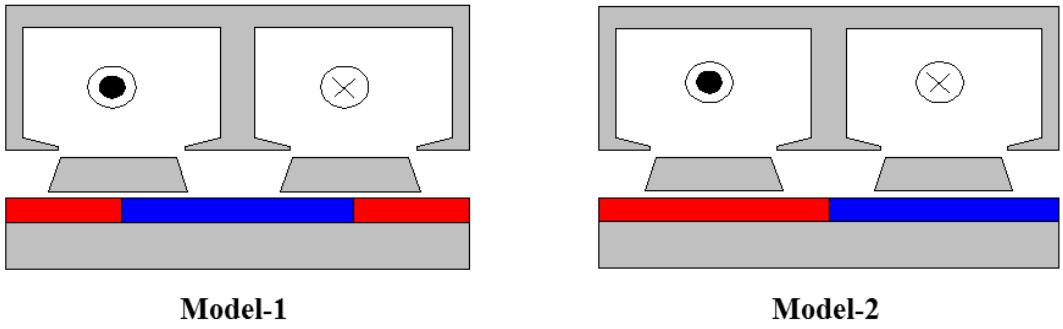

(a) PS-SPSS-SPMTM

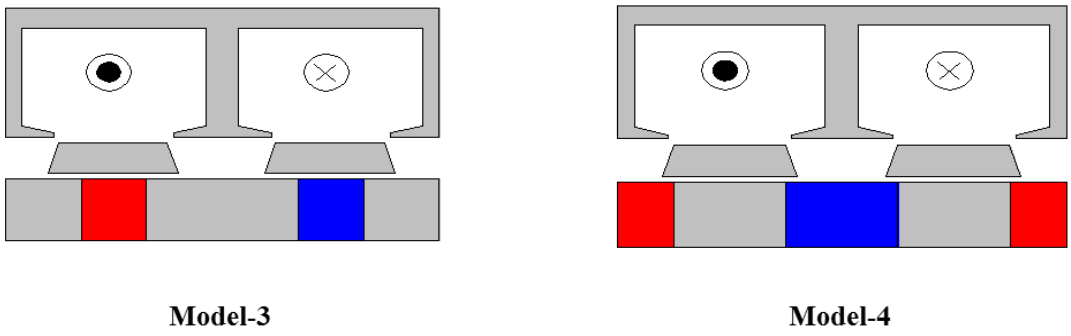

(b) PS-SPSS-IPMTM

Fig. 6.2 Analysed machines.

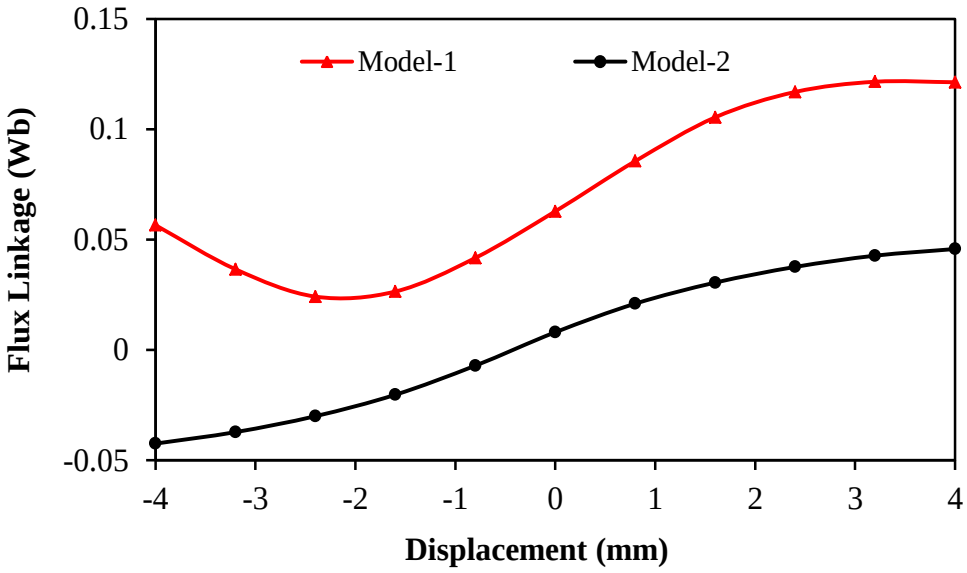

Fig. 6.3 Flux linkage comparison of PS- SPSS-SPMTM models.

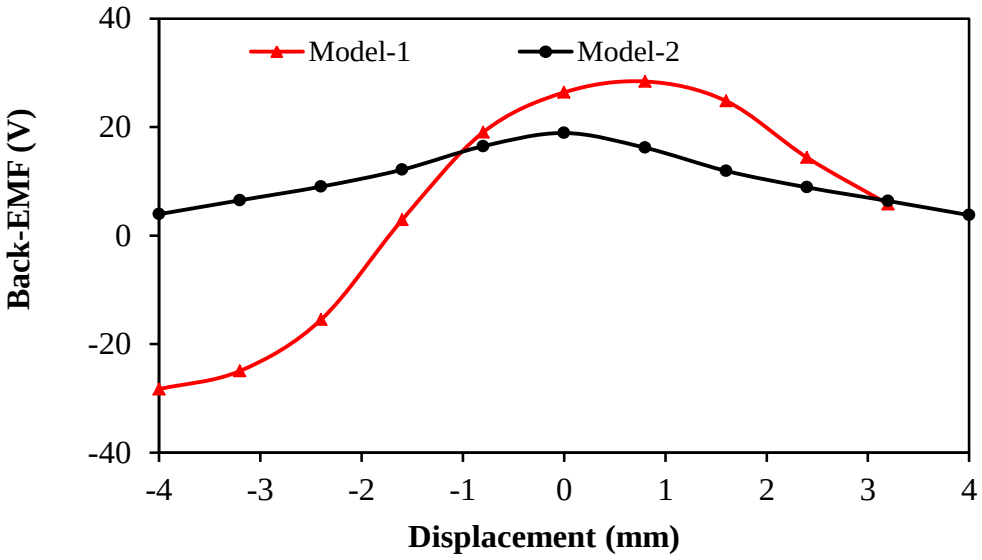

Fig. 6.4 Back-EMF comparison of PS- SPSS-SPMTM models.

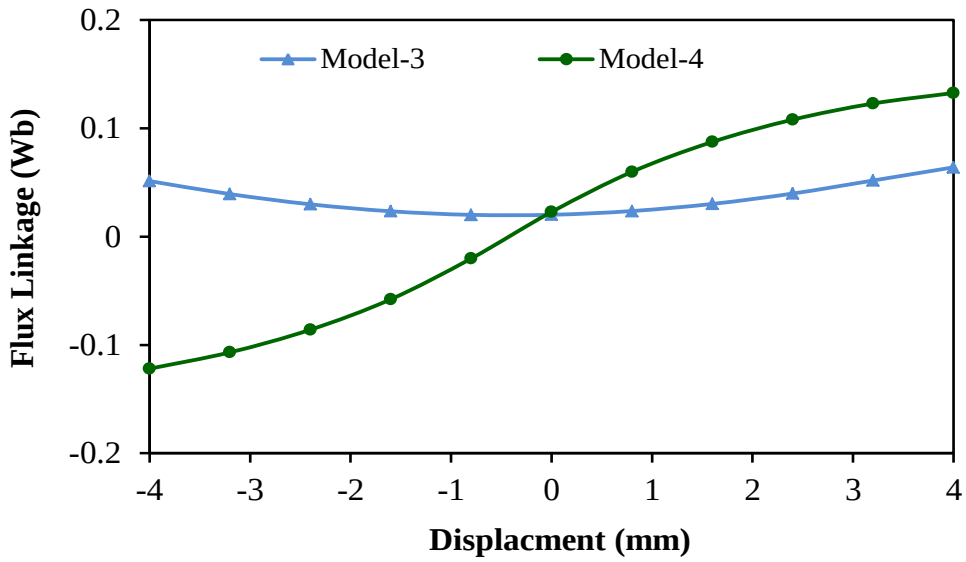

Fig. 6.5 Flux linkage comparison of PS- SPSS-IPMTM models.

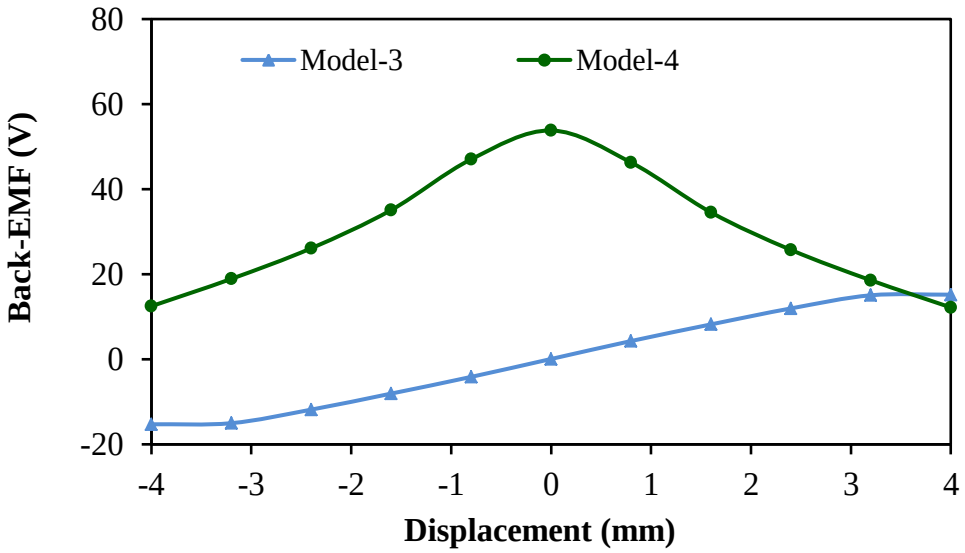

Fig. 6.6 Back-EMF comparison of PS- SPSS-SPMTM models.

6.4 Impact of Mover Pole Pitch on Machine Performances

In this section the influence of the mover pole pitch on the performance of the proposed machines is investigated. Each machine, i.e. PS-SPSS-SPMTM and PS-SPSS-IPMTM, has been designed with three different mover pole pitches, i.e. smaller than stator slot pitch, equal and larger than stator slot pitch. It should be noted that all the other dimensions of the understudying machines are not changed, in order to carry out equitable comparison.

Open circuit flux distributions of the PS-SPSS-SPMTMs and PS-SPSS-IPMTMs are shown in Fig. 6.7 and Fig. 6.8, when the flux linkage is maximum positive, zero and maximum negative, respectively. It can be clearly seen that the direction of the flux linkage changes with the mover position. Also, it should be noted that all machines exhibit similar flux line patterns. Flux linkage variations with mover displacement of the PS-SPSS-SPMTMs are compared in Fig. 6.9, whilst Fig. 6.11 compares flux linkage of the PS-SPSS-IPMTMs. On the other hand, Fig. 6.10 and Fig. 6.12 illustrate back-EMF profile with the mover displacement for PS-SPSS-SPMTMs and PS-SPSS-IPMTMs, respectively. It shows that for both configurations, i.e. PS-SPSS-SPMTM and PS-SPSS-IPMTM:

- The machines with mover pole pitch equal to the stator slot pitch exhibit the highest flux linkage and subsequently the highest back-EMF among other machines;

• The machines with mover pole pitch smaller than the stator slot pitch have the lowest flux linkage as well as back-EMF compared to other machines.

Such phenomena can be specifically described as when the mover pole pitch is shorter the mover iron pieces would be saturated, and the flux lines go from the PM to outer stator back-iron through the stator tooth without contribution to any flux linkage. In contrast, in case of longer mover pole pitch, flux line short circuit will be created in which the flux lines pass from the PM to the edges of the mover iron pieces, and return to the inner stator back-iron, and consequently they do not contribute to flux linkage. Hence, it can be seen that when the mover pole pitch of the proposed machines is equal to the stator slot pitch, the best performances could be delivered. Therefore, the mover pole pitch has been chosen to be equal to the stator slot pitch.

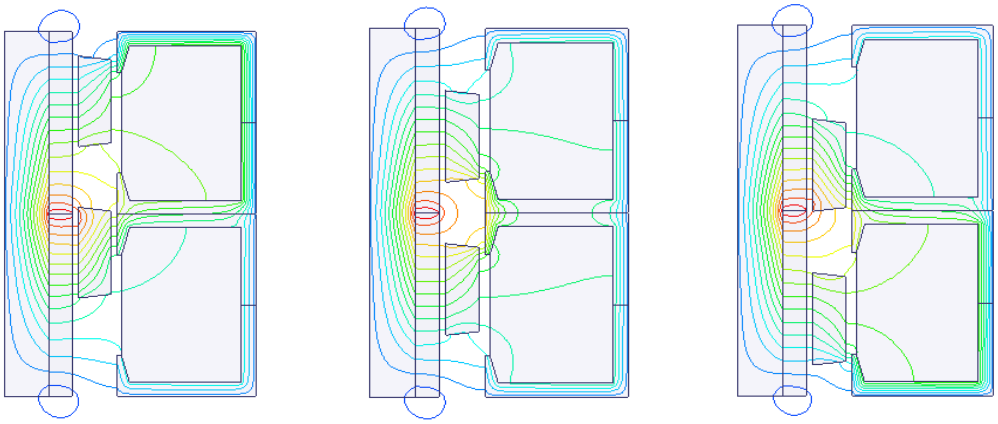

Max. Positive Displacement (+4) **Zero Displacement (0)** **Max. Negative Displacement (-4)**

(a)

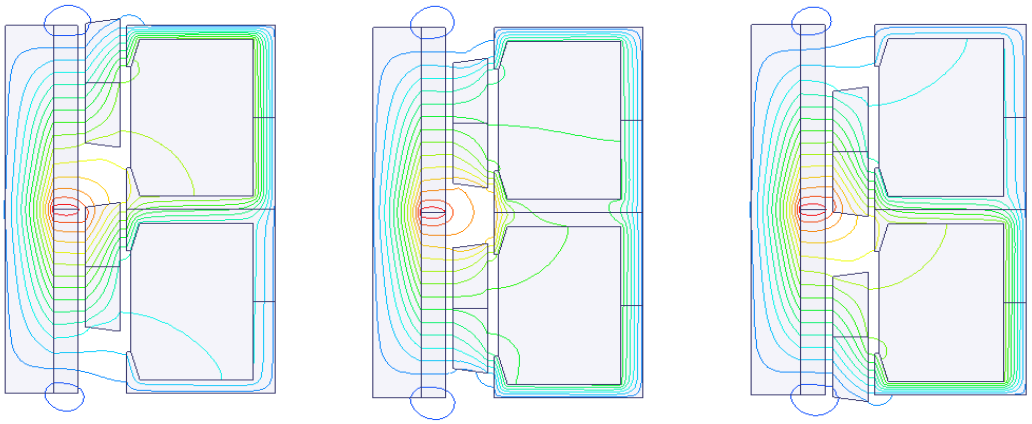

Max. Positive Displacement (+4) **Zero Displacement (0)** **Max. Negative Displacement (-4)**

(b)

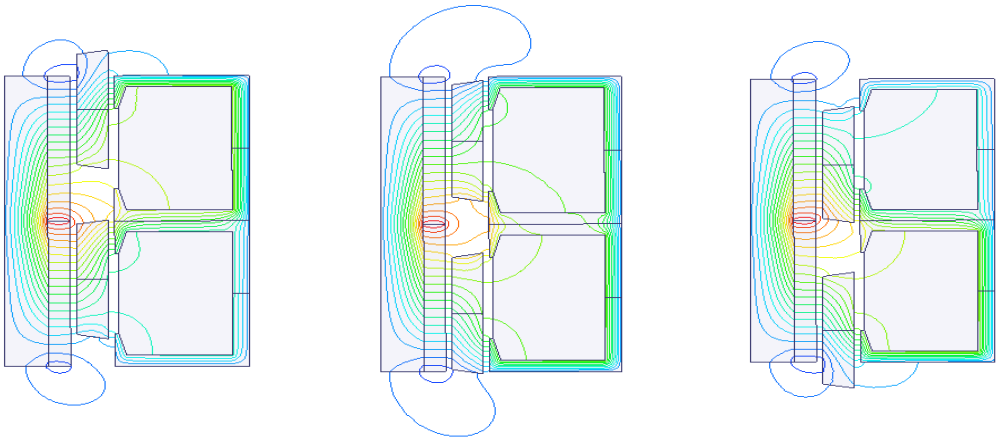

(c)

Fig. 6.7 Open-circuit field distributions of PS-SPSS-SPMTMs (displacement unit=mm).

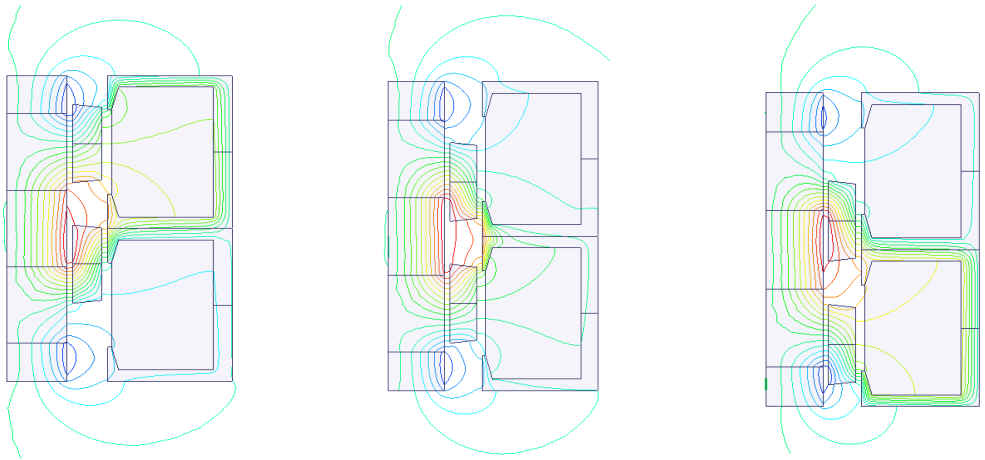

(a)

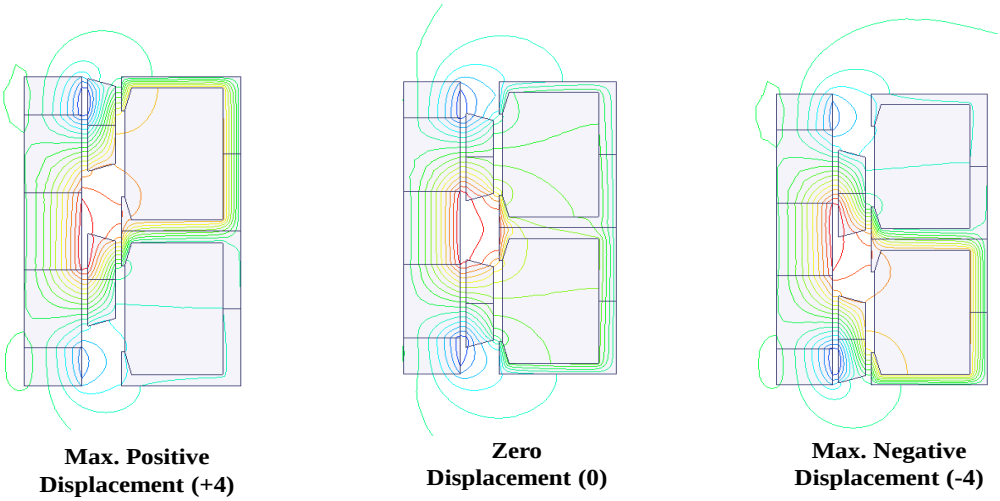

(b)

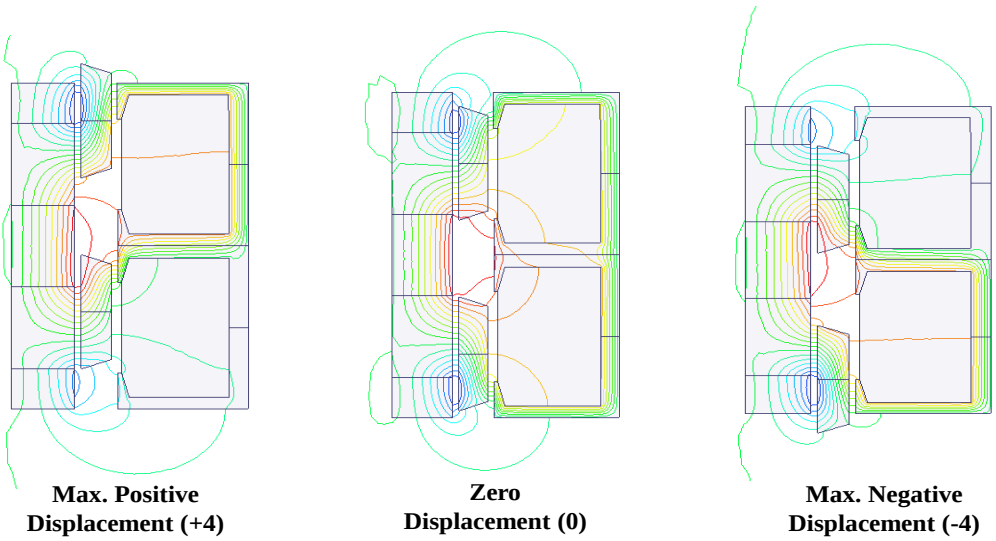

(c)

Fig. 6.8 Open-circuit field distributions of PS-SPSS-IPMTMs (displacement unit=mm).

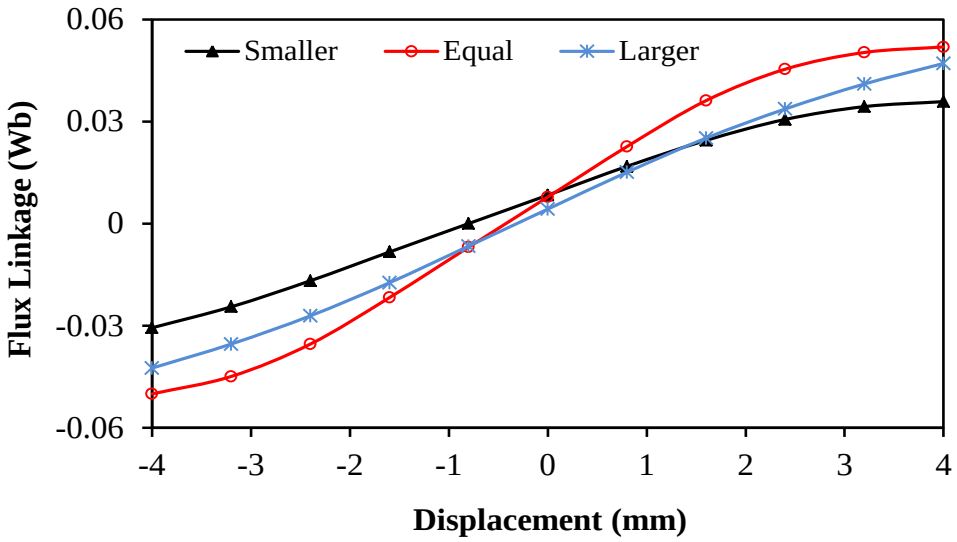

Fig. 6.9 Flux linkage comparison of PS- SPSS-SPMTMs.

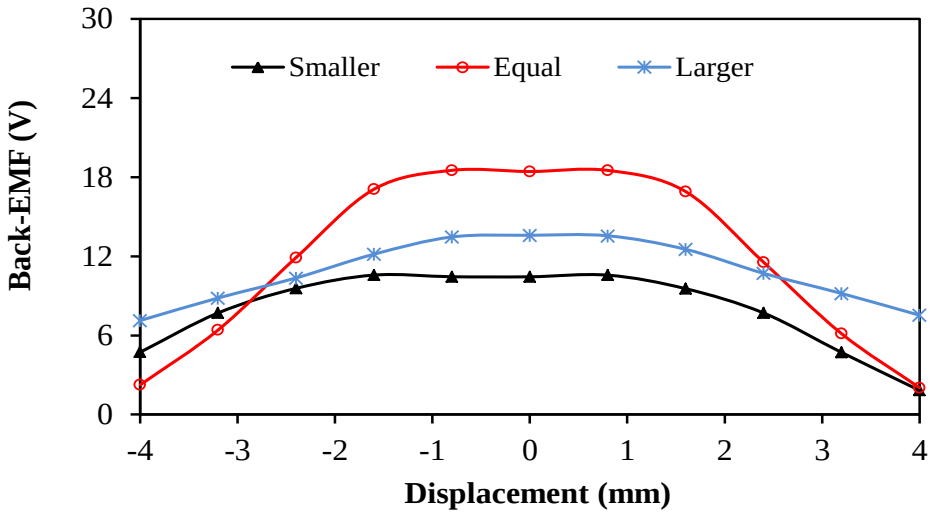

Fig. 6.10 Back-EMF comparison of PS-SPSS-SPMTMs.

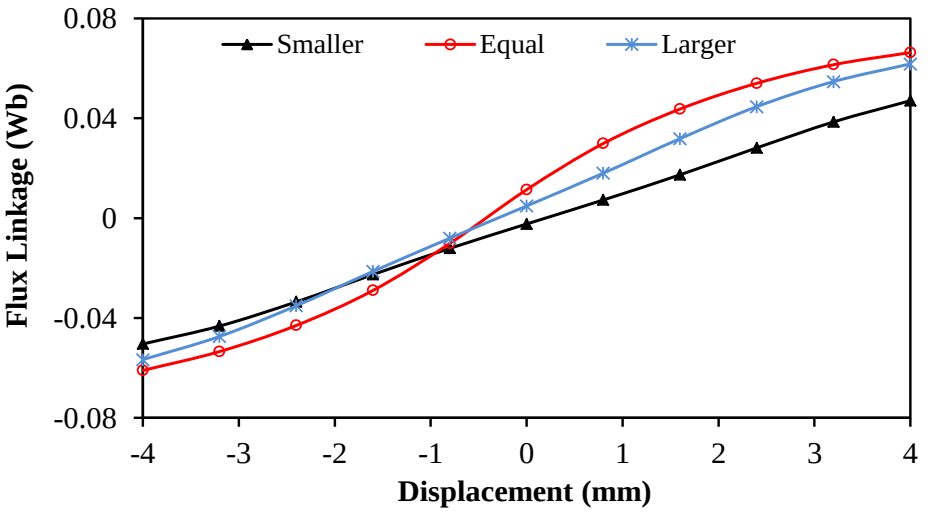

Fig. 6.11 Flux linkage comparison of PS- SPSS-IPMTMs.

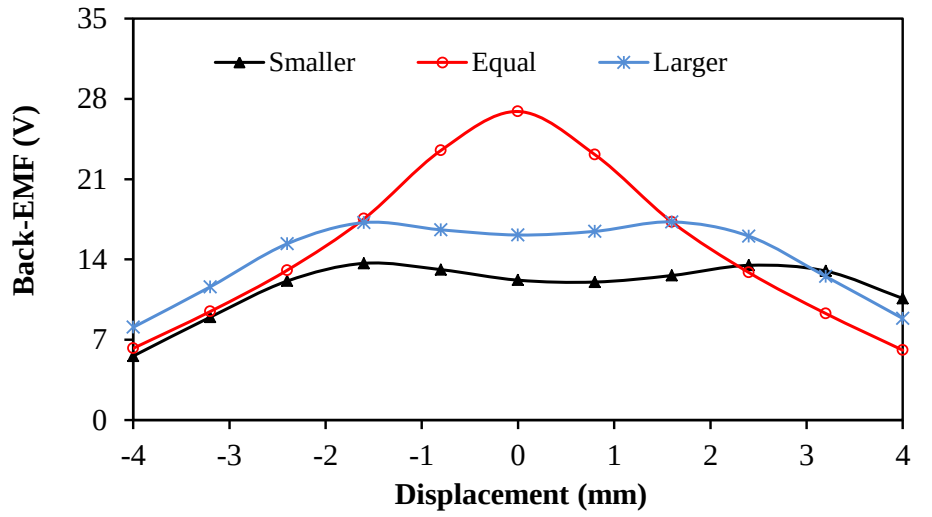

Fig. 6.12 Back-EMF comparison of PS- SPSS-IPMTMs.

6.5 Machine Optimizations

Global optimization has become a prevalent technique in machine design optimization. Hence, this section presents the global optimizations for the proposed machines in order to achieve maximum thrust force. The outer radius, machine active length, and current density are maintained constant through the optimization procedure. The parameters, which are varied during this optimization process, are defined in Table 6.2, while the main design parameters are illustrated in Fig. 6.13. Global optimization has been performed by utilizing a GA and FE model. The objective of the global optimization is to obtain the maximum average thrust force value with the initial and restriction values of the machine parameters. Table 6.3 presents the initial, constrain and optimal values of the design parameters that are optimized for maximum thrust force.

Table 6.2 Definitions of the optimized parameters

SR	Split ratio	$\frac{MGO}{OSR}$
TMPWR	Top mover pole pitch width ratio	$\frac{TMPW}{MPP}$
BMPWR	Bottom mover pole width pitch width ratio	$\frac{BMPW}{MPP}$
OSTWR	Outer stator tooth width ratio	$\frac{OSTW}{OSSP}$
OSSOR	Outer stator slot opening ratio	$\frac{OSSO}{OSSP}$
OSBITHR	Outer stator back iron thickness ratio	$\frac{OSBITH}{OSTH}$
TPMR	PM pole ratio	$\frac{TPM}{ISPP}$

In Table 6.2, $MTH, TMPW, BMPW$ and MPP are radial thickness, top piece width, bottom piece with and pole pitch, of the mover, respectively. $OSTW, OSSO, OSBITH,$ $OSTH$ and OSSP indicate tooth width, slot opening, back iron thickness, total height and slot pitch of the outer stator, respectively. $ISR, ISBITH$ and $ISPP$ represent radius and pole pitch of the inner stator, respectively, while TPM is magnet pitch. GI and GO correspond to the inner and the outer air-gap, respectively. The machine configuration with their optimal parameter values are shown in Fig.1.6.

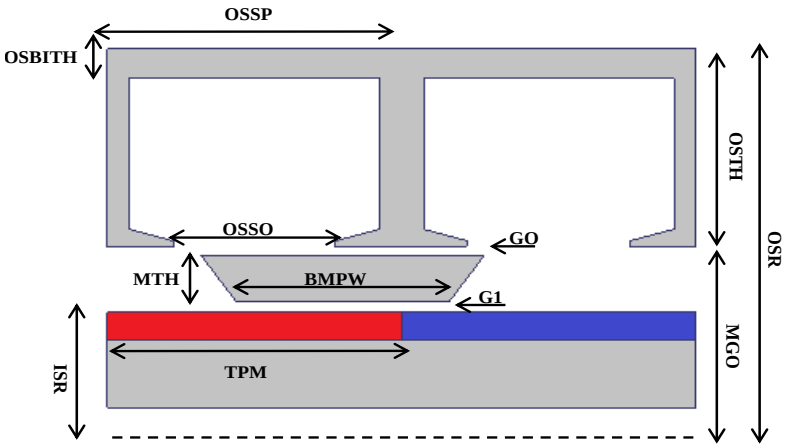

(a) PS- SPSS-SPMTM

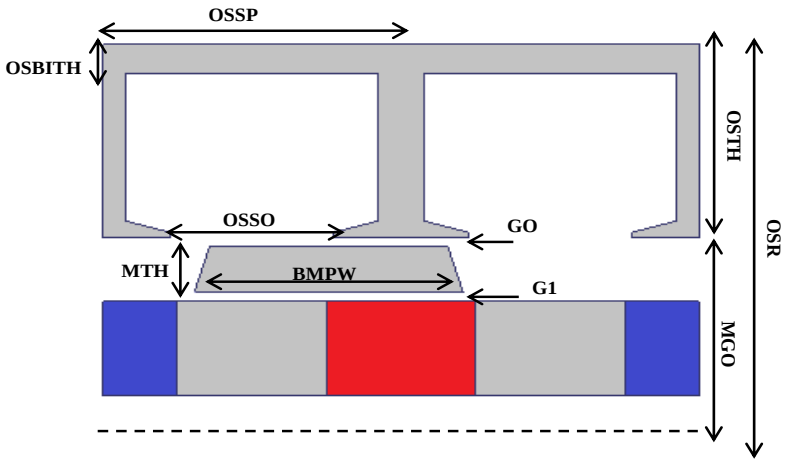

(b) PS- SPSS-IPMTM

Fig. 6.13 Main design parameters.

Table 6.3 Initial, restriction and optimal values of optimization parameters

Items	Initial	Restriction	Optimal		
			SPM	IPM-1	IPM-2
SR	0.5	[0.3, 0.75]	0.58	0.6	0.58
TMPWR	0.8	[0.3, 0.9]	0.73	0.75	0.85
BMPWR	0.6	[0.3, 0.9]	0.796	0.55	0.5
OSTWR	0.15	[0.1, 0.35]	0.17	0.167	0.17
OSSOR	0.5	[0.18, 0.7]	0.628	0.633	0.627
OSBITHR	0.15	[0.1, 0.3]	0.12	0.14	0.12
TPMR	-	[0.4, 0.9]	0.86	0.7	0.59
MTH (mm)	4	[3, 5.5]	3.5	3.5	3.5

6.6 Analysis of Machine Performances

6.6.1 Comparison of No-load and Load Performances

Open circuit flux distributions of the optimally designed machines are shown in Fig. 6.14, Fig. 6.15, and Fig. 6.16 , when the flux linkage is maximum negative, zero and maximum positive, respectively. It can be clearly seen that the direction and magnitude of the flux linkage change with the mover position. Also, it should be noted that all machines exhibit similar flux line patterns. However, PS-SPSS-IPMTM-2 suffers from high flux leakage at both ends, due to the PM location on the both ends of its inner stator. Flux linkage variations with mover displacement of the three machines are compared in Fig. 6.17. It shows that the PS-SPSS-IPMTM-2 has the highest flux linkage among other machines. This is because of the largest amount of PM usage in such configuration. On the contrary, the PS-SPSS-IPMTM-1 exhibits the lowest flux linkage compared to the other machines, owing to the lowest PM volume. Fig. 6.18. compares the profile of back-EMF with the mover displacement for the analysed machines. Higher back-EMF can be achieved by the PS-SPSS-IPMTM-2, since it has the highest flux linkage. Furthermore, open circuit cogging forces of the understudying machines, which may result in machine noise and vibration, are illustrated in Fig. 6.19, whilst their thrust forces versus mover displacement are compared in Fig. 6.20. It can be noted that the highest thrust force is for PS-SPSS-IPMTM-2. On the other hand, PS-SPSS-SPMTM produces the lowest cogging force compared to PS-SPSS-IPMTM topologies, which is beneficial for applications requiring smooth operation. Moreover, the lowest thrust force and the highest cogging force are for the SPSS-IPMTM-1.

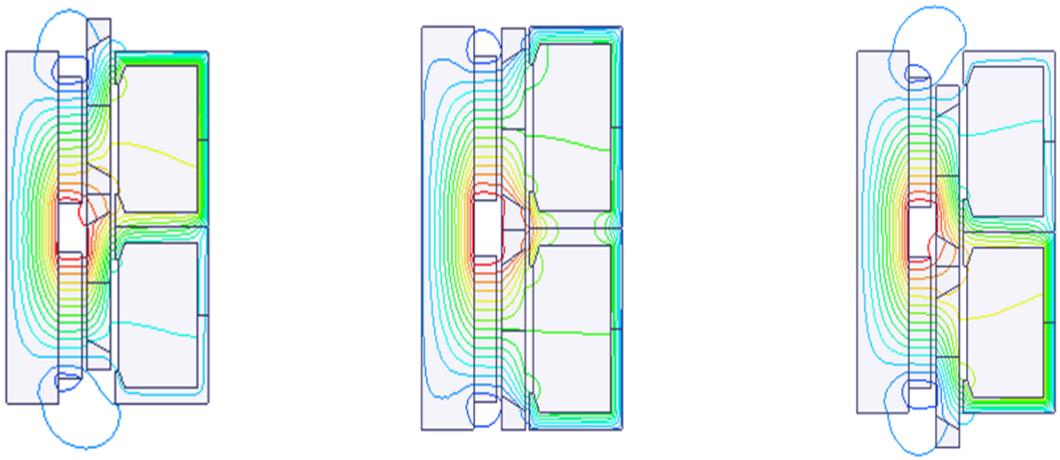

Fig. 6.14 Open-circuit field distributions of PS-SPSS-SPMTM (displacement unit=mm).

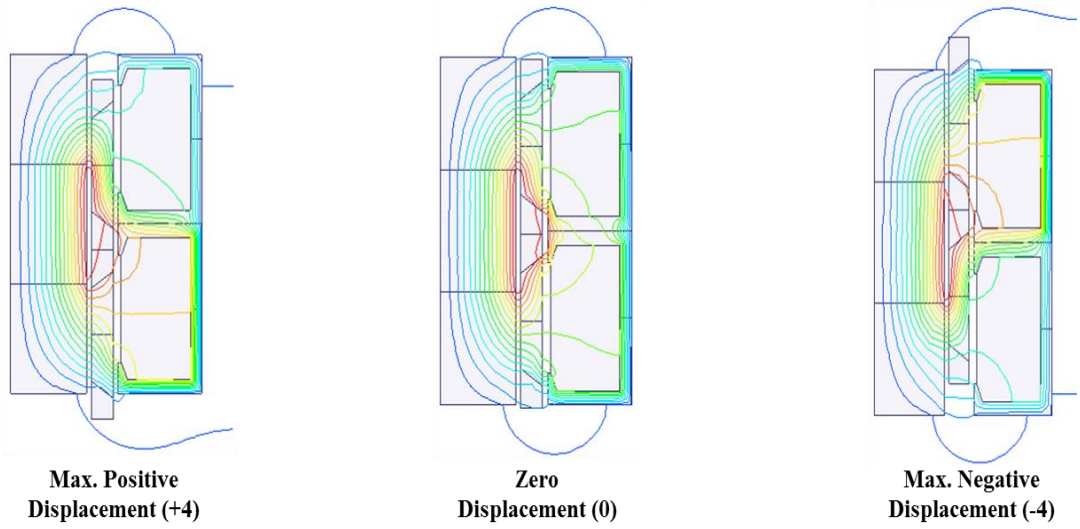

Fig. 6.15 Open-circuit field distributions of PS-SPSS-IPMTM-1 (displacement unit=mm).

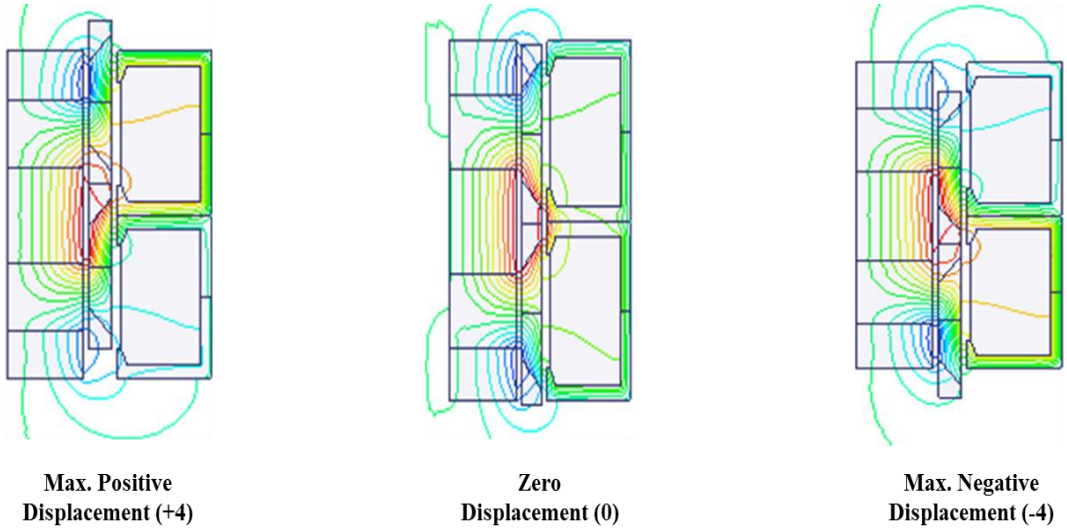

Fig. 6.16 Open-circuit field distributions of PS-SPSS-IPMTM-2 (displacement unit=mm).

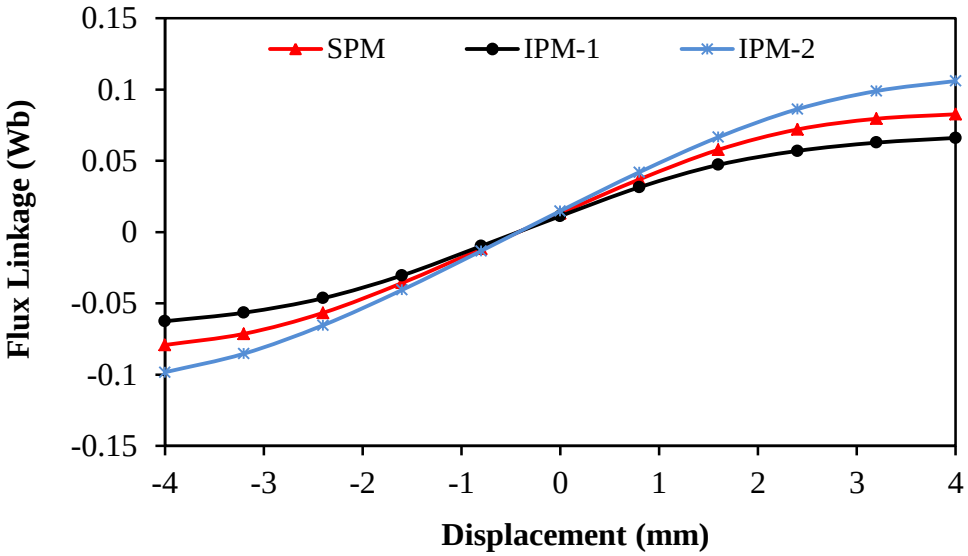

Fig. 6.17 Flux linkage comparison.

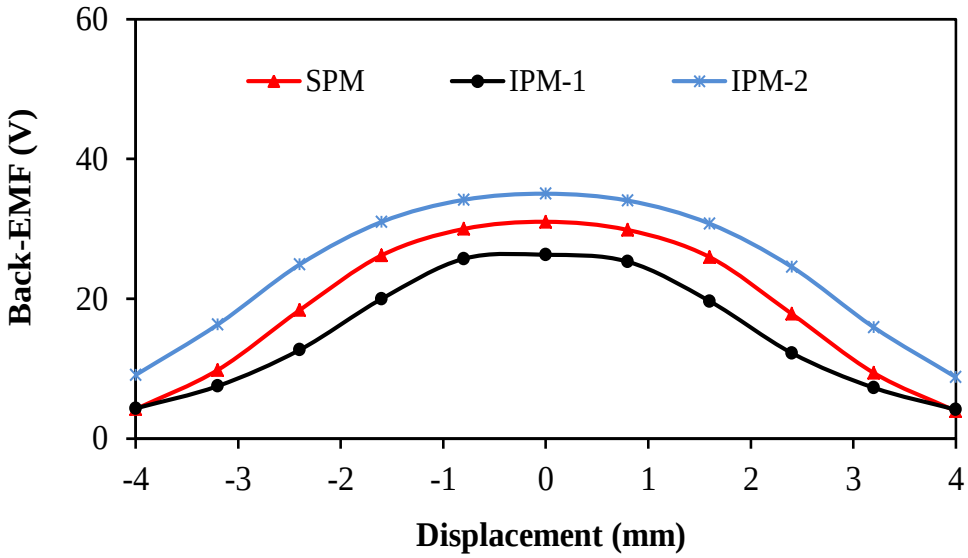

Fig. 6.18 Back-EMF comparison at velocity of 1m/s.

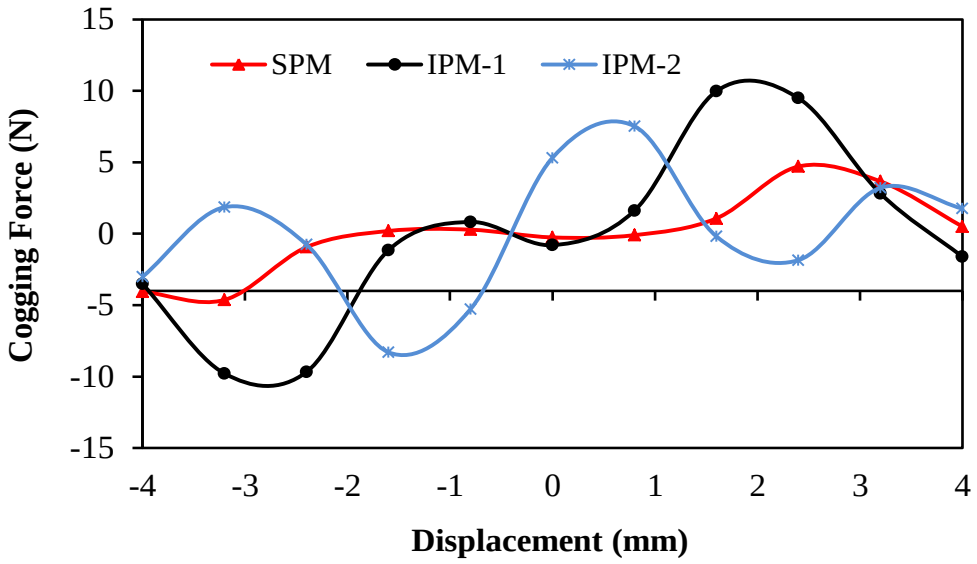

Fig. 6.19 Cogging force comparison.

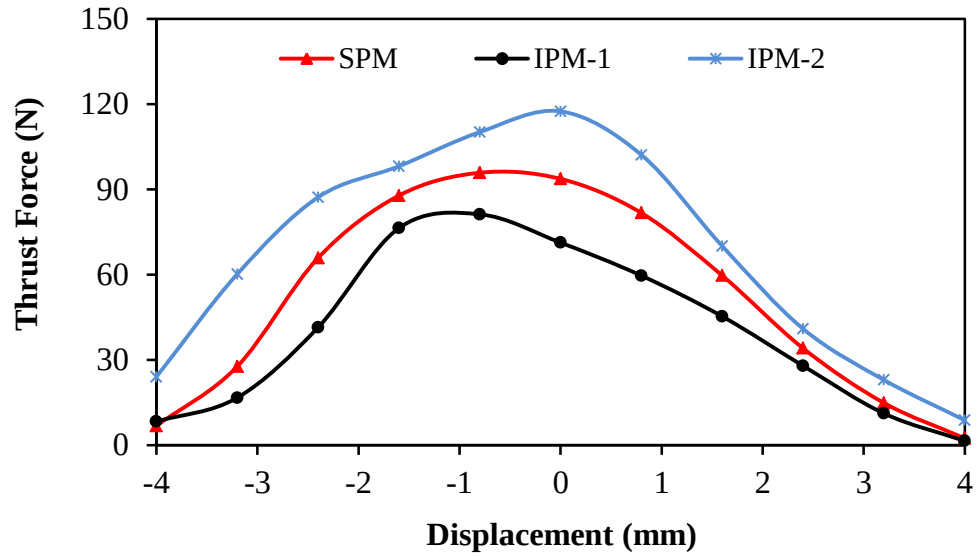

Fig. 6.20 Thrust force comparison.

6.6.2 Loss Comparison

Generally, the electrical machine performance, particularly the thermal behaviour and the efficiency, are strongly affected by losses. Therefore, losses should be taken into consideration. The method explained in Chapter 3 is utilized to determine the losses in all the proposed machines. Iron loss variations with the velocity for all machines are compared in Fig. 6.21. The highest iron loss is shown by the PS-SPSS-IPMTM-2. In contrast, the PS-SPSS-IPMTM-1 exhibits the lowest iron loss compared to other topologies. Furthermore, Fig. 6.22 illustrates the magnet eddy current loss with the velocity for the three machines. It can be seen that the proposed machines have very low

magnet eddy current loss. Hence, it can be concluded that the potential problem in conventional machine, i.e. high PM temperature caused by eddy loss, can be significantly reduced by using PS-PM configuration. It should be noted that both PS-SPSS-IPMT topologies have less magnet eddy current loss compared to that of PS-SPSS-SPMTM.

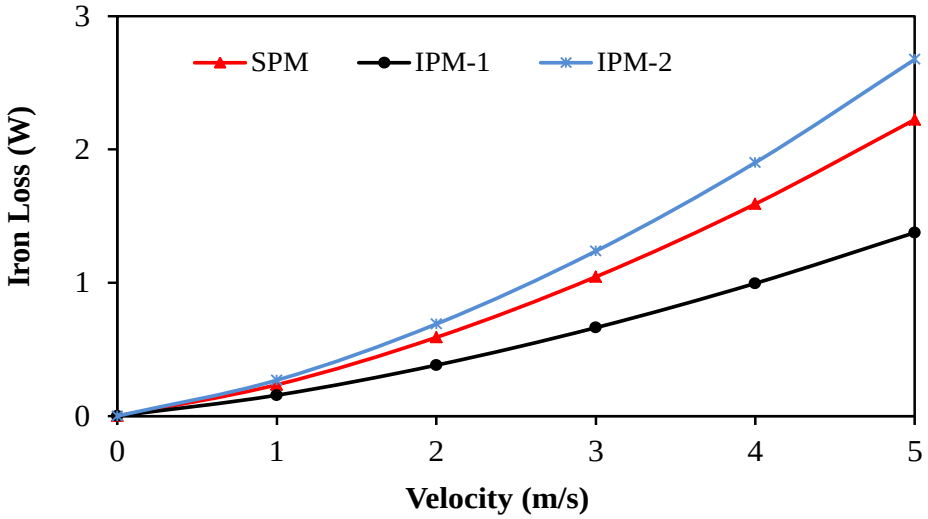

Fig. 6.21 Iron loss comparison.

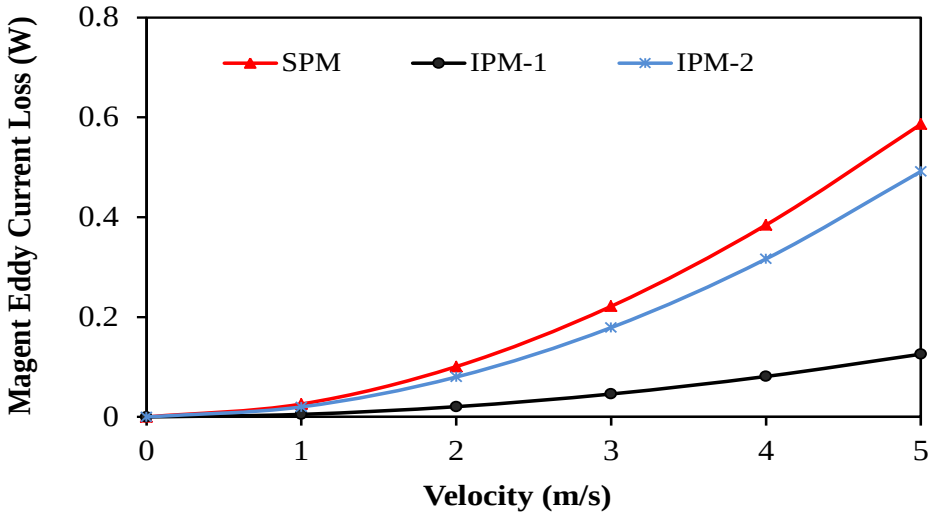

Fig. 6.22 Magnet eddy current loss comparison.

Table 6.4 summarizes the analysed machine specifications, where v_m, v_{PM} and M_m represent the total machine volume, the permanent magnet volume and the mover mass, respectively. All the machines have the same active volume as well as mover mass, while the magnet volume is different. The magnet usage in the PS-PSS-IPMTM-2 is about 46% and 34% higher than that of the PS-PSS-IPMTM-1 and the PS-PSS-

SPMTM, respectively. The machine performances can be summarized as follows: the highest flux linkage and back-EMF and consequently the highest thrust force are found in the PS-PSS-IPMTM-2. In contrast, the PS-PSS-IPMTM-1 produces the lowest thrust force among the other machines, due to the lowest flux linkage and back-EMF. On the other hand, the PS-PSS-SPMTM shows comparable thrust force performance to that of the PS-PSS-IPMTM-2. Additionally, the lowest cogging force can be achieved by PS-SPSS-SPMTM, whilst the highest one is for the PS-PSS-IPMTM-1. In terms of loss, the PS-PSS-IPMTM-1 has the lowest iron and magnet eddy current losses among the other machines. Although the PS-PSS-IPMTM-2 shows higher iron loss compared to the PS-PSS-SPMTM, the later has higher magnet eddy current loss than the former.

Table 6.4 Design specifications of the analysed machines

Items	v_m	v_{PM}	M_m
	cm^3	cm^3	g
PS-SPSS-SPMTM	181.64	10.58	146.874
PS-SPSS-IPMTM-1	181.64	12.952	146.874
PS-SPSS-IPMTM-2	181.64	19.88	146.874

6.7 Summary

Based on the partitioned stator concept, new SPSS-PMTMs have been proposed in this chapter. The influence of alignment of the PM poles with the stator teeth or the stator slots is investigated. It is concluded that the PM poles must be aligned with the outer stator slots to obtain the oscillated movement of the mover in PS-SPSS-PMTMs. Moreover, under same design specification and optimization conditions, the proposed machines have been optimized for maximum thrust force. The machine performances are analysed and compared. It is observed that the proposed machines possess the merits of light mover mass and low magnet eddy current loss. Furthermore, the PS-PSS-SPMTM can achieve a comparable thrust force to that of the PS-PSS-IPMTM-2, but the magnet usage in such topology is about 34% less compared to that of the PS-PSS-IPMTM-2. Despite the fact that the PS-PSS-IPMTM-1 has the lowest open circuit and on load performances among the other topologies, it shows the lowest iron as well as magnet eddy current losses compared to the other machines.

Chapter7. Comparison of PS-PM Linear Machines with Their Conventional Counterparts

7.1 Introduction

In the previous Chapters, i.e. 3, 4 and 6, novel PS-PM linear machines, including planner, tubular and single-phase short stroke tubular machines, were designed and analysed. The idea of having dual active stators with one passive mover has been adopted on these machines. This is because such a configuration inherits the benefits of better inner machine space utilization as well as avoiding the compromise between the electrical and magnetic loadings. Consequently, the major obstacles in the stator PM machines can be overcome.

In order to discuss the advantages and disadvantages of the proposed machines compared to their existing counterparts, this chapter introduces a comparison between the PS-PM linear machines and their corresponding conventional machines. The comparison will include the configuration, the operating principle and the electromagnetic performance.

7.2 Comparison of PS-FRPM Linear Machine with Conventional FRPM and SFPM Linear Machines

7.2.1 Configuration and Operation Principle

Fig. 7.1 shows cross-sections of the understudying machines. It can be clearly noted that all topologies have one passive part. On the contrary, the other part is different, i.e. both conventional machines have one active part in which the PMs and the armature windings are located. On the other hand, the excitation sources of the PS-FRPM linear machine are on separate parts. It should be mentioned that all the machines have the same following features:

- Winding configurations, i.e. concentrate winding
- No. of turns per phase
- Slot/pole combinations
- Active length and length in Z-direction
- Velocity and current density

The other machine parameters that were determined by global optimization are listed in Table 7.1.

It is worth mentioning that from the perspective of operating principle, all the understudying machines operate under the same operation principle. They all work under what is known as the switched flux concept as it illustrated in Chapters 2 and 3.

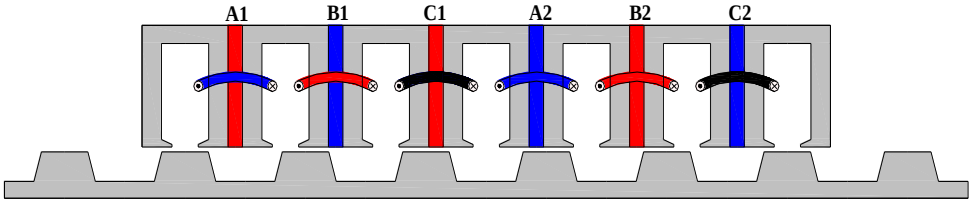

(a) SFPM linear machine

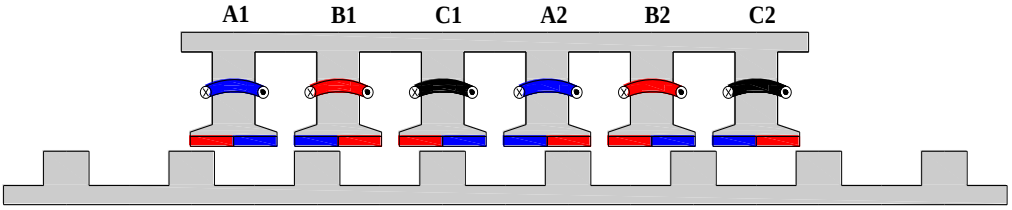

(b) FRPM linear machine

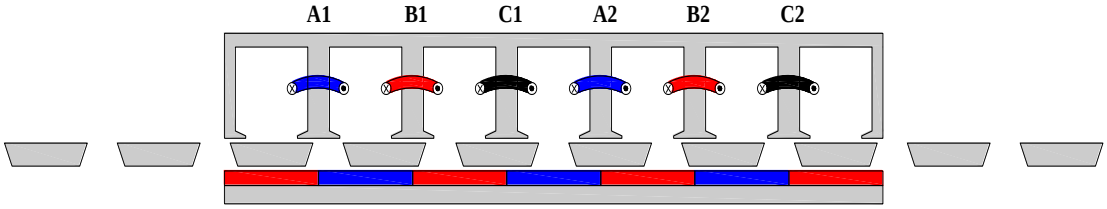

(c) PS-FRPM linear machine

Fig. 7.1 Machines configurations with globally optimized dimensions.

Table 7.1 Machine specifications

Item	SFPM	FRPM	PS-FRPM
Split ratio	0.33	0.33	0.37
Tooth width	4.6 mm	9.6 mm	5.4 mm
Stator back-iron thickness	-	-	2.8 mm
Slot area	113.9 mm^2	103.2 mm^2	167.7mm^2
PM volume	12.4 cm^3	6 cm^3	12.4 cm^3
Mover back-iron thickness	3.7 mm	3.9	-
Stator pole width	11 mm	10.24 mm	-
Stator pole height	6 mm	7 mm	-
Top mover piece width	-	-	20.74 mm
Bottom mover piece width	-	-	16.7 mm

7.2.2 Electromagnetic Performance

In Chapters 2 and 3 the performances of the conventional SFPM and FRPM, as well as the PS-FRPM linear machines, were analysed based on their global optimized configurations. In the following section the performances of the above mentioned machines will be compared. Table 7.2 summarizes the performance of the machines. It can be observed that the highest flux linkage is obtained by the SFPM linear machine followed by the PS-FRPM linear machine, while the FRPM linear machine exhibits the lowest flux linkage of the other machines. It should be mentioned that both the SFPM and PS-FRPM linear machines have asymmetric flux linkage waveforms, due to the longitudinal end effect, whilst an almost symmetrical flux linkage waveform can be achieved by the FRPM linear machine. Moreover, as a consequence of the highest flux linkage, the SFPM linear machine has the highest back-EMF. In contrast, the lowest one is for the FRPM linear machine.

Despite the fact that the PS-FRPM linear machine shows about 8% less back-EMF than that of the SFPM linear machine, it has about 24% higher thrust force compared to the SFPM linear machine. This is because the PS-FRPM linear machine takes the advantage of a larger slot area, leading to lower winding phase resistance and subsequently better electrical loading. On the other hand, the FRPM linear machine offers the lowest thrust force capability of the other machines. Moreover, both the PS-FRPM and FRPM linear machines have the advantage of low thrust force ripple due to low cogging force, while the SFPM possesses the highest thrust force ripple compared to the other machines. In addition, in terms of the windings inductances, both the conventional machines exhibit similar self-inductance, while the PS-FRPM linear machine has the lowest self-inductance value. Their mutual inductances are slightly different. Furthermore, in terms of mutual coupling between the machine phases, the PS-FRPM linear machine shows the lowest mutual coupling compared to other machines. Thereby, it can be deduced that a better fault tolerance capability can be obtained by such a configuration, i.e. the PS-FRPM linear machine. It is worth noting that the mutual coupling is expressed as a percentage of the self-inductance to mutual-inductance. Furthermore, the SFPM linear machine has the highest average normal force, while the lowest value of such feature is for the FRPM linear machine. It can be noted that the PS-FRPM shows about 40% lower and 18.9% higher normal force compared to the SFPM and FRPM linear machines, respectively.

Table 7.2 Machines performances comparison

Item	SFPM	FRPM	PS-FRPM
Flux linkage (Wb)	0.024	0.016	0.022
Back-EMF (V)	5.4	3.6	4.9
Average thrust force (N)	61.7	35.7	81
Average normal force (N)	590	286	353
Thrust force ripple	55.8%	29.5%	20.6%
Self-inductance (mH)	2.5	2.45	2.35
Mutual-inductance (mH)	-0.74	-0.92	-0.5
Phase coupling	30%	38.4%	21%

7.2.3 Loss Comparison

Iron losses of the three machines for both no-load and on load conditions are shown in Fig. 7.2 and Fig. 7.3, respectively. It can be seen that the FRPM linear machine has the lowest no-load and load iron losses amongst all the machines. On the other hand, the highest iron loss for load condition is produced by the PS-FRPM linear machine, followed by the SFPM linear machine. Furthermore, the variation of magnet eddy current loss with mover position at rated current density and rated velocity are illustrated in Fig. 7.4. It is obvious that the highest magnet eddy current loss is for the FRPM linear machine, while both SFPM and PS-FRPM have a similar average loss. Moreover, comparisons of magnet eddy current losses for all machines at rated current density for different velocities are shown in Fig. 7.5 and Fig. 7.6, respectively. It can be found that the lowest load magnet eddy current loss can be obtained by the SFPM linear machine. In contrast, the FRPM linear machine exhibits the highest no-load and load magnet eddy current losses amongst all the machines.

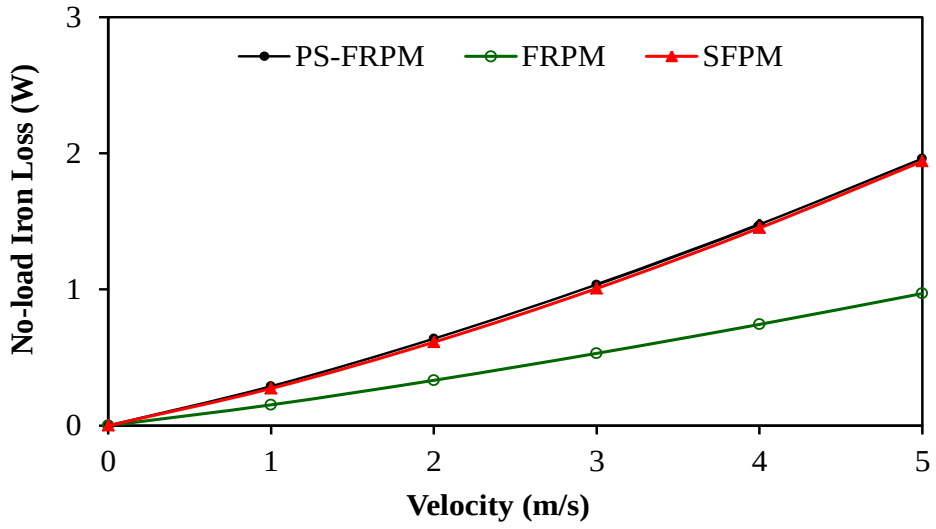

Fig. 7.2 No-load iron loss comparison.

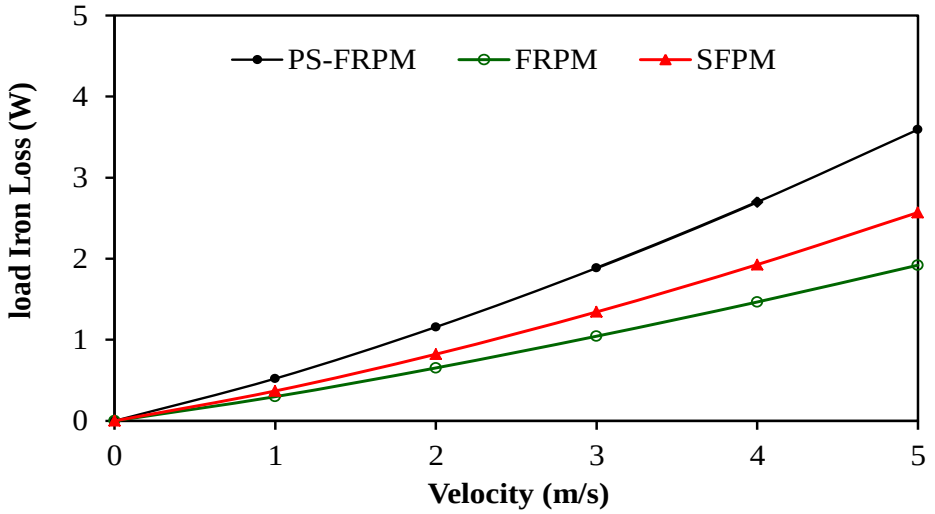

Fig. 7.3 Load iron loss comparison.

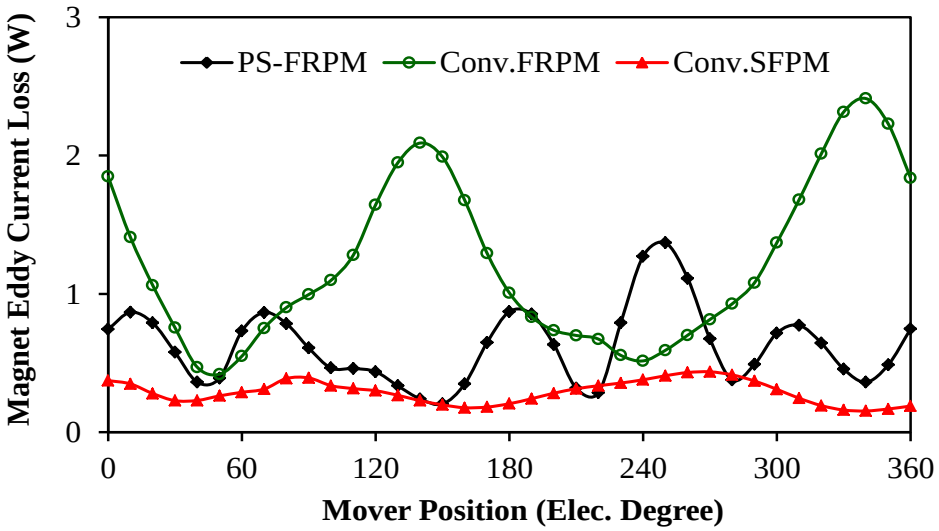

Fig. 7.4 Magnet eddy current loss variation with mover position.

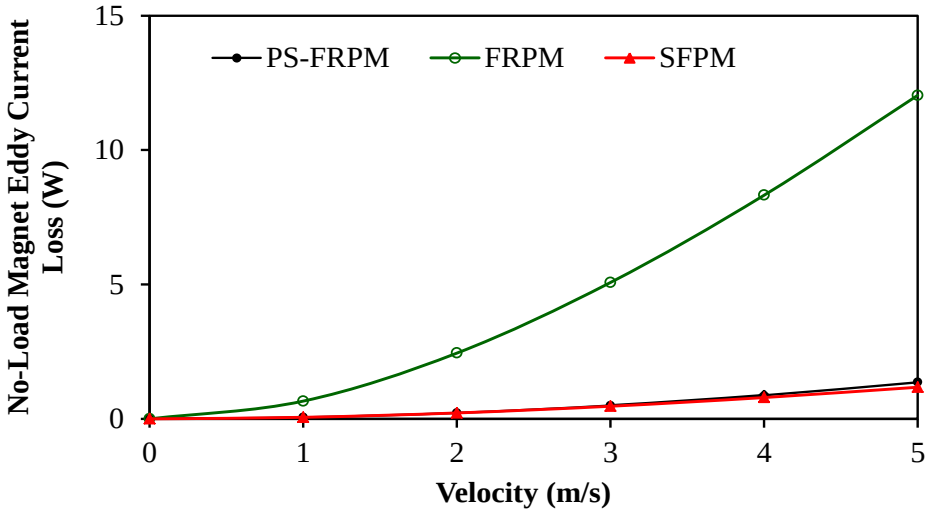

Fig. 7.5 No-load magnet eddy current loss comparison.

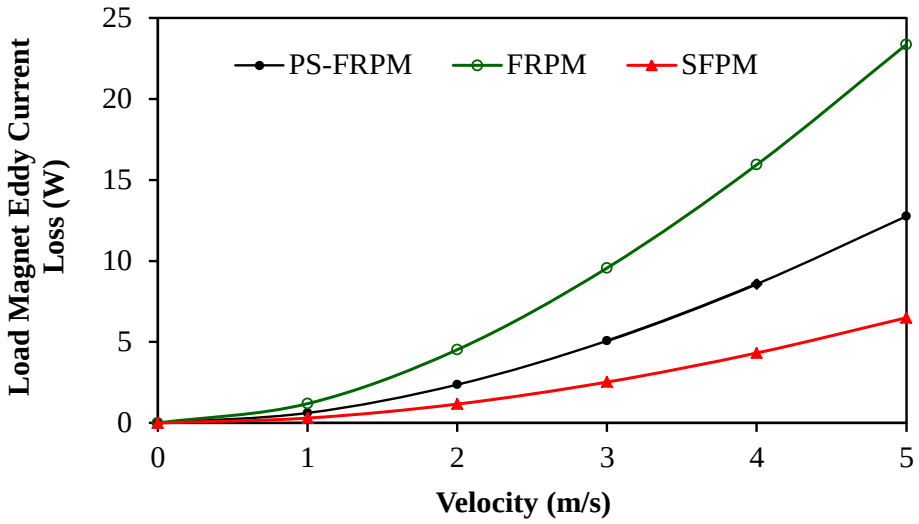

Fig. 7.6 Load magnet eddy current loss comparison.

7.3 Comparison of PS-PM Tubular Machines with a Conventional SFPM Counterpart

7.3.1 Configuration and Operating Principle

Both the configurations and operating principles of the PS-PM tubular machines were explained in Chapter 4. Therefore, only the configuration as well as the operation principle of the conventional SFPM tubular machine will be discussed. It should be mentioned that the machine has been designed with the same general specifications as those given in Chapter 4, which are listed again in Table 7.3, while Fig. 7.7 shows 2D-axisymmetry of the three machines. Unlike the PS-PM tubular machines, which consist of two stators and one mover, the SFPM tubular machine has one stator and one mover. One stator pole of the SFPM tubular machine comprises a pair of two iron rings and one PM ring, which is sandwiched between the iron rings. The armature windings are also accommodated in the stator, with a double-layer winding configuration, i.e. two coils, which belong to two phases are located in adjacent slots. It is worth noting that all compared machines have the same winding configuration. The mover is a salient pole structure made of iron. Despite the configuration differences of the three machines, they share the same operating principle. A constant flux is produced by the permanent magnet, whereas the direction and the amplitude of this flux vary when the mover moves. Hence, a back electromotive force (EMF) will be induced. Additionally, a thrust force will be generated when the coils are fed by appropriate currents due to the interaction of the permanent magnet flux linkage and the armature current field.

It should be mentioned that both the PS-SPM and PS-IPM tubular machines were optimized for maximum thrust force in Chapter 4, hence, in order to perform a fair comparison the SFPM tubular machine will be optimized under the same optimization conditions of the PS-PM tubular machines. Fig. 7.8 illustrates the main design parameters of the SFPM tubular machine. The definitions of the parameters, which will be varied during the optimization process, are illustrated in Table 7.4. On the other hand, the restriction, the initial and the optimal values of these parameters are listed in Table 7.5.

Table 7.3 Design parameters of tubular machines

Items	PS-SPM/PS-IPM	SFPM
Number of phases	3	
Number of mover poles within the stator	5	
Number of stator slots	6	
Outer stator slot pitch	23.6mm	
Inner stator slot pitch	23.6mm	-
Mover pole pitch	28.32mm	
Outer air gap radial length (GO)	1 mm	
Inner air gap radial length (GI)	1 mm	-
Outer stator radius (OSR)	35mm	
Inner stator radius (ISR)	13.5mm	-
Mover radius (MR)	19.5mm	

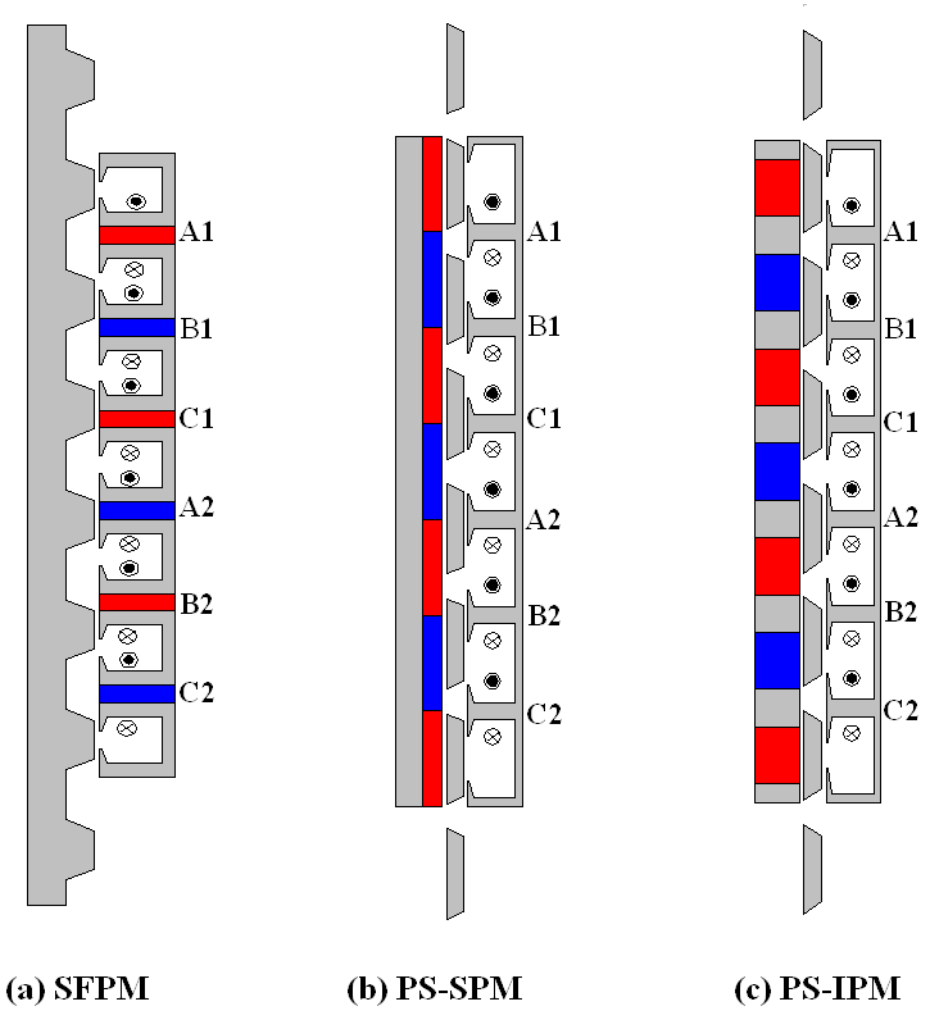

Fig. 7.7 Machines configurations.

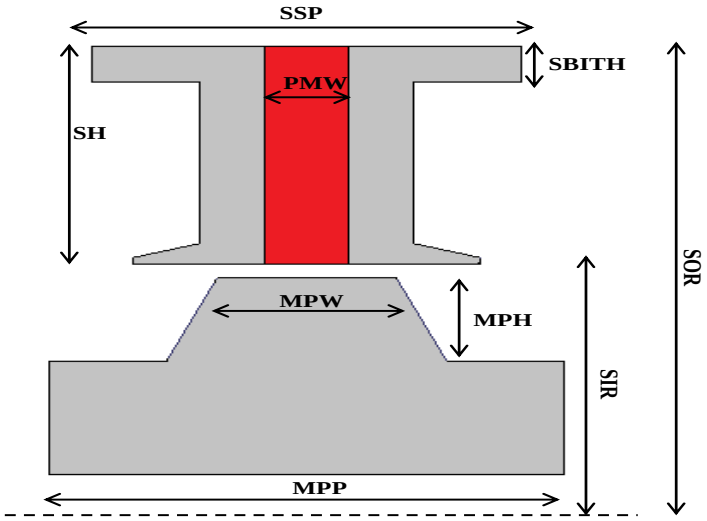

Fig. 7.8 Major design parameters of SFPM tubular machine.

Table 7.4 Definition of optimized parameters

Items	Symbols	Definitions
Split ratio	*SR*	$\frac{SIR}{SOR}$
Stator back iron thickness ratio	*SBITHR*	$\frac{SBITH}{SH}$
Stator teeth width ratio	*STWR*	$\frac{STW}{SSP}$
Mover pole width ratio	*MPWR*	$\frac{MPW}{MPP}$
Mover pole highest ratio	*MPHR*	$\frac{MPH}{MH}$

where SIR, SOR, SBITH, SH, STW and SSP indicate stator inner and outer radiuses, stator back-iron thickness, stator height, stator tooth width and stator slot pitch, respectively. MPW and MPH are mover pole width and height respectively, while MH and MPP represent mover height and mover pole pitch.

Table 7.5 Initial, restriction and optimal values of optimized parameters

Items	Initial	Restriction	Optimal
SR	0.5	[0.3, 0.7]	0.52
SBITHR	0.2	[0.1, 0.3]	0.164
STWR	0.207	[0.1, 0.3]	0.197
MPWR	0.25	[0.1, 0.4]	0.349
MPHR	0.5	[0.2, 0.5]	0.33
PMTH	3mm	[3mm, 6mm]	4.54mm

7.3.2 Electromagnetic Performance

Fig. 7.9 shows phase A open circuit flux linkages of the above mentioned machines. It is obvious that the highest flux linkage can be obtained by the SFPM tubular machine due to the flux focusing and larger amount of PMs usage. In contrast, the PS-SPM tubular machine exhibits the lowest flux linkage. It can be clearly deduced that all machines exhibit asymmetry flux linkage, this is because of the longitudinal end effect. Phase A back-EMFs of the machines are compared in Fig. 7.10. The highest back-EMF can be achieved by the SFPM tubular machine since it has the highest flux linkage. Generally, one of the main problems of the PM machine is the attraction force between the PM and stator iron, which results in an unfavourable force known as cogging force

that causes force ripple, vibration and noise [WAN12]. Fig. 7.11 shows the cogging force of the machines. Apparently, the PS-SPM tubular machine has the lowest cogging force among the other machines. On the other hand, PS-IPM tubular machine delivers the highest cogging force, and consequently the highest thrust force ripple.

The characteristics of average thrust force versus copper loss, for all machines are illustrated in Fig. 7.12. It can be seen that although the SFPM tubular machine has higher back-EMF compared to PS-SPM tubular machine, both the PS-SPM and SFPM tubular machines exhibit an almost same thrust force capability. This is because of PS-SPM tubular machine has larger slot area. In addition, the PS-IPM tubular machine has a slightly higher thrust force due to the presence of the reluctance force.

In order to investigate the magnet utilization in the understudying machines, the average thrust forces per total magnet volume as functions of copper loss for all machines are depicted in Fig. 7.13. It is clearly to realise that better magnet utilization can be achieved by the PS-IPM tubular machine. Furthermore, Fig. 7.14 compares the thrust force for all machines with the mover position under fixed copper loss (70W). It can be seen that PS-IPM shows the highest average thrust force.

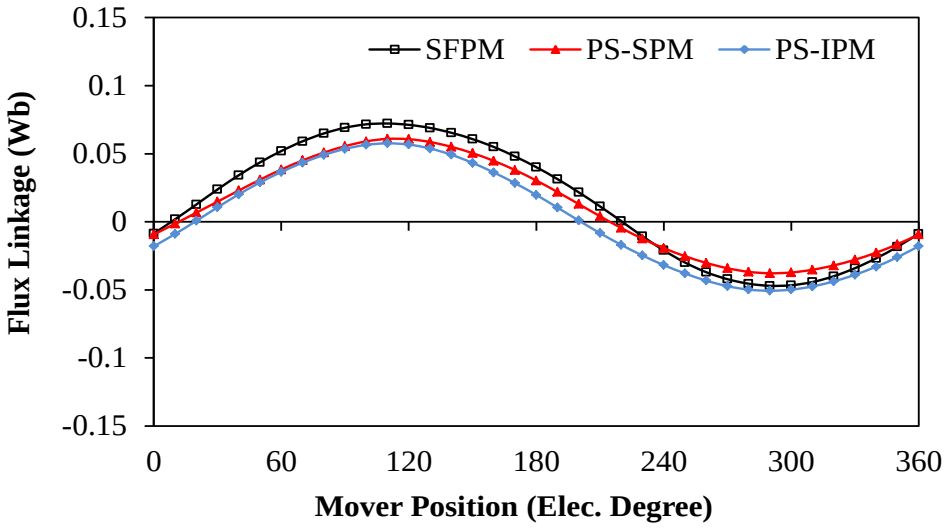

(a) Waveform

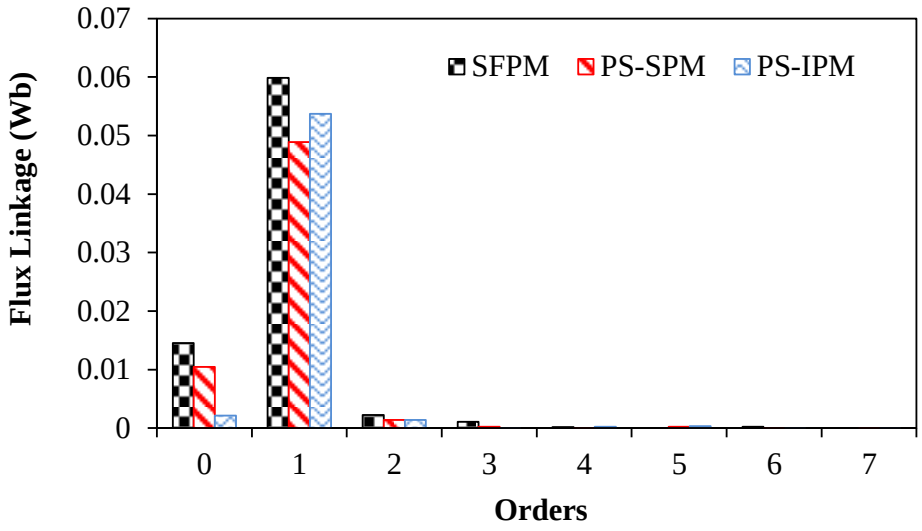

(b) Spectrum

Fig. 7.9 Flux linkage comparison.

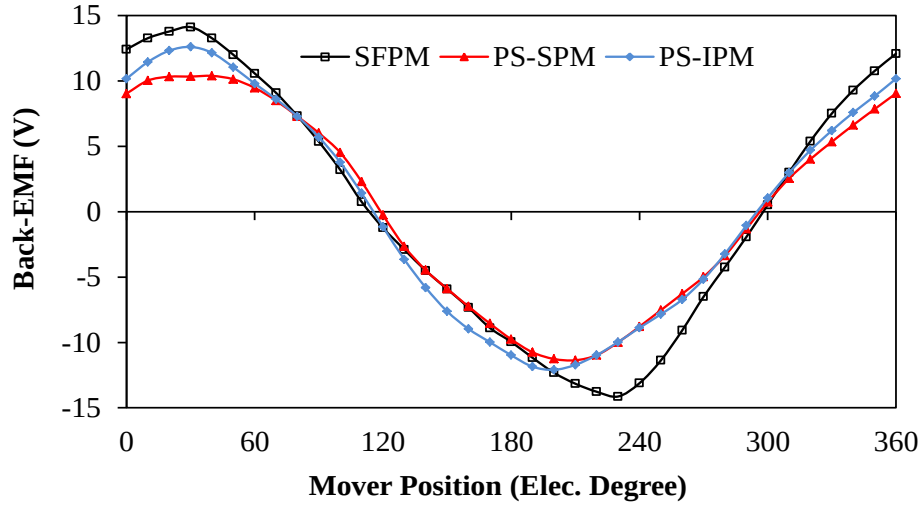

(a) Waveform

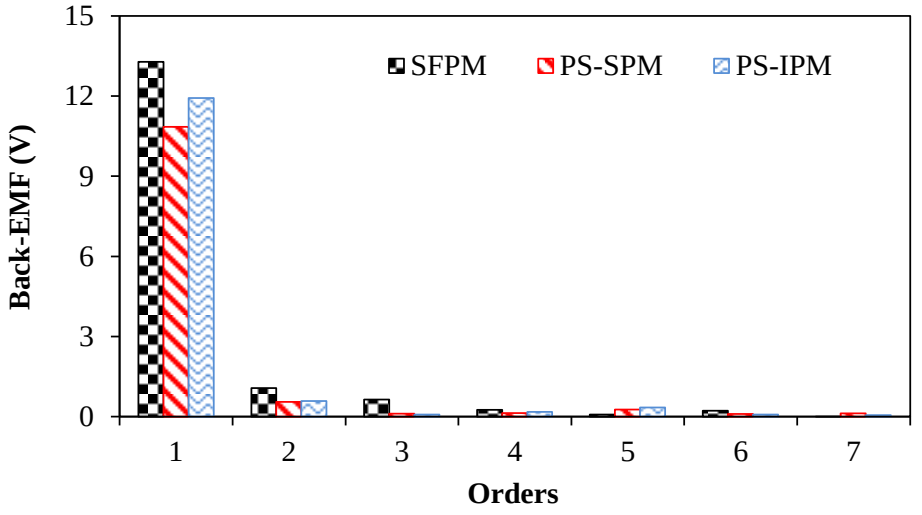

(b) Spectrum

Fig. 7.10 Back-EMF comparison.

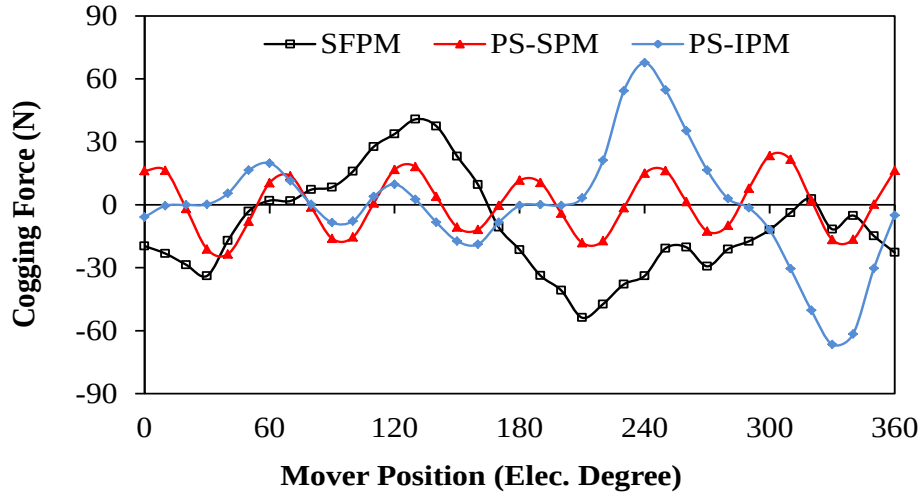

Fig. 7.11 Cogging force comparison.

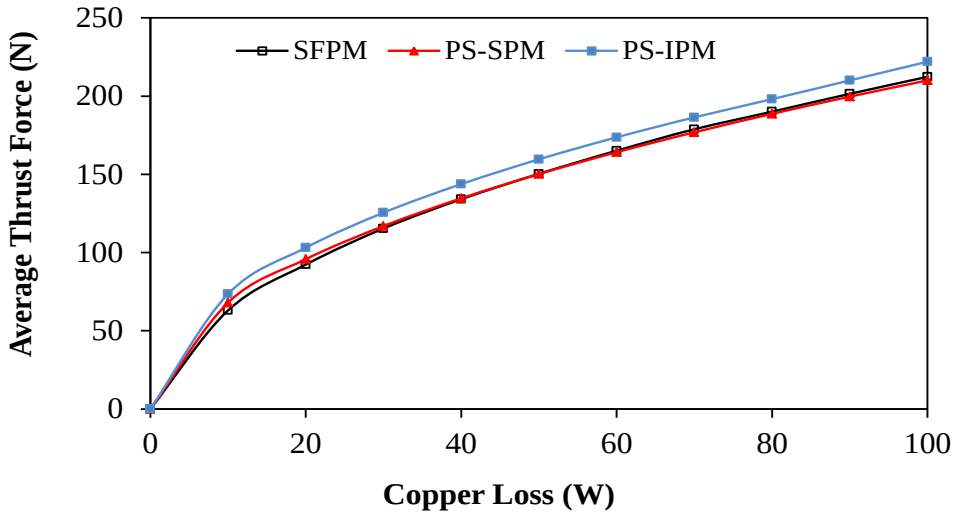

Fig. 7.12 Average thrust force variation with copper loss.

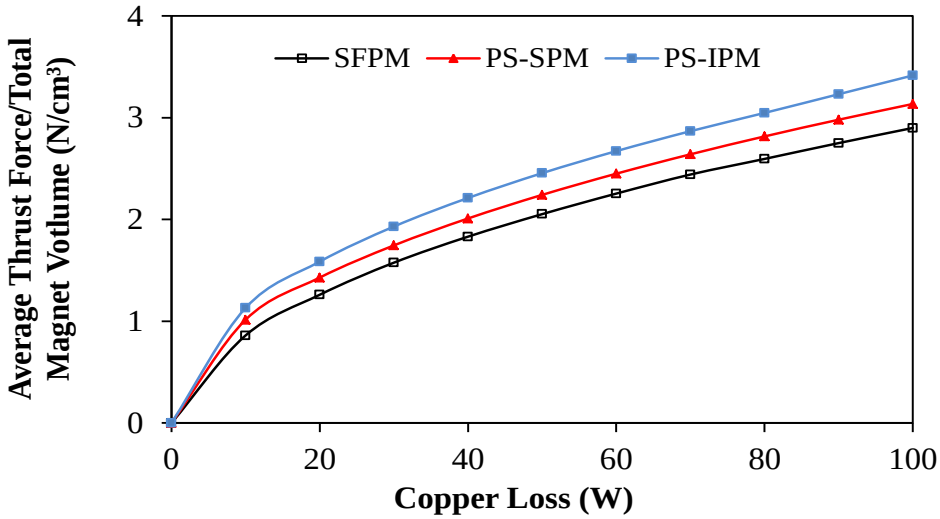

Fig. 7.13 Average thrust force /magnet volume variation with copper loss.

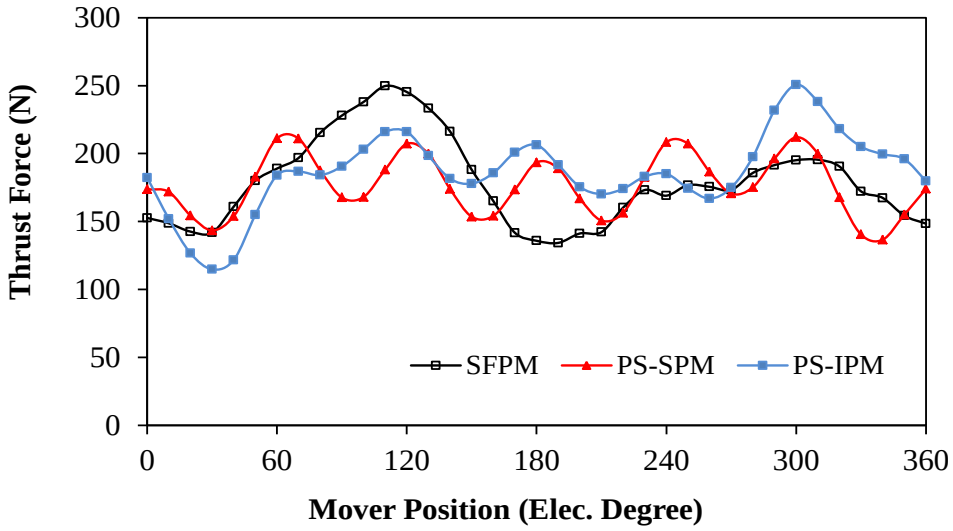

Fig. 7.14 Comparison of thrust force under fixed copper loss (70W).

7.3.3 Loss Comparison

The losses of the machines have been predicted and compared using the approach, which explained in Chapter 3. Iron loss of the aforementioned machines under both no-load and on load conditions, are shown in Fig. 7.15 and Fig. 7.16, respectively. Obviously, the PS-SPM tubular machine has the lowest no-load and load iron losses among the other machines. On the other hand, the highest iron losses for both no-load and load conditions are produced by the PS-IPM tubular machine. Furthermore, the SFPM tubular machine exhibits slightly higher iron loss compared to PS-SPM tubular machines. The magnet eddy current losses for all machines are illustrated in Fig. 7.17 and Fig. 7.18, respectively. It can be noted that the magnet eddy current loss of the PS-IPM tubular machine is very small and can be neglected compared to other machines. In contrast, the SFPM tubular machine exhibits the highest no-load and load magnet eddy current losses among the other machines. This can be explained by Fig. 7.19, which illustrates the air gap flux densities at load for all machines. It should be mentioned that the air gaps of both PS-PM tubular machines are the inner air gaps, which are located between the inner stator and the mover. Apparently, the SFPM tubular machine has the richest harmonic components of the other machines. Moreover, the lowest air gap harmonic components are delivered by PS-IPM tubular machine.

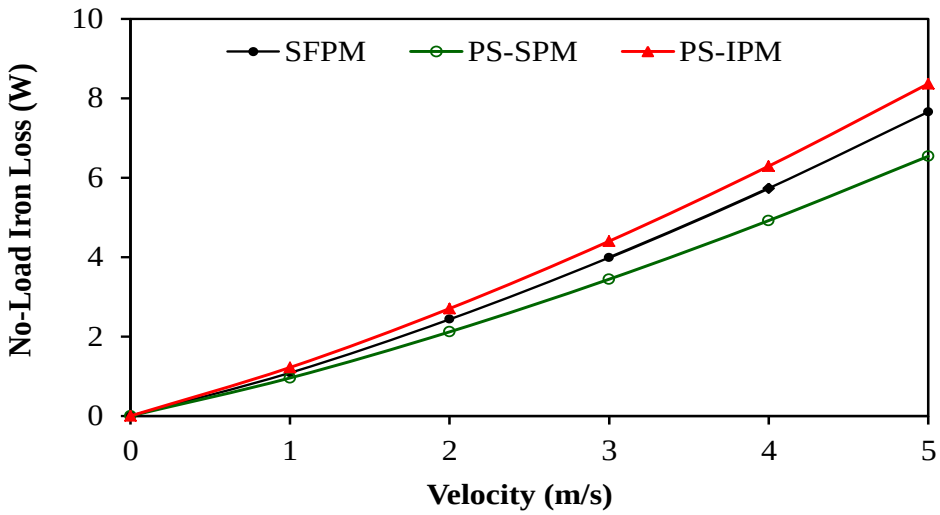

Fig. 7.15 No-load iron loss comparison.

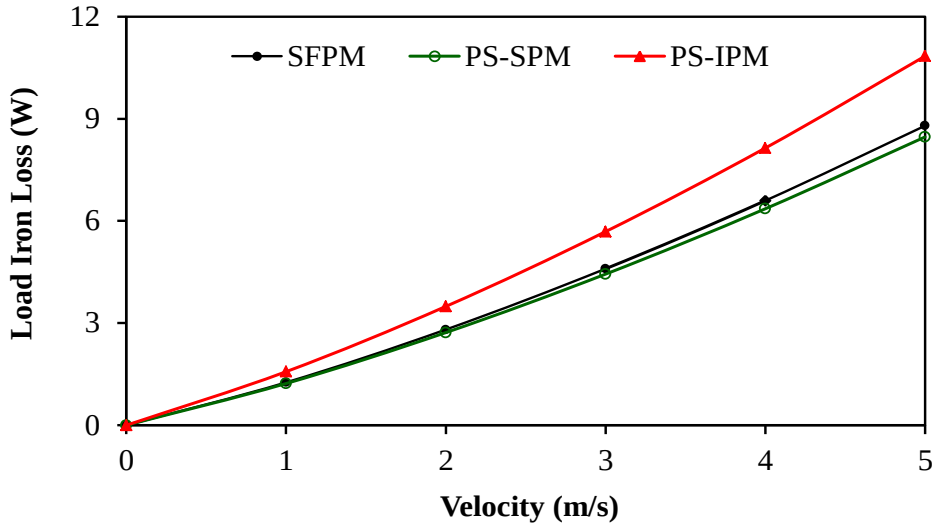

Fig. 7.16 Load iron loss comparison.

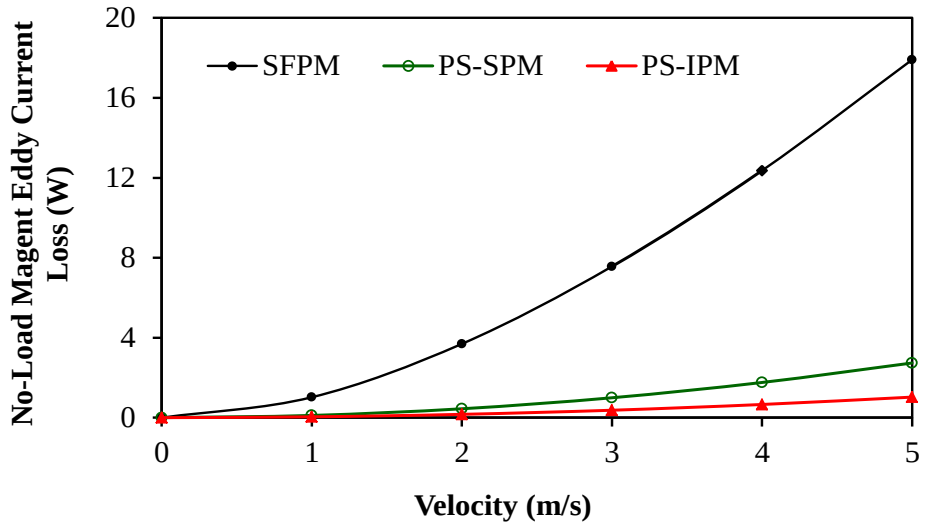

Fig. 7.17 No-load magnet eddy current loss comparison.

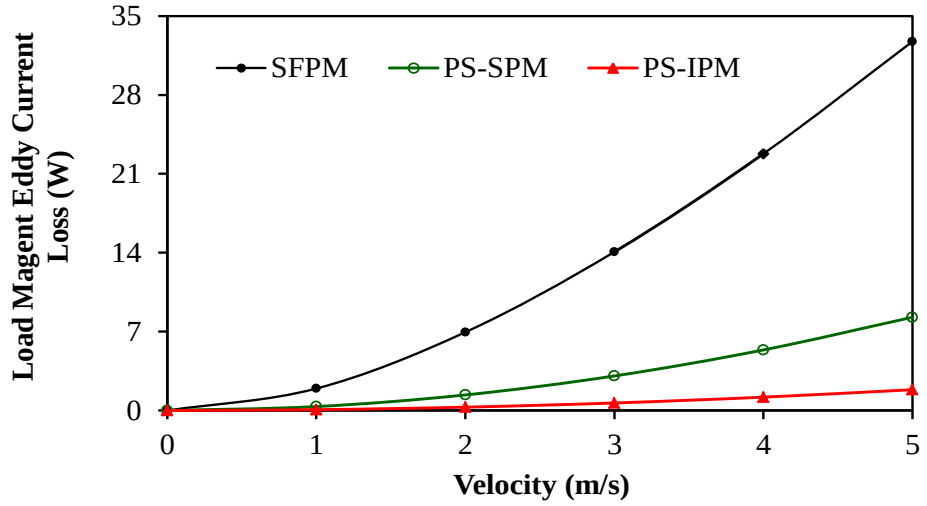

Fig. 7.18 Load magnet eddy current loss comparison.

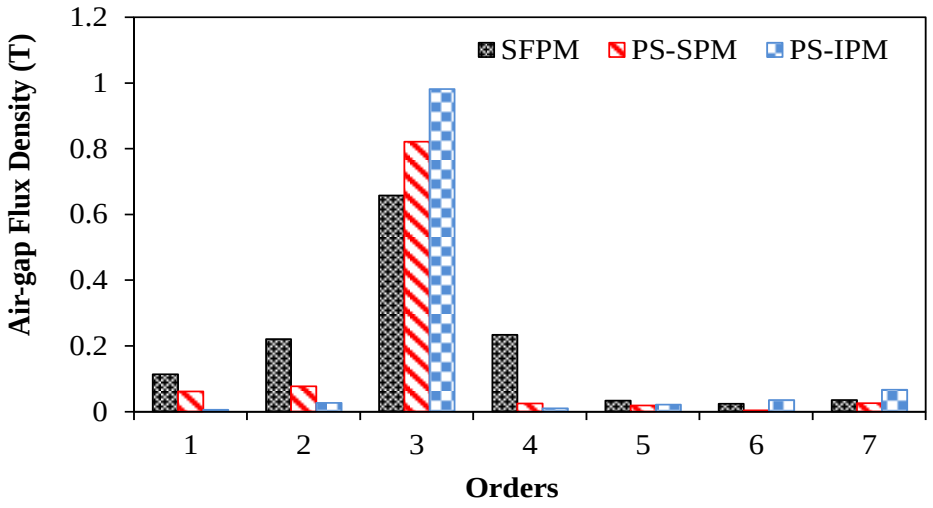

Fig. 7.19 Air-gap flux density under load condition of understudying machines.

7.3.4 PM Demagnetization Withstand Capability Comparison

For some applications, PM tubular machines may be needed to work at harsh circumferences, i.e. high temperature as well as high electrical loading. Therefore, the possibility of the PM demagnetization risk will be presented. Hence, to maintain a reliable performance in such operating conditions, PM tubular machines with good demagnetization withstand capability would be more preferable. In order to assess the understudying machines from the demagnetization withstand capability aspect, the PM demagnetization risk of these machines will be evaluated. In Chapter 5, the PM demagnetization risk of both PS-PM tubular machines was assessed. It was observed that the risk of PM demagnetization does not exist in such machines. Thus the PM demagnetization risk of the SFPM will be investigated under the same conditions that were used for the PS-PM tubular machines.

Flux density distributions for north and south poles of the SFPM tubular machine are depicted in Fig. 7.20. It should be noted that some of the PM edges partially lose their magnetization and some of them also have flux densities equal to knee point. Hence, it can be concluded that the SFPM tubular machine can work at 120°C but with the risk of permanent magnet demagnetization, since some of its PMs may lose their magnetization under such conditions.

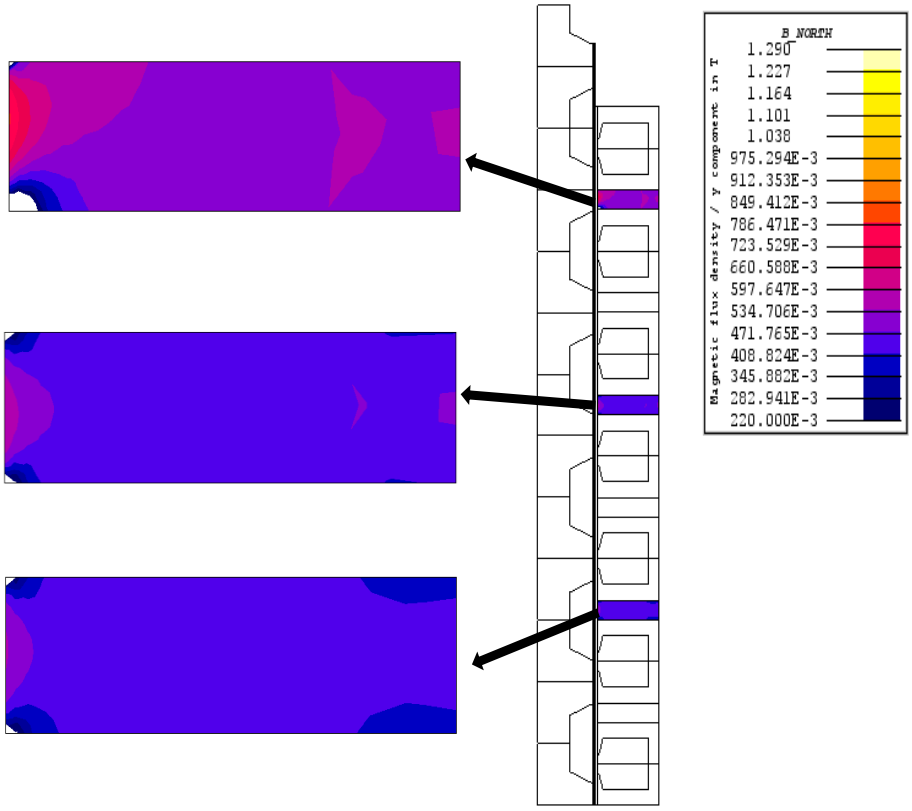

(a) North-pole

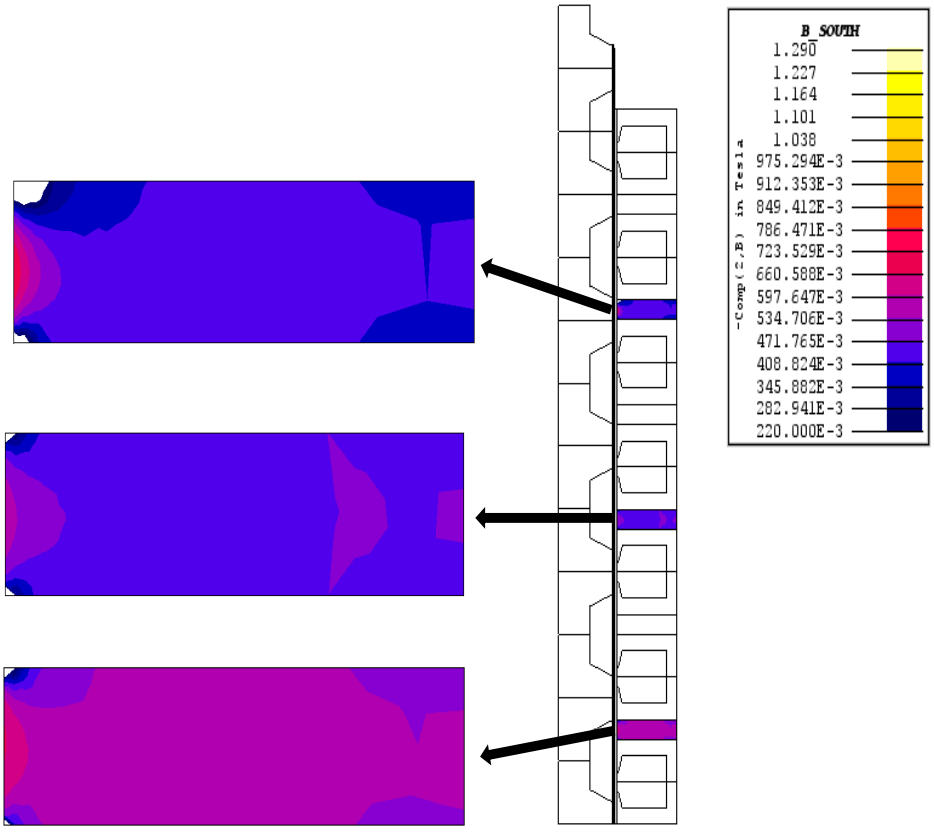

(b) South-pole

Fig. 7.20 PMs flux density distributions SFPM tubular machine.

The performances of the machines are summarized in Table 7.6. In terms of flux linkage and back-EMF the SFPM tubular machine has the highest values compared to both PS-PM tubular machines. Furthermore, in terms of cogging force and thrust force ripple, the PS-SPM tubular machine shows the lowest values of the other machines. The highest thrust force capability and the best magnet utilization can be achieved by the PS-IPM. In contrast, the SFPM tubular machine has the lowest PM utilization compared to both PS-PM tubular machines. Additionally, the highest self-inductance can be obtained by the PS-IPM tubular machine, and also both PS-PM tubular machines have lower mutual coupling component compared to the SFPM tubular machine, which is preferable for fault tolerance capability. Moreover, the PS-IPM tubular machine has the lowest no-load and load magnet eddy current losses, while it shows the highest iron loss compared to other machines. The lowest no-load and load iron losses are shown by the PS-SPM machine.

Table 7.6 Machines performances summaries

Items	SFPM	PS-SPM	PS-IPM
Flux linkage fundamental (Wb)	0.051	0.039	0.043
Back-EMF fundamental (V)	11.3	8.7	9.5
Peak cogging force (N)	53	24	68
Average thrust force (N)	178.8	176.9	186
Thrust force ripple	53%	40%	62%
Total PM volume (cm^3)	73.23	66.99	65.1
Average thrust force/magnet volume (N/cm^3)	2.4	2.64	2.8
Self-inductance (phase A) (mH)	3.04	2.8	3.5
Mutual coupling components	-30%	-23.5%	-22.5%
Iron loss (W) load	1.25	1.22	1.57
Magnet eddy current loss (W) load	2.24	0.35	0.074
Copper loss (W)	70	70	70

7.3.5 Machines Optimization under the Same Permanent Magnet Volume

The machines have been compared with different magnet volumes, i.e. the optimal magnet volume for each machine. Although the magnet cost is a crucial factor, it will be useful if the machines are re-compared with the same magnet volume. It is worth mentioning that the magnet volume of both the PS-SPM and SFPM tubular machines are adjusted to be equal to the magnet volume of the PS-IPM tubular machine, since it has the lowest magnet volume of all the machines. Hence, both the PS-SPM and SFPM tubular machines have been optimized with a fixed magnet volume i.e. $65cm^3$. It should be mentioned that the split ratios for both machines are kept equal to their

optimal values. This is because the variation of this parameter will directly affect the magnet volume. The varied parameters through the optimization process and their optimal values for both machines are listed in Table 7.7 and Table 7.8, respectively.

Table 7.7 Optimized parameters for PS-SPM tubular machine

parameter	symbol	Optimal value
Mover thickness	*MTH*	3.8
Top mover pieces width ratio	*TMPWR*	0.66
Bottom mover pieces width ratio	*BMPWR*	0.78
Outer stator teeth width ratio	*OSTWR*	0.13
Outer stator slot opening ratio	*OSSOR*	0.4

Table 7.8 Optimized parameters for SFPM tubular machine

parameter	symbol	Optimal value
Stator back iron thickness ratio	*SBITHR*	0.14
Mover pole highest ratio	*MPHR*	0.37
Mover pole width ratio	*MPWR*	0.4
Stator teeth width ratio	*STWR*	0.2

Fig. 7.21 compares the variation of the average thrust force with different copper losses for all machines. It can be seen that with identical magnet volumes, the PS-IPM tubular machine still has the highest average thrust force capability among the other machines. Moreover, the thrust force capability of the SFPM tubular machine is reduced due to the magnet volume reduction. Hence, it shows the lowest thrust force compared to PS-PM tubular machine topologies. In contrast, PS-SPM tubular machine thrust force capability is not significantly affected since the slot area of the re-optimized machine is increased. Thereby, the machine resistance is reduced, which allows an increase in the machine electrical loading under fixed copper loss. Fig. 7.22 shows the magnet utilization for the machines. It can be noted that the PS-IPM and PS-SPM tubular machines exhibit better magnet utilization compared to the SFPM tubular machine.

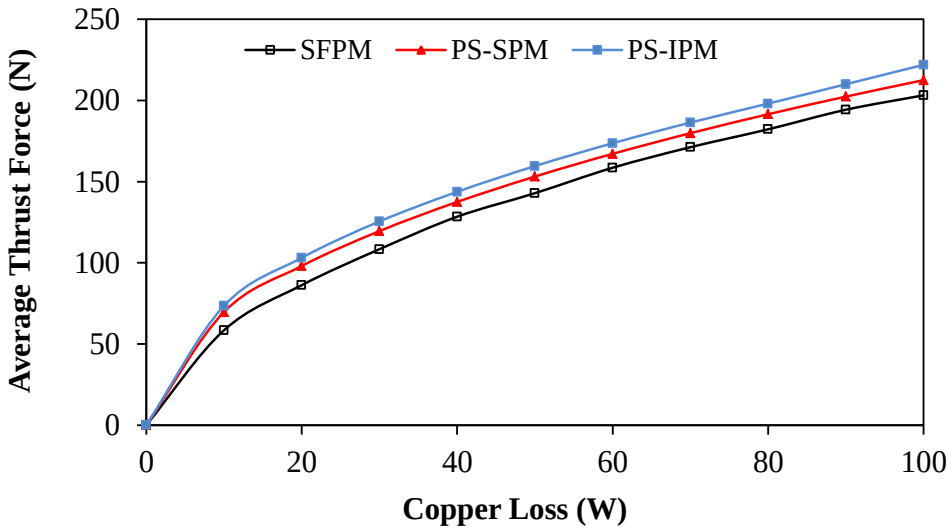

Fig. 7.21 Average thrust force variation with copper loss under same PM volume.

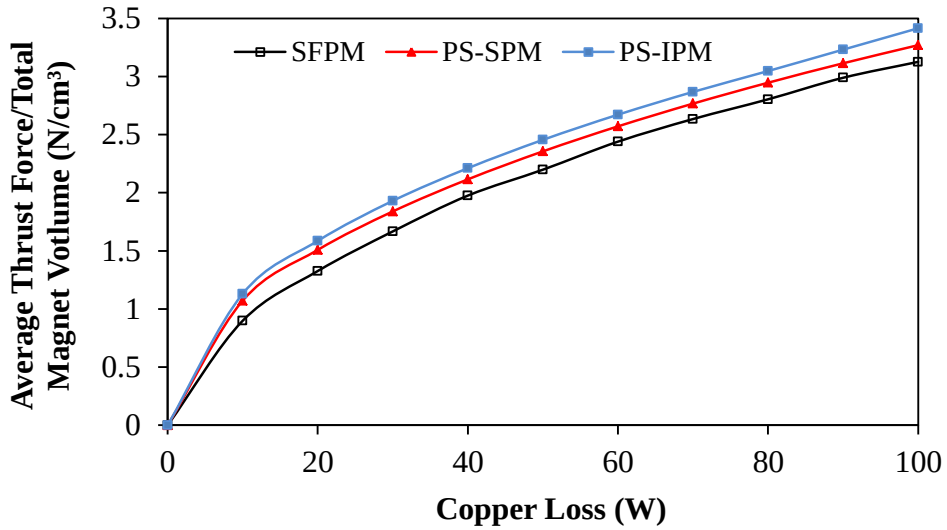

Fig. 7.22 Average thrust force /magnet volume variation with copper loss under same PM volume.

7.4 Comparison of PS-SPSS-SPMTM with a Conventional Single-Phase Short Stroke Surface Mounted Permanent Magnet Tubular Machine

7.4.1 Configuration and Operating Principle

A comparison between the PS-SPSS-SPMTM and the conventional single-phase short stroke surface mounted permanent magnet tubular machine (SPSS-SPMTM) is introduced in this section. The conventional SPSS-SPMTM consists of an E-shaped core stator with two annular windings while the mover has two poles PM with radial magnetization, Fig. 7.23. For a fair comparison, the conventional SPSS- SPMTM has been designed with the same major design parameters of the PS-SPSS-SPMTM. Furthermore, it has been globally optimized under the same optimization conditions of the PS-SPSS-SPMTM. Table 7.9 illustrates the definitions of the varied parameters during the optimization and a schematic diagram of the main design parameters of the conventional machine is shown in Fig. 7.24.

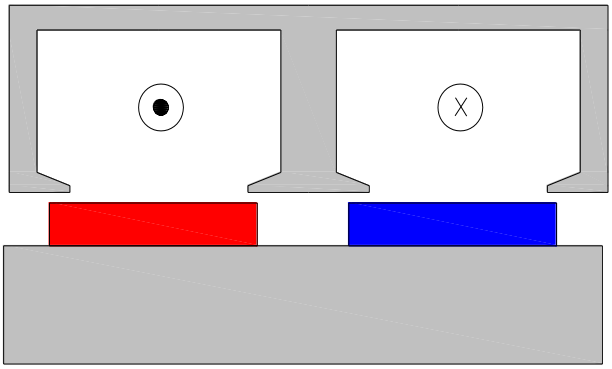

Fig. 7.23 SPSS-SPMTM cross-section.

Table 7.9 Definition of optimized parameters

Items	Symbols	Definitions
Split ratio	*SR*	$\frac{SOR}{SIR}$
Stator tooth width ratio	*STWR*	$\frac{STW}{SSP}$
Stator slot opening ratio	*SSOR*	$\frac{SSO}{SSP}$
Stator back iron thickness ratio	*SBITHR*	$\frac{SBITH}{STH}$
PM pole ratio	*TPMR*	$\frac{TPM}{MPP}$

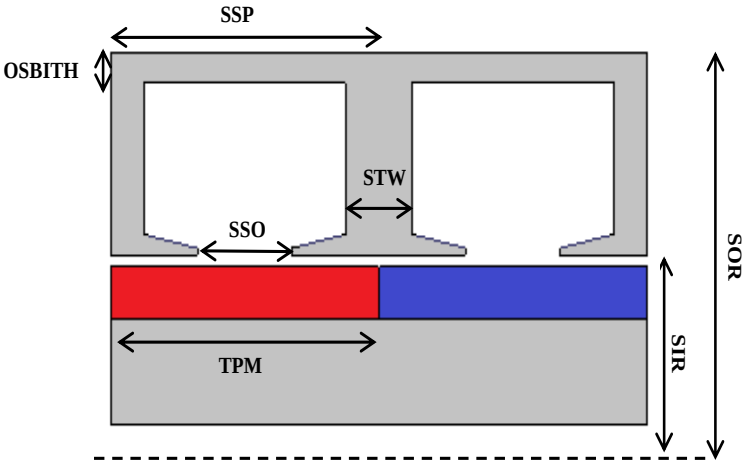

Fig. 7.24 Major design parameters of SPSS-SPMTM.

where $SOR, SIR, STW, SSO, SBITH$ and SSP represent stator outer radius, stator inner radius, stator tooth width, stator slot opening, stator back iron thickness and stator slot pitch, respectively. TPM and MPP indicate PM pole pitch and mover pole pitch, respectively. The initial, the restriction and the optimal values of varied parameters during the optimization are illustrated in Table 7.10.

Table 7.10 Initial, restriction and optimal values of optimized parameters

Items	Initial	Restriction	Optimal
SR	0.5	[0.3, 0.75]	0.52
STWR	0.2	[0.1, 0.3]	0.185
SSOR		[0.3, 0.9]	
SBITHR	0.15	[0.1, 0.3]	0.133
TPMR	1	[0.6, 1]	0.85

7.4.2 Electromagnetic Performance

Fig. 7.25 shows flux distributions of the conventional SPM machine due to the PMs only for three mover positions, i.e., at positive maximum, negative maximum and zero flux linkage. It can be noted that although both the conventional and the proposed machines have similar flux distribution patterns, the proposed machine has higher flux leakage at the edges. Due to this, the conventional machine exhibits slightly more linear flux linkage variation compared to the proposed machine, Fig. 7.26, and consequently, flatter back-EMF, Fig. 7.27. Furthermore, open circuit forces for both machines are compared in Fig. 7.28. Obviously, the proposed machine produces lower cogging force compared to the conventional machine, which is beneficial for applications requiring high reliability. Fig. 7.29 illustrates thrust force variation with the displacement for both machines. It can be seen that the thrust force variation of the proposed machine is

similar to its back-EMF profile. On the other hand, the thrust force-displacement characteristic profile of the conventional machine is different from its back-EMF profile, due to cogging force effect. Furthermore, the conventional machine has a slightly higher thrust force at the centre point compared to the proposed machine.

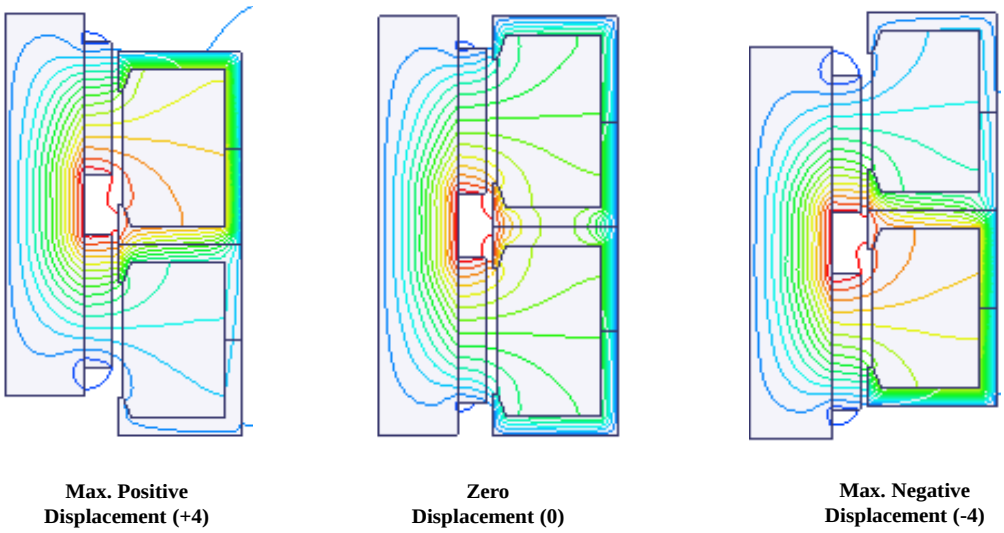

Fig. 7.25 Open-circuit field distributions SPSS-SPMTM (displacement unit=mm).

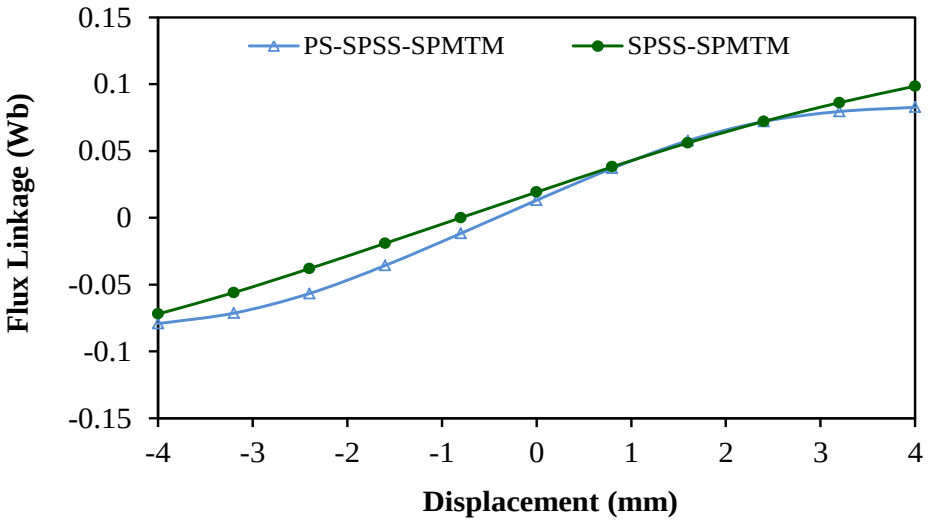

Fig. 7.26 Flux linkage comparison.

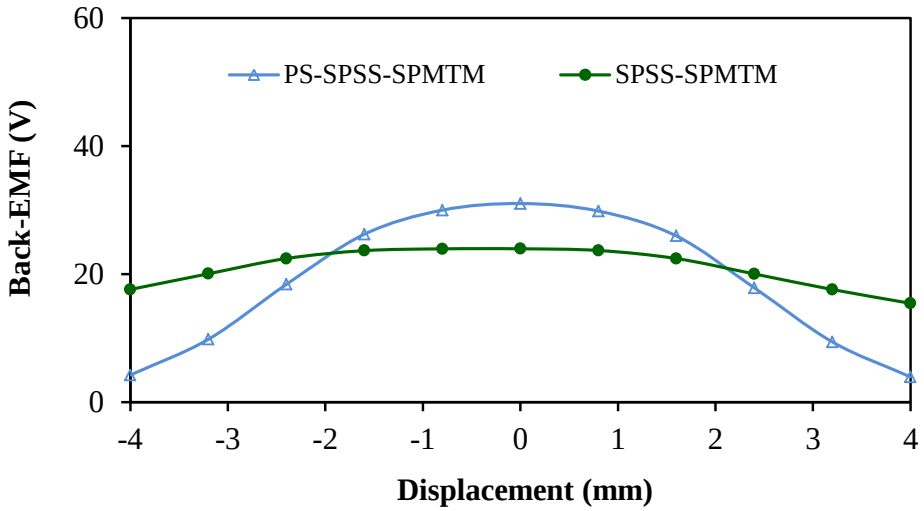

Fig. 7.27 Back-EMF comparison.

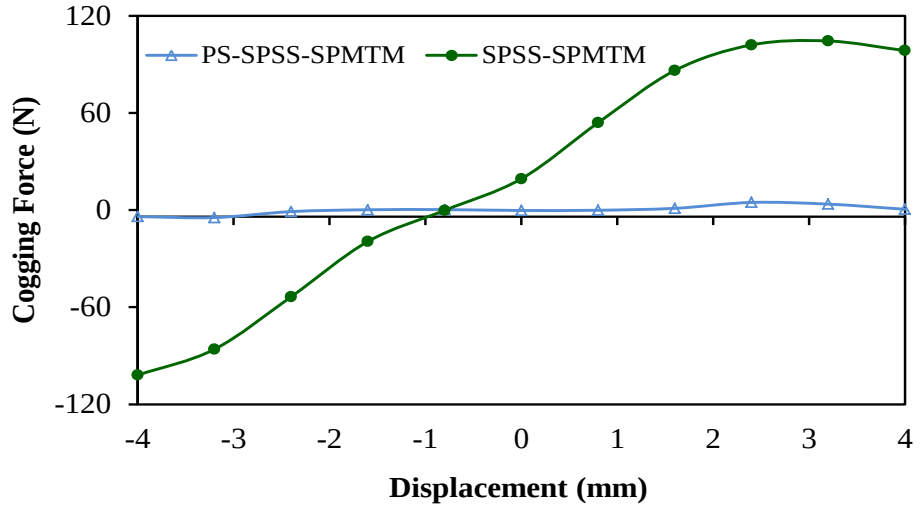

Fig. 7.28 Cogging force comparison.

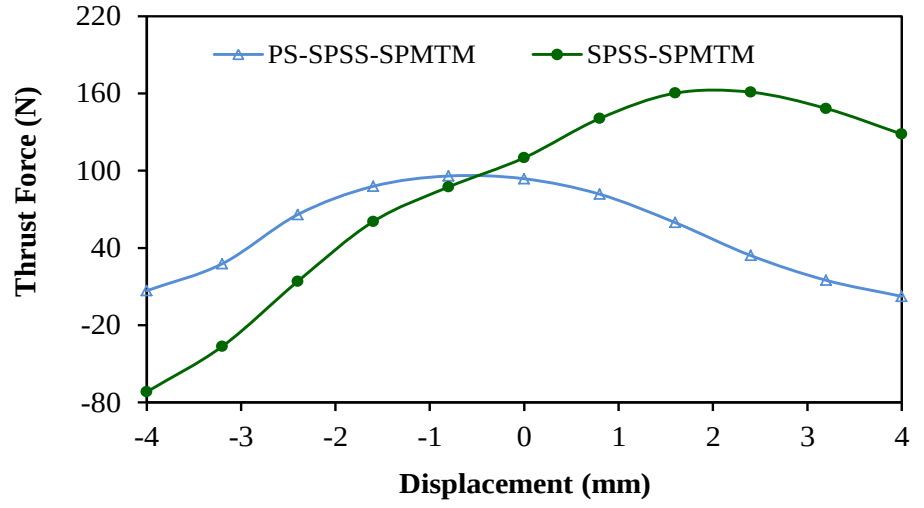

Fig. 7.29 Thrust force comparison.

7.4.3 Loss Comparison

Iron loss variations with velocity for both machines for no-load and load conditions are depicted in Fig. 7.30 and Fig. 7.31, respectively. However, both machines have low iron loss; the proposed machine shows about 24% higher iron loss. Fig. 7.32 and Fig. 7.33 illustrate magnet eddy current loss with velocities for both the understudying machines with no-load and load conditions. It can be seen that the proposed machine has about 95% less magnet eddy current loss than that of the conventional machine. Hence, it can be concluded that the main conventional machine problem, i.e. high PM temperature caused by eddy loss can be significantly reduced by PS-SPM configuration. It is worth mentioning that at low velocity operation condition, the majority of linear machine losses are contributed by the copper loss. This is because such loss is frequency independent. On the other hand, both iron and magnet eddy current losses will increase with the velocity.

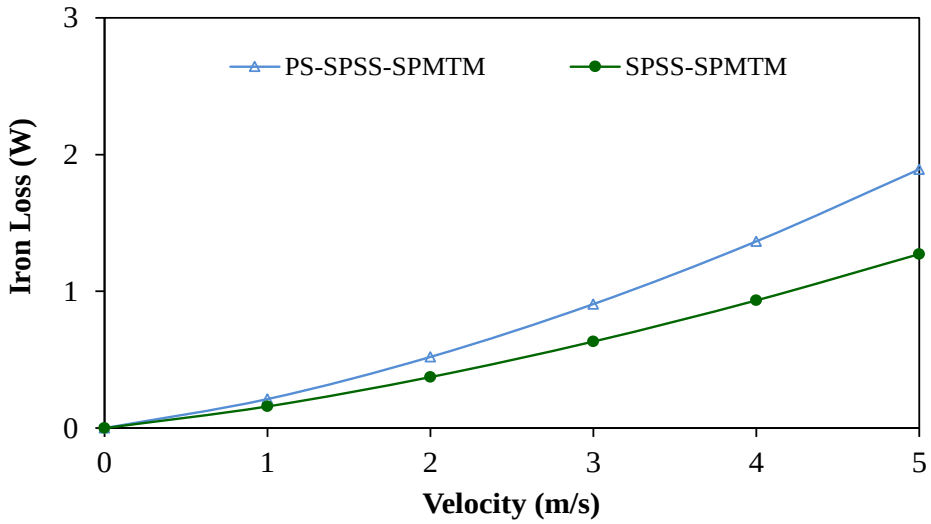

Fig. 7.30 No-load iron loss comparison.

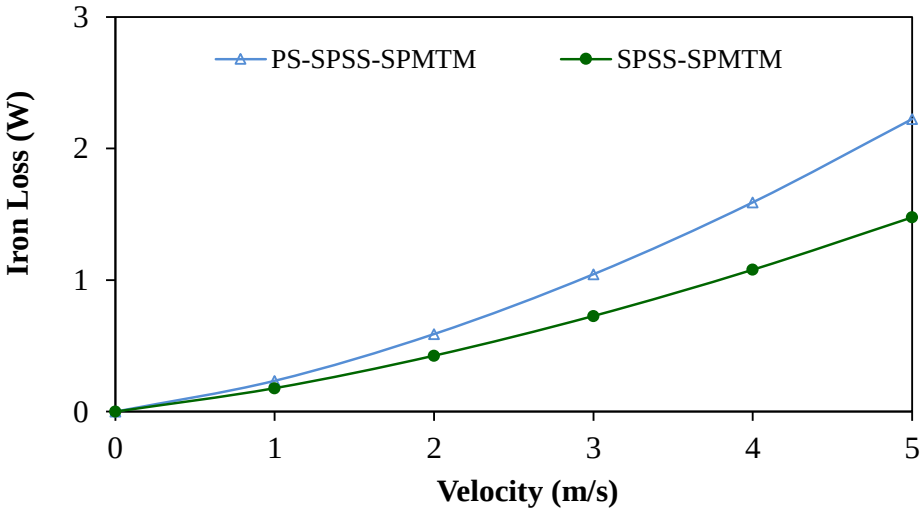

Fig. 7.31 Load iron loss comparison.

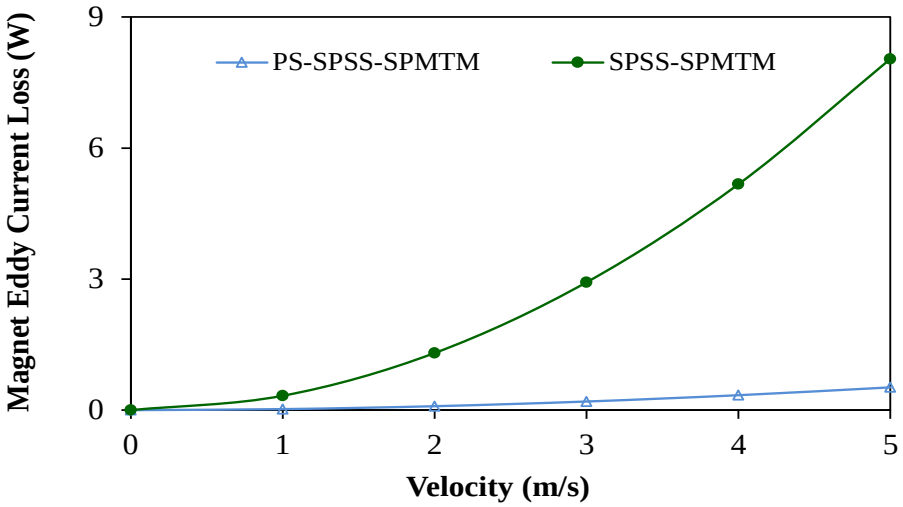

Fig. 7.32 No-load magnet eddy current loss comparison.

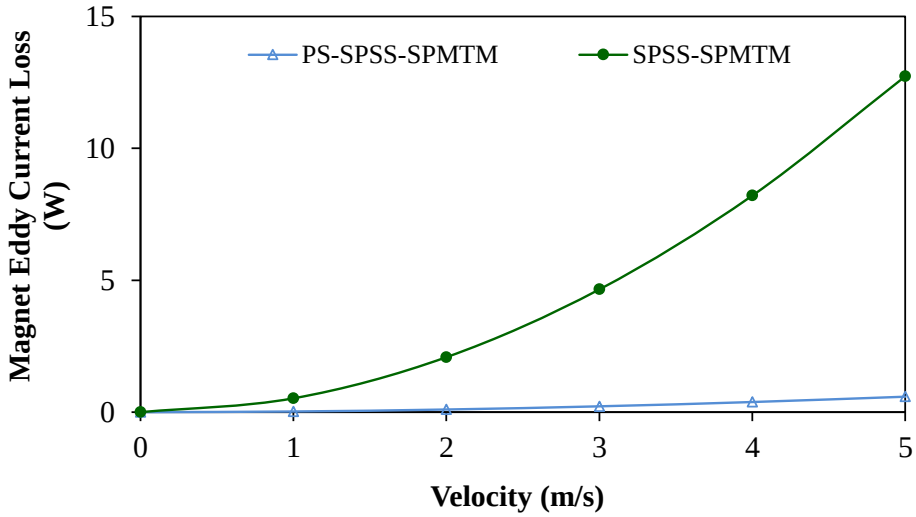

Fig. 7.33 Load magnet eddy current loss comparison.

7.5 Summery

In this chapter comprehensive comparisons between the PS-PM linear machines and their conventional correspondences are presented. It is worth noting that the comparison has been carried out with the same specifications and the same design optimization techniques for the PS-PM linear machines and their conventional counterparts. Overall, the PS-PM linear machines have the advantage of overcoming the conflict between the electric and magnet loadings. In addition, the machines show good demagnetization withstand capabilities compared to their conventional corresponding machines. Moreover, the flat PS-FRPM linear machine possesses the advantage of the highest force capability and the lowest thrust force ripple compared to both conventional SFPM and FRPM linear machines. Furthermore, it has been shown that the PS-IPM tubular machine exhibits the highest thrust force capability compared to other topologies, while both PS-SPM and SFPM tubular machines have almost the same thrust force capability. Moreover, the PS-SPM topology has lower peak-peak cogging force than the other machines, and consequently it exhibits less thrust force ripple. Furthermore, the magnet utilization has been investigated. It has been found that better magnet utilization can be obtained with such a PS-PM tubular machine topology. In terms of iron loss the PS-SPM tubular machine exhibits the lowest value compared to other machines. On the other hand, the conventional SFPM tubular machine produces the highest no load and load magnet eddy current loss among the other machines, due to the richer air gap flux density harmonic components. Moreover, the PS-SPSS-SPMTM has the merits of lighter mover mass, lower cogging force and about 95% less eddy current magnet loss compared to its conventional counterpart.

Chapter8. General Conclusions

8.1 Introduction

Novel PS-PM linear machines have been developed in this thesis by adopting the idea of dual active stators and one passive mover. Three different types of linear machines are investigated, namely

- PS-FRPM flat linear machine.
- PS-PM tubular linear machines.
- PS-PM single phase short stroke tubular linear machines.

This chapter is the conclusions, which can be deduced from the research that has been carried out in this thesis and underlines the future work that can be conducted to expand the work of this study.

8.2 SFPM and FRPM Conventional Flat Linear Machines

Two double salient PM linear machines, i.e. SFPM and FRPM linear machines are designed, optimized and compared under the same design and optimization considerations. The following conclusions can be obtained.

- The FRPM linear machine shows balanced back-EMF waveforms, whilst the SFPM linear machine has unbalanced back-EMF waveforms due to the longitudinal end effect.
- Higher thrust force capability can be achieved by the SFPM linear machine. However, the FRPM linear machine has lower thrust force ripple compared to the SFPM linear machine.
- Both machines show PM thickness restriction, i.e. each machine has an optimal PM thickness by which the highest average thrust force can be obtained.
- PM demagnetization risk is presented in both machines.

8.3 PS-FRPM Flat Linear Machine

A novel flat linear machine referenced to as a PS-FRPM linear machine is developed, in order to overcome the disadvantages of the conventional FRPM and SFPM linear machines, such as the conflict between electrical and magnetic loadings as well as the risk of the PMs demagnetization. The operation principle and the force production mechanism are explained. Furthermore, the major design parameters are

optimized to achieve maximum thrust force. In addition, with constant stator slot number, PS-FRPM linear machines having different mover pole numbers are designed, analysed and compared to determine the optimal mover pole number in terms of the highest back-EMF and the highest thrust force capability. Moreover, the influence of the longitudinal end effect on the machine performance is investigated. The machine demagnetization withstand capability is analysed. The following conclusions can be observed:

- The machine operation is based on the concept of the switched flux.
- Similar to the SFPM machine, the thrust force of the proposed machine is produced by many field harmonics.
- The machine takes the advantage of large slot area leading to the reduction of the winding resistance and consequently reduce the copper loss.
- The machine has unbalanced back-EMF due to the longitudinal end effect.
- The PMs of the proposed machine is separated from the armature windings leading to the reduction of armature reaction, and therefore, the proposed machine shows low magnet eddy current loss.
- The proposed machine exhibits good PM demagnetization withstand capability.

8.4 PS-PM Tubular Machines

Two novel PS-PM tubular machines, i.e. PS-SPM and PS-IPM, are introduced. The structures as well as the operation principles of both machines are explained. The machines are optimized for maximum thrust force, and the influence of major design parameters on the machine performances are investigated. Moreover, PS-SPM and PS-IPM tubular machines with different mover poles are designed, analysed and compared. In addition, PS-SPM and PS-IPM tubular machines having single-layer windings are designed and compared to doubly layer winding counterparts. Furthermore, the performances of both PS-SPM and PS-IPM tubular machines are compared. It is shown that:

- The optimal mover pole number for maximum thrust force equals to stator slot number – 1, for both machines.
- PS-PM tubular machines with single-layer winding show higher thrust force capability as well as better PM utilization compared to their double-layer winding counterparts.

- Lower thrust force ripple can be obtained by the single-layer winding PS-PM tubular machines compared to the double-layer winding PS-PM tubular machines.
- The PS-IPM tubular machine has higher thrust force and better PMs utilization compared to the PS-SPM tubular machine.
- In terms of thrust force ripple, the PS-SPM tubular machine exhibits lower cogging force and consequently lower thrust force ripple than the PS-IPM tubular machine.
- Both PS-PM tubular machines have good demagnetization withstand capability. However, due to the flux fringing and leakage, some edges of the PMs of the PS-IPM tubular machine experience demagnetization.

8.5 Single-Phase Short Stroke Permanent Magnet Tubular Machines with Partitioned Stator

Based on the concept of the dual active stators and one passive mover, new partitioned stator single-phase short-stroke permanent magnet tubular machines are designed. The machine structures are discussed. The impact of the inner stator permanent magnet pole alignment with the outer stator teeth or slots is investigated. Furthermore, three machines with different mover pole pitches are designed, in order to determine the best mover pole pitch in terms of the highest flux linkage and back-EMF. Moreover, the machines are optimized for maximum thrust force, and the electromagnetic performances of the designed machines are analysed and compared. The following conclusions are obtained:

- In order to achieve the oscillated movement of the mover in the proposed machines, the PM poles should be aligned with the outer stator slots.
- The best performance in terms of the highest flux linkage, back-EMF and thrust force can be obtained when the mover pole pitch equals the stator slot pitch.
- By considering the above mentioned results, three machines, i.e. PS-PSS-SPMTM, PS-PSS-IPMTM-1 and PS-PSS-IPMTM-2, are analysed and compared. It is found that:
    - All the three machines have the advantages of light mover mass as well as low magnet eddy current loss.

- Although the total magnet volume of the PS-PSS-SPMTM is less than that of the PS-PSS-IPMTM-2, it shows a comparable thrust force compared to the PS-PSS-IPMTM-2.
- The PS-PSS-IPMTM-1 has the lowest no-load and load performances compared to other machines.
- The PS-PSS-SPMTM shows the lowest cogging force compared to other machines.
- In terms of iron loss and magnet eddy current loss the PS-PSS-IPMTM-1 has the lowest losses compared to other machines.

8.6 Comparison of PS-PM Linear Machines with Their Conventional Counterparts

In order to assess the proposed PS-PM linear machines, a comparison between such machines and their conventional counterpart machines are carried out. It is shown that:

A. Comparison of the PS-FRPM flat linear machine with the SFPM and FRPM flat linear machines

The merits of the PS-FRPM flat linear machine:

- ✓ The highest force capability, i.e. about 55% and 24% higher thrust force than that of the conventional FRPM and SFPM linear machines, respectively.
- ✓ The highest force density.
- ✓ The best demagnetization withstand capability.
- ✓ The lowest thrust force ripple.
- ✓ The highest electrical loading as well as magnetic loading capabilities.
- ✓ Overcoming the conflict between the electrical and magnetic loadings, this can be considered as the main problems of the existing double salient PM linear machines.
- ✓ About 40% lower normal force than that of the SFPM linear machine**.**

The demerits of the PS-FRPM flat linear machine:

- o Asymmetric flux linkage leading to unbalanced back-EMFs, which are inherent features of many linear machines due to the longitudinal end effect.
- o About 18.9% higher normal force than that of the conventional FRPM linear machine.

- Manufacturing complexity.

B. Comparison of the PS-PM tubular machines with the conventional SFPM tubular machine

The merits of the PS-PM tubular machines:

- ✓ Better permanent magnet utilization.
- ✓ Lower mover mass.
- ✓ Lower magnet eddy current loss.
- ✓ Higher thrust force capability.
- ✓ Higher force density.
- ✓ Wider slot area which results in reduce the phase resistance.
- ✓ Better demagnetization withstand capability.

The demerits of the PS-PM tubular machines:

- The PS-IPM shows high thrust force ripple, due to the high cogging force.
- Manufacturing complexity.

C. Comparison of PS-SPSS-SPMTM with the conventional SPSS-SPMTM

The merits of the PS-SPSS-SPMTM:

- ✓ Lower cogging force.
- ✓ Lower mover mass.
- ✓ Lower magnet eddy current loss.
- ✓ Lower magnet volume.
- ✓ Comparable thrust force capability compared to the conventional SPSS-SPMTM.
- ✓ A good candidate for harsh environment conditions without risk of permanent magnet high temperature problem.

The demerits of the PS-SPSS-SPMTM:

- Higher iron loss by 24% compared to the conventional SPSS-SPMTM.
- Manufacturing complexity.

8.7 Future Works

Although an essential work on the designing, optimizing, and comparison of PS-PM linear machines has been carried out in this thesis, the following areas may be of interest that could be investigated:

- Further investigation on the PS-IPM tubular machine would be how to minimize the cogging force and consequently reduce the thrust force ripple. The thrust force ripple of the PS-IPM tubular machine is quite high. However, this could be reduced by the controller, it would be more efficient to reduce the cogging force in the design stage to enhance the servo operation.
- Multi-phase PS-PM linear machines can be designed for fault tolerant capability.
- PS-FRPM linear machine with consequent pole PM can be designed, analysed and compared with PS-FRPM linear machine. Such topology would be of interest in terms of the reducing the total PM usage.
- A study can be carried out to investigate new stator/mover combinations for the PS-PM linear machines without the restriction of even stator pole number, i.e., investigation of the PS-PM linear machines with odd stator pole number.
- Although the dynamic performance of the PS-FRPM linear machine was simulated by MATLA/Simulink, further work is needed to experimentally verify the dynamic performance of the PS-PM linear machines.
- Thermal analysis of the PS-PM linear machines can be carried out, which will be helpful in the machine cooling requirements.
- A comparison between PS-FRPM linear machines having a fractional slot concentrated winding and an integer slot overlapping winding would be of interest.

References

[ABB08] A. Y. M. Abbas, J. E. Fletcher "Efficiency evaluation of linear permanent magnet synchronous machines using the synthetic loading method" *in Proc. Power Electronics Specialists (PESC) Conf.*, pp. 3074-3080, 2008.

[ABD13] I. I. Abdalla, T. Ibrahim, and N. M. Nor, "Comparative study of permanent magnet configurations of short-stroke linear motor for reciprocating compressor in household refrigerator application," *ITEE*, vol. 2, no. 1, pp.16-24, February, 2013.

[ABD14] S. E. Abdollahi and S. Vaez-Zadeh, "Back-EMF analysis of a novel linear flux switching motor with segmented secondary," *IEEE Trans. Magnetics*, vol. 50, no. 4, pp. 1-9, April 2014.

[AKM89] R. Akmese and J. F. Eastham, "Dynamic performance of a brushless DC tubular drive system," *IEEE Trans. Magnetic*, vol.25, no.5, pp.3269-3271, September, 1989.

[AKM92] R. Akmese, and J. F. Eastham, "Design of permanent magnet flat linear motors for standstill applications," *IEEE Trans. Magnetics*, vol. 28, no. 5, pp. 3042 – 3044, September, 1992.

[AMA05] Y. Amara, J. Wang and D. Howe, "Analytical prediction of eddy-current loss in modular tubular permanent-magnet machines," *IEEE Trans. Energy Conversion*, vol. 20, no. 4, pp. 761-770, December. 2005.

[AMA13] Y. Amara, G. Barakat, J. Paulides and E. Lomonova, "Overload capability of linear flux switching permanent magnet machines," *Applied Mechanics and Materials*, vols.416-417, pp.345-352, September, 2013

[AND13] M. Andriollo, L. Dall'Ora, and A. Tortella, "Electromagnetic parameter characterization of a short-stroke linear PM generator for renewable energy application," *in Proc. Clean Electrical Power Int. Conf.*, vol., no., pp.383-390, June 2013.

[ARW10] A. S. Thomas, Z.Q. Zhu, R. L. Owen, G. W. Jewell and D. Howe, "Multiphase flux-switching permanent-magnet brushless machine for aerospace application," *IEEE Trans. Industry Applications*, vol.45, no.6, pp.1971-1980, November/December, 2009.

[ASH10] M. Ashabani, Y. Abdel-Rady, I. Mohamed and J. Milimonfared, "Optimum design of tubular permanent magnet motors for thrust characteristics improvement by combined taguchi-neural network approach," *IEEE Trans.*

Magnetic, vol.46, no.12, pp.4092-4100, December, 2010.

[AWA16] C. C. Awah, Z. Q. Zhu, Z. Z. Wu, H. L. Zhan, J. J. Shi, D. Wu and X. Ge , "Comparison of Partitioned Stator Switched Flux Permanent Magnet Machines Having Single- or Double-Layer Windings," *IEEE Trans. Magnetics*, vol. 52, no. 1, pp. 1-10, January, 2016.

[BIA03] N. Bianchi, S. Bolognani, D. Corte and Tonel, "Tubular linear permanent magnet motors: An overall comparison," *IEEE Trans. Industry Applications*, vol.39, no.2, pp. 466-475, March, 2003.

[BIA06] N. Bianchi, S. Bolognani, M. D. Pre and G. Grezzani, "Design considerations for fractional-slot winding configurations of synchronous machines," *IEEE Trans. Industrial Applications*, vol.42, no.4, pp.997-1006, July, 2006.

[BOL12] I. Boldea, L. Tutelea and M. Topor, "Theoretical characterization of three phase flux reversal machine with rotor-PM flux concentration," in *Proc. Optimization of Electrical and Electronic Equipment (OPTIM) Conf.,* pp. 472–476, 2012.

[BOL98] I. Boldea, C. Wang, B. Yang and S. Nasar, "Analysis and design of Flux-reversal linear permanent magnet oscillating machine," *in Proc. IEEE Industry Applications Conf.*, vol. 1, pp. 12–15, October, 1998.

[BOL99] I. Boldea and S. A. Nasar, "Linear electric actuators and generators," *IEEE Trans. Energy Conversion*, vol.14, no.3, pp.712-717, September, 1999.

[CAI11] J. Cai, Q. Lu, Y. Jin, C. Chen and Y. Ye, "Performance investigation of multi-tooth flux-switching PM linear motor," *in Proc. Electrical Machines and Systems Int. Conf.*, August, 2011.

[CAI14] J. Cai, Q. Lu, X. Huang, Y. Ye and Y.Fang, "Performance investigation of a novel multi-tooth switched-flux linear motor," *in Proc. Ecological Vehicles and Renewable Energies(EVER) Conf.,* March, 2014.

[CAO11a] R. Cao, M. Cheng, C. Mi, W. Hua and W. Zhao, "A linear doubly salient permanent-magnet motor with modular and complementary structure," *IEEE Trans. Magnetics*, vol. 47, no. 12, pp. 4809-4821, December, 2011.

[CAO11b] R. Cao, M. Cheng, C. Mi, W. Hua and W. Zhao, "A hybrid excitation flux-switching permanent magnet linear motor for urban rail transit," *in Proc. IEEE Vehicle Power and Propulsion Conf.,* pp. 1-5, September, 2011.

[CAO12] R. Cao, M. Cheng, C. Mi, W. Hua and W. Zhao, "Modelling of

complementary and modular linear FSPM motor for urban rail transit," *IEEE Trans. Energy Conversion*, vol.27, no.2, pp.489-497, June, 2012.

[CAO13a] R. Cao, M. Cheng and W. Hua, "Investigation and general design principle of a new series of complementary and modular linear FSPM motors," *IEEE Trans. Industrial Electronics*, vol.60, no.12, pp.5436-5446, December, 2013.

[CAO13b] R. Cao, M. Cheng, C. Mi, W. Hua and W. Zhao, "Complementary and modular linear flux-switching motors with different motor and stator pole pitch," *IEEE Trans. Magnetics*, vol.49, no.4, pp.1493-1504, April, 2013.

[CHA08] K. T. Chau, C. C. Chan and C. Liu, "Overview of permanent-magnet brushless drives for electric and hybrid electric vehicles," *IEEE Trans. Ind. Electron*., vol. 55, no. 6, pp. 2246–2257, Jun. 2008.

[CHE08] X. Chen, Z. Q. Zhu, D. Howe, and J. S. Dai, "Comparative study of alternative permanent magnet linear oscillating actuators," *in Proc. Electrical Machines and System Int. Conf.*, pp.2826-2831, October, 2008.

[CHE09] J. T. Chen, "High-torque direct-drive flux-switching PM brushless AC machines," *Ph.D. thesis*, University of Sheffield, Sheffield, U.K. 2009.

[CHE10] J. T. Chen and Z. Q. Zhu, "Winding configurations and optimal stator and rotor pole combination of flux-switching PM brushless AC machines," *IEEE Trans. Energy Conversion*, vol. 25, no. 2, pp. 293-302, June, 2010.

[CHE11] M. Cheng, W. Hua, J. Zhang and W. Zhao, "Overview of stator-permanent magnet brushless machines," *IEEE Trans. Industrial Electronics*, vol. 58, no. 11, pp. 5087-5101, November, 2011.

[CHE12] X. Chen and Z. Q. Zhu, "Modelling and evaluation of linear oscillating actuators," *in Proc. Electrical Machines and Systems Int. Conf.* , vol. 1, no. 4, pp.517-524, 2012.

[CHU07] S. U. Chung, D. H. Kang, J. H. Chang, J. W. Kim and J. Y. Lee, "New configuration of flux reversal linear synchronous motor," *in Proc. Electrical Machines Int. Conf.*, pp. 864–867, October, 2007.

[CHU08] S. U. Chung, H. J. Lee and S. M. Hwang, "A novel design of linear synchronous motor using FRM topology," *IEEE Trans. Magnetics*, vol. 44, no. 6, pp. 1514–1517, June, 2008.

[CHU11] S. U. Chung, H. Lee, D. K. Hong, J. Y. Lee, B. C. Woo and D. H. Koo, "Development of flux reversal linear synchronous motor for precision position control," *International Journal of Precision Engineering and*

Manufacturing, vol. 12, no. 3, pp. 443-450, June, 2011.

[CLA95] R. E. Clark, D. S. Smith, P. H. Mellor and D. Howe, "Design optimisation of moving-magnet actuators for reciprocating electro-mechanical systems," *IEEE Trans. Magnetics*, vol. 31, no. 6, pp. 3746-3748, November, 1995.

[DAV15] D. J. Evans and Z. Q. Zhu, "Novel partitioned stator switched flux permanent magnet machines," *IEEE Trans. Magnetics*, vol. 51, no. 1, pp. 1-14, January, 2015.

[DEO97] R. P. Deodhar, I. Boldea and T. Miller, "The flux-reversal machine: a new brushless doubly salient permanent-magnet machine," *IEEE Trans. Industry Applications*, vol. 33, no. 4, pp. 925-934, July, 1997.

[DOR03] D. G. Dorrell, I. Chindurza and F. Butt, "Operation, theory and comparison of the flux reversal machine Is it a viable proposition?" *in Proc. Power Electron Drive System Int. Conf.*, pp. 253–258, 2003.

[DU11a] Y. Du, K. T. Chau, M. Cheng, Y. Fan, Y. Wang, W. Hua and Z. Wang, "Design and analysis of linear stator permanent magnet Vernier machines," *IEEE Trans. Magnetics*, vol. 47, no. 10, pp. 4219-4222, October, 2011.

[DU11b] Y. Du, K. T. Chau, M. Cheng, Y. Fan, W. Zhao and X. Li, "Theory and comparison of linear stator permanent magnet Vernier machine," *in Proc. Electrical Machines and Systems Int. Conf.*, pp. 1-4, 2011.

[DU12] Y. Du, K. T. Chau, M. Cheng, Y. Fan, Z. Wang and F. Li, "A linear stator permanent magnet Vernier HTS machine for wave energy conversion," *IEEE Trans. Applied Super Conductivity*, vol. 22, no. 3, pp. 5202505-5202505, June, 2012.

[DU13] Y. Du, M. Cheng and K. T. Chau, "Simulation of the linear primary permanent magnet Vernier machine system for wave energy conversion," *in Proc. Electrical Machines and Systems Int. Conf.*, pp.262-266, October, 2013.

[ELR04] A. M. EL-Refaie, D. W. Novotny and T. M. Jahns, "A simple model for flux weakening in surface PM synchronous machines using back-to-back thyristors," *IEEE Power Electronics Letters*, vol.2, no. 2, pp. 54-57, June, 2004.

[FAN13] Z. Fang, W. Zhao, J. Ji, J. Zhao, D. Zhang and Y. Du, "A primary-permanent-magnet Vernier linear machine with improved fault-tolerant capability," *in Proc. Electrical Machines and Systems Int. Conf.*, pp. 1882-

1885, October, 2013.

[FAR15] J. D. McFarland, T. M. Jahns and A. M. EL-Refaie, "Analysis of the Torque Production Mechanism for Flux-Switching Permanent-Magnet Machines," *IEEE Trans. on Industry Applications*, vol. 51, no. 4, pp. 3041-3049, July, 2015.

[FAS14] A. Fasolo, L. Alberti and N. Bianchi, "Performance comparison between switching-flux and IPM machines with rare-earth and ferrite PMs," *IEEE Trans. Industry Applications.*, vol. 50, no. 6, pp. 3708–3716, November, 2014.

[FEI12] W. Fei, P. C. Luk, J. shen, Y. Wang and M. Jin, "A Novel permanent magnet flux switching machine with an outer-rotor configuration for in-wheel light traction applications," *IEEE Trans. Industry Applications.*, vol. 45, no. 5, pp. 1496–1506, September, 2012.

[GAN11] A. Gandhi, A. Mohammadpour, S. Sadeghi and L. Parsa, "Double-sided FRLSM for long-stroke safety-critical applications," *in Proc. IEEE Ind. Electron. Soc. IECON 37th Ann. Conf.*, pp. 4186–4191, November, 2011.

[GAN12] A. Gandhi and L. Parsa, "Double-sided flux-switching linear synchronous machine with yokeless translator," *in Proc. IEEE Energy Conversion Congress and Exposition Conf.*, pp.2676-2680, 2012.

[GAN13] A. Gandhi, and L. Parsa, "Thrust optimization of a flux-switching linear synchronous machine with yokeless translator," *IEEE Trans. Magnetics*, vol.49, no.4, pp.1436-1443, April, 2013.

[GAN15] A. Gandhi, and L. Parsa, "Hybrid Flux-Switching Linear Machine with Fault-Tolerant Capability," *2015 IEEE International Electric Machines & Drives Conf. (IEMDC*), 2015, pp. 715-720.

[HEL09] R. Hellinger and P. Mnich, "Linear motor-powered transportation: history, present status, and future outlook," *in Proc. IEEE*, vol.97, no.11, November, 2009.

[HOA07] E. Hoang, M. Lecrivain and M. Gabsi, "A new structure of a switching flux synchronous polyphased machine with hybrid excitation," *in Proc. Eur. Power Electronic and Applications Conf.*, pp.1-8, September, 2007.

[HOA97] E. Hoang, A. Ben Ahmed, and J. Lucidarme, "Switching flux permanent magnet polyphase synchronous machines," *in Proc. Power Electronics and Applications Conf.*, vol. 3, pp. 903–908, 1997.

[HUA05] W. Hua, Z. Q. Zhu, M. Cheng, Y. Pang and D, Howe, " Comparison of flux-switching and doubly-salient permanent magnet brushless machines," *in Proc. 8th Int. Elect. Syst. Conf.,* pp. 165–170, Mach, 2005.

[HUA06] W. Hua, Z. Q. Zhu, M. Cheng and D. Howe, "Design of flux-switching permanent magnet machine considering the limitation of inverter and flux-weakening capability," *in Proc. 41st Industry Applications Conf.,* pp.2403-2410, 2006.

[HUA10] W. Hua, Z. Wu and M. Cheng, "A novel three-phase flux-reversal permanent magnet machine with compensatory windings," *in Proc. Electrical Machines and Systems Int. Conf.* , pp.1117-1121, 2010.

[HUA11a] L. Huang, H. Yu, M. Hu, J. Zhao and Z. Cheng, "A novel flux-switching permanent magnet linear generator for wave energy extraction," *IEEE Trans. Magnetic,* vol.47, no.5, pp.1034-1037, May, 2011.

[HUA11b] L. Huang, H. Yu, M. Hu, S, Zhou and L. Hao, "Fault-tolerant performance of a novel flux-switching permanent magnet linear machine based on harmonic current injection," *IEEE Trans. Magnetic,* vol.47, no.10, pp.3224-3227, October, 2011.

[HUA13] L. Huang, H. Yu, M. Hu and H. Liu, "Study on a long primary flux-switching permanent magnet linear motor for electromagnetic launch systems," *IEEE Trans. Plasma Science,* vol.41, no.5, pp.1138-1144, May, 2013.

[HWA12] C. C. Hwang, P. L. Li and T. Liu, "Design and analysis of a novel hybrid excited linear flux switching permanent magnet motor," *IEEE Trans. Magnetic,* vol.47, no.11, pp.2969-2972, November, 2009.

[IBR08] T. Ibrahim, J. Wang, and D. Howe, "Analysis and experimental verification of a single-phase, quasi-Halbach magnetized tubular permanent magnet motor with non-ferromagnetic support tube," *IEEE Trans. Magnetics,* vol.44, no.11, pp.4361-4364, November, 2008.

[IMA14] T. Imada and S. Shimomura, "Magnet Arrangement of linear PM Vernier machine," *in Proc. Electrical Machines and Systems Int. Conf.,* pp. 3642-3646, 2014.

[ISH95] A. Ishizaki, T. Tanaka, K. Takasaki and S. Nishikata, "Theory and optimum design of PM Vernier motor," *in Proc. Electrical Machines and Drives Int. Conf.,* pp. 208-212, September, 1995

[JI13] J. Ji, S. Yan, W. Zhao, G. Liu, and X. Zhu, “Minimization of cogging force in a novel linear permanent-magnet motor for artificial hearts,” *IEEE Trans. Magnetics*, vol. 49, no. 7, pp. 3901–3904, July, 2013.

[JIN09] M. J. Jin, C. F. Wang, J. X. Shen and B. Xia, “A modular permanent-magnet flux-switching linear machine with fault-tolerant capability” *IEEE Trans. Magnetic*, vol.45, no.8, pp.3179-3186, August, 2009.

[JIN09] M. J. Jin, C. F. Wang, J. X. Shen and B. Xia, "A modular permanent-magnet flux-switching linear machine with fault-tolerant capability," *IEEE Trans. Magnetics*, vol. 45, no. 8, pp. 3179-3186, August, 2009.

[KAN12] M. Kang, J. Ji, G. Liu and W. Zhao, “A new tubular fault-tolerant permanent-magnet motor for active vehicle suspension,” *in Proc. IEEE industrial Electronic Society Conf.*, pp.4082-4086, 2012.

[KIM09] T. H. Kim, “A study on the design of an inset-permanent-magnet-type flux-reversal machine,” *IEEE Trans. Magnetics*, vol. 45, no. 6, pp. 2859–2862, June, 2009.

[KRO10] D. C. J. Krop, L. Encica and E. A. Lomonoova, “Analysis of a novel double sided flux switching linear motor topology,” *in Proc. Electrical Machines Int. Conf.*, pp.1-5, 2010.

[LAI75] E. R. Laithwaite, “Linear electric machines-a personal view,” *IEEE Proc.*, vol.63, no.2, February, 1975.

[LI07] Y. Li and C. Mi, “Doubly salient permanent-magnet machine with skewed rotor and six-state commutating mode,” *IEEE Trans. Magnetic*, vol.43, no.9, pp.3623-3629, September, 2007.

[LI13a] Y. Li, Q. Lu, J .Chen and Z. Q. Zhu, “Research on combinations of primary and secondary pole numbers for linear switched-flux PM machines with odd pole number of primary,” *Appl. Mech. Mater.*, vol.416-417, pp.401-407, July 2013.

[LI13b] L. Li, M. Ma and C. C. Chan, “Detent force analysis in permanent magnet linear synchronous motor considering longitudinal end effects,” *in Proc. IEEE Electrical Machines and Systems Conf.*, pp.9-15, 2013.

[LIA92] Y. Liao, F. Liang and T. A. Lipo, “A novel permanent magnet motor with doubly salient structure,” *in Proc. Industry Applications Soc.* Annu. Meeting, pp. 308–314, October, 1992.

[LIU13] G. Liu, L. Chen, W. Zhao, Y. Jiang and L. Qu, "Internal model control of

permanent magnet synchronous motor using support vector machine generalized inverse," *IEEE Trans. Industrial Informatics*, vol. 9, no. 2, pp. 890-898, May 2013.

[LIU14] X. Liu, C. Zou, Y. Du and F. Xiao, " A linear consequent pole stator permanent magnet Vernier machine," *in Proc. Electrical Machines and Systems Int. Conf.,* pp.1753-1756, October, 2014.

[LU14] Q. Lu, Y. Li, Y. Ye, J. T. Chen and Z. Q. Zhu, "A Linear Switched-Flux PM Machine with 9/10 Primary/Secondary Pole Number," *in proc. Ecological Vehicles and Renewable Energies Int. Conf*., 2014.

[LU15] Q. Lu, H. Li, X. Huang, D. Ye, Y. Fang and Y. Ye, "Investigation of double-sided multi-tooth switched-flux linear motor," *in proc. Electrical Machines and Systems Int. Conf.*, pp. 237-242, 2015.

[LU16] Q. Lu, J. Shi, X. Huang, Y. Fang and Y. Ye, "Performance of partitioned primary linear switched flux PM machines," *in Proc. on Electrical Machines Int. Conf.*, pp. 2486-2491, 2016.

[MCL88] G. W. Mclean, "Review of recent progress in linear motors," *in Proc. IEE-Electric Power Applications Conf.* , pp. 380-416, 1988.

[MER55] F. W. Merrill, "Permanent magnet excited synchronous motors," in *Electrical Engineering*, vol. 74, no. 2, pp. 143-143, February, 1955.

[MIL89] T. J. E. Miller, "Brushless permanent magnet and reluctance motor derives," *Oxford University Press, UK,* pp. 17-18, 1989.

[MIN10] W. Min, J. T. Chen, Z. Q. Zhu, Y. Zhu and G. H. Duan, "optimization of linear flux switching permanent magnet motor," *in Proc. IEEE Vehicle Power and Propulsion Conf.,* September, 2010.

[MIN11] W. Min, J. T. Chen, Z. Q. Zhu, Y. Zhu, M. Zhang and G. H. Duan, "Optimization and comparison of novel E-core and C-core linear switched flux PM machines*," IEEE Trans. Magnetic*, vol.47, no.8, pp.2134-2141, August, 2011.

[MOG96] J. S. Moghani and J. F. Eastham, "The dynamic response of a linear brushless DC motor," *in Proc. Power Electronics, Drives and Energy Systems for Industrial Growth Conf.*, vol.1, pp. 542-545, 1996.

[MOR08] D. S. More, H. Kalluru and B. G. Fernandes, "d-q equivalent circuit representation of three-phase flux reversal machine with full pitch winding," *In Proc. IEEE Power Electron Conf.*, pp. 1208–1214, September, 2008.

[MOR10a] D. S. More and B. G. Fernandes, “Power density improvement of three phase flux reversal machine with distributed winding,” *IET Electric Power Applications*, vol. 4, no. 2, pp. 109–120, February, 2010.

[MOR10b] D. S. More and B. G. Fernandes, “Analysis of flux-reversal machine based on fictitious electrical gear,” *IEEE Trans. Energy Conversion*, vol. 25, no. 4, pp. 940–947, December, 2010.

[MOR13] D. S. More and B. G. Fernandes, “Modelling and performance of three phase 6/14 pole flux reversal machine,” *IET Electric Power Appl*ications, vol. 7, no. 2, pp. 131–139, February, 2013.

[NAI16] S. S. Nair, V. I. Patel and J. Wang, “Post-demagnetization performance assessment for interior permanent magnet AC machines,”*IEEE Trans. Magnetic*, vol.52, no.4, pp.8102810, April, 2016.

[OWE08] R. L. Owen, Z. Q. Zhu, A. S. Thomas, G. W. Jewell and D. Howe, "Fault-Tolerant Flux-Switching Permanent Magnet Brushless AC Machines," *in Proc. IEEE Industry Applications Society Annual Meeting,* pp. 1-8, 2008.

[PAN08] Y. Pang, Z. Q. Zhu, D. Howe, S. Iwasaki, R. Deodhar and A. Pride, “Investigation of iron loss in flux-switching PM machines,” *in Proc. Power Electronic, Machines and Drives, 4th IET Conf.*, pp.460-464, 2008.

[PEL11] G. Pellegrino and C. Gerada, “Modelling of flux reversal machines for direct drive applications,” *in Proc. Power Electronics and Application European Conf.* pp.1-10, 2011.

[POL03] H. Polinder, J. G. Slootweg, M. J. Hoeijmakers, and J. C. Compter, “Modling of a linear PM machine including magnetic saturation and end effects: maximum force to current ratio,” *IEEE Trans. On Industry*, vol.2, no.6, pp.1681-1688, November/December, 2003.

[RAU55] S. E. Rauch and L. J. Johnson “Design principles of flux-switching alternators,” *AIEE Tans. Power Application Systems, part III*, vol.74, no.3, pp.1261-1268, January, 1955.

[RAU55] S. E. Rauch and L. J. Johnson, “Design principle of flux-switching alternators,” *AIEE Trans*. vol.137, no. 1, pp. 1261-1268, January, 1955.

[RIN07] R. Rinkeviciene, S. Lisauskas and V. Batkauskas, “Application and analysis of linear induction motors in mechatronic systems,” *Doctoral school of energy-and geo-technology*, 15-20 January, 2007.

[ROS05] M. Rosu, J. Saitz and A. Arkkio, “Hysteresis model for finite-element

analysis of permanent magnet demagnetization in a large synchronous motor under fault condition," *IEEE Trans. Magnetic,* vol.41, no.6, pp.2118-2123, June, 2005.

[SAD71] G.V. Sadler and A. W. Davey, "Applications of linear induction motors in industry," *in Proc. Institution of Electrical Engineers Conf.,* pp.765-776, 1971.

[SAN97] M. Sanada, S. Morimoto and Y. Takeda, "Interior permanent magnet linear synchronous motor for high-performance drives," *IEEE Trans. Industry Applications*, vol. 33, no. 4, pp. 966-972, July, 1997.

[SHI12] H. K. Shin, T. H. Kim and C. J. Kim, "Demagnetization characteristic analysis of inset-type-flux-reversal machines," *in Proc. Electrical Machines and Systems Int. Conf.,* pp.1-4, 2012.

[SI08] J. Si, X. Wang, H. Chen, S. Yang and L. Jiao, "Analysis of detent force in a discontinuous primary type permanent magnet linear synchronous motor," *in Proc. IEEE Electrical Machines and Systems Conf.,* pp.3443-3448, 2008.

[SPO03] D. Spooner and L. Haydock, " Vernier hybrid machines," *IEE Trans. Electrical Power Application*, vol. 150, no. 6, pp. 655-662, November, 2003.

[WAN01] C. X.Wang, I. Boldea, and S. A. Nasar, "Characterization of three phase flux reversal machine as an automotive generator," *IEEE Trans. Energy Conversion,* vol. 16, no. 1, pp. 74–80, March, 2001.

[WAN04] J. Wang and D. Howe, "Design optimization of radially magnetized, iron-cored, tubular permanent-magnet machines and drive systems," *IEEE Trans. Magnetics*, vol. 40, no. 5, pp. 3262-3277, September, 2004.

[WAN07] J. Wang, D. Howe, and Z. Lin, "Comparative study of winding configurations of short-stroke, single phase tubular permanent magnet motor for refrigeration applications," *in Proc. Industry Applications Conf.,* pp.311-318, 23-27 September, 2007.

[WAN08] C. F. Wang, J. X. Shen, L. L. Wang, and K. Wang, "A novel permanent magnet flux-switching linear motor," *in Proc. Power Electronics, Machines and Drives (PEMD) 4th IET Conf.,* pp.116-119, 2008.

[WAN08a] J. Wang, W. Wang, R. Clark, K. Atallah and D. Howe, "A tubular flux-switching permanent magnet machine," *Applied Physics*, vol.103, no.7, pp. 07f105-1-07f105-3, 2008.

[WAN08b] J. Wang, W. Wang, K. Atallah, and D. Howe, "Comparative studies of linear

permanent magnet topologies for active vehicle suspension," *in Proc. IEEE Vehicle Power and Propulsion Conf.*, pp., September, 2008.

[WAN08c] J. Wang, W. Wang, K. Atallah and D. Howe, "Design considerations for tubular flux-switching permanent magnet machines," *IEEE Trans. Magnetics*, vol.44, no. 11, November, 2008.

[WAN08d] J. Wang, Z. Lin, D. Howe, "Analysis of a short-stroke, single-phase, quasi-Halbach magnetized tubular permanent magnet motor for linear compressor applications," *Electric Power Applications, IET* , vol.2, no.3, pp.193-200, May, 2008.

[WAN09] C. F. Wang, J. X. Shen, Y. Wang, L. L. Wang and M. J. Jin, "A new method for reduction of detent force in permanent magnet flux-switching linear motors," *IEEE Trans. Magnetic*, vol.45, no.6, pp.2843-2846, June, 2009.

[WAN10] J. Wang, D. Howe, and Z. Lin, "Design optimization of short-stroke single-phase tubular permanent-magnet motor for refrigeration applications," *IEEE Trans. Industrial Electronics*, vol.57, no.1, pp.327-334, January, 2010.

[WAN12] D. Wang, X. Wang, and S. Y. Jung, "Reduction on Cogging Torque in Flux Switching Permanent Magnet Machine by Teeth Notching Schemes," *IEEE Trans. Magnetics*, vol 48, no.11, pp.4228-4231, November, 2012.

[WAN15] X. Wang, F. Wei, B. Xu, H. Feng and X. Xu, "A novel complementary and modular tubular permanent magnet flux-switching motor," *in Proc. LDIA*, 2015.

[WAN99] C. Wang, S. A. Nasar and I. Boldea, "Three-phase Flux reversal machine (FRM)," *in Proc. IEEE Electrical Power Applications Conf.*, vol. 146, no. 2, March, 1999.

[WU16] Z. Wu; Z. Zhu, "Comparative analysis of end effect in partitioned stator flux reversal machines having surface-mounted and consequent pole permanent magnets," *IEEE Trans. Magnetics* , no.99, pp.1-1, July, 2016.

[XIA14] F. Xiao, X. Liu, Y. Du, K. Shi and P. Xu, "A c-core linear flux-switching permanent magnet machine with positive additional teeth," *in Proc. Electrical Machines and Systems Int. Conf.,* pp. 1757-1761, October, 2014.

[XU14a] L. Xu, W. Zhao, G. Liu and et al, "Design and analysis of a new linear hybrid excited flux reversal motor with inset permanent magnets," *IEEE Trans. Magnetics*, vol. 50, no. 11, pp. 8202204, November, 2014.

[XU14b] L. Xu, J. Ji, G. Liu, Y. Du, and H. Liu "Design and analysis of linear fault-

tolerant permanent-magnet vernier machines," *Scientific World Journal,* Vol. 2014, pp. 1-8, 2014.

[YAN13] L. Yanxin, L. Oinfen, J. Chen and Z. Q. Zhu, "Research on combinations of primary and secondary pole numbers for linear switched-flux PM machines with odd pole number of primary," *Appl. Mech. Mater.,* vol.416-417, pp. 401-407, July 2013.

[YAN14] L. Yan, W. L. Zongxia, C. Chen and M. Chen, "Design and modelling of three phase flux-switching permanent linear motor," *in Proc. IEEE Chinese Guidance, Navigation and control, pp.2675*-2680, August, 2014.

[YOU11] Y. J. You, S. Chang, C. Kun and W. B. Jie, "Three-dimensional magnetic field analysis and experiment research of flux-switching permanent magnet machine," *in Proc. International Transportation, Mechanical, and Electrical Engineering Conf.*, December, 16-18, 2011.

[YU07] H. Yu and B. Fahimi, "A direct control scheme to achieve maximum acceleration in linear induction motor," *in Proc. IEEE Electric Machines and Drives Conf.,* pp.977-983, 2007.

[ZHA10] G. Zhao, L. Tian, Q. Shen and R. Tang, "Demagnetization analysis of permanent magnet synchronous machines under short circuit fault," *in Proc. Pacific Power and Energy Engineering Conf.,* pp. 1-4, 2010.

[ZHA14] W. Zhao, J. Ji, G. Liu, Y. Du and M. Cheng, "Design and analysis of a new modular linear flux-reversal permanent-magnet motor," *IEEE Trans. Applied Superconductivity,* vol. 24, no. 3, June, 2014.

[ZHA15a] B. Zhang, M. Cheng, J. Wang and S. Zhu, "Optimization and analysis of a yokeless linear flux-switching permanent magnet machine with high thrust density," *IEEE Trans. Magnetics*, vol. 51, no. 11, pp. 1-4, November, 2015.

[ZHA15b] B. Zhang, M. Cheng and J. Wang, "Comparison of multi-tooth flux-switching linear permanent magnet motors with different magnet polarity and module displacement," *in Proc. LDIA,* 2015.

[ZHE14] P. Zheng, Y. Sui, C. Tong, J. Bai, B. Yu, and F. Lin, "A novel single-phase flux-switching permanent magnet linear generator used for free-piston stirling engine," *J. Applied physics*, vol.115, no. 17E711, pp.17E711-1-17E711-3, 2014.

[ZHE15] P. Zheng, Y. Sui, B. Yu, L. Cheng, and W. Wang, "A tubular single-phase dual-stator flux-switching PM oscillating generator with series magnetic

circuit," *in Proc. Magnetics Conf. (INTERMAG)*, vol., no., pp.1-1, 11-15 May, 2015.

[ZHO11] S. Zhou, H. Yu, M. Hu, C. Jiang, and L. Hao, "Reduction of cogging force in a linear flux-switching permanent-magnet brushless AC machine for direct-drive applications," *IEEE Trans. Magnetic*, vol.47, no.10, pp.3252-3255, October, 2011.

[ZHO12a] S. Zhou, H. Yu, M. Hu, C. Jiang and L. Huang, "Nonlinear equivalent magnetic circuit analysis for linear flux-switching permanent magnet machines," *IEEE Trans. Magnetics*, vol. 48, no. 2, pp. 883-886, February, 2012.

[ZHO12b] P. Zhou, D. Lin, Y. Xiao, N. Lambert and M. A. Rahman, "Temperature dependent demagnetization model of permanent magnet for finite element analysis," *IEEE Trans. Magnetics*, vol.48, no.2, pp.1031-1034, February, 2012.

[ZHU00] Z. Q. Zhu and D. Howe, "Influence of design parameters on cogging torque in permanent magnet machines," *IEEE Trans. Energy Convers.*, vol. 15, no. 4, pp. 407–412, December, 2000.

[ZHU05] Z. Q. Zhu, "Analysis of cogging torque in brushless machines having nonuniformly distributed stator slots and stepped rotor magnets," *IEEE Trans. Magnetics*, vol. 41, no. 10, pp. 3910-3912, October, 2005.

[ZHU07] Z. Q. Zhu and D. Howe, "Electrical machines and drives for electric, hybrid and fuel cell vehicles," *Proc. IEEE*, vol. 95, no. 4, pp. 746–765, April, 2007.

[ZHU08] Z. Q. Zhu, X. Chen, J. T. Chen, D. Howe and J. S. Dai, "Novel linear flux-switching permanent magnet machines," *in Proc. Electrical Machines and Systems Int. Conf.*, pp. 2948-2953, 2008.

[ZHU08a] Z. Q. Zhu, J. T. Chen, Y. Pang, D. Howe, S. Iwasaki and R. Deodhar, "Analysis of a novel multi-tooth flux-switching PM brushless AC machine for high torque direct-drive applications," *IEEE Trans. On Magnetics*, vol.44, no.11, pp.4313-4316, November, 2008.

[ZHU08b] Z. Q. Zhu, X. Chen, D. Howe and J. S. Dai, "Novel linear flux-switching permanent magnet machines," *in Proc. IEEE Electrical Machines and Systems Conf.*, pp.2948-2953, 2008.

[ZHU08c] Z. Q. Zhu, Y. Pang, J. T. Chen, R. L. Owen, D. Howe, S. Iwasaki, R. Deodhar and A. Pride, "Analysis and reduction of magnet eddy current loss

in flux-switching permanent magnet machines," *in Proc. Power Electronic, Machines and Drives (PEMD), Conf.,* pp.120-42, *2008*.

[ZHU08d] Z. Q. Zhu, Y. Pang, J. T. Chen, Z. P. Xia and D. Howe, "Influence of design parameters on the output torque of flux-switching permanent machines," *in Proc. IEEE Vehicle Power and propulsion Conf. (VPPC),* September 3-5,2008.

[ZHU08e] Z. Q. Zhu, X. Chen, D. Howe, and S. Iwasaki, "Electromagnetic Modeling of a Novel Linear Oscillating Actuator," *IEEE Trans. Magnetics*, vol.44, no.11, pp.3855-3858, November, 2008.

[ZHU09] Y. U. Zhu, S. G. Lee, K. S. Chung and Y. H. Cho, "Investigation of auxiliary poles design criteria on reduction of end effect of detent force for PMLSM," *IEEE Trans. Magnetic*, vol.45, no.6, pp.2863-2866, June, 2009.

[ZHU10] Z. Q. Zhu and J. T. Chen, "Advanced flux-switching permanent magnet brushless machines," *IEEE Trans. Magnetic,* vol.46, no.6, pp.1447-1452, June, 2010.

[ZHU11a] Z. Q. Zhu and Z. Azar, "Influence of end-effect and cross-coupling on torque-speed characteristics of switched flux permanent magnet machines," *in Proc. Power Electronics Int. Conf.,* Asia, May 30-June3, 2011.

[ZHU11b] Z. Q. Zhu and X. Liu, "Individual and global optimization of switched flux permanent magnet motors," *in Proc. IEEE Electrical Machines and Systems Conf.*, pp.1-6, 2011.

[ZHU15] Z. Q. Zhu, Z. Z. Wu, D.J. Evans, and W. Q. Chu, "Novel electrical machines having separate PM excitation stator," *IEEE Trans. Magnetics*, vol.51, no.4, pp.1-9, April, 2015.

[ZHU16] Z. Q. Zhu, H. Hua, D. Wu, J. T. Shi and Z. Z. Wu, "Comparative study of partitioned stator machines with different pm excitation stators," *IEEE Trans. Industry Applications*, vol. 52, no. 1, pp. 199-208, January, 2016.

[ZHU97] Z.Q. Zhu, Z.P. Xia, D. Howe, and P. H. Mellor, "Reduction of cogging force in linear permanent magnet motors," *in Proc. IEE-B*, vol.144, no.4, pp.277-282, 1997.

[ZOU12] J. Zou, M. Zhao, Q. Wang, J. Zou, and G. Wu, "Development and analysis of tubular transverse flux machine with permanent magnet excitation," *IEEE Trans. Industrial Electronics,* vol.59, no.5, May, 2012.

[ZYI07] A.W. Zyi, "Design, construction and evaluation of a modified tubular linear

synchronous motor," *PhD thesis*, University of Witwatersrand, Johannesburg, March, 2007.

[ZYL99] A. W. van Zyl, C. G. Jeans, R. J. Cruise and C. F. Landy, "Comparison of force to weight ratios between a single-sided linear synchronous motor and a tubular linear synchronous motor," *in proc. Electric Machines and Drives Int. Conf.*, pp. 571-573, 1999.

Appendices

Appendix A

A.1 Dynamic Performance of the PS-FRPM Linear Machine

The dynamic performance of the PS-FRPM linear machine will be investigated using the Matlab/Simulink. A mathematical model of the machine is described in d-q frame using Park Transformation in which the three stationary phases can be represented by two rotatory phases using the following transformation.

$$\begin{bmatrix} X_d \\ X_q \end{bmatrix} = \frac{2}{3}\begin{bmatrix} cos\ k & cos\left(k-\frac{2\pi}{3}\right) & cos\left(k+\frac{2\pi}{3}\right) \\ -sin\ k & -sin\left(k-\frac{2\pi}{3}\right) & -sin\left(k+\frac{2\pi}{3}\right) \end{bmatrix}\begin{bmatrix} Xa \\ Xb \\ Xc \end{bmatrix} \quad \text{(A.1)}$$

where *X* could be current, voltage, inductance, and k is the angle between the rotation and fixed coordinate system.

The voltage equation of the PS-FRPM linear machine in (abc) frame can be expressed as:

$$\begin{aligned} V_a &= RI_a + \frac{d\psi_a}{dt} \\ V_b &= RI_b + \frac{d\psi_b}{dt} \\ V_c &= RI_c + \frac{d\psi_c}{dt} \end{aligned} \quad \text{(A.2)}$$

$$\begin{aligned} \psi_a &= L_{aa}I_a + L_{ab}I_b + L_{ac}I_c + \psi_{pma} \\ \psi_b &= L_{ba}I_a + L_{bb}I_b + L_{bc}I_c + \psi_{pmb} \\ \psi_c &= L_{ca}I_a + L_{cb}I_b + L_{cc}I_c + \psi_{pmc} \end{aligned} \quad \text{(A.3)}$$

$$\begin{aligned} \psi_{pma} &= \psi_{pm}\cos(\theta) \\ \psi_{pmb} &= \psi_{pm}\cos\left(\theta-\frac{2\pi}{3}\right) \\ \psi_{pmc} &= \psi_{pm}\cos\left(\theta+\frac{2\pi}{3}\right) \end{aligned} \quad \text{(A.4)}$$

The voltage equations of the understudying machine in d-q frame can be obtained from (3.24) and (3.25), respectively. On the other hand, d-q flux linkage can be determined by

$$\psi_d = \psi_{pm} + L_d I_d \tag{A.5}$$

$$\psi_q = L_q I_q \tag{A.6}$$

Current in d-q can be obtained from equations (3.24), (3.25), (A.5) and (A.6)

$$I_d = \frac{1}{L_d}\left[\int \left(V_d + \omega_e L_q I_q - R I_d\right) dt - \psi_{pm}\right] \tag{A.7}$$

$$I_q = \frac{1}{L_d} \int \left(V_q + \omega_e\left(\psi_{pm} + L_d I_d\right) - R I_q\right) dt \tag{A.8}$$

The machine thrust force is calculated by (3.29)

The electromagnetic performance of the PS-FRPM linear machine can be simulated by representing (A.7), (A.8) and (3.29) in Matlab/Simulink as shown in Fig. A.1.

In order to simulate the dynamic performance of the machine, the mechanical equation in which the machine velocity can be determined should be represented and added to the machine model. Usually, the mechanical equation of the linear machine can be expressed as:

$$F_{thrust} = m\frac{dV}{dt} + K_f V + F_{external} \tag{A.9}$$

where m and K_f are mover mass and friction factor respectively. The machine velocity can be calculated according to equation (A.9) as follows.

$$V = \frac{1}{m} \int \left(F_{thrust} - F_{external} - K_f V\right) dt \tag{A.10}$$

Fig. A.2 displays the Simulink model to calculate machine velocity

Fig. A.1 Simulink model representing current and force calculations.

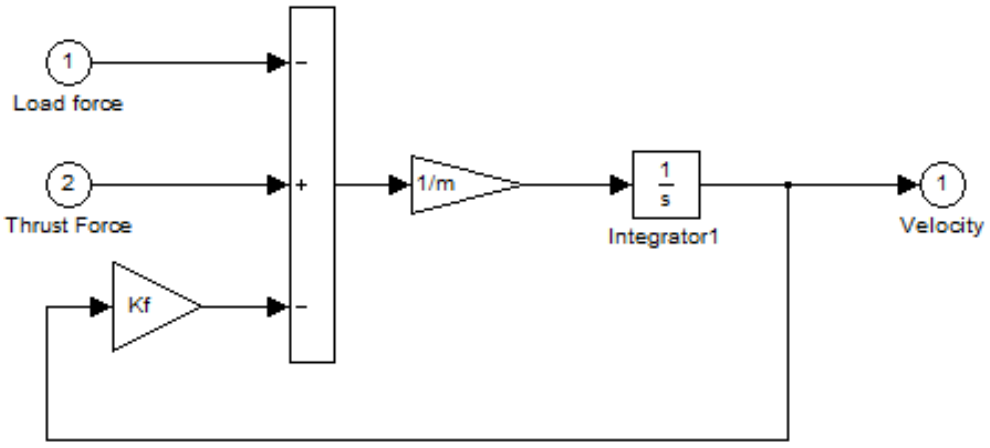

Fig. A.2 Simulink model representing velocity calculation.

A.2 Field Oriented Control

It has been confirmed that field orient control strategy is an appropriate choice for low speed applications with high performance drive. In this method both the machine speed and current are used as feedbacks. FOC is known as indirect control method since the force, which is produced by the machine is controlled by the current controller.

FOC method has been used to control PS-FRPM linear machine in this section. Fig. A.3 presents the control structure. It can be seen that there are two control loops, i.e. velocity loop that controls the machine velocity and current loops (for both i_d and i_q), which control the machine thrust force.

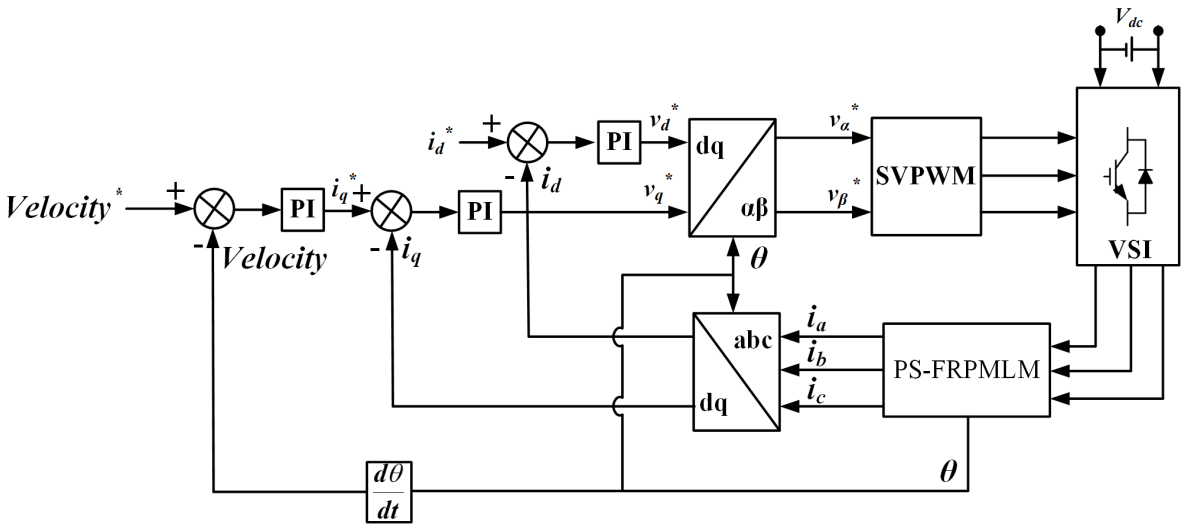

Fig. A.3 Schematic of the PS-FRPM linear machine drive.

Fig. A.4 shows the velocity of the machine under different load conditions, i.e. no-load, full load. It is obvious that the response time of the velocity regulator, when the machine load condition is changed from no-load to full load and vice versa is less than 0.1s. It can be concluded that the machine velocity remains almost constant during the changing of the load. The thrust forces under no-load and load condition are presented in Fig. A.5. It can be noted that the overshoot of the thrust force when the load condition is changed is very small, which means the regulators are tuned very well to have this fact response. Mover position is shown in while illustrates armature current with different load conditions.

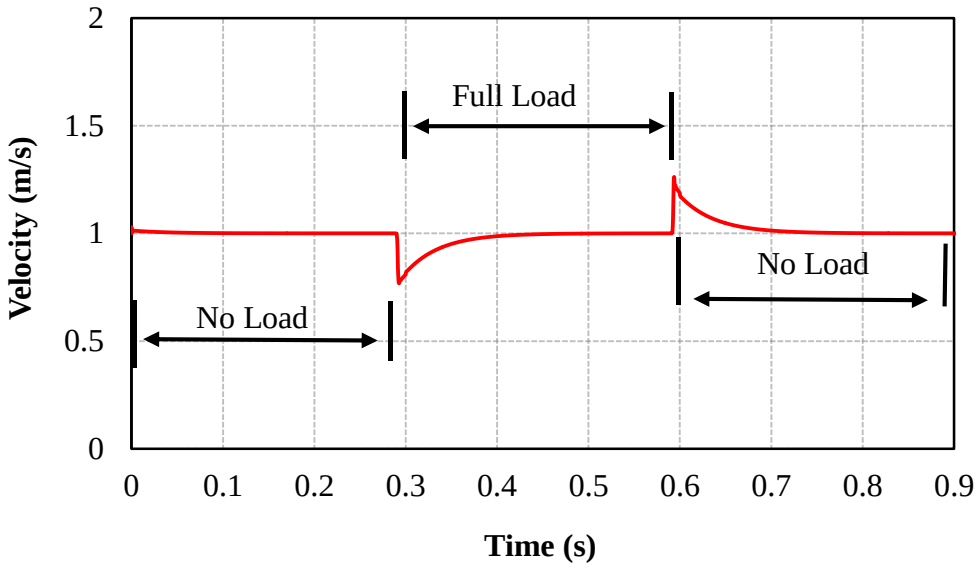

Fig. A.4 Velocity with different load conditions.

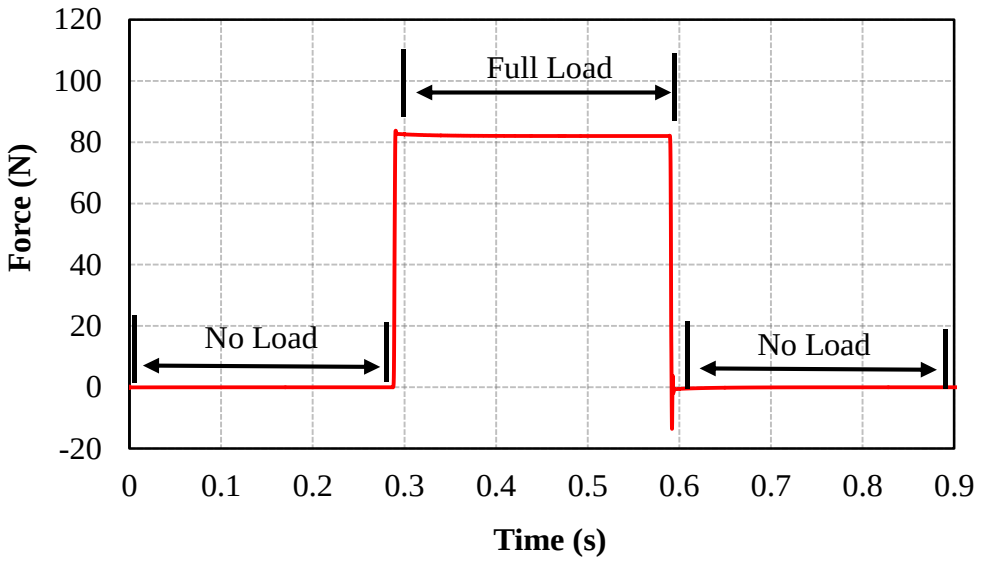

Fig. A.5 Thrust force with different load conditions.

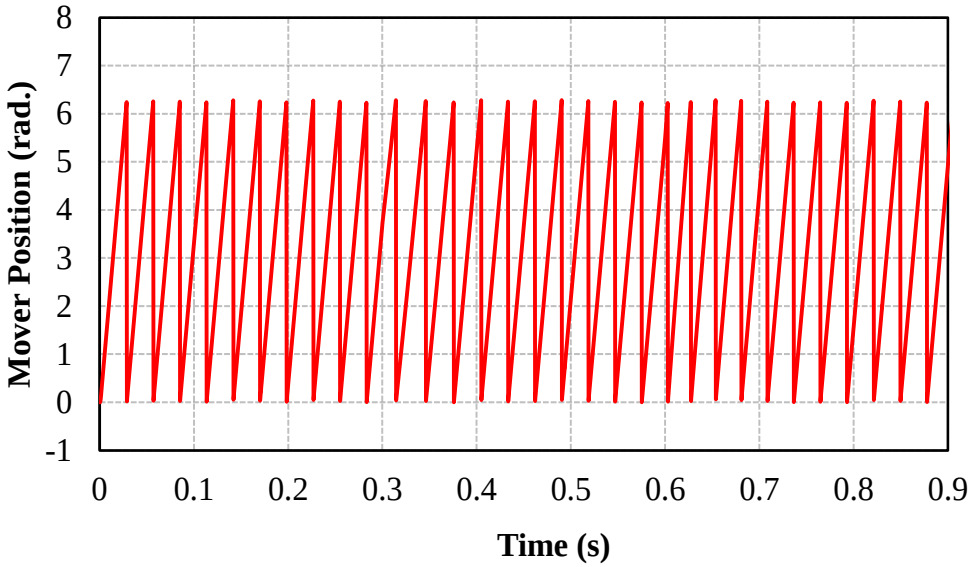

Fig. A.6 Mover position with different load conditions.

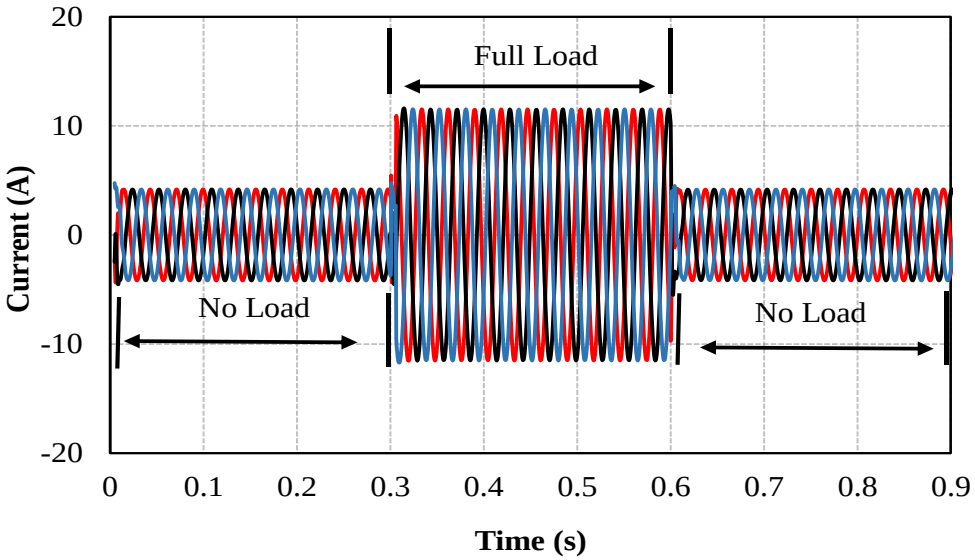

Fig. A.7 Armature current with different load conditions.

Appendix B

B.1Prototype Drawings

The prototype for the PS-FRPM linear machine is shown in B.1, while B.2 and Fig. B.3 illustrate cogging force test rig and a side view of the porotype, respectively. It is worth mentioning that the definition of each part in is listed in Table B.1. On the other hand, the outer stator lamination drawing and the mover drawing are depicted in B.4. The BH curves of the outer stator and the one of the inner stator and the mover are shown in Fig. B.5.

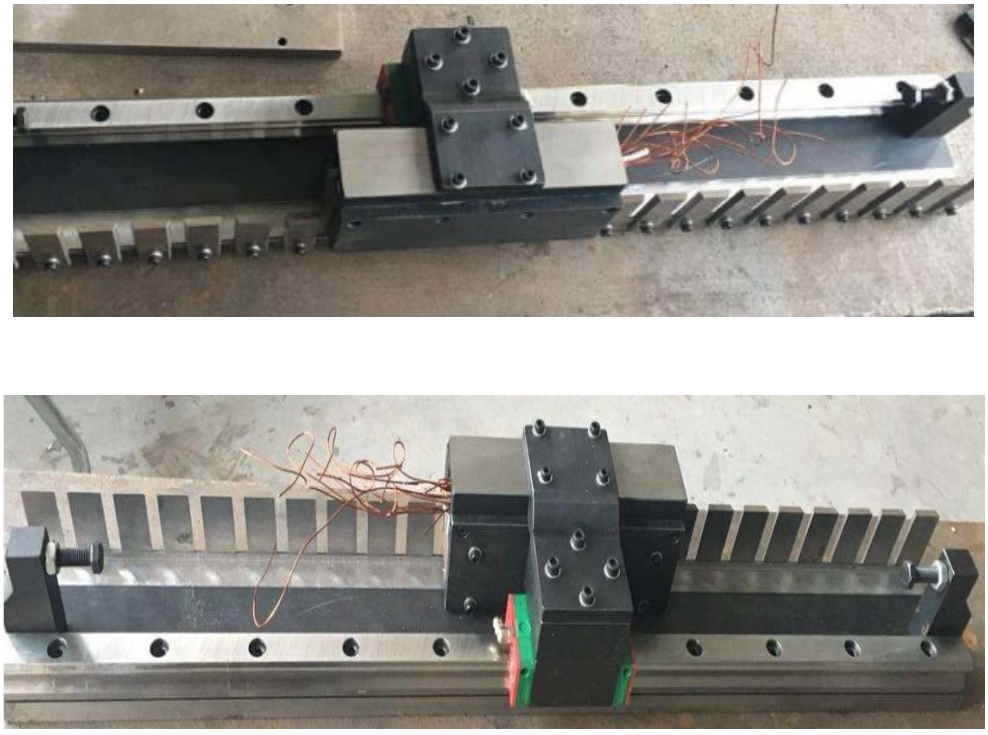

Fig. B.1 Prototype of PS-FRPM linear machine.

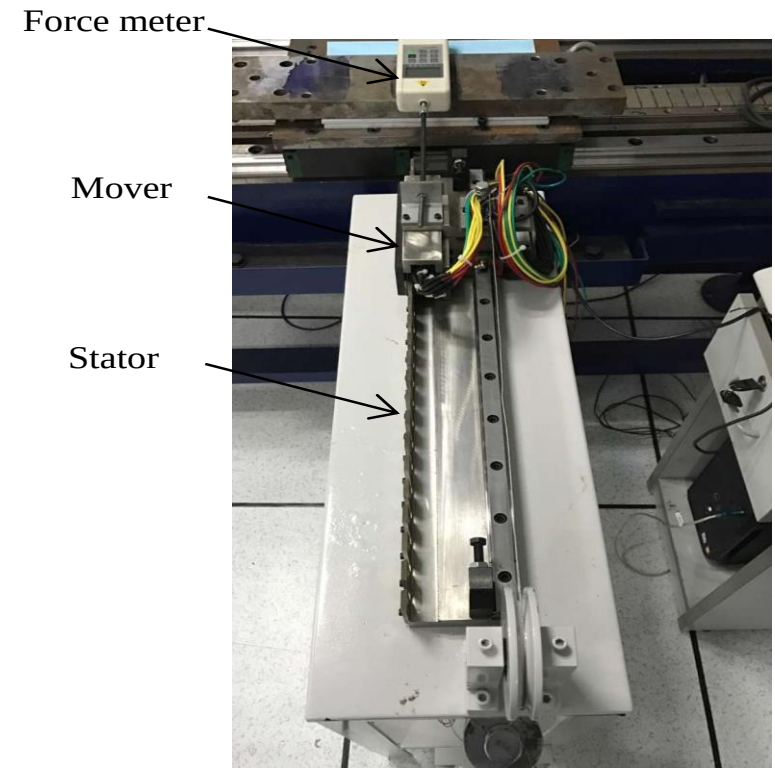

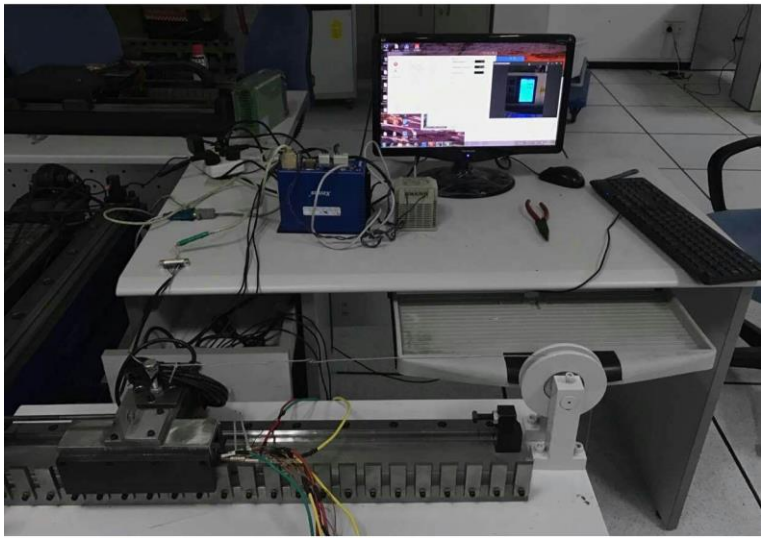

Fig. B.2 Experimental test rig.

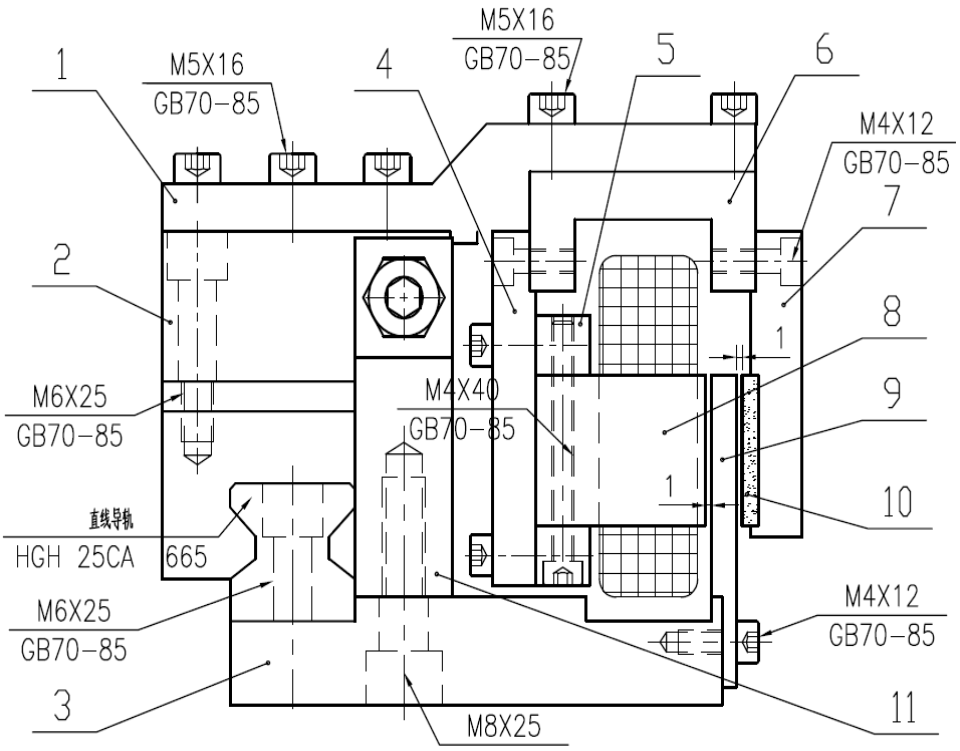

Fig. B.3 Side view of the prototype.

Table B.1 Definition of the parts in

Part No.	Definition
1	Machine frame
2	Slider
3	Mover pieces holder
4	Stator frame
5	Stator 1 back-iron
6	Stators holder
7	PM back-iron
8	Stator lamination
9	The mover
10	The PM

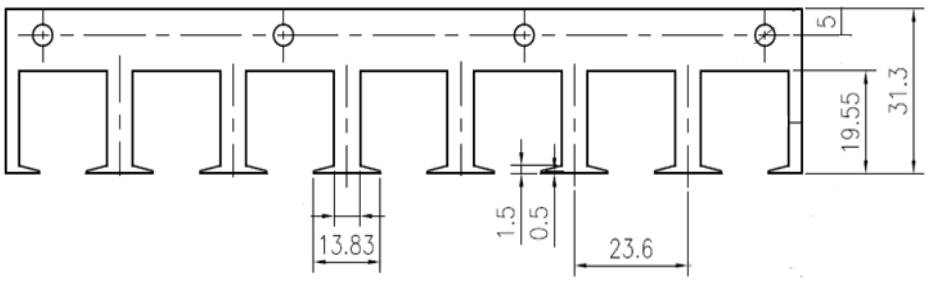

(a) Outer stator

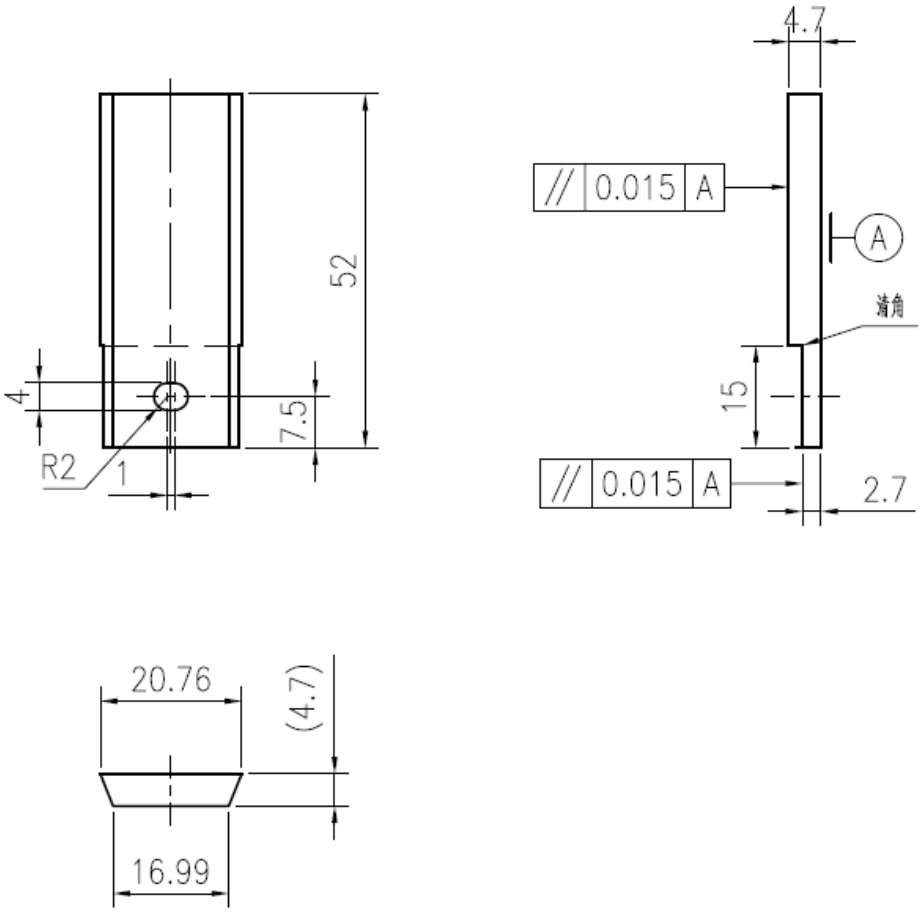

(b) Mover

Fig. B.4 Prototype drawing.

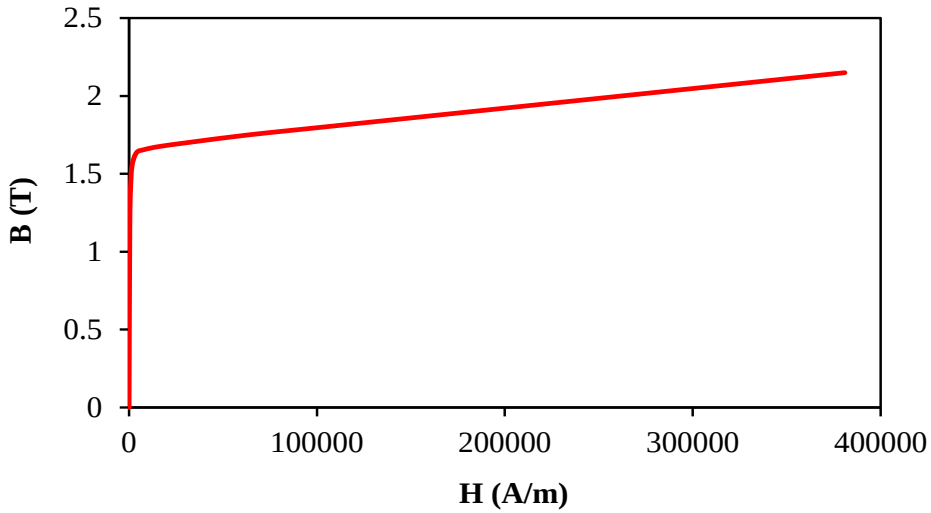

(a) BH curve of the outer stator laminations

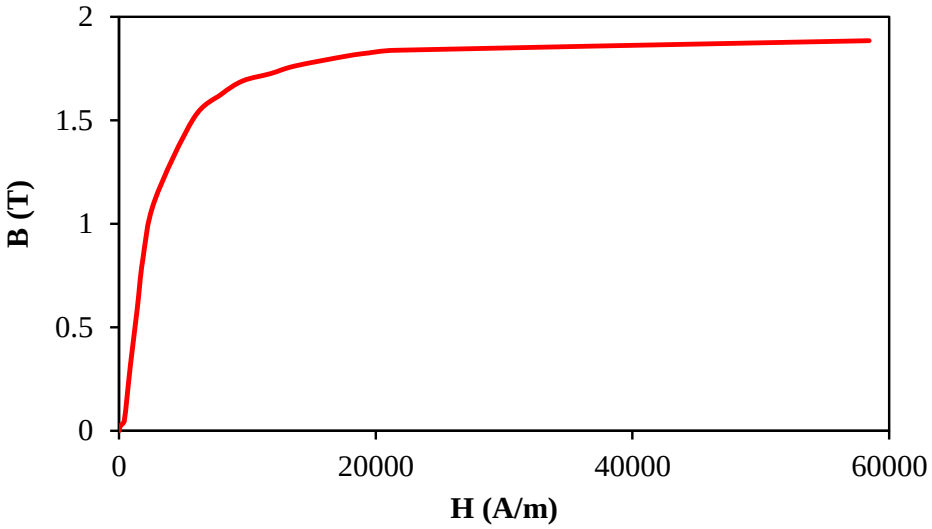

(b) BH curve of the inner stator and the mover

Fig. B.5 BH curves.

Publications

Journal papers

[1]. A. L. Shuraiji, Z. Q. Zhu and Q. F. Lu, "A novel partitioned stator flux reversal permanent magnet linear machine*," IEEE Trans. Magnetics*, vol. 52, no. 1, pp. 1-6, Jan. 2016.

[2]. Z. Q. Zhu, A. L. Shuraiji and Q. F. Lu, "Comparative study of tubular partitioned stator permanent magnet machines," *IEEE Trans. Magnetics*, vol. 52, no. 1, pp. 1-7, Jan. 2016.

[3]. Z. Q. Zhu, A. L. Shuraiji and Q. F. Lu, "Single-phase short stroke permanent magnet tubular machines with partitioned stator," submitted to *IEEE Trans. Magnetics.*

Conference papers

[1]. A. L. Shuraiji, Z. Q. Zhu and Q. F. Lu, "A novel partitioned stator flux reversal permanent magnet linear machine," *The tenth International Conference on Ecological Vehicles and Renewable Energies (EVER15),* Monti-Carlo, Monaco, March 31- April 2, 2015.

[2]. Z. Q. Zhu, A. L. Shuraiji and Q. F. Lu, "Comparative study of tubular partitioned stator permanent magnet machines," *The tenth International Conference on Ecological Vehicles and Renewable Energies (EVER15),* Monti-Carlo, Monaco March 31- April 2, 2015.

[3]. A. L. Shuraiji, Z. Q. Zhu and Q. F. Lu, "Comparative study of two flux reversal permeant magnet linear machine topologies," *The tenth International Symposium on Linear Drives for Industry Applications (LDIA15*), Aachen, Germany, July 27-29, 2015.

[4]. A. L. Shuraiji, Z. Q. Zhu and Q. F. Lu, "Comparative study of different doubly salient PM tubular machine topologies," *The eighth International Conference on Power Electronic, Machines and Drives (PEMD16),* April 19-21, Glasgow, Scotland, UK.